Real Time Analysis of Atmospheric Single Particles in Urban Environments using Aerosol Time of Flight Mass Spectrometry

A thesis submitted to

THE NATIONAL UNIVERSITY OF IRELAND, CORK

for the degree of

DOCTOR OF PHILOSOPHY

By

Eoin Joseph McGillicuddy

Based on research carried out at

Department of Chemistry
&
Environmental Research Institute

Supervisor

Professor John Sodeau

Head of Department

Professor Martyn Pemble

University College Cork _____ December 2014

Table of Contents

Declaration

The work presented in this thesis was performed at the Department of Chemistry and Environmental Research Institute, University College Cork during the academic years 2009 - 2014. Unless otherwise acknowledged, this thesis is the independent work of the author. This material has not been submitted to any institution, including University College Cork, for the purpose of obtaining any other degree or any other qualification.

_____

Eoin J McGillicuddy

Dedication

Do m'athair agus mo mháthair

Quotation

Eochair feasa foghlaim

Preface

The work presented in this thesis belongs to a body of research carried out at University College Cork and during field studies in Paris and Barcelona. This work is linked to an EU funded project titled Megacities: Emissions, urban, regional and Global Atmospheric POLlution and climate effects, and Integrated tools for assessment and mitigation (MEGAPOLI) - Project Reference Number: (FP7-ENV-2007.1.1.2.1) and a Marie Curie Action project titled Solving Aerosol Problem by Using Synergistic Strategies (SAPUSS) - Project Reference Number: (FP7-PEOPLE-2009-IEF-254773)**.**

In co-operation with Dr Robert Healy and Dr Ian O'Connor, this author was responsible for the operation and maintenance of UCC's aerosol time-of-flight mass spectrometer (ATOFMS) during the MEGAPOLI monitoring campaign in Paris. The ATOFMS deployed in Barcelona during the SAPUSS campaign was on loan from Professor Deborah S. Gross of Carleton College MN USA and was operated and maintained throughout the deployment by the author. The ATOFMS data analysis presented and discussed in this work was carried out by this author with the exception of the scaling procedure carried out on the Paris dataset by Dr Robert Healy and the ART-2a analysis carried out on the Barcelona dataset, which was completed by Dr Manuel Dall'Osto, and used to inter-compare different ATOFMS analysis methods. The ATOFMS measurements were inter-compared with coincident measurements carried out during the monitoring campaigns. In Paris, AMS and BC data were provided by PSI and IfT, while metal concentrations in Paris were provided by LCSE and LCE – IRA. In Barcelona, ATOFMS measurements were compared with PIXE measurements carried out by Dr Franco Lucarelli and Dr Silvia Nava at the LABEC laboratory of INFN in Florence. Further to the ATOFMS operated by the author a second ATOFMS, operated by Dr David Beddows and Dr Johanna Gietl with data analysis completed by Dr Manuel Dall'Osto, was also included in the comparison with the PIXE analysis.

Acknowledgements

Research is not a singular endeavour and it is only right to acknowledge those who have helped (and possibly hindered) the completion of this work. Firstly I would like to thank the man who encouraged me to commence this journey, my very own Pied Piper, Professor John Sodeau. I would like to take this occasion to express my sincere gratitude to John for the opportunity he gave me to complete these studies and supervision he has provided throughout the last few years. I would also like to thank Dr John Wenger for all the advice, encouragement and opportunity he has given me through the years. The knowledge and insight into the world of atmospheric research and specifically the ATOFMS given to me by Dr Robert Healy has been invaluable. I sincerely thank Rob for showing me the ropes of the instrument and allowing me to become part of the MEGAPOLI experience. Rob is the most approachable, helpful and understanding post-doc I could have asked for and I thank you for all the help.

During my years in the CRAC lab I have come into contact with many people who I have enjoyed nights out and general shenanigans with, therefore I would like to thank all these people for their friendship during my studies; Ian, Dave O'Connor, Ruairi, Jovanna, Eoin "Legs" Wilson, Trevor, Dave Healy, Stig, Arnaud, Jenny, Danny, Yang, Dean, Iusti, Ivan, Stephen and everyone else who I have worked with in the lab through my time here. I would like to mention a few people specifically for their friendship throughout my studies, Dave Healy for driving to Barcelona with me and making enough ice-cream stops to cross the Sahara. My gym buddy Dave O'Connor who along with Ruairi, Trevor and "Legs" Wilson made up many a good quiz team (trophies prove this). Jovanna I would like to thank for all the chats to break the silence in the ERI and also the adventure to Corsica. I must pay special tribute to Ian O'Connor for joining me on many of the adventures I have undertaken during my time in the CRAC lab, be they campaigns, conferences or rugby matches… I will get you up the Eiffel Tower someday.

I have been fortunate in my time in the CRAC lab to travel to many locations with members of the group. These journeys to Paris, Barcelona, Orlando, Grenada,

Prague, Santorini, Dublin and Galway have all been made more enjoyable by the presence and carry on of my partners in crime. Sorry about the snoring though.

List of abbreviations and acronyms

AFL	Aerodynamic Focussing Lens
AMS	Aerosol Mass Spectrometer
AQEG	Air Quality Expert Group
ART-2a	Adaptive resonance theory-based neural network
ATOFMS	Aerosol Time of Flight Mass Spectrometer
BBOA	Biomass Burning Organic Aerosol
BC	Black Carbon
CCN	Cloud Condensation Nuclei
COA	Cooking-related Organic Aerosol
D/I	Desorption/Ionisation
D_a	Aerodynamic Diameter
DAURE	Determination of the sources of atmospheric Aerosols in Urban and Rural Environments in the Western Mediterranean
DMS	Dimethyl Sulfide
DRCL	Decoupled Residual/Convective Layer
EC	Elemental Carbon
ECD	Effective Cut Diameter
ENCHILADA	Environmental chemistry through intelligent atmospheric data analysis
EPA	Environmental Protection Agency
ETS	Environmental Tobacco Smoke
GC-MS	Gas Chromatography Mass Spectrometry
GF	Hygroscopic Growth Factors
HOA	Hydrocarbon-like Organic Aerosol
HPLC	High-Performance Liquid Chromatography
HR-ToF-AMS	High-Resolution Time-of-Flight Aerosol Mass Spectrometer

HYSPLIT	Hybrid Single Particle Lagrangian Integrated Trajectory Model
IARC	International Agency for Research on Cancer
IC	Ion Chromatography
ICP-MS	Inductively Coupled Plasma Mass Spectrometry
IN	Ice Nuclei
IPCC	Intergovernmental Panel on Climate Change
LAMPAS	Laser Mass Analysis of Particles in the Airborne State
LHVP	Laboratoire d'Hygiène de la Ville de Paris
LPDM	Lagrangian Particle Dispersion Model
LV-OOA	Low Volatility Oxidized Organic Aerosols
MAAP	Multi-Angle Absorption Photometer
MEGAPOLI	Megacities: Emissions, urban, regional and Global Atmospheric Pollution and climate effects, and integrated tools for assessment and mitigation
MOUDI	Micro-Orifice Uniform-Deposit Impactor
MS	Mass Spectrometry
MSA	Methane Sulfonic Acid
Nd:YAG	Neodymium-doped Yttrium Aluminium Garnet
OC	Organic Carbon
OM	Organic Matter
OOA	Oxidized Organic Aerosols
PAH	Polycyclic Aromatic Hydrocarbon
PALMS	Particle Analysis by Laser Mass Spectrometer
PILS	Particle Into Liquid Sampler
PIXE	Particle-induced X-ray emission
PM	Particulate Matter
PMF	Positive Matrix Factorisation

PMT	Photomultiplier tube
POA	Primary Organic Aerosol
PSAT	Particulate matter Source Apportionment Technology
PSL	Polystyrene Latex spheres
PTR-MS	Proton Transfer Reaction Mass Spectrometer
RB	Rural Background
rBC	Refactory Black Carbon
RF	Radiative Forcing
RH	Relative Humidity
RS	Road Site
RSMS-II	Rapid Single Particle Mass Spectrometer II
SAPUSS	Solving Aerosol Problems Using Synergistic Strategies
SIA	Secondary Inorganic Aerosol
SIE	Selective Ion Electrodes
SML	Surface Mixed Layer
SOA	Secondary Organic Aerosol
St	Stokes number
SV-OOA	Semi-volatile Oxidized Organic Aerosols
TC	Torre Collserola
TDMPS	Twin Differential Mobility Particle Sizer
TM	Torre Mapfre
TMA	Trimethylamine
TOF	Time-of-Flight
UB	Urban Background
VOC	Volatile Organic Compounds
WBOA	Wood Burning Organic Aerosol
WHO	World Health Organization

WMB	Western Mediterranean Basin
XRF	X-ray fluorescence
YAADA	Yet Another ATOFMS Data Analyzer

Abstract

The composition of atmospheric aerosols is an important factor in determining their impact on climate and health. In order to determine the size-resolved chemical composition of single particles in real-time an aerosol time-of-flight mass spectrometer (ATOFMS) was deployed at urban background sites in Paris and Barcelona during the MEGAPOLI and SAPUSS monitoring campaigns respectively.

The particle types detected during the MEGAPOLI campaign included several carbonaceous species, metal-containing types and sea-salt. Elemental carbon particle types were highly abundant, with 86% due to fossil fuel combustion and 14% attributed to biomass burning. Furthermore, 79% of the EC was apportioned to local emissions and 21% to continental transport. The carbonaceous particle types were compared with quantitative measurements from other instruments, and while direct correlations using particle counts were poor, scaling of the ATOFMS counts greatly improved the relationship.

During SAPUSS carbonaceous species, sea-salt, dust, vegetative debris and various metal-containing particle types were identified. Throughout the campaign the site was influenced by air masses altering the composition of particles detected. During North African air masses the city was heavily influenced by Saharan dust. A regional stagnation was also observed towards the end of the campaign leading to a large increase in carbonaceous particle counts. While the ATOFMS provides a list of particle types present during the measurement campaigns, the data presented is not directly quantitative. The quantitative response of the ATOFMS to metals was examined by comparing the ion signals within particle mass spectra and to hourly mass concentrations of; Na, K, Ca, Ti, V, Cr, Mn, Fe, Zn and Pb. The ATOFMS was found to have varying correlations with these metals depending on several issues such as matrix effects. The strongest correlations were observed for Al, Fe, Zn, Mn and Pb.

Overall the results of this work serve to highlight the excellent ability of the ATOFMS technique in providing composition and mixing state information on atmospheric particles at high time resolution. However they also show its limitations in delivering quantitative information directly.

1 Introduction

Contents

1.1 Aerosols

Aerosols are defined as relatively stable suspensions of solid or liquid particles in a gas (Finlayson-Pitts and Pitts, 2000). Aerosols therefore include both the particles and the gas in which the particles are suspended. However, in atmospheric chemistry literature usage of the term is rather loose (Wayne, 2000), and the term aerosol is often used to just denote the particles (Finlayson-Pitts and Pitts, 2000). Aerosols present in the atmosphere can originate from natural or anthropogenic sources. The interest in studying physical and chemical properties of aerosol is due to the actual and suspected effects of aerosol on both global climate and human health. The following chapter will present a brief introduction to the sources, composition, physical properties and effects of atmospheric aerosols.

1.2 Sources and Chemical Composition of Aerosols

Particles can be released directly into the atmosphere, or may be generated *in situ* through chemical reactions. Particles injected directly into the atmosphere are termed primary emissions whereas those formed in the atmosphere due to chemical processing, such as gas to particle conversion, nucleation or condensation of species onto existing particles, are termed secondary emissions (Calvo et al., 2013; Finlayson-Pitts and Pitts, 2000; Hobbs, 2000; Monks et al., 2009; Pöschl, 2005). The composition of atmospheric aerosols varies depending on the location, with urban and remote sites having different aerosol regimes (Finlayson-Pitts and Pitts, 2000).

Both natural and anthropogenic emissions have primary and secondary components. Table 1.1 provides a brief list of the main chemical species present in aerosols and the major sources of these components (AQEG, 2005). Natural sources of atmospheric aerosols include: biogenic emissions, mineral dust, sea spray, volcanic eruptions and lightning (Calvo et al., 2013).

Primary components	Major Sources
Sodium chloride	Sea salt.
Elemental carbon	Black carbon (soot) is formed during high temperature combustion of fossil fuels such as coal, natural gas and oil (diesel and petrol) and biomass fuels such as wood chips.
Trace metals	These are present at very low concentrations and include Pb, Cd, Ni, Cr, Zn and Mg. They are generated by metallurgical processes, such as steel making, or by impurities found in or additives mixed into fuels used by industry. Metals in particles are also derived from mechanical abrasion processes, e.g. during vehicle motion and break and tyre wear.
Mineral components	These minerals are found in coarse dusts from quarrying, construction and demolition work and from wind-driven dusts. They include Al, Si, Fe and Ca.
Secondary components	**Major Sources**
Sulphate	Formed by the oxidation of sulphur dioxide (SO_2) in the atmosphere to form sulphuric acid, which can react with ammonia (NH_3) to give ammonium sulphate.
Nitrate	Formed by the oxidation of nitrogen oxides (NO_x – which consists of nitric oxide (nitrogen monoxide, NO) and nitrogen dioxide (NO_2) in the atmosphere to form nitric acid, which can react with NH_3 to give ammonium nitrate. Also present as sodium nitrate.
Water	Some components of the aerosol form of particulate matter, such as ammonium sulphates and ammonium nitrates, take up water from the atmosphere.
Primary and secondary components	**Major Sources**
Organic carbon	Primary organic carbon comes rom traffic or industrial combustion sources. Secondary organic carbon comes from the oxidation of volatile organic compounds (VOCs). There may be several hundred individual components. Some of these trace organic compounds, such as certain polycyclic aromatic hydrocarbons, are highly toxic.

Table 1.1 Components of particulate matter. Adapted from (AQEG, 2005)

Biogenic particle emissions can be due to: seeds, pollen, spores, bacteria, protozoa, fungi, viruses, algae, and fragments of animals and plants (Hobbs, 2000), while biogenic emissions of Volatile Organic Compounds (VOCs) can form secondary particles namely Secondary Organic Aerosol (SOA) (Pöschl, 2005). Further, wildfires and forest fires are a natural source of biomass burning released carbonaceous particles.

Mineral dust emissions are generated mainly by the action of wind on the Earth's surface. The major sources of dust are deserts, dry lake beds and semi-arid surfaces, although any soil may be a source of mineral/crustal emissions (Calvo et al., 2013). The composition of mineral dust aerosol reflects the soil from which it was derived and includes components like aluminium, calcium, silicates and iron (AQEG, 2005; Duffy, 2011). For wind-blown particles to be injected into the atmosphere the wind

has to be above a frictional speed, which is dependent on the size and contents of the particle. (Hobbs, 2000).

The oceans are also an important source of atmospheric aerosols. Primary marine aerosol results in sea salt minerals such as sodium, chloride, calcium, magnesium and sulfate being emitted to the atmosphere as a consequence of mechanical disruption of the sea surface (Finlayson-Pitts and Pitts, 2000; Hobbs, 2000; O'Dowd et al., 1997). Secondary marine aerosols are formed by gas-to-particle conversion, heterogeneous nucleation and condensation or homogeneous nucleation (O'Dowd et al., 1997). Secondary marine aerosol formation results in the formation of non-sea-salt (NSS) sulfate and organic particles (O'Dowd et al., 1997). Marine aerosol is in fact a major contributor to the atmospheric sulfur budget because phytoplankton produce dimethyl sulfide (DMS) (Ayers and Gillett, 2000; Wayne, 2000). The subsequent atmospheric oxidation of DMS results in the formation of methane sulfonic acid (MSA) and NSS-sulfate which causes an increase in cloud loading as it acts as cloud condensation nuclei, CCN (Ayers and Gillett, 2000; Wayne, 2000).

Volcanic eruptions, while unpredictable, are an important source of natural primary and secondary aerosols. Primary particles emitted are in the form of ash and contain contributions from many species including S, Pb, Cr, Cu, Fe, Ti, V, A1, Ba, Ca, K and Na (Allard et al., 2000). The main secondary contribution from volcanic eruptions is secondary sulfate due to the vast quantities of SO_2 released by eruptions; SO_2 can undergo oxidation in the atmosphere to produce sulfate particles (Calvo et al., 2013; Thomas et al., 2009). Another natural source of secondary species is lightning because it is a natural source of nitrogen oxide (NO_X) gases which are involved in the atmospheric formation of nitrate in aerosols (Calvo et al., 2013).

Anthropogenic emissions sources include traffic, industrial activities, domestic fuel burning, power generation and incineration (Calvo et al., 2013). Carbonaceous aerosol is a major component released by anthropogenic activity. It consists of Elemental Carbon (EC) or Black Carbon (BC) and Organic Carbon (OC). The terms EC and BC are often used interchangeably with the difference between the two largely due to the analysis method used. EC is determined using thermal methods while BC is measured by optical methods (Lavanchy et al., 1999). The EC emitted by combustion is directly emitted into the atmosphere due to the incomplete burning

of fuels (i.e. primary emissions). However, OC can be both primary and secondary in origin with the contribution changing depending on the time of year and meteorological conditions (Minguillón et al., 2011; Pio et al., 2011; Yu et al., 2004). For example, in Barcelona it was found that ~47 % of the OC was primary whereas at a rural site, downwind of the city, the OC was predominantly of secondary origin (~85 %) (Minguillón et al., 2011).

The major anthropogenic sources of carbonaceous particles include fossil fuel burning from vehicular traffic, power generation, industrial activities, shipping, and home heating. Carbonaceous particles also result from incineration, biomass burning, cooking and tobacco smoke (Dall'Osto et al., 2012; Dennis et al., 2002; Healy et al., 2009; Morawska and Zhang, 2002; Pöschl, 2005). Traffic emissions include: carbonaceous particles related to the combustion of gasoline and diesel fuels, along with non-exhaust emissions such as road dust re-suspension and tyre and brake wear (Amato et al., 2009a; Amato et al., 2009b; Calvo et al., 2013; Dall'Osto et al., 2014). Industrial and incineration emissions can be a source of many metallic elements, such as V and Ni from shipping (Healy et al., 2009), Pb and Zn from incineration (Moffet et al., 2008) and Fe, Zn, Ni and Pb from steelworks (Dall'Osto et al., 2008). Other sources of metals in particles are exhaust and non-exhaust traffic emissions, biomass combustion, coal combustion and other industrial processes (Sanderson et al., 2014). Crustal elements and dust can also be released into the atmosphere, from a range of other human activities including mining, quarrying, building and agricultural practices (Calvo et al., 2013; Hobbs, 2000)

Emissions of the inorganic gases SO_2, NO_X, and ammonia can lead to the formation of secondary particles in the atmosphere. In addition to the natural sources, anthropogenic emissions produce a large amount of these gases, e.g., SO_2 from coal combustion and shipping, NO_X from traffic emissions and ammonia from farming, traffic and industrial activities (Finlayson-Pitts and Pitts, 2000). SO_2 can be oxidised to form H_2SO_4, while NO_X can undergo oxidation to form HNO_3. These acidic species can be neutralised by ammonia to form ammonium sulfate and ammonium nitrate particles respectively. Under atmospheric conditions, the production of ammonium sulfate is favoured and most of the sulfate must therefore be neutralised prior to ammonium nitrate production (Finlayson-Pitts and Pitts, 2000; Pathak et al.,

2009). While ammonia is the major base present in the atmosphere, amines have also been observed in particles as aminium salts of nitrate and sulfate (Pratt et al., 2009). Amines can be emitted by industrial activities, traffic, farming and sewage plants (Angelino et al., 2001; Rehbein et al., 2011). Further to the production of secondary species through the homogeneous gaseous reactions mentioned above, heterogeneous reactions may occur between gaseous species and particles, e.g., the reaction of gaseous HNO_3 with sea salt particles (Finlayson-Pitts and Pitts, 2000).

$$NaCl_{(S)} + HNO_{3(g)} \rightarrow HCl_{(g)} + NaNO_{3(s)}$$

Secondary species may also be formed through aqueous phase reactions in fogs, clouds and on particle surfaces (Finlayson-Pitts and Pitts, 2000).

1.3 Aerosol Physical Properties

1.3.1 Size

The size of atmospheric particles is measured and expressed as an effective diameter. Several types of effective diameters are used; the principle one is the aerodynamic diameter (D_a), which is defined as the diameter of a sphere of unit density, 1 g cm^{-3}, that has the same terminal falling speed in air as the particle under consideration (Finlayson-Pitts and Pitts, 2000). Other effective diameter measurements include mass-normalized diameter, electrical-mobility diameter, volume-equivalent diameter and the geometric or physical diameter (Buseck and Adachi, 2008).

The size distribution of particles is broken into several modes, which are linked to their likely origins, chemical characteristics and removal processes (Finlayson-Pitts and Pitts, 2000; Whitby et al., 1974; Willeke and Whitby, 1975). The most general separation of particles, based on particle size, splits particles into fine and coarse modes. Particles with diameters < 2.5 μm are identified as fine particles while particles with diameters > 2.5 μm are described as coarse particles (Finlayson-Pitts and Pitts, 2000). The fine mode of the distribution contains most of the particle number while the coarse mode of the distribution can contain most of the particle volume (Willeke and Whitby, 1975). The fine mode of the particle distribution can

be further separated into nucleation, Aitken and accumulation modes. Nucleation mode particles are in the size range < 0.01 μm. Particles with diameters between 0.01 and 0.08 μm are in the transient or Aitken nuclei range and those with diameters between ~ 0.08 and 1-2 μm are assigned to the accumulation range. (Finlayson-Pitts and Pitts, 2000). The size distribution of atmospheric particles is shown in Figure 1.1.

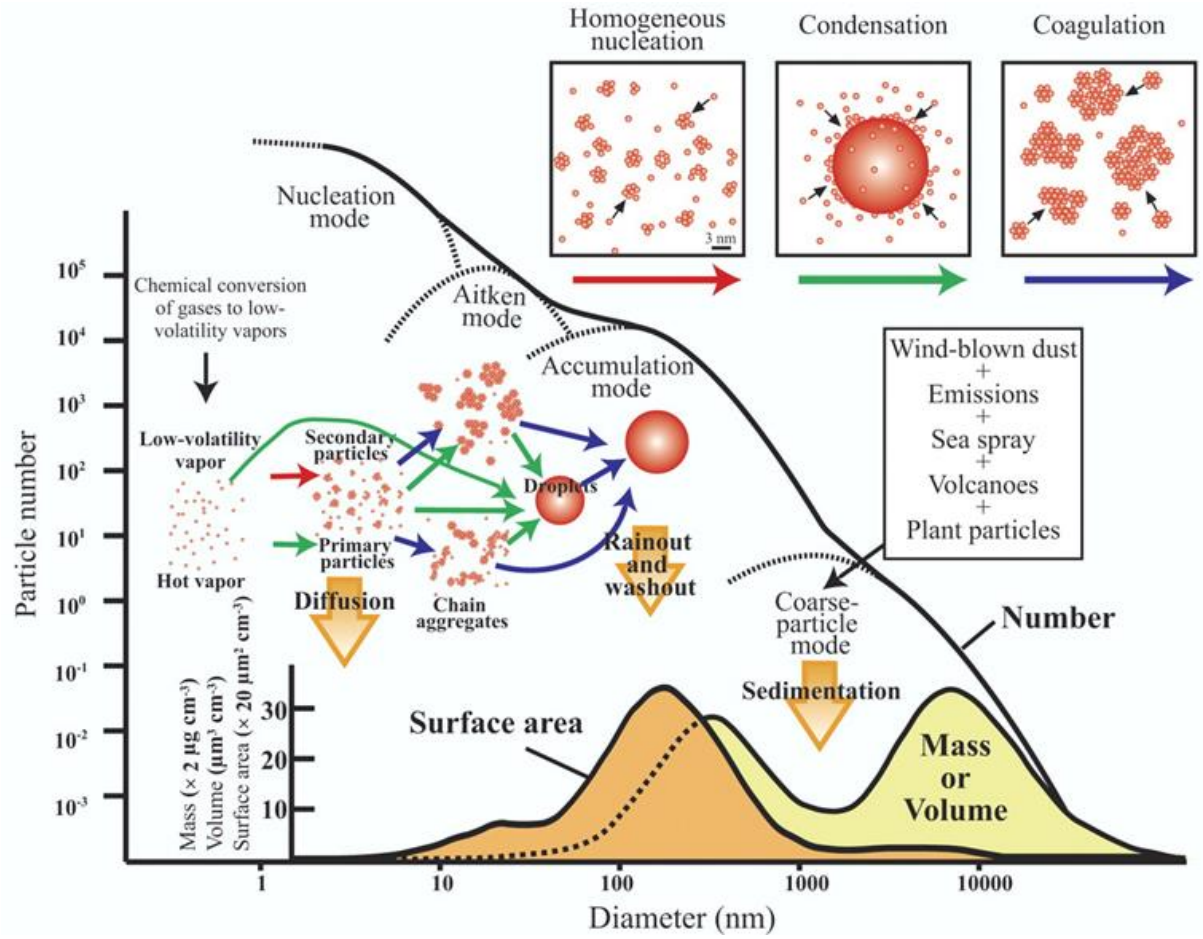

Figure 1.1 Schematic of the size distribution of atmospheric aerosol particles for various parameters (number, N; mass, M; volume, V; surface area, S). (Buseck and Adachi, 2008).

Nucleation mode particles originate through gas-to-particulate conversion of hot combustion vapour after condensation. Sulfur, nitrogen and organic carbonaceous

species all undergo gas-to-particulate conversion to form particles. These particles initially have small diameter < 10 nm although the high number of these particles results in coagulation and the formation of larger particles in the Aitken mode (Finlayson-Pitts and Pitts, 2000; Hobbs, 2000). Accumulation mode particles are formed by the coagulation of smaller particles or the condensation of gases onto existing particles and particles left behind after cloud drops evaporate (Hobbs, 2000). Finally, coarse mode particles are usually produced by mechanical processes such as grinding, wind, or erosion and include sea-salt, dust and fly ash (Hobbs, 2000; Willeke and Whitby, 1975). Figure 1.2 shows the size distribution of atmospheric aerosols from specific sources.

The size of atmospheric particles is an important factor as the residence time of the particle is influenced by the diameter (Hobbs, 2000). Large particles (> 20 μm) have a residence time of around 1 day and can be lost via sedimentation caused by gravity, impaction onto surfaces and precipitation. Small particles (< 0.01 μm) have much shorter residence times due to coagulation (forming larger particles) and diffusion into clouds. Particles in the range 0.2 to 2 μm exhibit longer residence times often extending to several days due to the low particle numbers found in this mode, which inhibits coagulation, leaving wet and dry deposition as the major sink in this size range. The extended residence time of these particles allows for their long range transport (Finlayson-Pitts and Pitts, 2000; Hobbs, 2000).

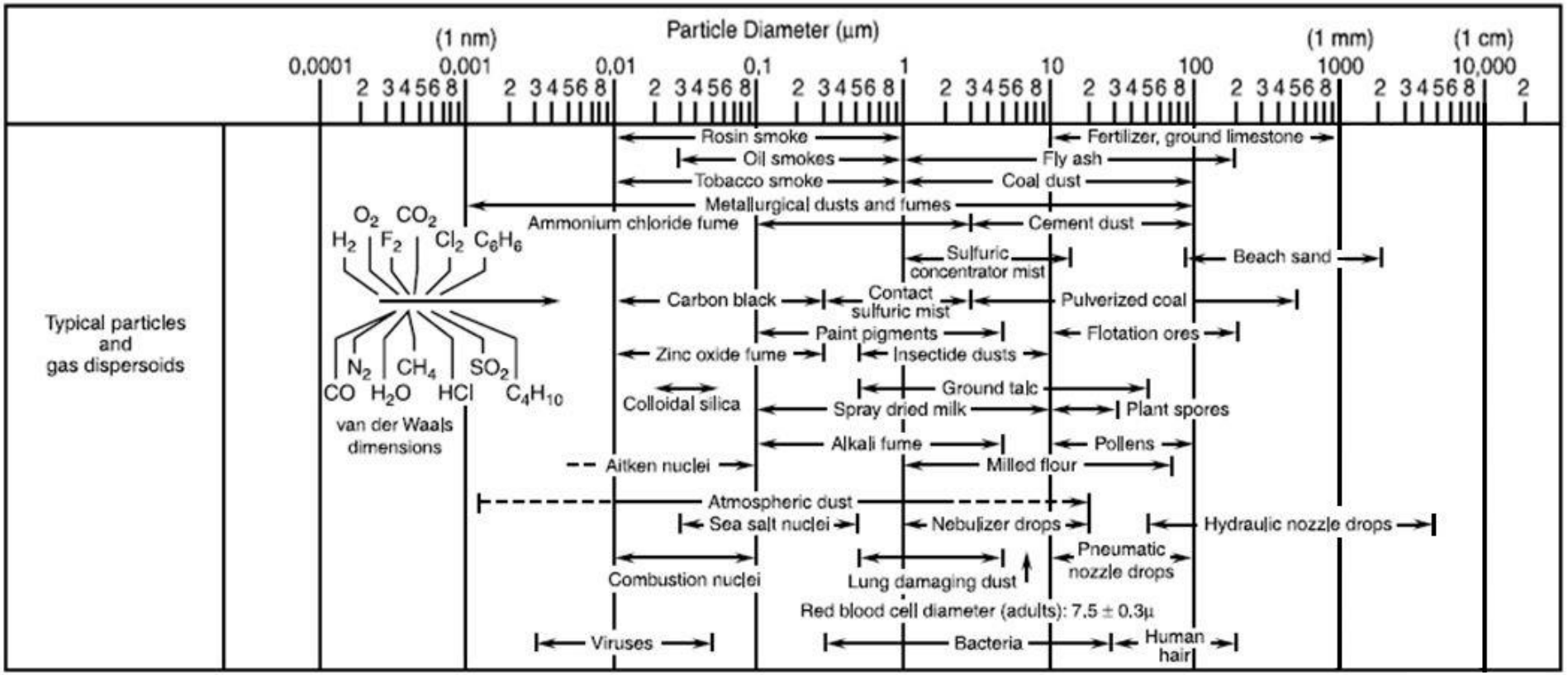

Figure 1.2 Size range of atmospheric aerosols from specific sources. Adapted from (Finlayson-Pitts and Pitts, 2000)

1.3.2 Morphology

The shape of aerosol particles varies depending on their origin, size and composition. Particles can take the form of hollow shells (combustion ash particles), crystals (sea salt and minerals), solid or hollow spheres, or be rod-shaped (Jones et al., 2006). The geomorphology of particles can vary and therefore an equivalent, or effective diameter is used for all of them regardless of shape, in order to express particle size (Finlayson-Pitts and Pitts, 2000). In reality particles exist in various geomorphological forms.

1.4 Effects of Atmospheric Aerosols

The reduction of visibility is the most easily identifiable characteristic of atmospheric pollution. This loss of visibility is primarily due to the presence of particulate matter in the atmosphere, which scatters light efficiently, giving the atmosphere a ‘‘hazy’’ appearance (Finlayson-Pitts and Pitts, 2000). Atmospheric aerosols from natural and anthropogenic sources can impact on the climate and on human health (Pöschl, 2005).

1.4.1 Climate Effects

Despite extensive study over recent years, atmospheric aerosols remain the most uncertain driver of global climate change (Heald et al., 2014; IPCC, 2013). The reason for the associated uncertainty is that atmospheric aerosols can have a warming or cooling effect depending on the chemical composition or physical properties of the particles (Heald et al., 2014; IPCC, 2013). Aerosols exert both direct and indirect effects on the radiative forcing (RF) of the climate which is defined as the change in the energy flux of solar radiation and terrestrial radiation in the atmosphere. Radiative forcing can be influenced by both natural and anthropogenic aerosols (Pöschl, 2005).

1.4.1.1 Direct Effects

Atmospheric aerosol particles can scatter and absorb incoming solar radiation, directly affecting climate forcing. Particles that scatter solar radiation have a negative (cooling) effect on RF while particles that absorb sunlight have a positive (warming) effect on it. Chemical composition, size and shape are factors that contribute to how much radiation is absorbed or scattered by the particles (Jacob, 1999; Schwartz, 1996; Stier et al., 2007). As shown in Figure 1.3, aerosols can cause positive or negative forcing effects depending on their composition (IPCC, 2007, 2013). The direct effect of materials such as sulfates leads to negative forcing or climate cooling and has been referred to as the "Whitehouse effect" (Schwartz, 1996). The composition specific effects of particles on climate forcing have been investigated (IPCC, 2007, 2013). Sulfate aerosol has a cooling effect on the atmosphere; primary and secondary organic aerosol, nitrate aerosol and mineral dust were also determined to promote an overall cooling affect. Black carbon aerosol has a warming effect on the atmosphere, while biomass burning emissions, where the black carbon and organic aerosol composition offset each other, results in a negligible effect on the RF (IPCC, 2007, 2013).

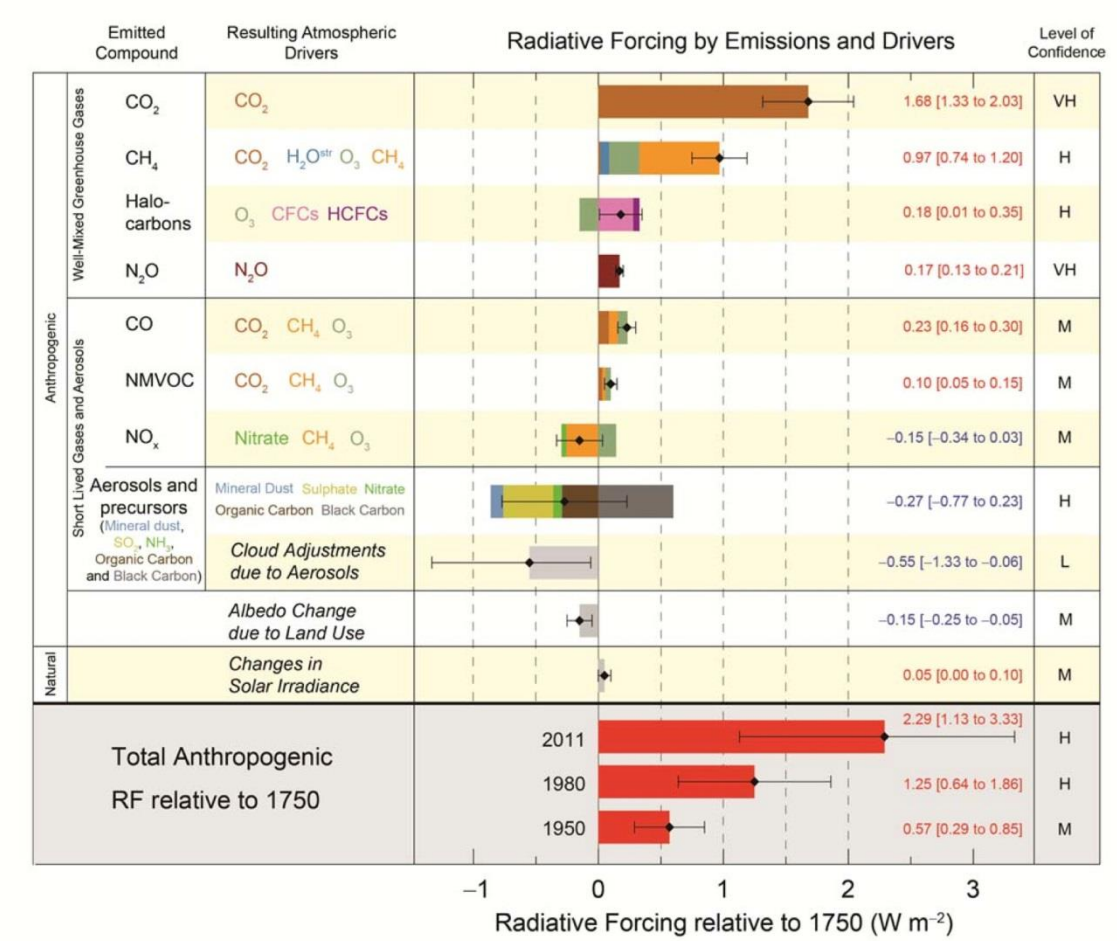

Figure 1.3 Radiative forcing estimates in 2011 relative to 1750 and aggregated uncertainties for the main drivers of climate change (IPCC, 2013).

1.4.1.2 Indirect effects

The indirect effect of atmospheric particles on climate arises from their ability to act as cloud condensation nuclei (CCN) or ice nuclei (IN) (Finlayson-Pitts and Pitts, 2000; Lohmann and Feichter, 2005). The role clouds play in radiative forcing is dependent on their altitude, size and the composition of the particles that form the cloud. Low level thick clouds, such as stratus, cumulus and stratocumulus, reflect incoming solar radiation and add to the overall planetary albedo effect. However high altitude thinner clouds, such as cirrocumulus, transmit solar radiation but have the ability to trap outgoing (long wavelength) radiation emitted from the Earth's surface (Finlayson-Pitts and Pitts, 2000). Many aerosol particles have the ability to grow into cloud droplets following the condensation of water vapour onto the particle. This nucleation process is driven by hygroscopic particles, termed cloud

condensation nuclei (CCN) (Jurányi et al., 2013), many of which contain sulfur due to its polarisable nature (Hobbs, 2000). Aerosols can affect cloud albedo in many ways, for example, the presence of aerosol results in more numerous, smaller cloud particles which reflect more solar radiation thereby increasing the Twomey effect. Smaller cloud particles decrease precipitation, thus prolonging the lifetime of the cloud. Non-CCN soot particles absorb solar radiation and may cause evaporation of cloud particles (termed a semi-direct effect) (Lohmann and Feichter, 2005). Finally, bacteria and fungal spores are thought to influence IN formation at somewhat higher temperatures than chemical particles (Després et al., 2012; Murray et al., 2012)

The 2013 IPCC report stated that the RF of the total aerosol effect in the atmosphere, which includes cloud adjustments due to aerosols, is *negative* (cooling). This results from a negative forcing from most aerosols and a positive contribution from black carbon absorption of solar radiation (IPCC, 2013). A schematic depicting both the direct and indirect effects of atmospheric aerosols is shown in Figure 1.4.

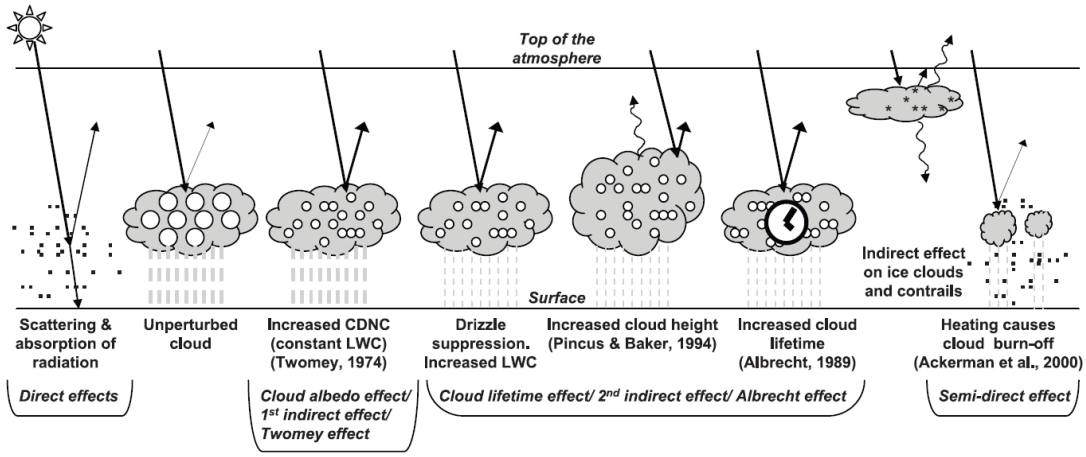

Figure 1.4 Schematic diagram showing the various radiative mechanisms associated with direct and indirect effects (IPCC, 2007)

1.4.2 Health Effects

"Clean air is considered to be a basic requirement of human health and well-being. However, air pollution continues to pose a significant threat to health worldwide" (WHO, 2006).

Every day humans inhale 13.5 kg of air therefore, the quality of the air is likely to have an impact on human health (Wayne, 2000). It is known that exposure to particulate matter has adverse effects on human health (Dockery, 2009; Dockery et al., 1993; Hoek et al., 2002; Pope and Dockery, 2006; Pope et al., 2002; Pöschl, 2005; U.S.EPA, 2009) (Dockery et al., 1993; Hoek et al., 2002; Pope and Dockery, 2006; Pope et al., 2002). Such health effects include increased morbidity and mortality from cardiovascular and respiratory conditions. In 2013 the WHO International Agency for Research on Cancer (IARC) classified outdoor air pollution, and specifically particulate matter, as carcinogenic to humans (Loomis et al., 2013). In 2010, it was estimated that 223,000 deaths from lung cancer worldwide resulted from exposure to air pollution (Loomis et al., 2013; Straif et al., 2013). Ambient pollution was estimated to cause 3.7 million premature deaths worldwide per year due to exposure to PM_{10} which cause cardiovascular and respiratory disease, and cancers (WHO, 2014).

Larger coarse particles with diameters > 10 µm do not penetrate beyond the upper respiratory system and are dealt with by the physical defence system of the body, which includes tiny hair-like projections present in the lining of the respiratory system that participate in mucociliary clearance mechanisms thereby trapping particles (Finlayson-Pitts and Pitts, 2000; Salvi and Holgate, 1999). Inhalable particles, those that can penetrate the respiratory system, are those with a diameter less than 10 µm (Pope and Dockery, 2006). PM_{10} (thoracic) particles can penetrate into the lower respiratory system, while $PM_{2.5}$ (respirable) particles can be breathed in more deeply and can penetrate into the gas-exchange region of the lung. Ultrafine particles < 100 nm have a very large surface area, with increasing degrees of lung penetration (Brunekreef and Holgate, 2002; Pope and Dockery, 2006). The human lung is able to respond to particulate matter that deposits on its surface through removal by scavenging cells called macrophages. However, these removal systems

may be overwhelmed by large particle numbers or by particle toxicity (Salvi and Holgate, 1999).

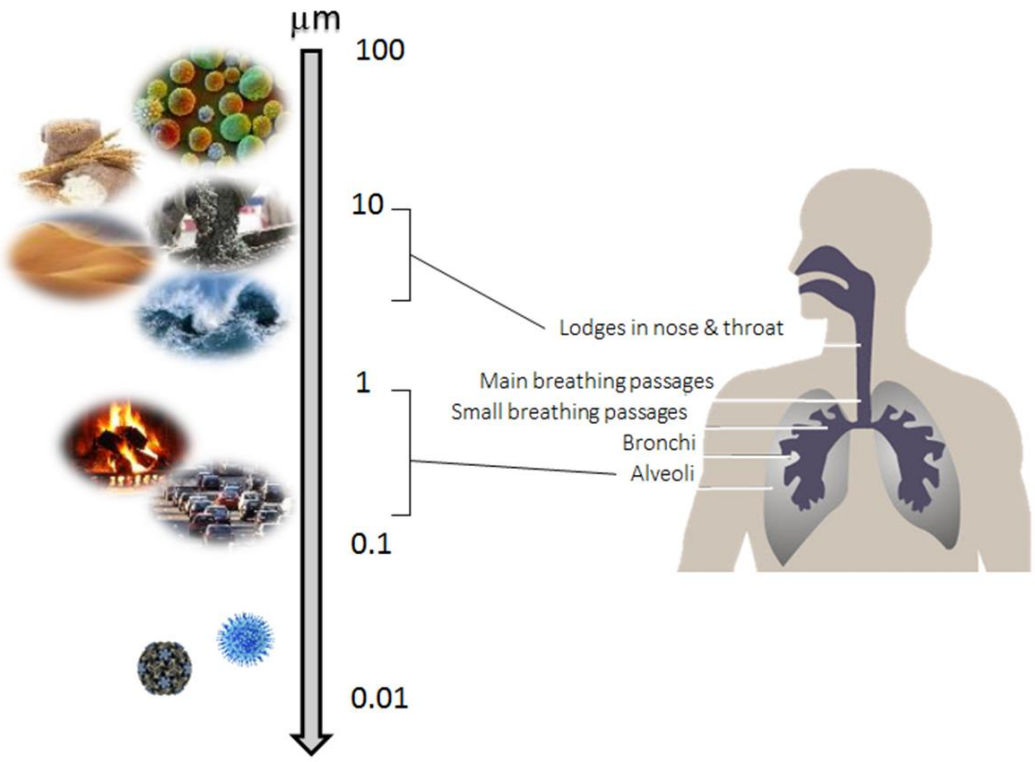

Figure 1.5 Diagram showing the extent to which different size particles can penetrate into the airway and lung systems (Courtesy of J. Arndt)

1.4.3 Air Quality Legislation

It is recognised that any increase in PM concentration above background levels found in both the United States and Western Europe can have an impact on human health and that there is little evidence to suggest a threshold PM level below which no adverse health effects would be anticipated (WHO, 2006). Therefore, any standard or guideline value is unlikely to provide complete protection for every individual against all possible adverse health effects of particulate matter (WHO, 2006).

The WHO has provided guideline targets for both PM_{10} and $PM_{2.5}$ mass. Annual mean and 24-hour mean mass values are included in order to take into account short term and long term exposure effects. For $PM_{2.5}$ the annual mean target is 10 μg m^{-3}, with a 24-hour mean of 25 μg m^{-3}. The PM_{10} targets are 20 μg m^{-3} and 50 μg m^{-3} for the annual and 24-hour mean respectively (WHO, 2006). In Europe the EU introduced the Clean Air For Europe directive (CAFÉ – Directive 2008/50/EC) (EU, 2008). In the USA it was found that, through the 1980s and 1990s, a reduction in the ambient fine particulate matter was associated with an increase in life expectancy: this result is attributed to the air quality control measures introduced over that period (Pope III et al., 2009).

1.5 Measurements of Aerosol Particles

In order to reduce PM levels it is important to understand the sources of aerosols, e.g. traffic, biomass burning, fossil fuel combustion etc., and, if possible, the contribution from specific sources should be quantified. Traditionally the chemical composition of atmospheric aerosols has been examined by off-line chemical analysis of particles collected onto filters (Finlayson-Pitts and Pitts, 2000; Heard, 2008; Prather et al., 2008). X-ray fluorescence (XRF), Particle-induced X-ray emission (PIXE), inductively coupled plasma mass spectrometry (ICP-MS) can all be used to identify elements in aerosol samples (Finlayson-Pitts and Pitts, 2000). Inorganic ions can be quantified using several techniques including ion chromatography (IC), selective ion electrodes (SIE), infrared and Raman spectroscopy and also mass spectrometry (MS) (Finlayson-Pitts and Pitts, 2000; Heard, 2008). Organic (OC) and elemental (EC) carbon can be measured and discriminated using thermal methods, digestion, extraction, and optical techniques. These approaches can provide the identification of organic and elemental carbon mass but there are a very large number of organic species present in atmospheric aerosols (Prather et al., 2008). However, these can be identified using: mass spectrometry (MS), high-performance liquid chromatography (HPLC) and gas chromatography mass spectrometry (GC-MS) (Finlayson-Pitts and Pitts, 2000; Heard, 2008).

While off-line measurements can employ many powerful analytical techniques in the identification and quantification of chemical species in atmospheric aerosols, there are several limitations (Finlayson-Pitts and Pitts, 2000; Heard, 2008). Firstly a sufficient amount of material has to be collected to pass the detection limits of the analytical techniques, which results in sampling times of several hours to days, limiting the time resolution of off-line measurements (Heard, 2008; McMurry, 2000). Several sampling artefacts can also skew off-line measurements: semi-volatile species may evaporate, collected particles may react with other particles or gases on the filter in the time between sampling and analysis, quartz filters can adsorb organic gases altering the OC fragments measured using GC-MS (Finlayson-Pitts and Pitts, 2000; Heard, 2008; McMurry, 2000; Prather et al., 2008).

Therefore on-line measurements have been developed in order to sample and analyse atmospheric aerosols in a continuous or real time fashion and to solve the problems associated with the bulk off-line measurements described above (Finlayson-Pitts and Pitts, 2000; Heard, 2008). Several fractions of aerosol are measured on-line individually and nitrate, sulfate elemental and organic carbon can all be measured using instruments targeted to measure these species specifically (Heard, 2008; McMurry, 2000). For example the nitrate portion of aerosol can be determined by collecting particles with a single stage impactor, then particles are subjected to flash vaporization and the emitted gasses are detected using a chemiluminescence NO_x analyser (McMurry, 2000). Other techniques such as Particle Into Liquid Sampler (PILS) can measure several ionic species by coupling the PILS with Ion Chromatography (PILS-IC) (Heard, 2008).

More recently a number of instruments have been developed to measure the mass spectra of atmospheric particles in real time. The fundamental principle of an aerosol mass spectrometer is to sample airborne particles, vaporize and ionize them, and then analyse them using mass spectrometry. A number of aerosol mass spectrometers have been developed including: Aerosol Time of Flight Mass Spectrometer (ATOFMS) (Gard et al., 1997; Prather et al., 1994), Aerosol Mass Spectrometer (Aerodyne AMS) (Jayne et al., 2000), Laser Mass Analysis of Particles in the Airborne State (LAMPAS) (Hinz et al., 1994), Particle Analysis by Laser Mass Spectrometer (PALMS) (Murphy and Thomson, 1995; Thomson et al., 2000) Rapid

Single Particle Mass Spectrometer II (RSMS-II) (Phares et al., 2002). An overview of these instruments is provided elsewhere (Pratt and Prather, 2012; Sullivan and Prather, 2005) and a comparison of the co-location of PALMS, ATOFMS, RSMS-II and AMS in ATLANTA is also outlined in the literature (Middlebrook et al., 2003).

The commercialised aerosol mass spectrometers most often used in ambient measurements are the ATOFMS (TSI) and AMS (Aerodyne). These instruments operate using two different principles. The ATOFMS is a Single Particle Mass Spectrometer and uses Laser desorption/ionisation and Time of Flight mass spectrometry. The ATOFMS provides quantitative size and largely qualitative composition (Gard et al., 1997; Heard, 2008). The AMS utilises thermal desorption, electron impact ionisation and quadrupole of TOF mass spectrometry and provides quantitative size and composition information but is unable to measure the refractory portion of atmospheric aerosol (Heard, 2008). As the ATOFMS can determine the chemical composition of individual particles it can determine whether aerosol is internally or externally mixed. Internally mixed particles have the same chemical composition as the bulk aerosol, whereas externally mixed aerosol contains particles of differing chemical composition (Finlayson-Pitts and Pitts, 2000).

The measurements undertaken as part of the work presented in this thesis involved the deployment of a commercially available ATOFMS (TSI model 3800). A full description of the operating principles of the ATOFMS along with data handling and analysis and a literature review of previous ATOFMS studies is provided in Chapter 2.

1.6 Overview

1.6.1 Aims of Research

The overall aims of this study can be summarised as follows:

- To deploy an Aerosol Time of Flight Mass Spectrometer (ATOFMS) at two urban background locations in Paris and Barcelona as part of the MEGAPOLI and SAPUSS monitoring campaigns respectively.

- To use the ATOFMS datasets to determine the size-resolved chemical composition of atmospheric single particles in the size range 100 to 3000 nm in real-time.

- Interpretation of the ATOFMS data to determine:
  (i) the types and sources of particles at the urban locations;
  (ii) to investigate local and regional particle sources;
  (iii) the influence of regional transport on PM composition in urban areas.

The results of the ATOFMS measurements are compared to coincident quantitative measurements at both measurement locations. Further to the comparison with other techniques, the ATOFMS analysis for the Barcelona data was compared with another type of computational analysis to compare results derived from the two approaches.

1.6.2 Overview of Thesis

A brief introduction to the sources, composition, physical properties and effects of atmospheric aerosols is presented in Chapter 1 of this thesis.

An overview of the operating principles for the ATOFMS and data analysis techniques used during the work described within this thesis is given in Chapter 2. A brief literature review of previous field studies undertaken using ATOFMS is also provided.

Chapter 3 provides an outline of the ATOFMS deployment in Paris during the MEGAPOLI campaign. The ATOFMS provided a list of the particle types present at the site during the period in the range 100 to 3000 nm.

The research described in Chapter 4 is centred on the deployment of an ATOFMS during the SAPUSS monitoring campaign in Barcelona.

Chapter 5 contains details on an investigation into the ability of the ATOFMS to quantitatively determine ambient metal concentrations by comparison with quantitative Particle induced X-ray Emission (PIXE) measurements.

1.7 References

Allard, P., Aiuppa, A., Loyer, H., Carrot, F., Gaudry, A., Pinte, G., Michel, A., Dongarrà, G., 2000. Acid gas and metal emission rates during long-lived basalt degassing at Stromboli Volcano. Geophysical Research Letters 27, 1207-1210.

Amato, F., Pandolfi, M., Escrig, A., Querol, X., Alastuey, A., Pey, J., Perez, N., Hopke, P.K., 2009a. Quantifying road dust resuspension in urban environment by Multilinear Engine: A comparison with PMF2. Atmospheric Environment 43, 2770-2780.

Amato, F., Pandolfi, M., Viana, M., Querol, X., Alastuey, A., Moreno, T., 2009b. Spatial and chemical patterns of PM10 in road dust deposited in urban environment. Atmospheric Environment 43, 1650-1659.

Angelino, S., Suess, D.T., Prather, K.A., 2001. Formation of aerosol particles from reactions of secondary and tertiary alkylamines: Characterization by aerosol time-of-flight mass spectrometry. Environmental Science & Technology 35, 3130-3138.

AQEG, 2005. Particulate Matter in the United Kingdom Summary. Defra, London. http://www.defra.gov.uk/environment/airquality/aqeg

Ayers, G.P., Gillett, R.W., 2000. DMS and its oxidation products in the remote marine atmosphere: implications for climate and atmospheric chemistry. Journal of Sea Research 43, 275-286.

Brunekreef, B., Holgate, S.T., 2002. Air pollution and health. The Lancet 360, 1233-1242.

Buseck, P.R., Adachi, K., 2008. Nanoparticles in the Atmosphere. Elements 4, 389-394.

Calvo, A., Alves, C., Castro, A., Pont, V., Vicente, A., Fraile, R., 2013. Research on aerosol sources and chemical composition: Past, current and emerging issues. Atmospheric Research 120-121, 1-28.

Dall'Osto, M., Beddows, D.C.S., Gietl, J.K., Olatunbosun, O.A., Yang, X., Harrison, R.M., 2014. Characteristics of tyre dust in polluted air: Studies by single particle mass spectrometry (ATOFMS). Atmospheric Environment 94, 224-230.

Dall'Osto, M., Booth, M.J., Smith, W., Fisher, R., Harrison, R.M., 2008. A study of the size distributions and the chemical characterization of airborne particles in the vicinity of a large integrated steelworks. Aerosol Science and Technology 42, 981-991.

Dall'Osto, M., Drewnick, F., Fisher, R., Harrison, R.M., 2012. Real-time measurements of nonmetallic fine particulate matter adjacent to a major integrated steelworks. Aerosol Science and Technology 46, 639-653.

Dennis, A., Fraser, M., Anderson, S., Allen, D., 2002. Air pollutant emissions associated with forest, grassland, and agricultural burning in Texas. Atmospheric Environment 36, 3779-3792.

Després, V.R., Huffman, J.A., Burrows, S.M., Hoose, C., Safatov, A.S., Buryak, G., Fröhlich-Nowoisky, J., Elbert, W., Andreae, M.O., Pöschl, U., 2012. Primary biological aerosol particles in the atmosphere: a review. Tellus B 64.

Dockery, D.W., 2009. Health effects of particulate air pollution. Annals of Epidemiology 19, 257-263.

Dockery, D.W., Pope, C.A., Xu, X., Spengler, J.D., Ware, J.H., Fay, M.E., Ferris, B.G., Speizer, F.E., 1993. An Association between Air Pollution and Mortality in Six U.S. Cities. New England Journal of Medicine 329, 1753-1759.

Duffy, S.J., 2011. Environmental Chemistry: A Global Perspective. Oxford University Press.

EU, 2008. Directive 2008/50/EC of the European Parliament and of the Council of Europe of 21 May 2008 on ambient air quality and cleaner air for Europe, in: EUROPE, T.E.P.A.O.T.C. (Ed.), Official Journal of the European Union.

Finlayson-Pitts, B.J., Pitts, J.N., 2000. Chemistry of the upper and lower atmosphere: theory, experiments, and applications. Academic Press, San Diego.

Gard, E., Mayer, J.E., Morrical, B.D., Dienes, T., Fergenson, D.P., Prather, K.A., 1997. Real-time analysis of individual atmospheric aerosol particles: Design and performance of a portable ATOFMS. Analytical Chemistry 69, 4083-4091.

Heald, C.L., Ridley, D.A., Kroll, J.H., Barrett, S.R.H., Cady-Pereira, K.E., Alvarado, M.J., Holmes, C.D., 2014. Contrasting the direct radiative effect and direct radiative forcing of aerosols. Atmos. Chem. Phys. 14, 5513-5527.

Healy, R.M., O'Connor, I.P., Hellebust, S., Allanic, A., Sodeau, J.R., Wenger, J.C., 2009. Characterisation of single particles from in-port ship emissions. Atmospheric Environment 43, 6408-6414.

Heard, D., 2008. Analytical techniques for atmospheric measurement. John Wiley & Sons.

Hinz, K.-P., Kaufmann, R., Spengler, B., 1994. Laser-Induced Mass Analysis of Single Particles in the Airborne State. Analytical Chemistry 66, 2071-2076.

Hobbs, P.V., 2000. Introduction to Atmospheric Chemistry: a companion text to Basic physical chemistry for the atmospheric sciences. Cambridge University Press, Cambridge; New York.

Hoek, G., Brunekreef, B., Goldbohm, S., Fischer, P., van den Brandt, P.A., 2002. Association between mortality and indicators of traffic-related air pollution in the Netherlands: a cohort study. The Lancet 360, 1203-1209.

IPCC, 2007. Climate change 2007: the physical science basis: contribution of Working Group I to the Fourth Assessment Report of the Intergovernmental

Panel on Climate Change. Cambridge University Press. Cambridge, United Kingdom and New York, NY, USA.

IPCC, 2013. Climate Change 2013, The Physical Science Basis Working Group I Contribution to the Fifth Assessment Report of the Intergovernmental Panel on Climate Change, in: Stocker, T.F., D. Qin, G.-K. Plattner, M. Tignor, S.K. Allen, J. Boschung, A. Nauels, Y. Xia, V. Bex and P.M. Midgley (Eds.). Cambridge University Press, Cambridge, United Kingdom and New York, NY, USA, 1535 pp.

Jacob, D., 1999. Introduction to Atmospheric Chemistry. Princeton University Press.

Jayne, J.T., Leard, D.C., Zhang, X., Davidovits, P., Smith, K.A., Kolb, C.E., Worsnop, D.R., 2000. Development of an aerosol mass spectrometer for size and composition analysis of submicron particles. Aerosol Science & Technology 33, 49-70.

Jones, T., Moreno, T., BéruBé, K., Richards, R., 2006. The physicochemical characterisation of microscopic airborne particles in south Wales: a review of the locations and methodologies. Science of the Total Environment 360, 43-59.

Jurányi, Z., Tritscher, T., Gysel, M., Laborde, M., Gomes, L., Roberts, G., Baltensperger, U., Weingartner, E., 2013. Hygroscopic mixing state of urban aerosol derived from size-resolved cloud condensation nuclei measurements during the MEGAPOLI campaign in Paris. Atmos. Chem. Phys. 13, 6431-6446.

Lavanchy, V.M.H., Gäggeler, H.W., Nyeki, S., Baltensperger, U., 1999. Elemental carbon (EC) and black carbon (BC) measurements with a thermal method and an aethalometer at the high-alpine research station Jungfraujoch. Atmospheric Environment 33, 2759-2769.

Lohmann, U., Feichter, J., 2005. Global indirect aerosol effects: a review. Atmospheric Chemistry and Physics 5, 715-737.

Loomis, D., Grosse, Y., Lauby-Secretan, B., Ghissassi, F.E., Bouvard, V., Benbrahim-Tallaa, L., Guha, N., Baan, R., Mattock, H., Straif, K., 2013. The carcinogenicity of outdoor air pollution. The Lancet Oncology 14, 1262-1263.

McMurry, P.H., 2000. A review of atmospheric aerosol measurements. Atmospheric Environment 34, 1959-1999.

Middlebrook, A.M., Murphy, D.M., Lee, S.H., Thomson, D.S., Prather, K.A., Wenzel, R.J., Liu, D.Y., Phares, D.J., Rhoads, K.P., Wexler, A.S., Johnston, M.V., Jimenez, J.L., Jayne, J.T., Worsnop, D.R., Yourshaw, I., Seinfeld, J.H., Flagan, R.C., 2003. A comparison of particle mass spectrometers during the 1999 Atlanta Supersite Project. Journal of Geophysical Research-Atmospheres 108, 8424, doi:10.1029/2001JD000660, D7.

Minguillón, M., Perron, N., Querol, X., Szidat, S., Fahrni, S., Alastuey, A., Jimenez, J., Mohr, C., Ortega, A., Day, D., 2011. Fossil versus contemporary sources of fine elemental and organic carbonaceous particulate matter during the DAURE campaign in Northeast Spain. Atmospheric Chemistry and Physics 11, 12067-12084.

Moffet, R.C., Desyaterik, Y., Hopkins, R.J., Tivanski, A.V., Gilles, M.K., Wang, Y., Shutthanandan, V., Molina, L.T., Abraham, R.G., Johnson, K.S., Mugica, V., Molina, M.J., Laskin, A., Prather, K.A., 2008. Characterization of aerosols containing Zn, Pb, and Cl from an industrial region of Mexico City. Environmental Science & Technology 42, 7091-7097.

Monks, P.S., Granier, C., Fuzzi, S., Stohl, A., Williams, M.L., Akimoto, H., Amann, M., Baklanov, A., Baltensperger, U., Bey, I., Blake, N., Blake, R.S., Carslaw, K., Cooper, O.R., Dentener, F., Fowler, D., Fragkou, E., Frost, G.J., Generoso, S., Ginoux, P., Grewe, V., Guenther, A., Hansson, H.C., Henne, S., Hjorth, J., Hofzumahaus, A., Huntrieser, H., Isaksen, I.S.A., Jenkin, M.E., Kaiser, J., Kanakidou, M., Klimont, Z., Kulmala, M., Laj, P., Lawrence, M.G., Lee, J.D., Liousse, C., Maione, M., McFiggans, G., Metzger, A., Mieville, A., Moussiopoulos, N., Orlando, J.J., O'Dowd, C.D., Palmer, P.I., Parrish, D.D., Petzold, A., Platt, U., Poeschl, U., Prevot, A.S.H., Reeves,

C.E., Reimann, S., Rudich, Y., Sellegri, K., Steinbrecher, R., Simpson, D., ten Brink, H., Theloke, J., van der Werf, G.R., Vautard, R., Vestreng, V., Vlachokostas, C., von Glasow, R., 2009. Atmospheric composition change - global and regional air quality. Atmospheric Environment 43, 5268-5350.

Morawska, L., Zhang, J., 2002. Combustion sources of particles. 1. Health relevance and source signatures. Chemosphere 49, 1045-1058.

Murphy, D., Thomson, D., 1995. Laser ionization mass spectroscopy of single aerosol particles. Aerosol Science & Technology 22, 237-249.

Murray, B., O'Sullivan, D., Atkinson, J., Webb, M., 2012. Ice nucleation by particles immersed in supercooled cloud droplets. Chemical Society Reviews 41, 6519-6554.

O'Dowd, C.D., Smith, M.H., Consterdine, I.E., Lowe, J.A., 1997. Marine aerosol, sea-salt, and the marine sulphur cycle: a short review. Atmospheric Environment 31, 73-80.

Pathak, R.K., Wu, W.S., Wang, T., 2009. Summertime PM2.5 ionic species in four major cities of China: nitrate formation in an ammonia-deficient atmosphere. Atmos. Chem. Phys. 9, 1711-1722.

Phares, D.J., Rhoads, K.P., Wexler, A.S., 2002. Performance of a single ultrafine particle mass spectrometer. Aerosol Science & Technology 36, 583-592.

Pio, C., Cerqueira, M., Harrison, R.M., Nunes, T., Mirante, F., Alves, C., Oliveira, C., Sanchez de La Campa, A., Artíñano, B., Matos, M., 2011. OC/EC ratio observations in Europe: Re-thinking the approach for apportionment between primary and secondary organic carbon. Atmospheric Environment 45, 6121-6132.

Pope, C.A., Dockery, D.W., 2006. Health effects of fine particulate air pollution: lines that connect. Journal of the Air & Waste Management Association 56, 709-742.

Pope, I.C., Burnett, R.T., Thun, M.J., et al., 2002. Lung cancer, cardiopulmonary mortality, and long-term exposure to fine particulate air pollution. Journal of the American Medical Association 287, 1132-1141.

Pope III, C.A., Ezzati, M., Dockery, D.W., 2009. Fine-particulate air pollution and life expectancy in the United States. New England Journal of Medicine 360, 376-386.

Pöschl, U., 2005. Atmospheric aerosols: composition, transformation, climate and health effects. Angewandte Chemie International Edition 44, 7520-7540.

Prather, K.A., Hatch, C.D., Grassian, V.H., 2008. Analysis of Atmospheric Aerosols. Annual Review of Analytical Chemistry 1, 485-514.

Prather, K.A., Nordmeyer, T., Salt, K., 1994. Real-time characterization of individual aerosol-particles using time-of-flight mass-spectrometry. Analytical Chemistry 66, 1403-1407.

Pratt, K.A., Hatch, L.E., Prather, K.A., 2009. Seasonal volatility dependence of ambient particle phase amines. Environmental Science & Technology 43, 5276-5281.

Pratt, K.A., Prather, K.A., 2012. Mass spectrometry of atmospheric aerosols-Recent developments and applications. Part II: On-line mass spectrometry techniques. Mass Spectrometry Reviews 31, 17-48.

Rehbein, P.J., Jeong, C.-H., McGuire, M.L., Yao, X., Corbin, J.C., Evans, G.J., 2011. Cloud and fog processing enhanced gas-to-particle partitioning of trimethylamine. Environmental Science & Technology 45, 4346-4352.

Salvi, S., Holgate, S.T., 1999. Mechanisms of particulate matter toxicity. Clinical & Experimental Allergy 29, 1187-1194.

Sanderson, P., Delgado-Saborit, J.M., Harrison, R.M., 2014. A review of chemical and physical characterisation of atmospheric metallic nanoparticles. Atmospheric Environment 94, 353-365.

Schwartz, S.E., 1996. The whitehouse effect—Shortwave radiative forcing of climate by anthropogenic aerosols: An overview. Journal. Aerosol. Science. 27, 359-382.

Stier, P., Seinfeld, J.H., Kinne, S., Boucher, O., 2007. Aerosol absorption and radiative forcing. Atmospheric Chemistry and Physics 7, 5237-5261.

Straif, K., Cohen, A., Samet, J., 2013. Air Pollution and Cancer. International Agency for Research on Cancer. Lyon, France.

http://w2.iarc.fr/en/publications/books/sp161/

Sullivan, R.C., Prather, K.A., 2005. Recent advances in our understanding of atmospheric chemistry and climate made possible by on-line aerosol analysis instrumentation. Analytical Chemistry 77, 3861-3885.

Thomas, H., Watson, I., Kearney, C., Carn, S., Murray, S., 2009. A multi-sensor comparison of sulphur dioxide emissions from the 2005 eruption of Sierra Negra volcano, Galápagos Islands. Remote Sensing of Environment 113, 1331-1342.

Thomson, D.S., Schein, M.E., Murphy, D.M., 2000. Particle analysis by laser mass spectrometry WB-57F instrument overview. Aerosol Science & Technology 33, 153-169.

U.S.EPA, 2009. EPA U.S. Integrated Science Assessment for Particulate Matter (Final Report). U.S. Environmental Protection Agency, Washington, DC, EPA/600/R-08/139F, 2009.

Wayne, R.P., 2000. Chemistry of atmospheres: an introduction to the chemistry of the atmospheres of Earth, the planets, and their satellites, 3rd ed. Oxford University Press, Oxford.

Whitby, K., Charlson, R., Wilson, W., Stevens, R., Lee, R.E., 1974. The size of suspended particle matter in air. Science 183, 1098-1100.

WHO, 2006. WHO Air quality guidelines for particulate matter, ozone, nitrogen dioxide and sulfur dioxide: global update 2005: summary of risk assessment.

http://www.who.int/phe/health_topics/outdoorair/outdoorair_aqg/en/

WHO, 2014. Burden of disease from Ambient Air Pollution for 2012. World Health Organization, Geneva.

Willeke, K., Whitby, K.T., 1975. Atmospheric aerosols: size distribution interpretation. Journal of the Air Pollution Control Association 25, 529-534.

Yu, S., Dennis, R.L., Bhave, P.V., Eder, B.K., 2004. Primary and secondary organic aerosols over the United States: estimates on the basis of observed organic carbon (OC) and elemental carbon (EC), and air quality modeled primary OC/EC ratios. Atmospheric Environment 38, 5257-5268.

2 Instrumentation and Methodology

Contents

2.1 Aerosol Time of Flight Mass Spectrometer (ATOFMS)

The instrument used for the atmospheric monitoring measurements undertaken as part of this work was an Aerosol Time of Flight Mass Spectrometer (ATOFMS), TSI model 3800, supplied by TSI Inc. Shoreview, MN USA. The ATOFMS was originally developed by Dr K. A. Prather and co-workers (Nordmeyer and Prather, 1994; Prather et al., 1994). The description of the original instrument and also a portable version suitable for field studies was published a few years later (Gard et al., 1997). The ATOFMS measures the size and chemical composition of single particles with aerodynamic diameters in the range 100-3000 nm. The core composition of single particles, for example elemental/organic carbon and transition metals, as well as secondary species such as nitrate and sulfate ions can be determined using this method. When combined with meteorological data, local and regional sources of particulate matter can be identified.

A schematic diagram of the ATOFMS (TSI, model 3800) is shown in Figure 2.1. It consists of three main operating regions described in detail in the following sections. Briefly, aerosol is drawn in through the inlet and into the sampling region where a particle beam is generated. The particles travel into the sizing region where they are detected by two lasers (532 nm) to determine the particles aerodynamic diameter. The particle then enters the mass spectrometer region and is hit by a pulsed laser (266 nm) to produce gaseous ions which enter the time-of-flight mass spectrometers to yield a positive and negative ion mass spectrum of the single particle.

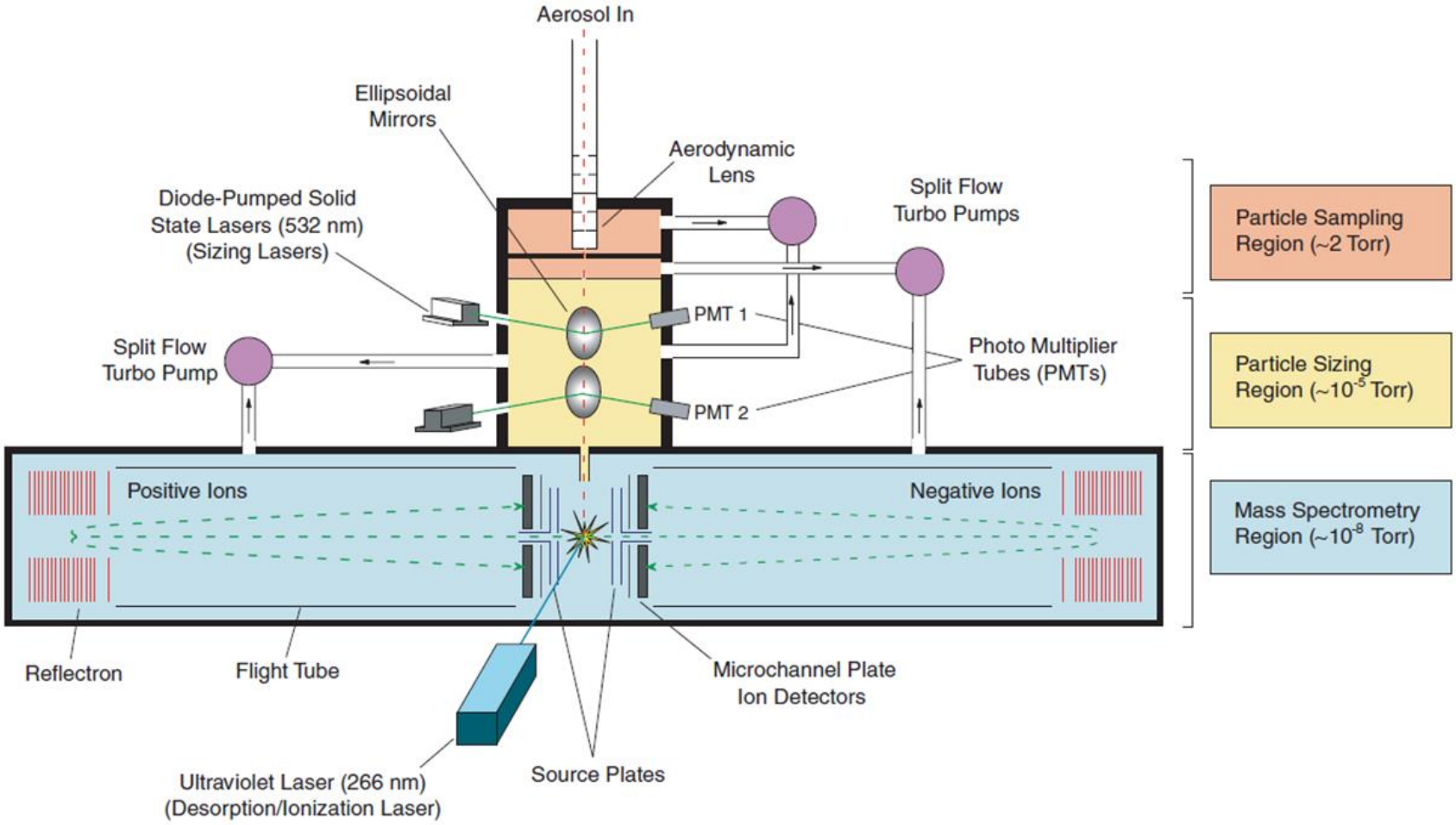

Figure 2.1 Schematic of Aerosol Time of Flight Mass Spectrometer (ATOFMS) (TSI, 2004b).

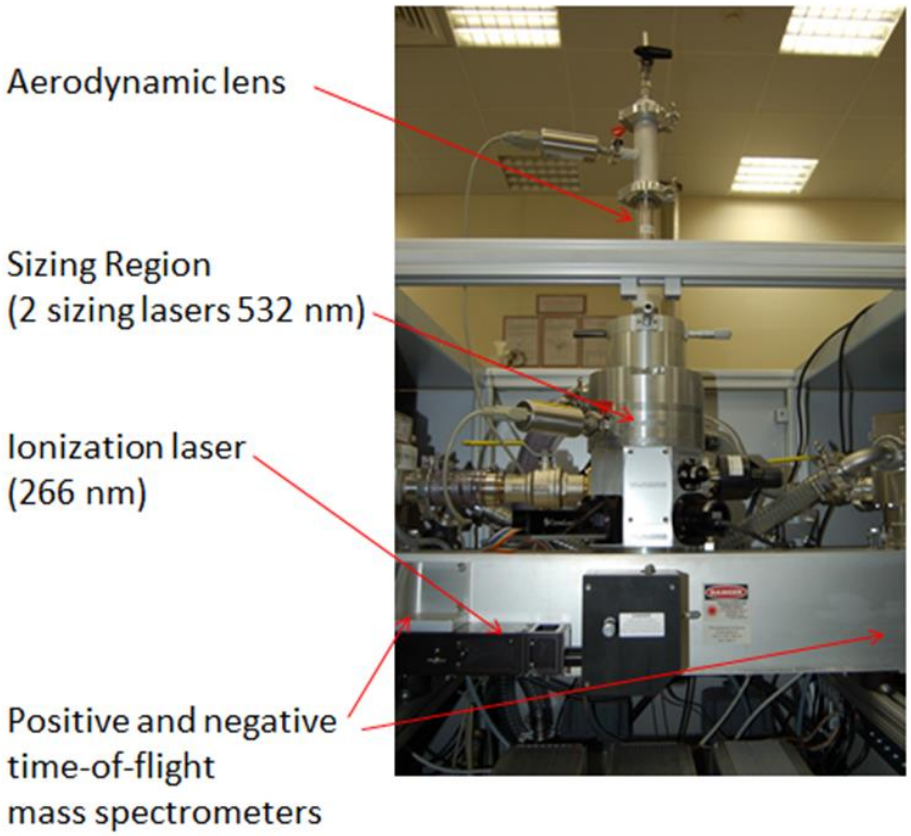

Figure 2.2 ATOFMS (TSI 3800) operating with Aerodynamic Lens inlet (TSI AFL 100).

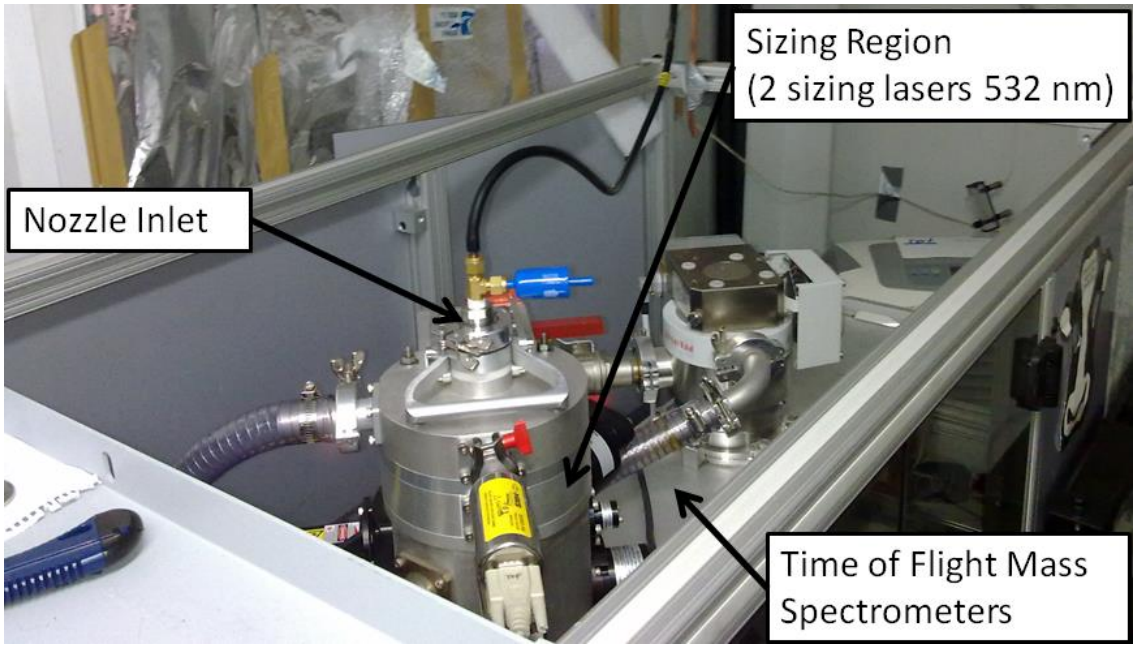

Figure 2.3 ATOFMS (TSI 3800) operating with converging nozzle inlet.

2.1.1 Particle Sampling

The particle sampling region of the ATOFMS TSI 3800 can be configured with two different inlet systems, one using an Aerodynamic Focussing Lens (Figure 2.2) and the other using a nozzle inlet (Figure 2.3).

The original setup of the ATOFMS utilised a converging nozzle inlet. Aerosol is drawn in through the converging nozzle at 0.9 L min^{-1} and into two differentially pumped regions separated by skimmers. This sampling region allows the pressure to be reduced from ~ 760 to ~10^{-4} torr as the particle leaves the sampling region and enters the sizing region. Once in transit through the inlet and skimmer array the particles are accelerated to a velocity characteristic of their aerodynamic diameter which allows for determination of the particle diameter later in the sizing region (Allen et al., 2000; Dall'Osto and Harrison, 2006; Snyder et al., 2009). The particle must travel along the centreline of the system in order to be drawn through the skimmers and into the sizing region. The transit of the particle through the inlet is governed by the Stokes number (St), which is related to the particle density and size, along with the orifice diameter and the gas velocity. If St = 1 the particle will travel along the centreline while particles with St < 1 follow the gas streamline. Particles with St > 1 cross the centreline at the orifice and diverge from the centre-line downstream (Johnston, 2000). A schematic of a converging nozzle inlet is shown in Figure 2.4.

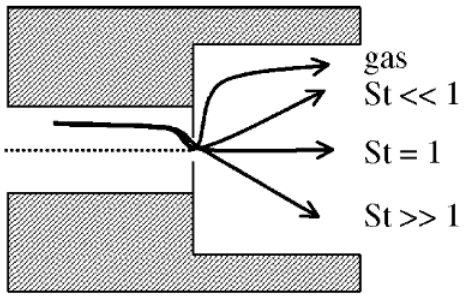

Figure 2.4 Schematic showing the operation of converging nozzle inlet (Johnston, 2000).

In order to increase the detection efficiency of the ATOFMS, an Aerodynamic Focussing Lens (AFL) was incorporated as a replacement for the converging nozzle inlet (Su et al., 2004). An AFL consists of a series of orifices with successively smaller diameters. The system consists of an initial flow limiting orifice a relaxation region, a series of aerodynamic lenses and an accelerating nozzle. The ATOFMS incorporating the AFL operates with an inlet flow rate of 0.1 L min^{-1} (TSI, 2007) as shown in Figure 2.5. The benefit that the lens system has over the nozzle inlet is that as the aerosol traverses the orifice, particles with St = 1 will follow the centre-line as before while, unlike the nozzle system, the larger particles that diverge from the centre-line with the nozzle remain unaltered by the time they encounter the second orifice. The smaller particles that in the nozzle system follow the gas streamline are entrained by the expanding and contracting gas streamlines (Johnston, 2000). This arrangement results in particles with a greater size range being incorporated into the focussed particle beam as it exits the lens system. Upon leaving the AFL, the final orifice controls supersonic gas expansion and acceleration of the particles to their terminal velocity, a factor that is based on aerodynamic diameter (Jayne et al., 2000; Johnston, 2000; Su et al., 2004).

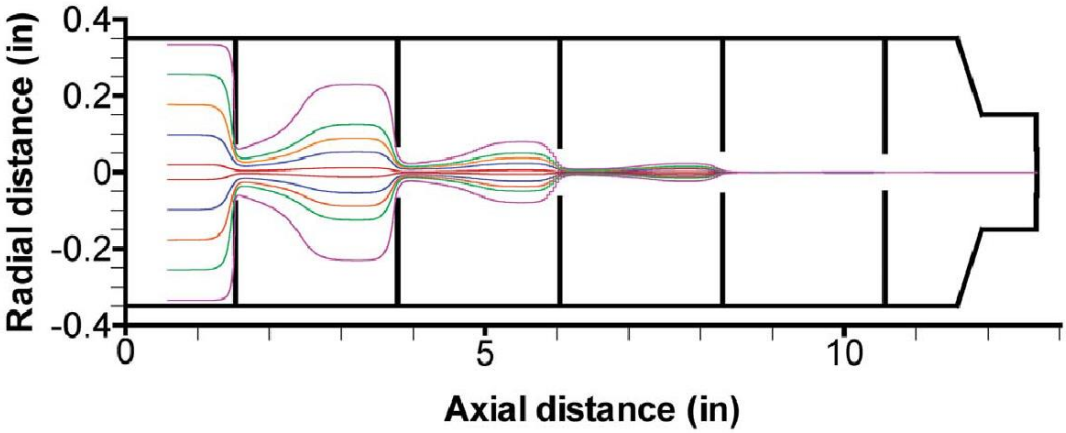

Figure 2.5 Schematic of the operation of an Aerodynamic Focussing Lens (AFL) (TSI, 2004b).

2.1.2 Particle Sizing

Following the sampling region, the particles enter the sizing region and travel at a velocity related to their diameter. The size of the particles is probed by two continuous-wave, diode-pumped, solid state lasers (532 nm 50 mW) that are arranged orthogonally and separated vertically by a distance of 6 cm. A schematic is shown in Figure 2.6. As the particle crosses the laser beam the scattered light is detected by a photomultiplier tube (PMT) and the signals from the two lasers are used to start and stop a clock registering the transit time (TSI, 2007). The transit time is then converted to aerodynamic diameter using a calibration curve carried out using Polystyrene Latex (PSL) spheres, particles of known diameters. The detection of smaller particles becomes increasingly difficult because they are unable to scatter enough light to be detected by the PMT. The ATOFMS operating with the converging nozzle inlet does not size particles < 200 nm while the ATOFMS operating with the AFL can detect particles ~150 nm in size. This improvement is due to alterations made to the sizing region such as replacing the glass windows with precision plano-convex focusing lenses with antireflection coating, replacing the polish formed mirrors with electroformed elliptical mirrors to improve the efficiency of the scattered light collection, incorporating a beam dump in place of the J-shaped light horns and the addition of a fast amplifier (Su et al., 2004).

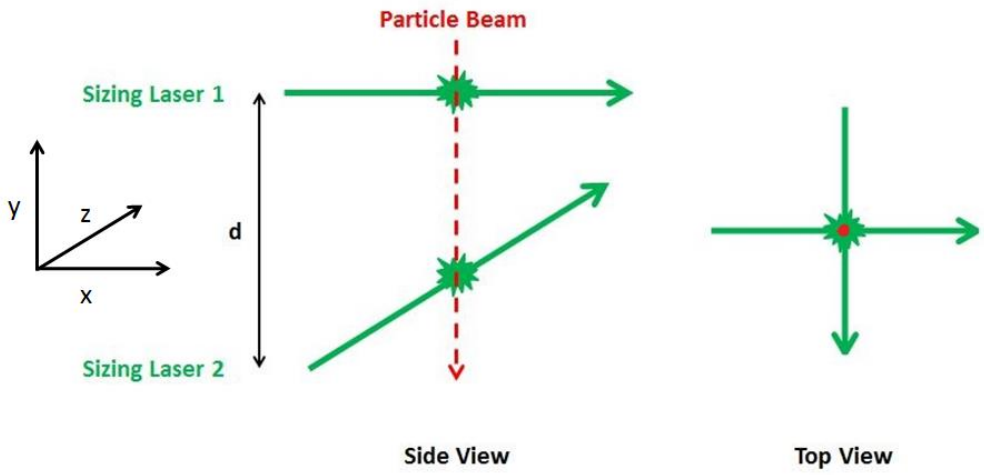

Figure 2.6 Operation of the sizing region of the ATOFMS.

2.1.3 Dual Ion Time of Flight Mass Spectrometer

Following transit through the sizing region the particle travels into the mass spectrometry region as shown in Figure 2.7. Here the particle is hit by a pulsed desorption/ionisation (D/I) Nd:YAG laser operating at 266 nm to generate gaseous ions for determining the chemical composition of the particle (TSI, 2004b, 2007). The D/I laser operates with a maximum output of 5 mJ/pulse with a pulse length of 5 ns and a maximum pulse rate of 20 Hz (TSI, 2004b, 2007).

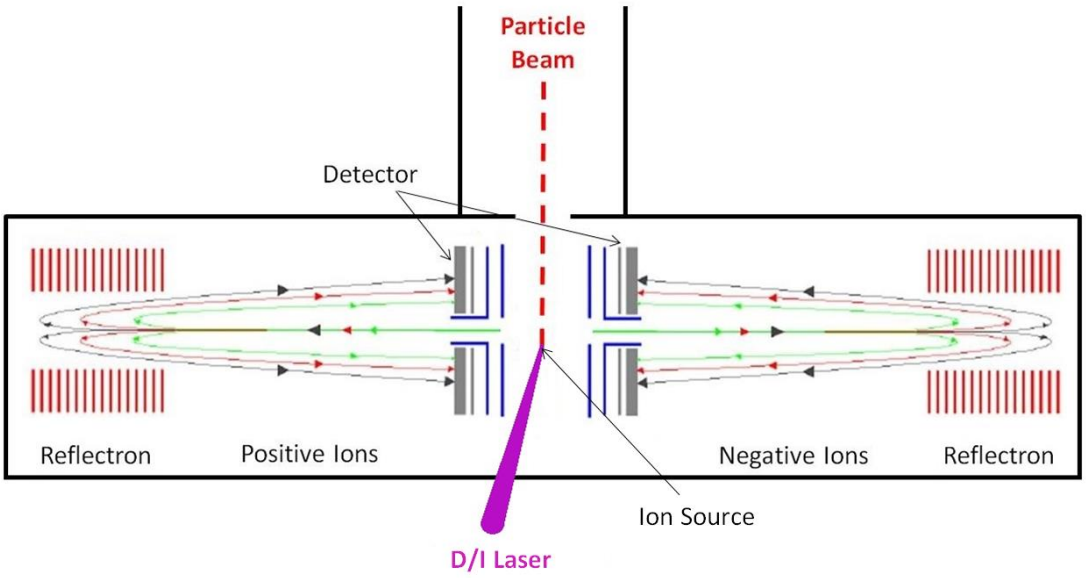

Figure 2.7 Schematic of the mass spectrometry region of the ATOFMS.

The transit time of the particles through the two laser velocimeter of the ATOFMS sizing region is used as a trigger for firing the D/I laser to hit the moving particle as it arrives at the centre of the ion source. The ATOFMS does not "hit" all of the sized particles. During the operation of the ATOFMS for this work 10 – 15% of the sized particles were successfully ionised. The D/I laser ablates the particle generating ions which then enter one of the two collinear time of flight (TOF) mass spectrometers, thus allowing the simultaneous detection of both positive and negative ions (Gard et al., 1997; Prather et al., 1994; TSI, 2007). The TOF technique is ideal for the analysis of single particles in real time as it can detect all the ions associated with a

single particle very rapidly. In contrast, scanning type mass spectrometers such as quadrupoles take considerably longer to generate a full mass spectrum as time is needed to scan through the full series of ions present which is not compatible with time constraints associated with the real time analysis.

The time of flight of ions is measured from a starting point (in the ATOFMS this is the ionisation event) until the ions arrive at the detector. In the ATOFMS, ions are generated at the ion source by the D/I laser, and accelerated into a flight tube due to a potential generated by source plates.

Ions with small *m/z* values reach a higher velocity than those with larger *m/z* and this causes separation of the ions as they travel along the flight tube. In regular TOF-MS the ions hit the ion detector at the end of the flight tube. However ions can acquire additional kinetic energy in the D/I process which results in ions with the same *m/z* attaining different velocities and causes peak broadening in the mass spectrum. In order to improve the quality of the mass spectrum, and reduce peak broadening, the ATOFMS employs a reflectron. In the reflectron (which is composed of a series of electrodes with a potential ramp applied) the ions slow down, stop, turn around and are accelerated back across the flight tube. Faster ions travel farther into the reflectron and have a longer residence time than slower ions with the same *m/z*, thus focussing ions of the same *m/z* to hit the detector at the same time reducing the peak width. Therefore the ions travel in a U shaped trajectory from the ion source through the flight tube into the reflectron back through the flight tube to the detector (Gard et al., 1997; Prather et al., 1994; TSI, 2004b). The resolution of the ATOFMS mass spectrometer is 500 m/Δm (TSI, 2004b).

2.2 Data Handling and Analysis

The commercially produced ATOFMS comes equipped with 2 different software programs MS-Control and MS-Analyze. MS-Control is the program that controls the operation of the ATOFMS during sampling and saves the particle size and mass spectrum information, along with the particle detection time and laser power used by

the D/I laser. This information is imported into other programs for further analysis (TSI, 2004a, 2007).

Prior to deployment of the ATOFMS in a measurement campaign, it is calibrated using a series of particles of known size. The particles used are PSL spheres with mean diameters of 240, 300, 400, 560, 700, 900 and 1300 nm. They are introduced into the ATOFMS using a nebuliser and the velocity of the particles between the two sizing lasers and the aerodynamic diameter are related using a calibration curve. In addition to the size calibration, the ATOFMS must also be calibrated for *m/z*. It is possible to perform this calibration prior to field studies using standard solutions containing metal salts, which produce ions with known *m/z*. However for the current study, the mass calibration was carried out using ambient data as many of the ions present in the ambient mass spectra present readily identifiable signals (e.g. EC fragments, K^+, Pb^+, nitrates and sulfates) that can be used in the calibration. The benefit of utilising ambient measurements for mass calibrations is that it allows calibrations to be undertaken every day, which minimises the effect of any changes in the TOF performance occurring during the campaign. The *m/z* calibration is carried out by visually examining the collected mass spectra. The time of flight of readily identifiable *m/z* peaks are noted. The signals used for the calibration are taken form many of the collected spectra in order to limit the possibility of errors. The selected signals are then used to produce a calibration curve which is then applied to the full dataset. The data are imported into the MS–Analyze program where the size calibration is applied and the *m/z* signals calibrated. While some querying procedures can be carried out using MS-Analyze, this program is only used for a "quick-look" at the ATOFMS data prior to detailed analysis using other software tools.

Detailed analysis of the ATOFMS data is performed using a software tool called Enchilada (Environmental chemistry through intelligent atmospheric data analysis) (Gross et al., 2010). Enchilada is a freeware SQL-based program for the analysis of single particle data developed at Carleton College Minnesota USA (Gross et al., 2010). The ATOFMS datasets are imported into this program and analysed using the *K*-means algorithm (MacQueen, 1967) where the *K* value is user defined. The centres of the clusters are defined by the first *K* particles, although it is possible to find cluster centres using a sub-sampling process. Each subsequent particle is placed

to its nearest centre, usually in Euclidean space. The value of *K* is increased until the distance between the particles and the centres is minimised i.e., where further clustering with increasing *K* fails to improve on the explanation for the clusters. At this point there are usually several clusters with a small population which indicates that the clustering is approaching the optimum *K* value.

After this stage there is a visual inspection step performed by the user where clusters are analysed to determine if they are composed of one particle type or if they are composed of two or more particle types, in which case this cluster must be re-analysed to separate these particle types from each other. Clusters exhibiting very similar average mass spectra, comparable temporal trends and size distributions are merged. There may also be several clusters containing very few particles (even just one particle in some cases) whose mass spectra are not calibrated correctly: these clusters are dismissed as unusable. When the number of clusters is finalised, the data is exported to data handling programs, such as Microsoft Excel or Igor Pro, which allow the temporal trends and size information to be investigated and interpreted along with other data, such as meteorological information. The finalised clusters are then labelled as particle types (Gross et al., 2010; Healy et al., 2010; Healy et al., 2009). The name of the particle types are based on the probable source or the dominant species in the average mass spectrum, e.g. sea-salt particles (source) or K-SUL particles (dominant species). Further analysis of the data allows the user to complete a source apportionment study where the different natural and anthropogenic pollutant sources of the particles can be assigned (Healy et al., 2010).

While the procedure described above was utilised throughout this study, another common method for the analysis of ATOFMS data is YAADA (Yet Another ATOFMS Data Analyzer). YAADA is a MATLAB based toolkit for the analysis of ATOFMS datasets using the adaptive resonance theory-based neural network (ART-2a) (Carpenter et al., 1991; Dall'Osto and Harrison, 2006; Song et al., 1999). In this analysis tool each spectrum is represented by a matrix of masses and intensities that is converted to a vector and subsequently normalized to unit length. A cluster vector is then created (from the first particle) and compared to each particle vector by taking their dot product. If a particle is similar enough (as dictated by a user-defined "vigilance factor") it will be assigned to that cluster, otherwise a new cluster is

created. When a particle is added to a cluster, the centre of that cluster moves in that direction to an extent controlled by the "learning rate". This process continues until all particles have been assigned to a cluster, and several iterations or passes are subsequently performed using the centres of those clusters.

Previously the results of ATOFMS datasets analysed by both Enchilada and YAADA have been compared (Giorio et al., 2012; Rebotier and Prather, 2007). It was found that while the ART-2a and *K*-means gave similar results there were differences in the average mass spectra of the same particle classes (Giorio et al., 2012). This was attributed to differences in the clustering procedures and the methods used to form the final particle types from the initial clusters. In general *K*-means was found to be quicker than ART-2a, although the accuracy and processing time of both algorithms depends on the user-defined constraints (Rebotier and Prather, 2007).

While the data analysis techniques discussed above were applied to the ATOFMS data collected as part of this work, Positive Matrix Factorisation (PMF) was applied to AMS and PIXE measurements which were compared to the ATOFMS results. PMF is a bilinear un-mixing receptor-only model used to describe measurements as a linear combination of several static factors (Crippa et al., 2013; Healy et al., 2010; Paatero and Tapper, 1994; Hopke, 2003). The uncertainties associated with each measurement is taken into account by the PMF technique (Paatero and Tapper, 1994; Hopke, 2003). This allows different measurements to be weighted based on their associated confidence in the PMF analysis. The application of PMF to the AMS and PIXE datasets are outlined in detail in Crippa et al. (2013) and Dall'Osto et al. (2013) respectively.

2.3 Deployment of ATOFMS in Field Studies

Aerosol Time of Flight mass spectrometers have been deployed during many field measurement campaigns in various environments since the development of the portable version (Gard et al., 1997). A review of many of these measurement campaigns is detailed elsewhere (Pratt and Prather, 2012). ATOFMS measurements

carried out at different locations over the last 10 – 15 years have resulted in a catalogue of "fingerprint" spectra for particles related to specific emission sources. These "fingerprints" from the literature are used in the analysis of data collected during field campaigns to assist in the identification of particle types. Here follows a short review of the major particle types of interest to this study.

Carbonaceous aerosol, comprised of Elemental Carbon (EC) and Organic Carbon (OC), has been detected in many ATOFMS measurements. Particles containing EC signals have previously been detected and been attributed to domestic combustion or traffic emissions (Healy et al., 2010). EC containing particle types were also detected in Mexico City (Moffet et al., 2008a), Atlanta (Liu et al., 2003) and California (Noble and Prather, 1996) and have been attributed to different sources such as industrial emissions and local fuel combustion. While EC is attributed to primary emitted particles, OC has been attributed to both primary and secondary organic aerosol in ATOFMS datasets. OC attributed to aged carbonaceous aerosol or SOA were measured in Mexico City (Moffet et al., 2008a), and California (Qin et al., 2012); it was also seen in fresh and aged combustion particles in ambient and laboratory measurements in Cork (Healy et al., 2010). OC has also been attributed to traffic emissions (Pastor et al., 2003). Furthermore EC and OC have been found mixed in particles in a process which has been attributed to OC condensing on EC particle types (Liu et al., 2003; Moffet et al., 2008a; Qin et al., 2012).

Fingerprint spectra attributed to specific fuel sources have also been identified in ATOFMS datasets. One of the most commonly detected particle types in ATOFMS measurements is due to biomass burning and has been observed in many different measurement locations (Dall'Osto and Harrison, 2006; Guazzotti et al., 2003; Healy et al., 2010; Moffet et al., 2008a; Qin and Prather, 2006; Silva et al., 1999; Zhou et al., 2006). Spectra related to domestic fuel sources such as coal, peat and wood have been identified in both ambient measurements and controlled combustion experiments, which allowed each of the particle types to be separated (Healy et al., 2010).

Particle types containing signals for calcium, sodium and EC have been identified in ATOFMS spectra and attributed to traffic-related emissions (Healy et al., 2010; Shields et al., 2008; Shields et al., 2007; Spencer et al., 2006). Traffic particles have

also been observed to contain OC fragments (Moffet et al., 2008a; Pastor et al., 2003; Spencer et al., 2006). These carbonaceous particle types are evident in many datasets due to the clear diurnal (rush hour) profile presented by the emissions. Particles containing signals for vanadium and nickel along with carbonaceous signals have also been attributed to heavy oil combustion, likely from industrial sources or shipping (Ault et al., 2009; Healy et al., 2009; Lake et al., 2004; Pastor et al., 2003).

All of the previously mentioned studies observed particles that contained secondary species such as nitrate, sulfate and ammonium ions. Such signals have been identified in many different particle types and are indicative of the processing of the particles after emission. In many ATOFMS datasets, fresh particles are distinguished from aged ones by the presence of these secondary species (Healy et al., 2010; Liu et al., 2003). To further aid identification of the level of atmospheric processing involved, ATOFMS mass spectra have been used to analyse the daily processing of nitrate-containing particles in London. The nitrate coating is removed around midday as the photolysis rate (to increase nitrate destruction) and temperature (for nitrate product evaporation) increases. These processes lead to a sulfate-containing core being revealed. The particle is then further processed at night, when temperatures drop, to regain the nitrate coating (Dall'Osto et al., 2009).

Sea-salt particle mass spectra have been detected in many monitoring campaigns (Dall'Osto and Harrison, 2006; Dall'Osto et al., 2006; Healy et al., 2010; Noble and Prather, 1997; Zhou et al., 2006). They are found to contain signals for sodium and chloride with the latter signal becoming diminished as the particles are processed and begin to uptake secondary species.

Industrial iron emissions have also been identified in ATOFMS datasets and iron-containing particles have been identified in emissions from steelworks (Dall'Osto et al., 2008; Furutani et al., 2011). Indeed the transport of industrial iron-containing particles from continental Europe was observed in London during the REPARTEE experiment (Harrison et al., 2012). In Mexico City as part of the MILAGRO campaign a particle type was observed with strong signals for zinc, lead and chloride (Moffet et al., 2008b). This was attributed to the incineration of waste, with the chloride ion being attributed to the burning of plastics (Moffet et al., 2008b).

Polycyclic Aromatic Hydrocarbons (PAHs) have been observed in several ATOFMS studies. PAHs present spectra with a broad number of signals associated with high molecular weight carbonaceous fragments, and are of particular interest due to the health effects associated with them (Nielsen et al., 1996). PAHs have been measured by ATOFMS and associated with traffic emissions in measurements undertaken in a road tunnel in California, where a number of the fragments related to specific PAHs were also identified (Gross et al., 2005; Gross et al., 2000). PAH-containing particles have also been measured in dynamometer studies using different fuels or fuel mixtures (Dutcher et al., 2011a; Dutcher et al., 2011b). In London a detected PAH particle type was attributed to SOA formed from the photochemical processing of VOCs emitted by traffic (Dall'Osto and Harrison, 2012). PAHs have also been measured at an industrial site and associated with steel-mill activity (Dall'Osto et al., 2012).

Dust particles have been identified in many studies. Ship-based ATOFMS measurements carried out during the ACE-Asia campaign found that the chemical composition of dust influences the uptake of secondary species with aluminosilicate and iron rich dust associated with sulfate and the calcium rich dust being mixed with nitrate (Sullivan et al., 2007a). The uptake of chloride by heterogeneous reaction with gaseous HCl was also identified in ATOFMS studies (Sullivan et al., 2007a; Sullivan et al., 2007b). The processing of Saharan dust during atmospheric transport was monitored using ATOFMS measurements (Dall'Osto et al., 2010). Samples were collected in the Sahara and ambient measurements were performed in Cape Verde and Ireland. It was found that the fresh particles contained no secondary species while ambient sample data obtained in Cape Verde included nitrate signals; particles sampled in Ireland contained nitrate, sulfate and methanesulfonate (Dall'Osto et al., 2010). In Mexico City, calcium and aluminosilicate dust types have been observed (Moffet et al., 2008a). In California an increase in ambient dust levels were observed during the Santa Ana Winds (Guazzotti et al., 2001). In Athens several dust particle types were attributed to dust: Ca-rich, Si dust and a more general soil dust type were observed. The final two dust classes (dust_veg and dust_gen_2) were attributed to vegetative debris (Dall'Osto and Harrison, 2006). The ATOFMS has previously measured vegetative emissions from grass mowing process and found to contain potassium and organo-nitrogen signals from plant debris

(Drewnick et al., 2008). Data was also obtained to generate identifying spectra for fungal spores and found to contain K, Na, CN, CNO and phosphate fragments (Fergenson et al., 2004).

Laboratory studies have been carried out to generate mass spectra for several amine species (Angelino et al., 2001). Mass spectra were generated for trimethylamine, di- and triethylamine, and di- and tripropylamine (Angelino et al., 2001). The reaction of amines with acidic species was also examined and it was concluded that the amines present in the particles were likely present in the form of aminium salts (Angelino et al., 2001). In Riverside California, particles were observed to contain signals associated with alkylamines and oxidised amines (Pratt et al., 2009). It was shown that amines in the particles were in the form of aminium salts of nitrate or sulfate in the summer, while during the autumn, nitrate and sulfate were preferentially associated with ammonium (Pratt et al., 2009). Trimethylamine (TMA) is an amine species previously identified in ambient ATOFMS spectra (McGuire et al., 2011; Rehbein et al., 2011). TMA is associated with agricultural emissions and these studies found that particles enriched in TMA occur during periods with high relative humidity or fog events with uptake on to existing particles that increases with increasing acidity (Rehbein et al., 2011). Another amine-containing particle type was identified in an indoor environment and attributed to Environmental Tobacco Smoke (ETS) as it contained mass spectral features associated with nitrosamines (Dall'Osto et al., 2007).

Many of these previously observed particle type mass spectral “fingerprints” are utilised throughout the analysis of the data collected during the ATOFMS deployments in this work.

2.4 References

Allen, J.O., Fergenson, D.P., Gard, E.E., Hughes, L.S., Morrical, B.D., Kleeman, M.J., Gross, D.S., Galli, M.E., Prather, K.A., Cass, G.R., 2000. Particle detection efficiencies of aerosol time of flight mass spectrometers under

ambient sampling conditions. Environmental Science & Technology 34, 211-217.

Angelino, S., Suess, D.T., Prather, K.A., 2001. Formation of aerosol particles from reactions of secondary and tertiary alkylamines: Characterization by aerosol time-of-flight mass spectrometry. Environmental Science & Technology 35, 3130-3138.

Ault, A.P., Moore, M.J., Furutani, H., Prather, K.A., 2009. Impact of emissions from the Los Angeles port region on San Diego air quality during regional transport events. Environmental Science & Technology 43, 3500-3506.

Carpenter, G.A., Grossberg, S., Rosen, D.B., 1991. ART 2-A: An adaptive resonance algorithm for rapid category learning and recognition. Neural networks 4, 493-504.

Crippa, M., DeCarlo, P.F., Slowik, J.G., Mohr, C., Heringa, M.F., Chirico, R., Poulain, L., Freutel, F., Sciare, J., Cozic, J., Di Marco, C.F., Elsasser, M., Nicolas, J.B., Marchand, N., Abidi, E., Wiedensohler, A., Drewnick, F., Schneider, J., Borrmann, S., Nemitz, E., Zimmermann, R., Jaffrezo, J.L., Prévôt, A.S.H., Baltensperger, U., 2013. Wintertime aerosol chemical composition and source apportionment of the organic fraction in the metropolitan area of Paris. Atmos. Chem. Phys. 13, 961-981.

Dall'Osto, M., Booth, M.J., Smith, W., Fisher, R., Harrison, R.M., 2008. A study of the size distributions and the chemical characterization of airborne particles in the vicinity of a large integrated steelworks. Aerosol Science and Technology 42, 981-991.

Dall'Osto, M., Harrison, R., Coe, H., Williams, P., Allan, J., 2009. Real time chemical characterization of local and regional nitrate aerosols. Atmospheric Chemistry and Physics 9, 3709-3720.

Dall'Osto, M., Harrison, R.M., 2006. Chemical characterisation of single airborne particles in Athens (Greece) by ATOFMS. Atmospheric Environment 40, 7614-7631.

Dall'Osto, M., Harrison, R.M., 2012. Urban organic aerosols measured by single particle mass spectrometry in the megacity of London. Atmos. Chem. Phys. 12, 4127-4142.

Dall'Osto, M., Harrison, R.M., Beddows, D.C.S., Freney, E.J., Heal, M.R., Donovan, R.J., 2006. Single-Particle Detection Efficiencies of Aerosol Time-of-Flight Mass Spectrometry during the North Atlantic Marine Boundary Layer Experiment. Environmental Science & Technology 40, 5029-5035.

Dall'Osto, M., Harrison, R.M., Charpantidou, E., Loupa, G., Rapsomanikis, S., 2007. Characterisation of indoor airborne particles by using real-time aerosol mass spectrometry. Science of the Total Environment 384, 120-133.

Dall'Osto, M., Drewnick, F., Fisher, R., Harrison, R.M., 2012. Real-Time Measurements of Nonmetallic Fine Particulate Matter Adjacent to a Major Integrated Steelworks. Aerosol Science and Technology 46, 639-653.

Dall'Osto, M., Harrison, R.M., Highwood, E.J., O'Dowd, C., Ceburnis, D., Querol, X., Achterberg, E.P., 2010. Variation of the mixing state of Saharan dust particles with atmospheric transport. Atmospheric Environment 44, 3135-3146.

Dall'Osto, M., Querol, X., Amato, F., Karanasiou, A., Lucarelli, F., Nava, S., Calzolai, G., Chiari, M., 2013. Hourly elemental concentrations in PM2.5 aerosols sampled simultaneously at urban background and road site during SAPUSS – diurnal variations and PMF receptor modelling. Atmos. Chem. Phys. 13, 4375-4392.

Drewnick, F., Dall'Osto, M., Harrison, R., 2008. Characterization of aerosol particles from grass mowing by joint deployment of ToF-AMS and ATOFMS instruments. Atmospheric Environment 42, 3006-3017.

Dutcher, D.D., Pagels, J., Bika, A., Franklin, L., Stolzenburg, M., Thompson, S., Medrano, J., Brown, N., Gross, D.S., Kittelson, D., 2011a. Emissions from soy biodiesel blends: A single particle perspective. Atmospheric Environment 45, 3406-3413.

Dutcher, D.D., Stolzenburg, M.R., Thompson, S.L., Medrano, J.M., Gross, D.S., Kittelson, D.B., McMurry, P.H., 2011b. Emissions from ethanol-gasoline blends: A single particle perspective. Atmosphere 2, 182-200.

Fergenson, D.P., Pitesky, M.E., Tobias, H.J., Steele, P.T., Czerwieniec, G.A., Russell, S.C., Lebrilla, C.B., Horn, J.M., Coffee, K.R., Srivastava, A., Pillai, S.P., Shih, M.T.P., Hall, H.L., Ramponi, A.J., Chang, J.T., Langlois, R.G., Estacio, P.L., Hadley, R.T., Frank, M., Gard, E.E., 2004. Reagentless detection and classification of individual bioaerosol particles in seconds. Analytical Chemistry 76, 373-378.

Furutani, H., Jung, J., Miura, K., Takami, A., Kato, S., Kajii, Y., Uematsu, M., 2011. Single-particle chemical characterization and source apportionment of iron-containing atmospheric aerosols in Asian outflow. Journal of Geophysical Research 116, D18204.

Gard, E., Mayer, J.E., Morrical, B.D., Dienes, T., Fergenson, D.P., Prather, K.A., 1997. Real-time analysis of individual atmospheric aerosol particles: Design and performance of a portable ATOFMS. Analytical Chemistry 69, 4083-4091.

Giorio, C., Tapparo, A., Dall'Osto, M., Harrison, R.M., Beddows, D., Di Marco, C., Nemitz, E., 2012. Comparison of three techniques for analysis of data from an Aerosol Time-of-Flight Mass Spectrometer. Atmospheric Environment 61, 316-326.

Gross, D.S., Atlas, R., Rzeszotarski, J., Turetsky, E., Christensen, J., Benzaid, S., Olson, J., Smith, T., Steinberg, L., Sulman, J., Ritz, A., Anderson, B., Nelson, C., Musicant, D.R., Chen, L., Snyder, D.C., Schauer, J.J., 2010. Environmental chemistry through intelligent atmospheric data analysis. Environmental Modelling & Software 25, 760-769.

Gross, D.S., Barron, A.R., Sukovich, E.M., Warren, B.S., Jarvis, J.C., Suess, D.T., Prather, K.A., 2005. Stability of single particle tracers for differentiating between heavy- and light-duty vehicle emissions. Atmospheric Environment 39, 2889-2901.

Gross, D.S., Galli, M.E., Silva, P.J., Wood, S.H., Liu, D.Y., Prather, K.A., 2000. Single particle characterization of automobile and diesel truck emissions in the Caldecott Tunnel. Aerosol Science and Technology 32, 152-163.

Guazzotti, S.A., Suess, D.T., Coffee, K.R., Quinn, P.K., Bates, T.S., Wisthaler, A., Hansel, A., Ball, W.P., Dickerson, R.R., Neususs, C., Crutzen, P.J., Prather, K.A., 2003. Characterization of carbonaceous aerosols outflow from India and Arabia: Biomass/biofuel burning and fossil fuel combustion. Journal of Geophysical Research-Atmospheres 108, 4485, doi:10.1029/2002JD003277, D15.

Guazzotti, S.A., Whiteaker, J.R., Suess, D., Coffee, K.R., Prather, K.A., 2001. Real-time measurements of the chemical composition of size-resolved particles during a Santa Ana wind episode, California USA. Atmospheric Environment 35, 3229-3240.

Harrison, R.M., Dall'Osto, M., Beddows, D.C.S., Thorpe, A.J., Bloss, W.J., Allan, J.D., Coe, H., Dorsey, J.R., Gallagher, M., Martin, C., Whitehead, J., Williams, P.I., Jones, R.L., Langridge, J.M., Benton, A.K., Ball, S.M., Langford, B., Hewitt, C.N., Davison, B., Martin, D., Petersson, K.F., Henshaw, S.J., White, I.R., Shallcross, D.E., Barlow, J.F., Dunbar, T., Davies, F., Nemitz, E., Phillips, G.J., Helfter, C., Di Marco, C.F., Smith, S., 2012. Atmospheric chemistry and physics in the atmosphere of a developed megacity (London): an overview of the REPARTEE experiment and its conclusions. Atmos. Chem. Phys. 12, 3065-3114.

Healy, R., Hellebust, S., Kourtchev, I., Allanic, A., O'Connor, I., Bell, J., Healy, D., Sodeau, J., Wenger, J., 2010. Source apportionment of PM 2.5 in Cork Harbour, Ireland using a combination of single particle mass spectrometry and quantitative semi-continuous measurements. Atmospheric Chemistry and Physics 10, 9593-9613.

Healy, R.M., O'Connor, I.P., Hellebust, S., Allanic, A., Sodeau, J.R., Wenger, J.C., 2009. Characterisation of single particles from in-port ship emissions. Atmospheric Environment 43, 6408-6414.

Hopke, P.K., 2003. The evolution of chemometrics. Analytica Chimica Acta 500, 365-377

Jayne, J.T., Leard, D.C., Zhang, X., Davidovits, P., Smith, K.A., Kolb, C.E., Worsnop, D.R., 2000. Development of an aerosol mass spectrometer for size and composition analysis of submicron particles. Aerosol Science & Technology 33, 49-70.

Johnston, M.V., 2000. Sampling and analysis of individual particles by aerosol mass spectrometry. Journal of Mass Spectrometry 35, 585-595.

Lake, D.A., Tolocka, M.P., Johnston, M.V., Wexler, A.S., 2004. The character of single particle sulfate in Baltimore. Atmospheric Environment 38, 5311-5320.

Liu, D.Y., Wenzel, R.J., Prather, K.A., 2003. Aerosol time-of-flight mass spectrometry during the Atlanta Supersite Experiment: 1. Measurements. Journal of Geophysical Research-Atmospheres 108, 8426, doi:10.1029/2001JD001562, D7.

MacQueen, J., 1967. Some methods for classification and analysis of multivariate observations, Proceedings of the fifth Berkeley symposium on mathematical statistics and probability. California, USA.

McGuire, M., Jeong, C.-H., Slowik, J., Chang, R.-W., Corbin, J., Lu, G., Mihele, C., Rehbein, P., Sills, D., Abbatt, J., 2011. Elucidating determinants of aerosol composition through particle-type-based receptor modeling. Atmospheric Chemistry and Physics 11, 8133-8155.

Moffet, R.C., de Foy, B., Molina, L.T., Molina, M.J., Prather, K.A., 2008a. Measurement of ambient aerosols in northern Mexico City by single particle mass spectrometry. Atmospheric Chemistry and Physics 8, 4499-4516.

Moffet, R.C., Desyaterik, Y., Hopkins, R.J., Tivanski, A.V., Gilles, M.K., Wang, Y., Shutthanandan, V., Molina, L.T., Abraham, R.G., Johnson, K.S., Mugica, V., Molina, M.J., Laskin, A., Prather, K.A., 2008b. Characterization of aerosols

containing Zn, Pb, and Cl from an industrial region of Mexico City. Environmental Science & Technology 42, 7091-7097.

Nielsen, T., Jørgensen, H.E., Larsen, J.C., Poulsen, M., 1996. City air pollution of polycyclic aromatic hydrocarbons and other mutagens: occurrence, sources and health effects. Science of the Total Environment 189, 41-49.

Noble, C.A., Prather, K.A., 1996. Real-time measurement of correlated size and composition profiles of individual atmospheric aerosol particles. Environmental Science & Technology 30, 2667-2680.

Noble, C.A., Prather, K.A., 1997. Real-time single particle monitoring of a relative increase in marine aerosol concentration during winter rainstorms. Geophysical Research Letters 24, 2753-2756.

Nordmeyer, T., Prather, K.A., 1994. Real-time measurement capabilities using aerosol time-of-flight mass-spectrometry. Analytical Chemistry 66, 3540-3542.

Paatero, P., Tapper, U., 1994. Positive matrix factorization: A non-negative factor model with optimal utilization of error estimates of data values. Environmetrics 5, 111-126.

Pastor, S.H., Allen, J.O., Hughes, L.S., Bhave, P., Cass, G.R., Prather, K.A., 2003. Ambient single particle analysis in Riverside, California by aerosol time-of-flight mass spectrometry during the SCOS97-NARSTO. Atmospheric Environment 37, 239-258.

Prather, K.A., Nordmeyer, T., Salt, K., 1994. Real-time characterization of individual aerosol-particles using time-of-flight mass-spectrometry. Analytical Chemistry 66, 1403-1407.

Pratt, K.A., Hatch, L.E., Prather, K.A., 2009. Seasonal Volatility Dependence of Ambient Particle Phase Amines. Environmental Science & Technology 43, 5276-5281.

Pratt, K.A., Prather, K.A., 2012. Mass spectrometry of atmospheric aerosols—Recent developments and applications. Part II: On-line mass spectrometry techniques. Mass Spectrometry Reviews 31, 17-48.

Qin, X., Pratt, K.A., Shields, L.G., Toner, S.M., Prather, K.A., 2012. Seasonal comparisons of single-particle chemical mixing state in Riverside, CA. Atmospheric Environment 59, 587-596.

Qin, X.Y., Prather, K.A., 2006. Impact of biomass emissions on particle chemistry during the California Regional Particulate Air Quality Study. International Journal of Mass Spectrometry 258, 142-150.

Rebotier, T.P., Prather, K.A., 2007. Aerosol time-of-flight mass spectrometry data analysis: A benchmark of clustering algorithms. Analytica Chimica Acta 585, 38-54.

Rehbein, P.J., Jeong, C.-H., McGuire, M.L., Yao, X., Corbin, J.C., Evans, G.J., 2011. Cloud and fog processing enhanced gas-to-particle partitioning of trimethylamine. Environmental Science & Technology 45, 4346-4352.

Shields, L.G., Qin, X.Y., Toner, S.M., Prather, K.A., 2008. Detection of ambient ultrafine aerosols by single particle techniques during the SOAR 2005 campaign. Aerosol Science and Technology 42, 674-684.

Shields, L.G., Suess, D.T., Prather, K.A., 2007. Determination of single particle mass spectral signatures from heavy-duty diesel vehicle emissions for PM2.5 source apportionment. Atmospheric Environment 41, 3841-3852.

Silva, P.J., Liu, D.Y., Noble, C.A., Prather, K.A., 1999. Size and chemical characterization of individual particles resulting from biomass burning of local Southern California species. Environmental Science & Technology 33, 3068-3076.

Snyder, D.C., Schauer, J.J., Gross, D.S., Turner, J.R., 2009. Estimating the contribution of point sources to atmospheric metals using single-particle mass spectrometry. Atmospheric Environment 43, 4033-4042.

Song, X.H., Hopke, P.K., Fergenson, D.P., Prather, K.A., 1999. Classification of single particles analyzed by ATOFMS using an artificial neural network, ART-2A. Analytical Chemistry 71, 860-865.

Spencer, M.T., Shields, L.G., Sodeman, D.A., Toner, S.M., Prather, K.A., 2006. Comparison of oil and fuel particle chemical signatures with particle emissions from heavy and light duty vehicles. Atmospheric Environment 40, 5224-5235.

Su, Y.X., Sipin, M.F., Furutani, H., Prather, K.A., 2004. Development and characterization of an aerosol time-of-flight mass spectrometer with increased detection efficiency. Analytical Chemistry 76, 712-719.

Sullivan, R., Guazzotti, S., Sodeman, D., Prather, K., 2007a. Direct observations of the atmospheric processing of Asian mineral dust. Atmospheric Chemistry and Physics 7, 1213-1236.

Sullivan, R.C., Guazzotti, S.A., Sodeman, D.A., Tang, Y.H., Carmichael, G.R., Prather, K.A., 2007b. Mineral dust is a sink for chlorine in the marine boundary layer. Atmospheric Environment 41, 7166-7179.

TSI, 2004a. MS-Analyze Software user manual Revision B.

TSI, 2004b. Series 3800 Aerosol Time-of-Flight Mass Spectrometers with Aerodynamic Focusing Lens Technology P/N 1933798 Rev. D.

TSI, 2007. Series 3800 Aerosol Time-of-Flight Mass Spectrometers (ATOFMS) with Aerodynamic Focusing Lens P/N 1930036, Revision C .

Zhou, L., Hopke, P.K., Venkatachari, P., 2006. Cluster analysis of single particle mass spectra measured at Flushing, NY. Analytica Chimica Acta 555, 47-56.

3 Characterisation of airborne single particles in Paris, France using ATOFMS

Contents

3.1 Introduction

3.1.1 Paris

Paris is one of the largest metropolitan areas in Europe with an urban population of around 11 000 000 people. The city and its suburbs are located in the flat terrain of the Paris Basin. The topography of the region results in the regional atmospheric conditions being influenced mainly by large scale (cyclonic scale) meteorological conditions.

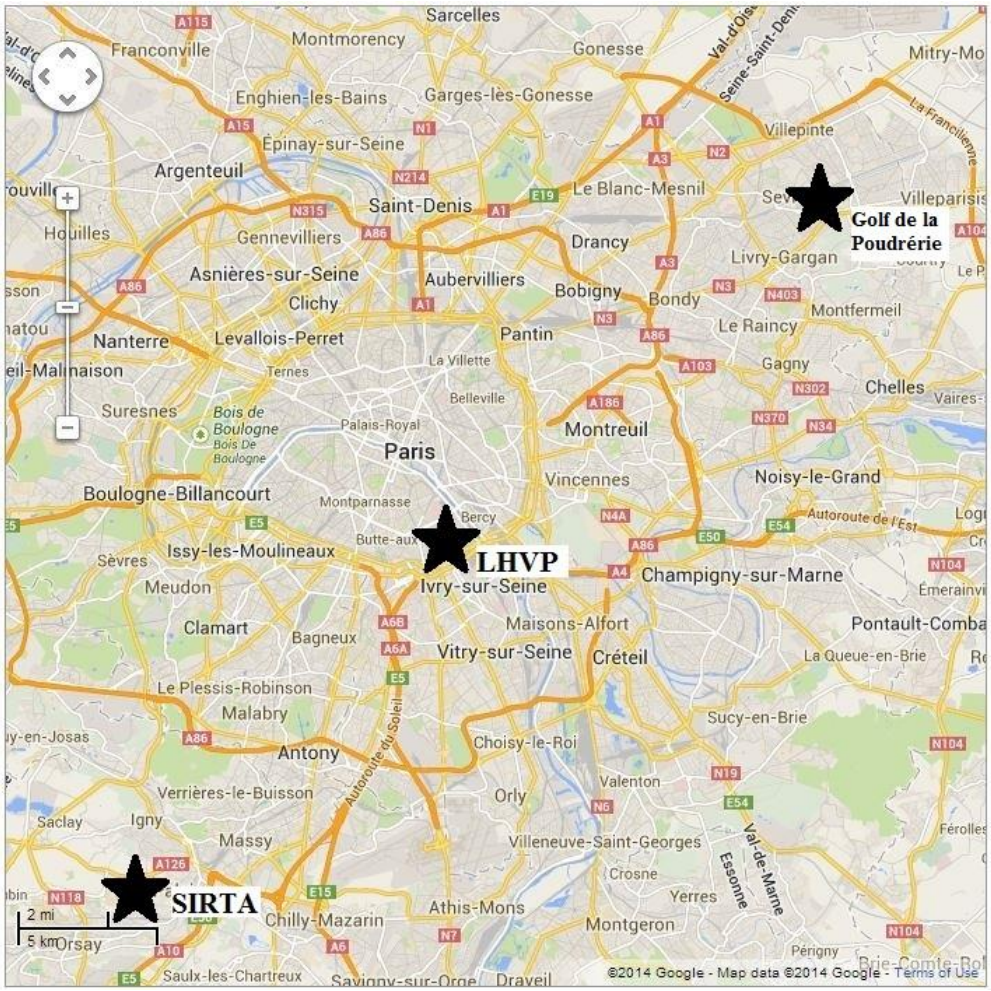

Figure 3.1 Map of Paris showing sampling sites used during MEGAPOLI.

3.1.2 Atmospheric monitoring in Paris

Numerous monitoring studies have been carried out in the Paris region to provide information on air quality and sources of pollution. A brief overview of the most relevant previous studies is presented here.

A one-year comprehensive chemical characterisation study of fine aerosols ($PM_{2.5}$) has been carried out at several measurement sites in and around Paris (Bressi et al., 2013a). It was observed that the highest $PM_{2.5}$ concentrations were measured from December to April (> 15 μg m^{-3}, on average). Levels were, on average, between 10 and 15 μg m^{-3} during most other months with the lowest levels of $PM_{2.5}$ (<10 μg m^{-3}) found during July and August. The highest levels of $PM_{2.5}$ were observed during air masses that originated in north-eastern Europe (continental air masses); high levels were also detected during periods with low boundary layer height and also low temperatures. The lowest levels of $PM_{2.5}$ were observed during marine air masses and precipitation. The chemical composition of the sampled $PM_{2.5}$ consisted of Organic Matter (OM) (38–47 %), nitrate (17–22 %), non-sea-salt sulfate (13–16 %), ammonium (10–12 %), Elemental Carbon (EC) (4–10 %), mineral dust (2–5 %) and sea salt (3–4 %). OM was mostly attributed to mid- and long-range transport of emissions with little influence of local traffic and wood burning. This argument was supported by the homogenous concentrations of OM across all the sampling sites. Secondary Inorganic Aerosol (SIA): nitrate, sulfate and ammonium ions were observed with similar co-variance at each of the sites. This finding was attributed to the transport of these pollutants to the city. Some sites did show increased levels of nitrate, ammonium and sulfate due to local traffic emissions of NO_x, NH_3 and SO_2. EC was attributed to local sources with 79% described as local emissions. This study found that 88% of the EC was related to fossil fuel combustion with the remaining 12% related to biomass burning. Sea salt was found to peak during Atlantic air masses and was detected at similar levels at all sites (Bressi et al., 2013a)

The data from this latter one year study, (Bressi et al., 2013a), was utilised in source apportionment models to determine the origins of fine aerosols in Paris (Bressi et al., 2013b). Positive Matrix Factorisation (PMF) was applied to the data and seven factors were obtained: ammonium sulfate-rich (27% of fine fraction), ammonium nitrate-rich (24%), heavy oil combustion (17%), road traffic (14%), biomass burning

(12%), marine aerosols (6%) and metal industries (1%). Further analysis was undertaken to determine the likely geographic origin of the different factors. Both the ammonium sulfate-rich and ammonium nitrate-rich factors were determined to be primarily from north-eastward mid- or long-range transport. Heavy oil combustion was determined to be associated with industrial activities and shipping emissions associated with northern France and the English Channel. The road traffic factor was attributed to local sources, while the biomass burning factor was associated with both locally emitted particles and particles imported from south of Paris. This study determined that more than half of the fine aerosol in Paris is transported into the city from continental Europe with local emissions contributing a quarter of the annually averaged fine aerosol mass (Bressi et al., 2013b).

The origin of particulate matter pollution episodes during wintertime in the Paris Basin has also been investigated using the CHIMERE model (Bessagnet et al., 2005). This study determined that there was a strong influence from Germany, the Netherlands and Belgium during pollution events with north-easterly air mass origins. It was determined that during most of the wintertime pollution events the outside contribution to PM reaches 50% while during non-event periods this contribution falls to 20% (Bessagnet et al., 2005).

The springtime contribution of regional and continental emissions in the Paris region has also been investigated (Sciare et al., 2010). It was observed, for periods with contributions from continental air masses, that $PM_{2.5}$ showed high variability with peaks of up to 70 $\mu g\ m^{-3}$. During these times ions contributed up to 75% of the fine aerosol mass. The carbonaceous aerosol was not influenced by long range transport and thus attributable to local sources. During marine air mass events, the carbonaceous aerosol comprised 75% of the fine particulate matter. Diurnal profiles were utilised to determine likely local or transported particles. Using this method BC and OC were attributed to local emissions, with BC presenting morning and evening maxima. The OC profile exhibited their highest levels in association with photochemical processing and a second peak concurrent with the BC evening peak. VOC measurements were carried out that showed a relationship between the oxygenated VOC (OVOC) and ion concentrations. The coincidence of these particles

detected during continental episodes showed that during these periods Paris was influenced by photochemically aged air masses (Sciare et al., 2010).

The contribution of semi-volatile aerosols to the fine aerosol fraction in Paris has been investigated (Favez et al., 2007). It was observed that $PM_{2.5}$ TEOM measurements underestimated the mass concentration by 50% and 35% in winter and summer respectively. These measurements agree with studies in other locations where the high discrepancy during the winter was likely due to the increased temperature difference between ambient conditions and the TEOM system. It was observed that the semi-volatile fraction in winter was mainly composed of ammonium nitrate with a contribution from organic compounds due to the low temperature and high relative humidity inducing condensation. During summer, the semi-volatile fraction was determined to be formed mainly by photochemical processes and was found to account for more than 50% of the SOA measured during the summer (Favez et al., 2007).

Several techniques were used to measure the contribution of wood burning to particulate matter during the winter in Paris (Favez et al., 2009). A relatively high WSOC/OC ratio of 0.35±0.05 was found. This result was concluded to be evidence of biomass burning, as such particles are particularly rich in WSOC. A higher aethalometer absorption exponent was measured in winter compared to the summer, attributed to a change in the chemical composition of the sampled aerosols. The associated absorption exponent was found to correlate with the OC/EC ratio, confirming the impact of organic aerosol on these samples. The diurnal profile of the absorption exponent displayed overnight peaks and was observed every day of the campaign, suggesting these particles were due to a local source. All of these results were determined to be indicative of brown carbon containing emissions being present in the Paris region. The events were attributed to wood burning as coal burning, the other likely source of brown carbon, is not a major fuel utilised in France. These measurements were used to determine the contribution of biomass burning to the $PM_{2.5}$ which was found to be 20 ± 10% (Favez et al., 2009).

3.1.3 MEGAPOLI Campaign

MEGAPOLI is a large scale EC-funded research project entitled: Megacities: Emissions, urban, regional and Global Atmospheric Pollution and climate effects, and integrated tools for assessment and mitigation (FP7-ENV-2007.1.1.2.1). A central component of the MEGAPOLI project was two atmospheric measurement campaigns in the metropolitan area of Paris in summer 2009 and winter 2010. The MEGAPOLI campaign concept and aims are outlined in detail elsewhere (Baklanov et al., 2010). In brief, the specific objectives of MEGAPOLI are: (i) to assess impacts of megacities and large air-pollution hot-spots on local, regional and global air quality; (ii) to quantify feedbacks among megacity air quality, local and regional climate, and global climate change; (iii) to develop improved integrated tools for prediction of air pollution in megacities (Baklanov et al., 2010).

The measurement campaigns carried out as part of the MEGAPOLI project took place in and around Paris during two intensive monitoring periods, 1–31 July 2009 and 15 January-15 February 2010. During these campaigns three primary fixed ground monitoring sites were utilised as shown in Figure 3.1. Four secondary fixed ground measurement sites, five mobile monitoring vehicles and an aircraft were also used during the campaign. The three primary monitoring sites were located at the Laboratoire d'Hygiène de la Ville de Paris (LHVP), SIRTA/IPSL and Golf de la Poudrérie à Livry-Gargan. The LHVP is an urban background site within the metropolitan area of Paris. The other sites SIRTA and Golf are suburban sites about 20 km to the south-west and 20 km north-east of the city respectively. The mobile units and the aircraft were utilised during the campaign to follow the Paris plume as the pollutants left the city and travelled into the wider Ile de France region. As the ATOFMS measurements were carried out during the winter campaign, only that period will be discussed here.

The ATOFMS results outlined in this work have been used as input to further analyses and these results have been published in several studies (Healy et al., 2014; Healy et al., 2013; Healy et al., 2012). These studies will not be discussed in detail here but pertinent results will be used as part of the discussion in Section 3.3.

During the wintertime monitoring campaign the aerosol chemical composition was analysed and source apportionment of the organic fraction was carried out (Crippa et al., 2013b). Measurements for this study were carried out primarily using an Aerodyne AMS and an aethalometer to classify and quantify the non-refractory and black carbon fractions respectively. The results showed that the composition of the aerosol was similar at all three primary monitoring sites during the winter campaign, suggesting that regional sources dominate over local emissions. The average chemical composition across the three sites was 30–36% organics, 28–29% nitrate, 12–14% ammonium, 7–13% black carbon, 14–16% sulfate, and 0.8–1.2% chloride.

Source apportionment studies were subsequently performed on the AMS data and returned a number of factors related to both primary and secondary organic aerosol. At the SIRTA site three primary sources (Hydrocarbon-like organic aerosol (HOA), biomass burning OA (BBOA) and cooking-related organic aerosol (COA)) and one secondary source (oxidized organic aerosols (OOA)) were identified. At the LHVP site all of these factors were also identified along with a second factor associated with oxygenated BBOA (OOA2-BBOA). Finally, HOA, BBOA, OOA and OOA2-BBOA were all identified at the Golf site. The average contribution of OOA at each site was found to be 57%, 58% and 74% for the LHVP, SIRTA and GOLF sites, respectively. The HOA contribution averaged 11-13% peaking around 16–19% during the morning rush hour. The BBOA contribution was 13-16% with a maximum of 17–19% during the evening peak. The COA fraction contributed 11% at SIRTA and 17% at LHVP to the total organic mass, but a maximum of 35% was detected at the LHVP during the two main meal-times, ca. 13:00 and 20:00. This study apportioned the BC to two different sources: traffic (76-80%) and biomass burning (20-24%) (Crippa et al., 2013b).

In a related study, Crippa et al. (2013a) used both gas (PTR-MS) and particle phase (AMS) measurements to examine whether this approach improved the source apportionment of the organic aerosol. The factors obtained, using AMS-PTRMS data from the LHVP site, were similar but some discrepancies were noted. Three primary sources were identified: traffic (6% of OA); cooking (18%) and wood burning (33%), along with two secondary fractions, low volatility (LV-OOA 24%) and semi-volatile oxygenated organic aerosol (SV-OOA 18%). Using this method the factor

associated with biomass burning was found to have a larger contribution than just by use of the AMS data. The differences observed in the source apportionment studies using the AMS-PTRMS as opposed to AMS alone occur because the former method allows greater separation of the factors (Crippa et al., 2013a).

The refactory black carbon (rBC) properties and hygroscopic growth factors (GF) were also analysed during the winter campaign (Laborde et al., 2013). Similar to the study of Crippa et al. (2013b), it was found that traffic emissions were the dominant contributor to rBC, with biomass burning only representing a minor contribution. The traffic rBC particles had no coating and were found to be non-hygroscopic, while the biomass particles were coated, larger and slightly hygroscopic. More hygroscopic particles were observed when the sampling site was influenced by aged or continental air masses. However, 95% of these background particles did not contain an rBC core and had a large non-refractory coating. The low hygroscopicity of the locally emitted particles means that such particles will exhibit lower CCN activity and therefore will have a longer residence time (Laborde et al., 2013).

Kamilli et al. (2014) also examined the hygroscopic properties of the aerosol and related it to the chemical composition derived from AMS and MAAP measurements at the LHVP site. The GF measured during the winter campaign was considerably higher than observed in summer 2009 and linked to a change in the chemical composition of the aerosol during the two seasons. The organic carbon fraction was found to be higher during the summer, thus reducing the hygroscopic growth factor, while the fraction of inorganic salts was higher during the winter measurements. The relative amounts of inorganic salts also changed during the winter with nitrate dominating whereas during the summer, sulfate dominated. These measurements also indicated little variation in the hygroscopic growth factors even under different meteorological conditions, which suggests that the size of the particles rather than chemical composition influences the hygroscopicity during specific periods (Kamilli et al., 2014).

During the winter campaign gas measurements of CO, NO_x and $^{13}CO_2$ were analysed to identify fossil fuel related emissions (Lopez et al., 2013). Traffic-like daily trends were observed for CO_2, CO and NO_x at the LHVP with higher levels detected on weekdays. Using radiocarbon (^{14}C) measurements, 77% and 23% of the CO_2

enhancements observed during the campaign were attributed to fossil fuel combustion (CO_2ff) and biospheric sources (CO_2bio) respectively. The CO_2bio was attributed to human respiration, biofuels, soil respiration and plant respiration. The CO_2ff fraction was further investigated using ^{13}C analysis and attributed to liquid (70%) and gas (30%) combustion with coal burning being negligible (Lopez et al., 2013).

Finally, a chemical transport model (particulate matter source apportionment technology, PSAT) was utilised to examine the contributions of local and regional sources to $PM_{2.5}$ in Paris during both the summer and winter MEGAPOLI measurement campaigns (Skyllakou et al., 2014). Overall it was predicted that only 13% of the $PM_{2.5}$ originated from local sources while mid-range and long-range sources contributed 36% and 51% respectively. The contributions to EC, SOA and sulfate were also examined. 57% of the EC was predicted to be local with 39% originating from mid-range transport and only 4% from long-range transport. Sulfate was dominated by transported emissions with 51% and 32% attributed to long- and mid-range transport respectively; only 17% was due to local emissions. SOA was also dominated by transported emissions with 81% and 17% attributed to long- and mid-range transport respectively. These modelled results compared favourably with measurements carried out during the campaigns (Skyllakou et al., 2014).

3.2 Methodology

3.2.1 Measurement Site

The ATOFMS measurements carried out during MEGAPOLI were performed at an urban background site located in the grounds of the Laboratoire d'Hygiène de la Ville de Paris (LHVP) (48°49'42"N, 2°21'33"E), which is in the 13th arrondissement. This measurement site has been used in previous campaigns (Favez et al., 2007; Sciare et al., 2010). The site was located close to Place d'Italie, a large roundabout and commercial area and Paris' main "Chinatown", Figure 3.2. The area is also surrounded by high rise residential buildings.

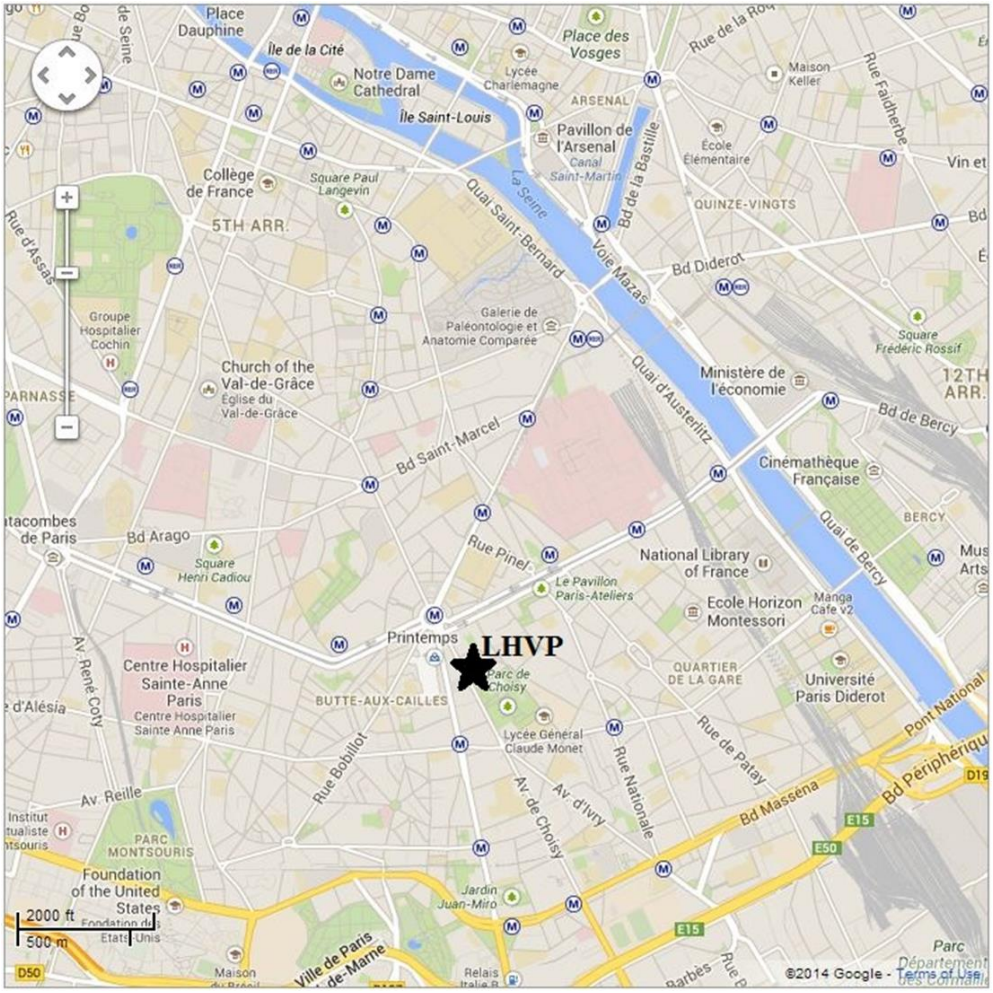

Figure 3.2 Map showing the location of the Laboratoire d'Hygiène de la Ville de Paris (LHVP) measurement site and the surrounding road network and other infrastructure.

3.2.2 ATOFMS Deployment

The ATOFMS was deployed at the rear of the LHVP building and close to a small park (Parc de Choisy) and roadway network. The type of ATOFMS used during the campaign was the TSI model 3800, fitted with an Aerodynamic Focusing Lens (TSI model AFL 100). The instrument was located in an air-conditioned van (Figure 3.3), and utilised a sampling line comprising of quarter-inch stainless steel tubing with an inlet 4 m above ground level. The final section of the sampling line was composed of a short section of quarter-inch flexible rubber tubing to connect the sampling line to the ATOFMS inlet (Healy et al., 2013; Healy et al., 2012). The ATOFMS was continuously operated at this site from 14/01/2010 to 11/02/2010.

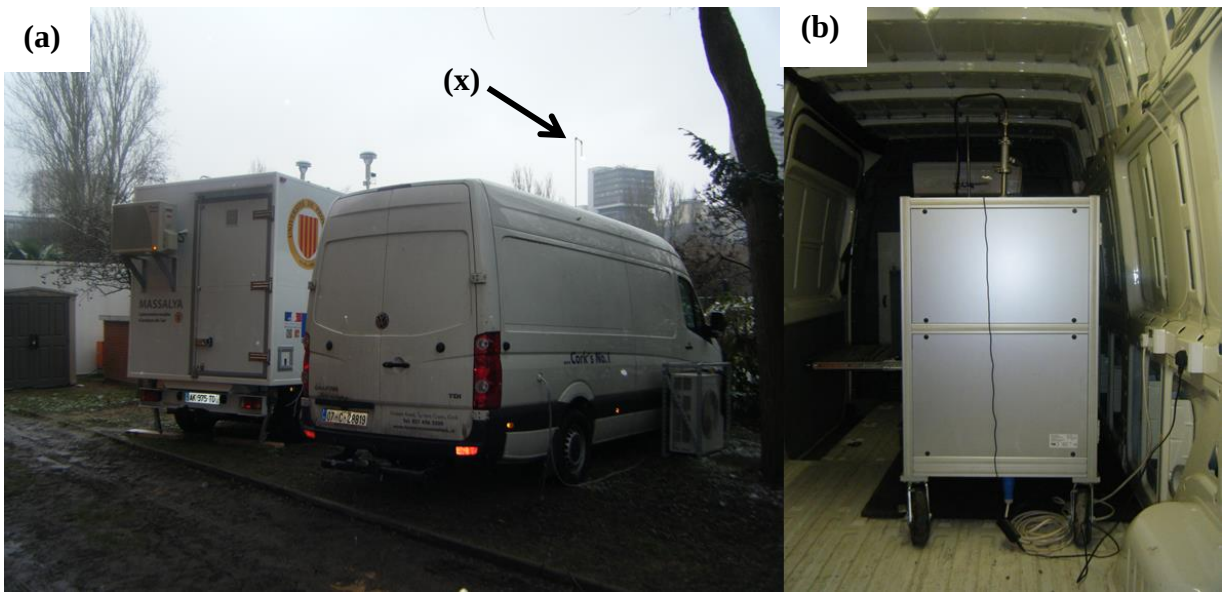

Figure 3.3 (a) The LHVP measurement site with the ATOFMS inlet marked (x). (b) The ATOFMS inside the van.

3.2.3 Meteorology

During the MEGAPOLI measurement campaign, Paris was influenced by several air masses of different origins. The aerosol transport events were determined by employing Lagrangian Particle Dispersion Model (LPDM) FLEXPART "retroplumes" (Stohl et al., 2005). The FLEXPART model enables more accurate assignment of aerosol transport events as the model takes into account turbulence and convection processes (Stohl et al., 2002). The FLEXPART model works by releasing 60000 theoretical particles from the receptor location and tracks the particles for twenty days backwards in time. For this study the model was initialised at three hour intervals with the particles released at a uniform rate over the three hours. The trajectory of the particles formed a "retroplume" that shows areas where the plume was likely to be influenced by ground level emissions. Full details on the model as employed during this campaign are described in detail elsewhere (Healy et al., 2012). Four distinct meteorological regimes were identified during the measurement period, sample trajectories from these periods are shown in Figure 3.4 (Healy et al., 2012), briefly they are as follows:

Period I (15 January 2010, 00:00 LT to 25 January 2010, 12:00 LT), this period was influenced by Atlantic air masses

Period II (25 January 2010, 12:00 LT to 28 January 2010, 00:00 LT), this period was characterised by a continental air mass which originated in Eastern Europe.

Period III (28 January 2010, 00:00 LT to 7 February 2010, 00:00 LT), during these days the city was influenced by a Polar-Atlantic air mass.

Period IV (7 February 2010, 00:00 LT to 11 February 2010, 17:00 LT), the air masses arriving at the city during these days originated in North-Eastern Europe travelling through the Benelux region prior to arriving in the city.

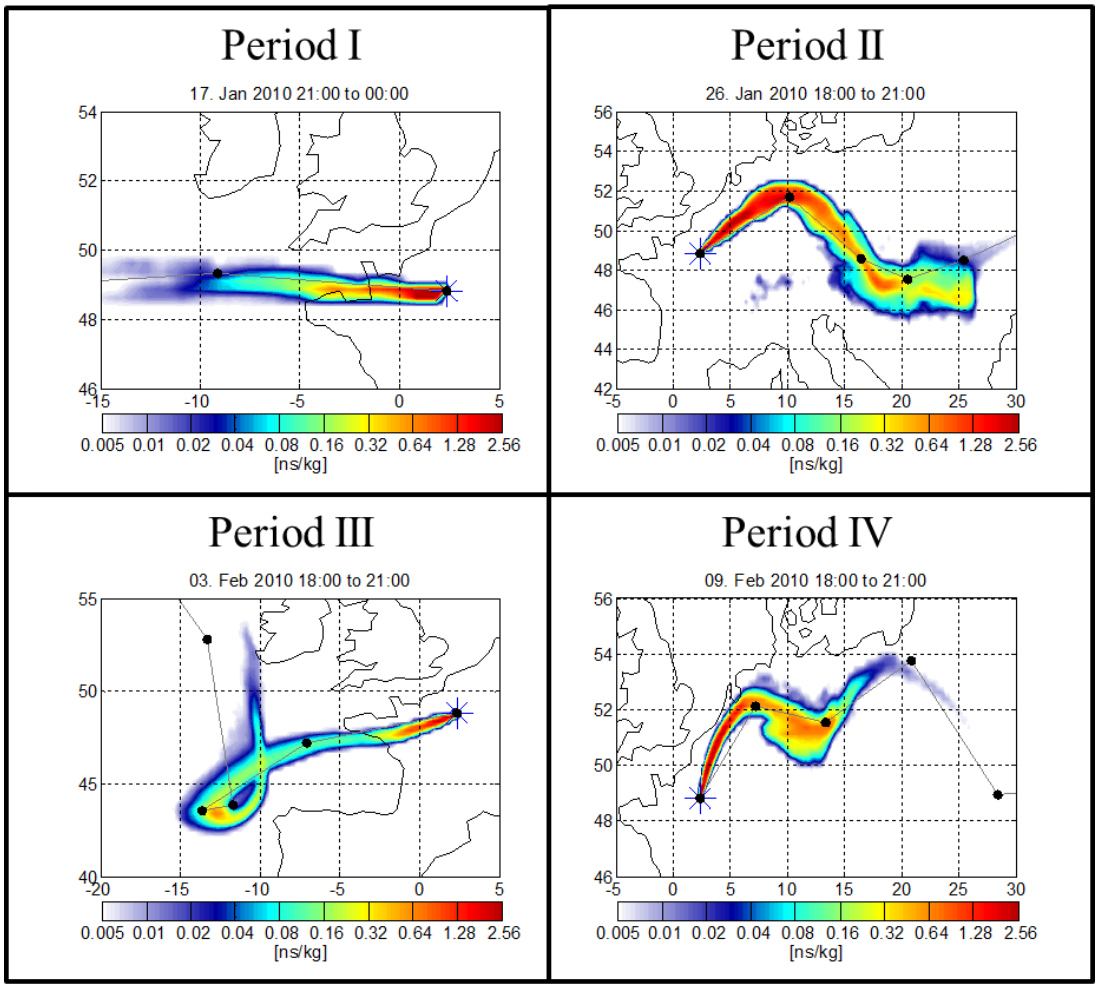

Figure 3.4 Characteristic potential emission sensitivities, the dots in the potential emission sensitivity plots correspond to the air mass age in days, and are positioned on the centroid of the retroplume position at that time (Healy et al., 2012).

3.3 Results and Discussion

3.3.1 Particle types detected by ATOFMS

Dual-ion particle mass spectra collected during the MEGAPOLI campaign were imported into ENCHILADA, a freeware SQL-based ATOFMS data analysis programme developed by Carleton College (Gross et al., 2010). The particles were clustered using the *K*-means algorithm with $K = 80$ (a value which was user defined). The 80 particle clusters were examined manually and grouped into 18 different

particle types described by the dominant species present in the average mass spectrum or by the source of the particle. The particle types were subsequently grouped into five general categories, which contain particle types with similar compositions or sources together, Table 3.1.

Each particle type is characterised by an average mass spectrum, particle size distribution and temporal profiles, both on a daily basis and for the whole campaign. The dependence of each particle type on wind direction was identified by plotting a wind rose. For the purposes of the following discussion, mass spectra, and temporal/daily trends are shown in the body of the text while the particle size distributions and wind roses are included in the Appendix.

General Category	Particle Type	Particle Number	%
Carbonaceous	EC Traffic	85289	5.06
	EC Biomass	26678	1.58
	Fresh Biomass OC	175102	10.38
	Aged Biomass OC	552225	32.75
	ECOCSOx	30295	1.80
	ECOCNOx	45748	2.71
	OCNOx	221270	13.12
	OCSOx	115443	6.85
	Transported Biomass OC	295212	17.51
	Amine Rich	36386	2.16
Metal Containing	Fe-Rich	10462	0.62
	Oil-V	13591	0.81
	Incineration (Pb-Cl)	1785	0.11
Sea-Salt	Sea Salt	47002	2.79
Aged Traffic	Aged Traffic	9007	0.53
PAH	K-PAH	14064	0.83
	OC-PAH	1972	0.12
	Ca-PAH	4698	0.28
Total		**1686229**	**100.00**

Table 3.1 Particle types determined by ENCHILADA (K-means) analysis of the ATOFMS data collected at the LHVP site in Paris.

3.3.1.1 Carbonaceous

Carbonaceous aerosol was the largest category of particle types detected during the MEGAPOLI campaign. Overall 1583648 particles were attributed to the ten types described as carbonaceous, representing 94% of the particles classified. Carbonaceous aerosol consists of two components; elemental carbon (EC) and organic carbon (OC). EC and OC are directly emitted into the atmosphere due to the incomplete burning of fuels. However, OC can also be formed *in situ* through gas-to-particle conversions of organic species (Pio et al., 2011; Yu et al., 2004).

EC Traffic

This particle type was identified as EC Traffic due to the following specific ions observed in the average mass spectrum shown in Figure 3.5(a) 12 $[C]^+$, 23 $[Na]^+$, 24 $[C_2]^+$, 36 $[C_3]^+$, 40 $[Ca]^+$, 48 $[C_4]^+$, 60 $[C_5]^+$, in the positive ion mass spectrum and 24 $[C_2]^-$, 36 $[C_3]^-$, 46 $[NO_2]^-$, 48 $[C_4]^-$, 62 $[NO_3]^-$, 97 $[HSO_4]^-$ in the negative ion mass spectrum. These peaks are all indicative of EC particles due to traffic emissions, with sodium and calcium attributed to lubricating oil (Shields et al., 2007). Similar particle types have previously been identified in ATOFMS spectra and attributed to traffic emissions (Healy et al., 2010; Moffet et al., 2008a; Shields et al., 2008).The size distribution of this particle type peaks around 200 – 250 nm which is fairly typical for combustion sources.

The daily trends are shown in Figure 3.1l, which indicates the occurrence of major peaks in the morning and evening during periods of heavy traffic. The temporal trend of EC Traffic is shown in Figure 3.6, which shows that the particle type is present throughout the campaign and presents a consistent diurnal profile. The presence of EC Traffic throughout the campaign, especially during the marine air mass periods, suggests that these particles are the product of local traffic emissions.

EC Biomass

The average mass spectrum for this particle type (Figure 3.5b) contained peaks 12 $[C]^+$, 23 $[K]^+$, 36 $[C_3]^+$, 39 $[K]^+$ in the positive mass spectrum and 24 $[C_2]^-$, 36 $[C_3]^-$, 46 $[NO_2]^-$, 48 $[C_4]^-$, 62 $[NO_3]^-$, 97 $[HSO_4]^-$ in the negative mass spectrum. Potassium is used in ATOFMS mass spectra as a tracer for biomass burning (Guazzotti et al.,

2003; Moffet et al., 2008a; Silva et al., 1999). Therefore this particle type was attributed to biomass burning due to the presence of potassium and elemental carbon fragments in the average mass spectrum; the results are similar to species detected and assigned previously (Healy et al., 2010). The particle size was also indicative of a combustion source with the sub-micron size distribution peaking around 300 nm. The 26678 EC Biomass particles detected during the sampling campaign represented 1.58% of all the classified particles at the LHVP site. This particle type exhibits a diurnal profile (Figure 3.11) that shows higher overnight levels but with a minimum at 06:00. Such a trend also suggests that the likely source of these particles is biomass burning. There is a slight peak during the day around noon.

The temporal trend of EC Biomass is shown in Figure 3.6, which shows that the particle type is present throughout the campaign and presents a consistent diurnal profile similar to that observed with EC Traffic. The presence of EC Biomass throughout the campaign suggests that these particles originate from local biomass burning.

Fresh Biomass OC and Aged Biomass OC

Two particle types were detected in this OC category. The first was classified as Fresh Biomass OC due to the following signals in the average mass spectrum, Figure 3.5(c): 23 $[Na]^+$ 27 $[C_2H_3]^+$, 39 $[K]^+$, 41 $[K]^+$, in the positive ion mass spectrum and 26 $[CN]^-$, 36 $[C_3]^-$, 42 $[CNO]^-$ 46 $[NO_2]^-$, 62 $[NO_3]^-$, 80 $[SO_3]^-$ 97 $[HSO_4]^-$ in the negative ion mass spectrum. Aged Biomass OC presented an average mass spectrum of the type shown in Figure 3.5(d) with signals at: 18 $[NH_4]^+$, 27 $[C_2H_3]^+$, 36 $[C_3]^+$, 39 $[K]^+$, 41 $[K]^+$ in the positive ion mass spectrum and 26 $[CN]^-$, 46 $[NO_2]^-$, 62 $[NO_3]^-$, 97 $[HSO_4]^-$, 125 $[H(NO_3)]^-$ in the negative ion mass spectrum. As stated previously the presence of a signal for potassium is indicative of biomass burning being the source of the particles (Harrison et al., 2012a; Healy et al., 2010; Silva et al., 1999). While the two types contain similar peaks in the mass spectra, the Aged Biomass OC exhibits much stronger signals for nitrate in the negative spectrum along with a signal for $H(NO_3)^-$ at *m/z* = -125 and ammonium (NH_4) *m/z* = +18. The latter signals in particular indicate that the particles have been processed via the condensation of ammonium nitrate onto Fresh Biomass OC particles. This

conclusion is supported by the size distributions of the particles, which peak at 420 nm and 350 nm for Aged and Fresh Biomass OC respectively.

Both particle types are present throughout the campaign suggesting a local source, Figure 3.7. As expected, Fresh Biomass OC presents a similar temporal profile as EC Biomass with a correlation of $R^2 = 0.71$ (plot not shown).

The daily trends for Fresh and Aged Biomass OC are shown in Figure 3.12. Fresh Biomass OC displays a maximum at 19:00 and gradually decreases to a minimum at 05:00. The Aged Biomass OC particle counts peak at 00:00 and fall to a minimum during the day at 14:00. The similar, yet time shifted profiles suggests that the Aged Biomass OC particles originate from ageing or processing of Fresh Biomass OC particles, as outlined above.

ECOCSOx

The particle type classified as ECOCSOx contained peaks for 12$[C]^+$, 17 $[NH_3]^+$, 18 $[NH_4]^+$, 23 $[Na]^+$, 36 $[C_3]^+$, 48 $[C_4]^+$, 60 $[C_5]^+$ in the positive ion mass spectrum and 24 $[C_2]^-$, 36 $[C_3]^-$, 46 $[NO_2]^-$, 48 $[C_4]^-$ 62 $[NO_3]^-$, 97 $[HSO_4]^-$ in the negative ion mass spectrum as shown in Figure 3.5(e). This particle type is likely due to the processing of fossil fuel combustion particles that have been emitted locally (Moffet and Prather, 2009). This is confirmed by the observed daily trend shown in Figure 3.13, which indicates maxima in the late morning and early afternoon. The particle size distribution is bimodal with a major peak at 250 nm and a minor peak around 450 nm. The smaller mode of the distribution is similar to that observed for EC Traffic while the larger mode is likely related to the further growth of particles as they are processed. The temporal profile of ECOCSOx (Figure 3.8) shows that the particle type is present throughout the campaign with large increases in counts observed at various times. One of the largest increases in the particle counts for $ECOCSO_X$ occurs on 18th January during a period of foggy weather characterised by low wind speed and high relative humidity. This suggests that $ECOCSO_X$ may be the result of heterogeneous processing of EC particles, emitted from local traffic sources.

OCSOx

This particle type contained peaks for 18 $[NH_4]^+$, 27 $[C_2H_3]^+$, 36 $[C_3]^+$, 39 $[C_2H_3]^+/[K]^+$, 43 $[C_2H_3O]^+$, 59 $[N(CH_3)_3]^+$ in the positive mass spectrum and 46 $[NO_2]^-$, 62 $[NO_3]^-$, 80 $[SO_3]^-$, 97 $[HSO_4]^-$, in the negative mass spectrum as shown in Figure 3.5(f). Similar particles have previously been identified and attributed to SOA or to processed organic aerosol internally mixed with sulfate. (Dall'Osto and Harrison, 2012; Moffet et al., 2008a; Qin et al., 2012). The daily trend of $OCSO_X$ (Figure 3.13) shows an increase during the day similar to that found for $ECOCSO_X$, which supports the identification of this particle type as processed locally emitted particles. The temporal profile of the various types (Figure 3.8) shows that $OCSO_X$ is observed in increased number on 18th January during the fog event. These particles are likely due to heterogeneous processing of locally emitted particles. While the increased particle counts during the fog event suggests the particles are partly due to local emissions, the temporal profile also exhibits increased counts during continental air masses, suggesting transported particles contribute to this particle type. The North Easterly wind dependance is also indicative of transported emissions. The size distribution observed for this particle type suggests that they have undergone some processing with a size distribution around 420 nm. As with similar particles observed in previous studies, it is not possible to determine if this particle type is due to SOA that has condensed on pre-existing inorganic particles during transport, SOA that has accumulated inorganic ions during transport or aged organic aerosol internally mixed with sulfate. In reality all of these sources likely contribute to the particle type.

$ECOCNO_X$

The particle type identified as $ECOCNO_X$ contained signals for 12$[C]^+$, 17 $[NH_3]^+$, 18 $[NH_4]^+$, 36 $[C_3]^+$, 48 $[C_4]^+$, 60 $[C_5]^+$ in the positive mass spectrum and 24 $[C_2]^-$, 36 $[C_3]^-$, 46 $[NO_2]^-$, 48 $[C_4]^-$ 62 $[NO_3]^-$, 97 $[HSO_4]^-$, 125 $[H(NO_3)]^-$ in the negative mass spectrum as shown in Figure 3.5(g). The average mass spectrum is similar to $ECOCSO_X$ but with a dominant nitrate signal along with a signal for $H(NO_3)^-$, indicative of highly processed particles. Similar particles have been identified in previous studies (Dall'Osto and Harrison, 2006; Moffet et al., 2008a). In contrast to $ECOCSO_X$ particles, which are local in origin, the $ECOCNO_X$ particles would

appear to be transported to the site. The temporal profile of the particle type (Figure 3.9) shows enhancements in the particle counts of $ECOCNO_X$ during Periods I and IV, which correspond with continental air masses. The presence of the highly aged $H(NO_3)^-$ fragment in the average mass spectrum indicates that these carbonaceous particles are processed as the air masses travel to Paris. $ECOCNO_X$ does not exhibit a clear diurnal profile in Figure 3.14 which suggests the particle is not influenced by local emissions. The particles present a bimodal size distribution with a dominant mode around 450 nm and a secondary mode around 250 nm. The dominance of the larger mode suggests that the particles have been processed with the size being much larger than fresh combustion particles. Finally the $ECOCNO_X$ particles display a North-North-Easterly wind dependence that is consistent with the intrusion of continental air masses from this direction.

$OCNO_X$

The $OCNO_X$ particle type displays peaks for 12$[C]^+$, 18 $[NH_4]^+$, 27 $[C_2H_3]^+$, 36 $[C_3]^+$, 39 $[C_3H_3]^+$/$[K]^+$, 43 $[C_2H_3O]^+$, 59 $[N(CH_3)_3]^+$ in the positive mass spectrum and 46 $[NO_2]^-$, 62 $[NO_3]^-$, 97 $[HSO_4]^-$, 125 $[H(NO_3)]^-$ in the negative mass spectrum as shown in Figure 3.5(h). Based on this composition, $OCNO_X$ particles,are likely due to the processing of local or regional combustion emissions or from SOA formation. The daily trend of the particle is similar to $ECOCNO_X$ (Figure 3.14), while the overall temporal trend (Figure 3.9) is in fact similar to Aged Biomass OC. The coincidence of $OCNO_X$ with the Aged Biomass OC supports the classification of this particle type as being due to local or regional combustion sources that have undergone processing. There is also a contribution from long-range sources as particle counts are observed to be higher during continental air masses. The size of the particles is larger than fresh combustion particles presenting a single mode around 460 nm. Particles presenting similar average mass spectra have previously been detected in ambient conditions and attributed to SOA or aged organic aerosol internally mixed with nitrate. (Moffet et al., 2008a; Qin et al., 2012).

Transported Biomass OC

The Transported Biomass OC particle type contained signals for 18 $[NH_4]^+$, 27 $[C_2H_3]^+$, 36 $[C_3]^+$, 39 $[K]^+$, 59 $[N(CH_3)_3]^+$ in the positive ion mass spectrum and 26

$[CN]^-$, 46 $[NO_2]^-$, 62 $[NO_3]^-$, 80 $[SO_3]^-$, 97 $[HSO_4]^-$, 125 $[H(NO_3)]^-$ in the negative ion mass spectrum as shown in Figure 3.5(i). The average mass spectrum is similar to Aged Biomass OC but with a diminished influence from nitrate and a stronger signal for sulfate. This particle type is identified as primarily being due to transported biomass particles that accumulated ammonium, nitrate and sulfate during transport. Figure 3.10 shows that the highest particle counts for this particle type were observed on 26-27 January and at the end of the campaign, i.e. during periods influenced by continental air masses from Eastern and North-Eastern Europe. The increase in particle number observed during the fog event on the 18th January, also indicates a contribution from local sources. The size distribution of the Transported Biomass OC is larger than the Fresh Biomass OC presenting a size distribution around 400 nm. The daily trend of the particles, Figure 3.15, does not show large variations during the day, confirming that they are not heavily influenced by local emissions but transported particles. The wind dependence of the Transported Biomass OC is North Easterly, which further confirms the influence of continental transported particles.

Amine Rich

This particle type contained peaks for 12 $[C]^+$, 18 $[NH_4]^+$, 27 $[C_2H_3]^+$, 36 $[C_3]^+$, 39 $[C_2H_3]^+/[K]^+$, 59 $[N(CH_3)_3]^+$ in the positive mass spectrum and 46 $[NO_2]^-$, 62 $[NO_3]^-$, 80 $[SO_3]^-$, 97 $[HSO_4]^-$ in the negative mass spectrum, as shown in Figure 3.5(j). It was found to be solely due to transport with the particles being exclusively detected during continental air masses; the signals were observed from 26-27 January and again at the end of the campaign (Figure 3.10). The results show a very strong North Easterly wind dependence, which is the direction associated with continental air masses. The daily trend for this particle type (Figure 3.15) is not of use in identifying their source as they are deemed to be wholly due to transported particles and therefore show no diurnal variation. The signal at *m/z* 59 in the positive mass spectrum is associated with trimethylamine (TMA), a chemical which has previously been identified in ATOFMS spectra (Angelino et al., 2001; McGuire et al., 2011; Rehbein et al., 2011). These studies observed that increases in TMA particle concentrations were associated with high relative humidity or fog events with uptake on to existing particles being related to particle acidity, the higher the acidity the

greater the uptake. (Rehbein et al., 2011). However, the Amine Rich particle type was not detected during fog events in Paris which confirms that the particles are associated with transport and not local emissions. The presence of TMA in particles in the wintertime in this campaign in Canada was associated with air masses that had travelled over agricultural areas associated with animal husbandry during periods of high relative humidity or fog or cloud processing (Rehbein et al., 2011). Therefore it is likely that such particles are formed during transport over agricultural areas, through the heterogeneous uptake of gaseous TMA by organic aerosol internally mixed with ammonium nitrate and sulfate, before arrival in Paris. The size of the particles support the above classification assignment of these particles with the distribution peaking around 450 nm a value that is consistent with organic aerosol that has undergone processing.

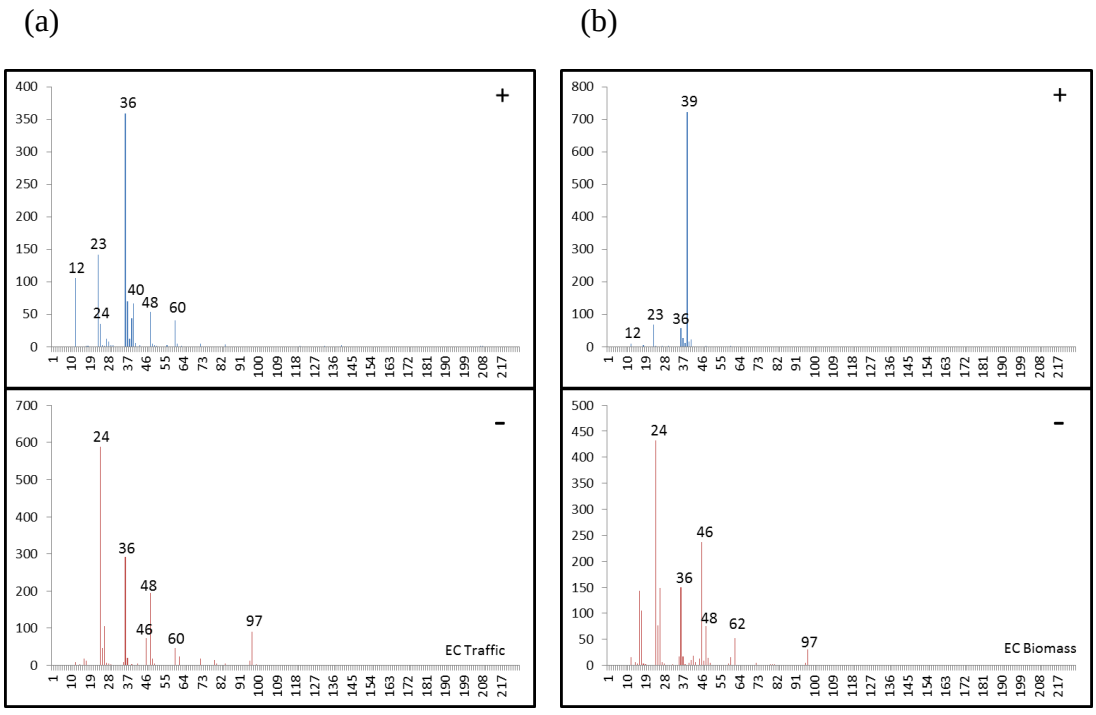

Figure 3.5 Average dual ion mass spectra for carbonaceous particle types; (a) EC Traffic, (b) EC Biomass, (c) Fresh Biomass OC, (d) Aged Biomass OC, (e) $ECOCSO_X$, (f) $OCSO_X$, (g) $ECOCNO_X$, (h) $OCNO_X$, (i) Transported Biomass OC and (j) Amine Rich with the relative ion intensity shown on the *y*-axis and *m/z* shown on the *x*-axis.

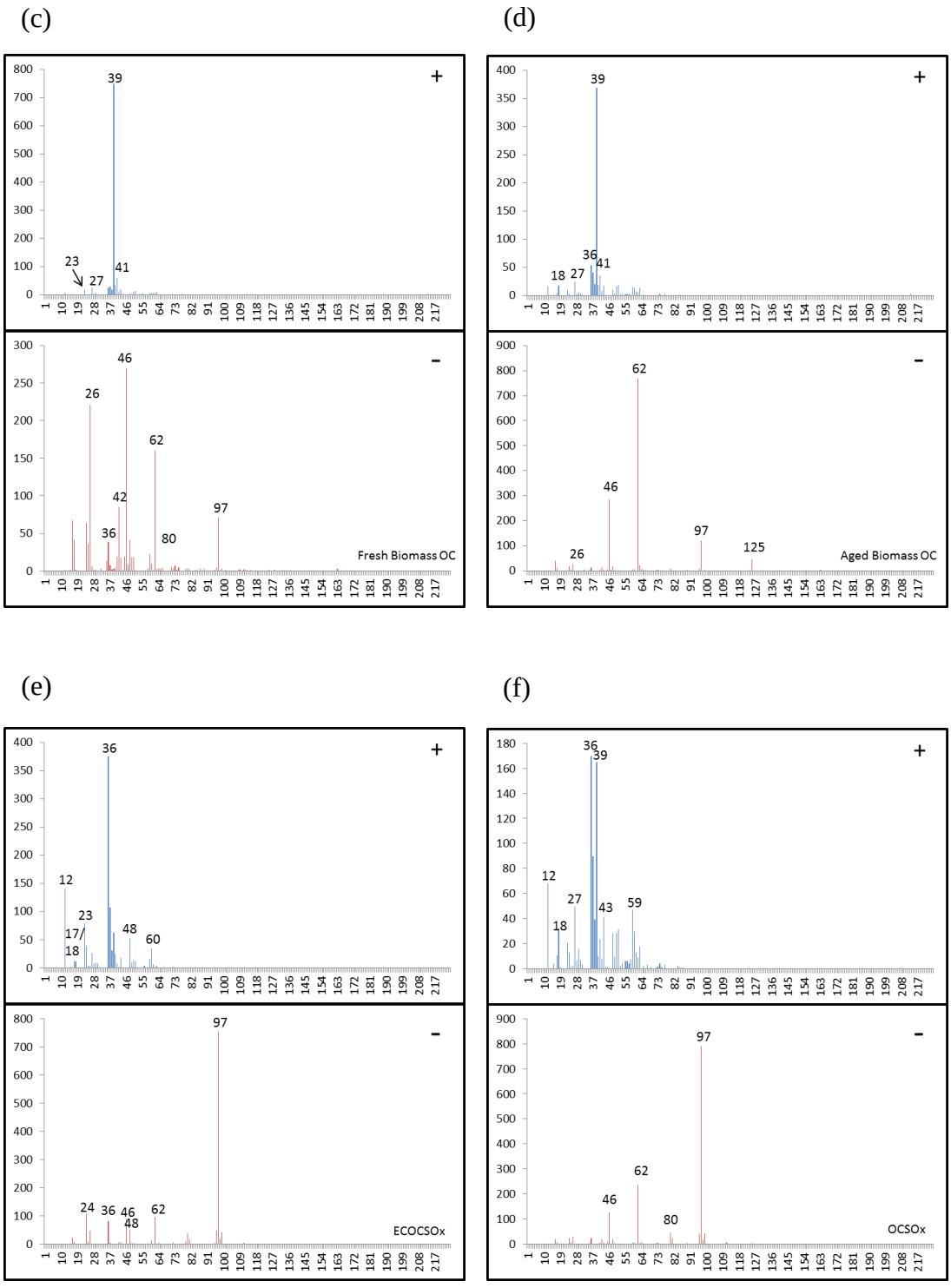

Figure 3.6 Average dual ion mass spectra for carbonaceous particle types; (a) EC Traffic, (b) EC Biomass, (c) Fresh Biomass OC, (d) Aged Biomass OC, (e) $ECOCSO_X$, (f) $OCSO_X$, (g) $ECOCNO_X$, (h) $OCNO_X$, (i) Transported Biomass OC and (j) Amine Rich with the relative ion intensity shown on the *y*-axis and *m/z* shown on the *x*-axis.

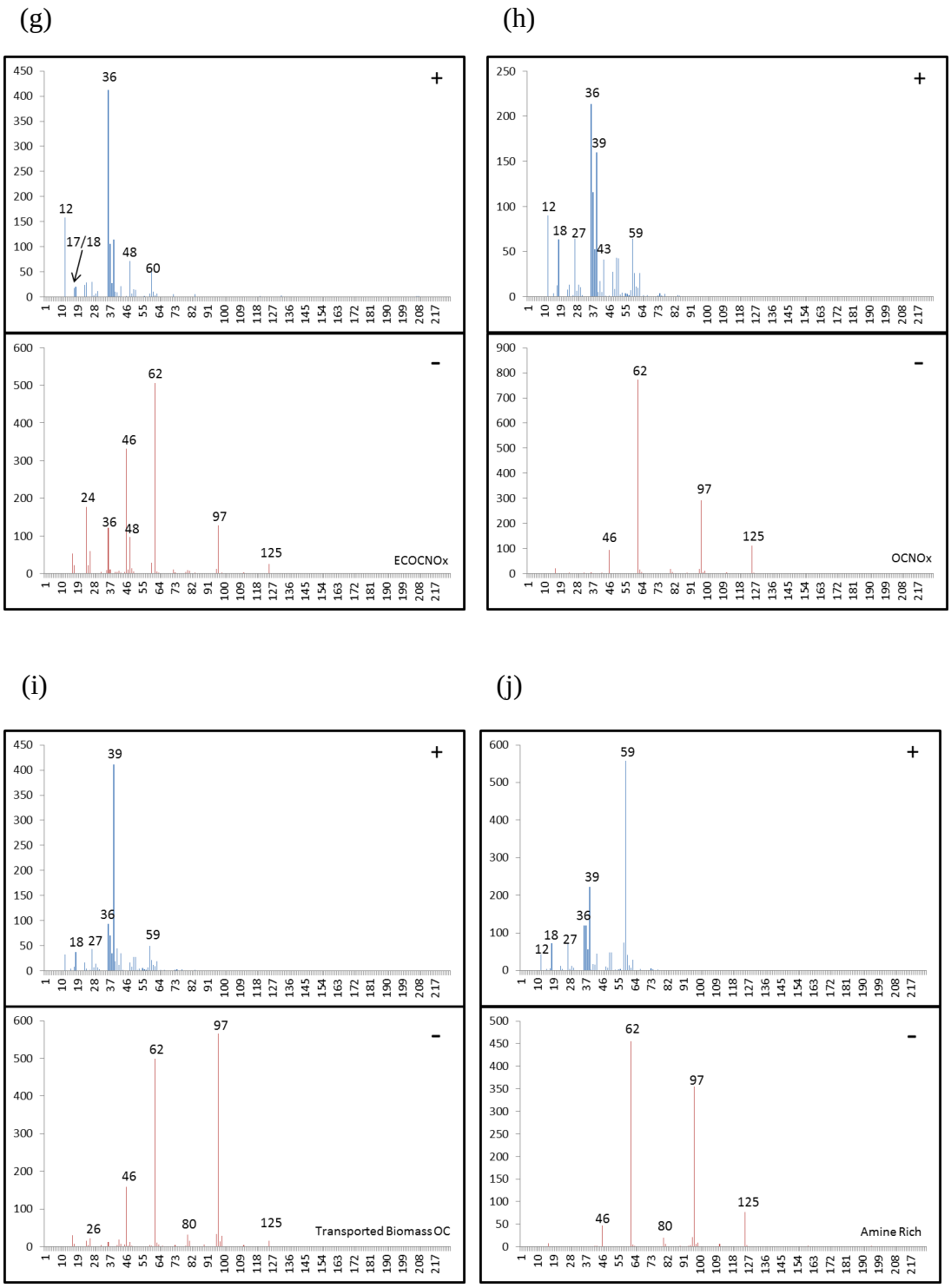

Figure 3.5 Average dual ion mass spectra for carbonaceous particle types; (a) EC Traffic, (b) EC Biomass, (c) Fresh Biomass OC, (d) Aged Biomass OC, (e) $ECOCSO_X$, (f) $OCSO_X$, (g) $ECOCNO_X$, (h) $OCNO_X$, (i) Transported Biomass OC and (j) Amine Rich with the relative ion intensity shown on the *y*-axis and *m/z* shown on the *x*-axis.

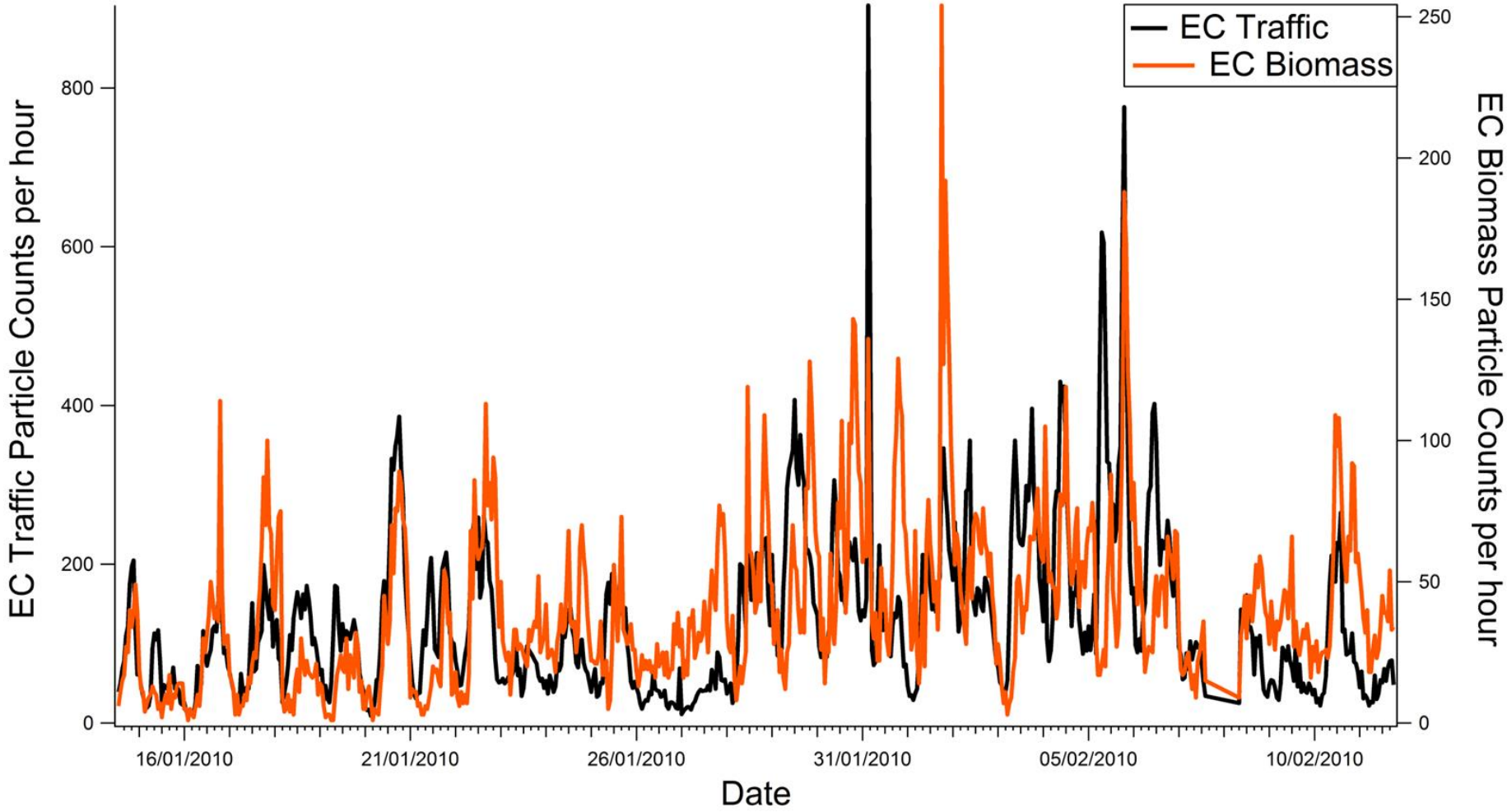

Figure 3.7 Temporal trends of EC Traffic and EC Biomass particle types during the MEGAPOLI measurement campaign.

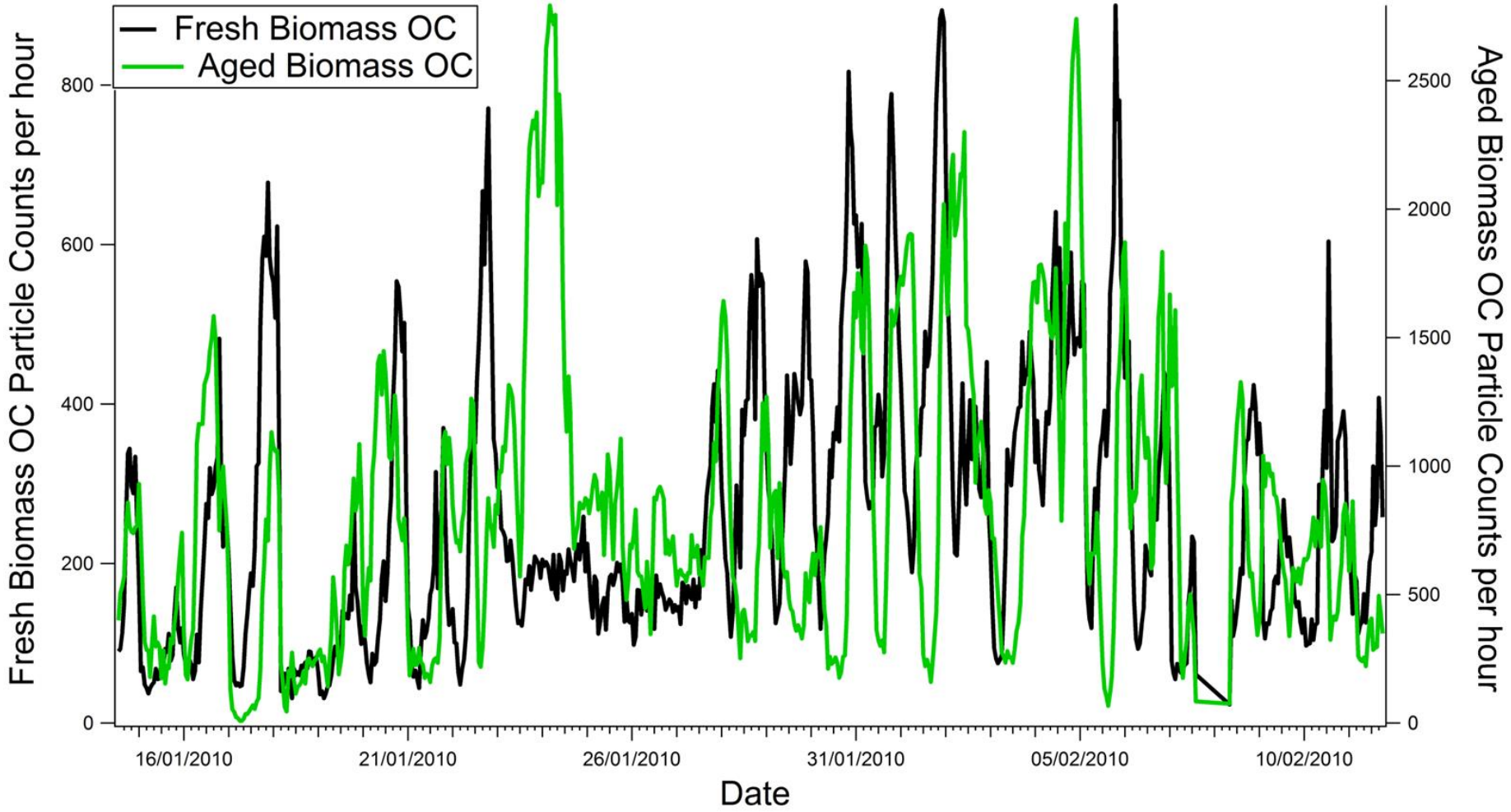

Figure 3.8 Temporal trends of Fresh Biomass OC and Aged Biomass OC particle types during the MEGAPOLI measurement campaign.

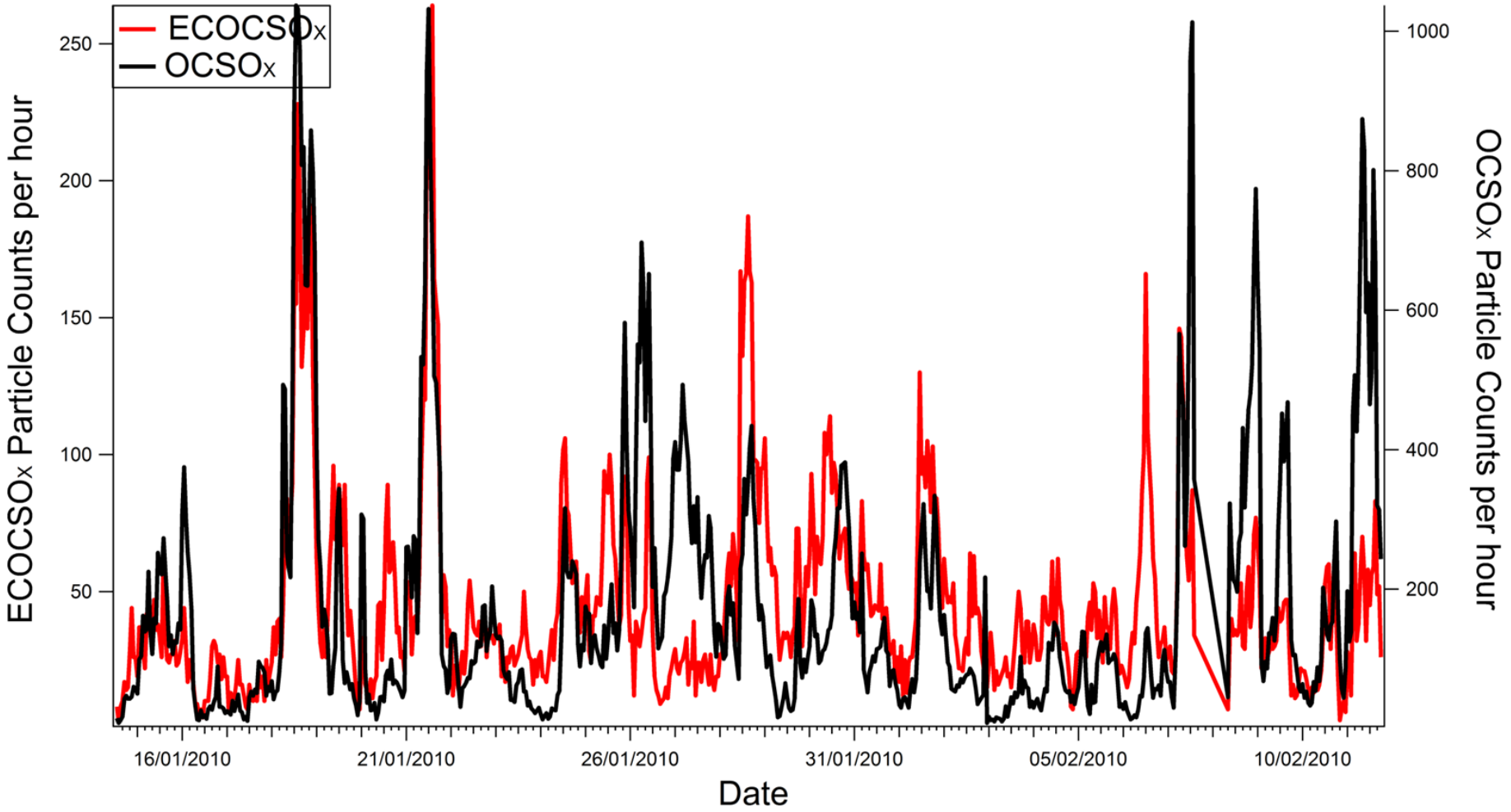

Figure 3.9 Temporal trends of $ECOCSO_X$ and $OCSO_X$ particle types during the MEGAPOLI measurement campaign.

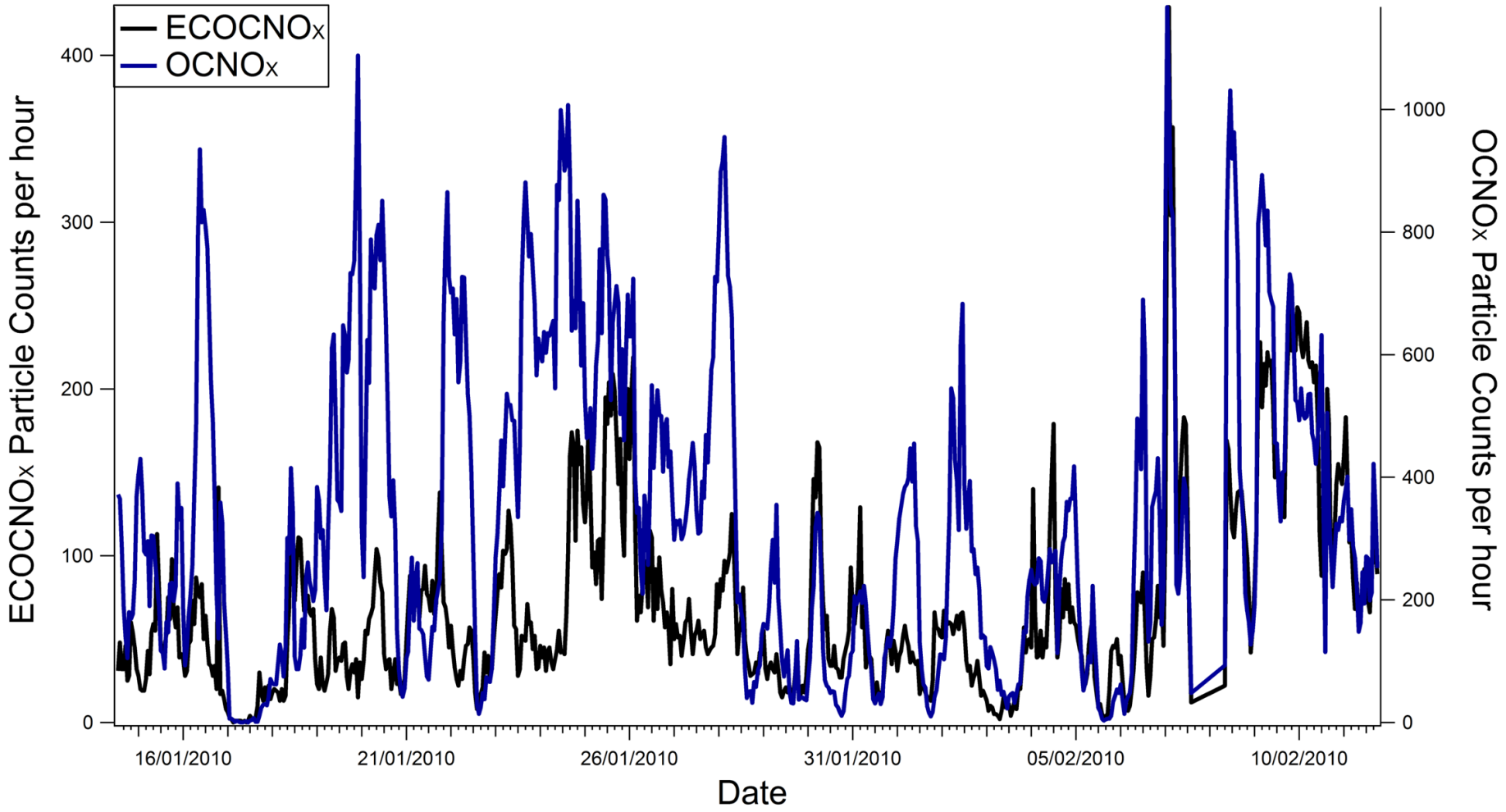

Figure 3.10 Temporal trends of $ECOCNO_X$ and $OCNO_X$ particle types during the MEGAPOLI measurement campaign.

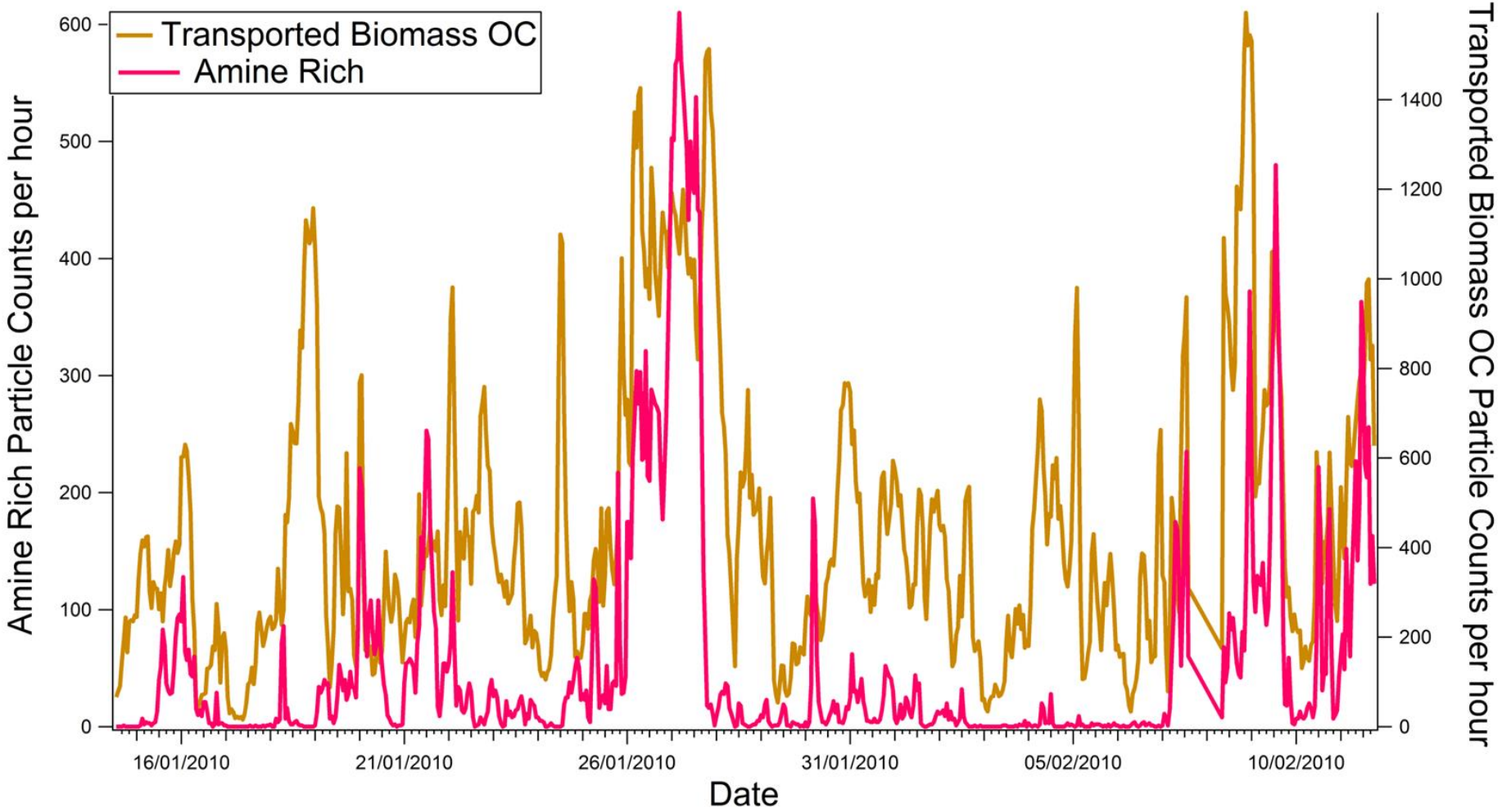

Figure 3.11 Temporal trends of Transported Biomass OC and Amine Rich particle types during the MEGAPOLI measurement campaign.

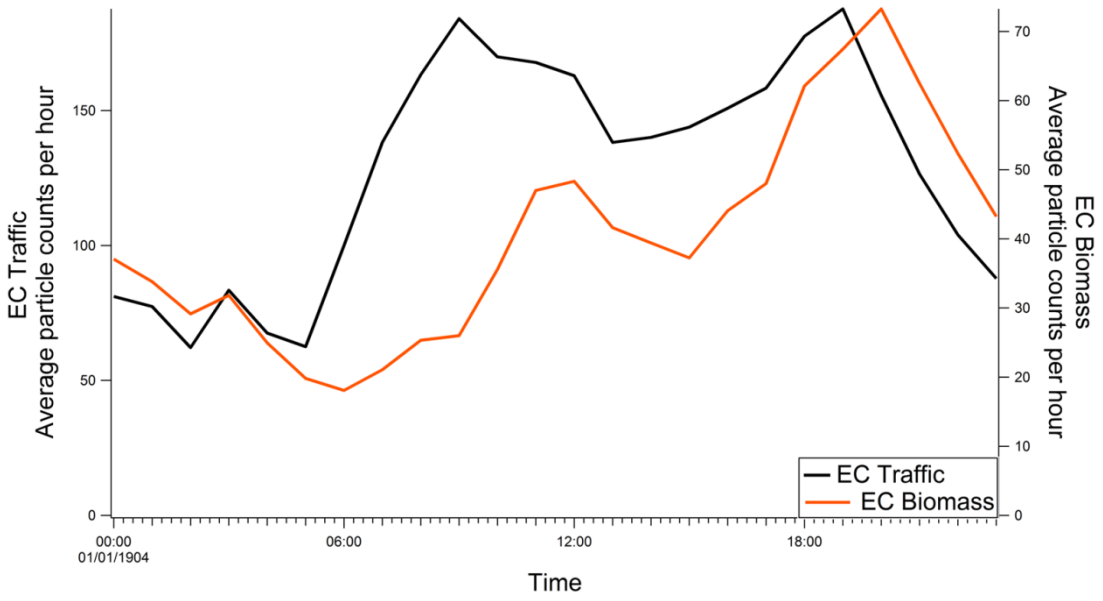

Figure 3.12 Daily trends of EC Traffic and EC Biomass particle types during the MEGAPOLI measurement campaign.

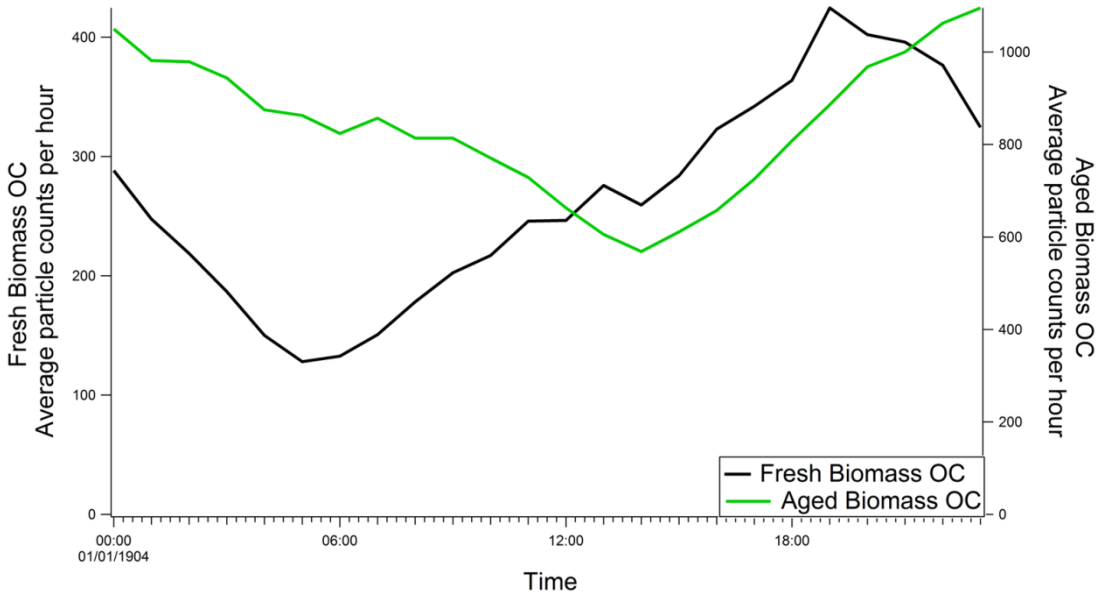

Figure 3.13 Daily trends of Fresh Biomass OC and Aged Biomass OC particle types during the MEGAPOLI measurement campaign.

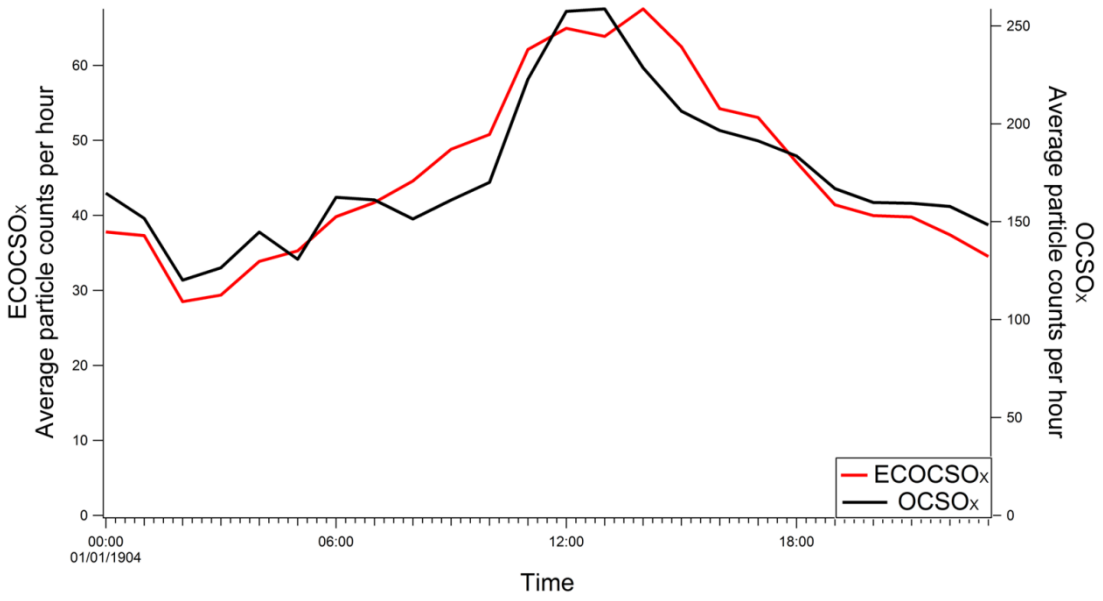

Figure 3.14 Daily trends of $ECOCSO_X$ and $OCSO_X$ particle types during the MEGAPOLI measurement campaign.

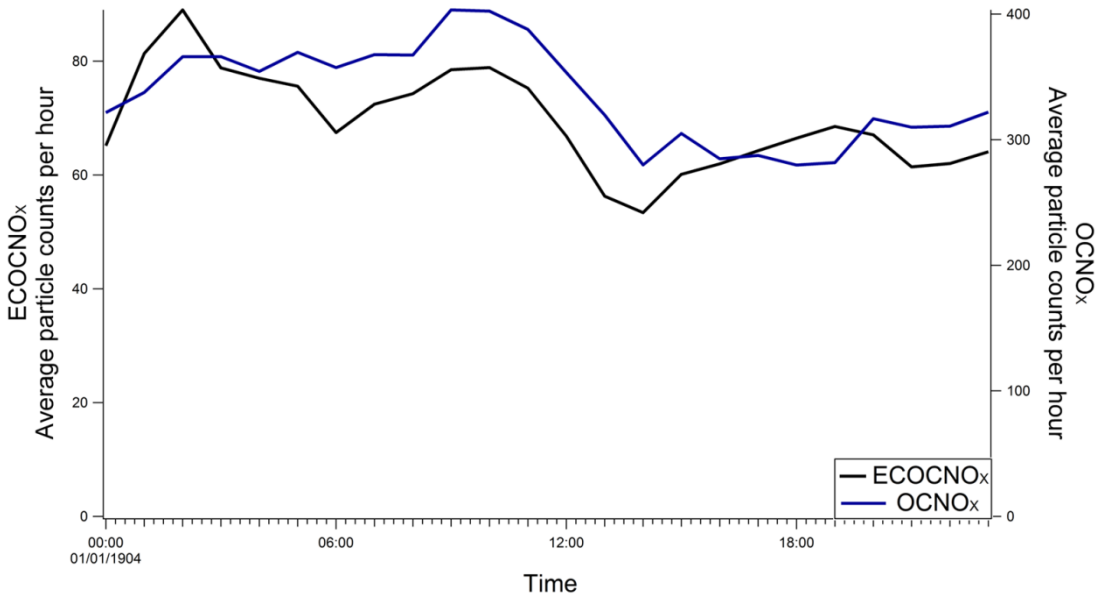

Figure 3.15 Daily trends of ECOCNOX and OCNOX particle types during the MEGAPOLI measurement campaign.

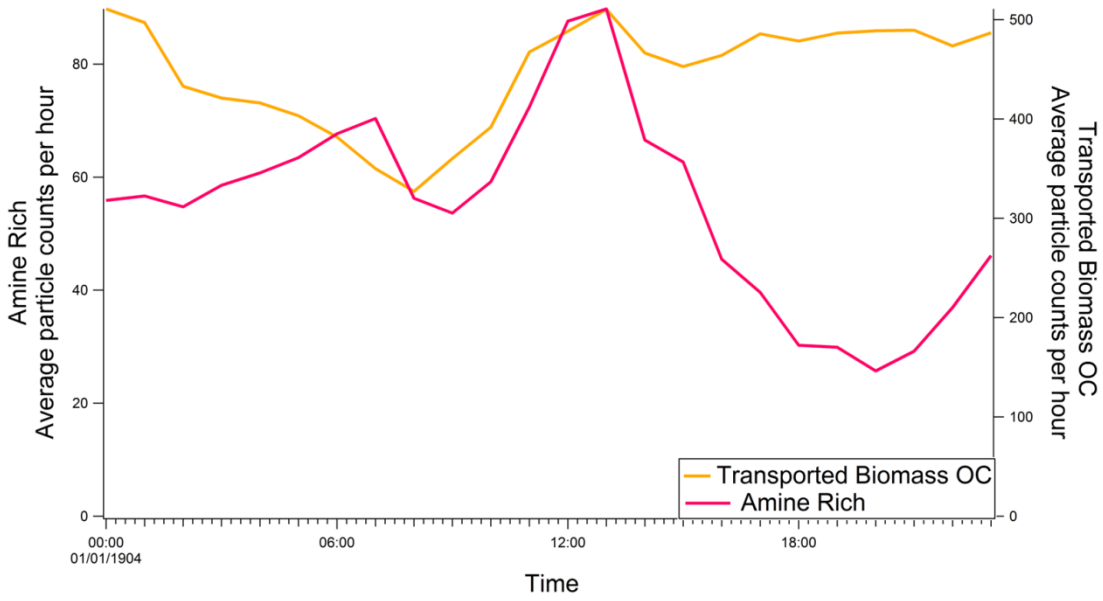

Figure 3.16 Daily trends of Transported Biomass OC and Amine Rich particle types during the MEGAPOLI measurement campaign.

3.3.1.2 Metal-Containing

Fe-Rich

The Fe-Rich particle type contains signals for: 39 $[K]^+$, 54 $[Fe]^+$, 56 $[Fe]^+$ in the positive ion mass spectrum and 46 $[NO_2]^-$, 62 $[NO_3]^-$, 97 $[HSO_4]^-$ in the negative ion mass spectrum (Figure 3.16 (a)). Similar particles have been observed in several ATOFMS datasets (Dall'Osto et al., 2008; Furutani et al., 2011) and attributed to industrial activities, such as steelmaking (Dall'Osto et al., 2008). The Fe-Rich particles were detected mainly during continental air mass intrusions as shown in the temporal profile, Figure 3.17. The wind rose indicates dependence to the North East, which is consistent with the other particle types associated with continental transport. The particle was found to have a size distribution around 500 nm which excludes crustal emissions being the source, as they may present a similar mass spectrum but are found mainly in the coarse mode. Interestingly, an increase in particle counts was observed on 18th January which coincides with some of the lowest wind speeds measured during the campaign. Although this suggests a local source for the particles, the air mass originated from the Atlantic Ocean and travelled over

industrial areas on the coast of France before arriving in Paris. These Fe-Rich particles are therefore identified as industrial emissions which are transported to the site during continental air masses with a possible contribution from locally or regionally emitted particles. A similar particle type was identified in London and attributed to the long range transport of industrial emissions from continental Europe (Harrison et al., 2012b).

Oil-V

The Oil-V particle type presented an average mass spectrum with signals for: 36 $[C]^+$, 51 $[V]^+$, 56 $[Fe]^+$, 58 $[Ni]^+$, 67 $[VO]^+$ in the positive ion mass spectrum and 46 $[NO_2]^-$, 62 $[NO_3]^-$, 97 $[HSO_4]^-$, 125 $[H(NO_3)]^-$ in the negative ion mass spectrum, Figure 3.16(b) This particle type has previously been associated with heavy oil combustion in California (Pastor et al., 2003) and Baltimore (Lake et al., 2004) and more specifically as shipping-related emissions in Cork (Healy et al., 2009). The Oil-V particle type was found to be present at different times during the campaign; higher particle counts were observed during periods when marine air masses influenced the measurement site (Figure 3.17). During periods with influences from marine air masses, the trajectory would bring the air mass over the shipping lanes and heavily industrialised areas to the North West of Paris. While the particle type is detected in higher number during the marine air masses it was also observed during the continental air masses, suggesting that the marine sector is not the only source of these particles. Local emissions due to heavy oil combustion or continental transport of these particles may also contribute to the number of the particles being detected. Previously particles presenting similar chemical composition and size distribution have been attributed to transported shipping or oil refining emissions (Ault et al., 2009). The particles detected in Paris were found to be larger (mode at 470 nm) than the freshly emitted shipping particles previously detected by Healy et al. (2009). The observation is likely due to the condensation of secondary species onto primary particle surfaces during transport or processing.

Incineration (Pb-Cl)

The average mass spectrum for the Incineration (Pb-Cl) particle type contains signals for: 36 $[Na]^+$, 36 $[C_3]^+$, 39 $[K]^+$, 63 $[Cu]^+$, 65 $[Cu]^+$, 206 $[Pb]^+$, 207 $[Pb]^+$, 208 $[Pb]^+$

in the positive ion mass spectrum and 35 $[Cl]^-$, 37 $[Cl]^-$, 46 $[NO_2]^-$, 62 $[NO_3]^-$, 97 $[HSO_4]^-$ in the negative ion mass spectrum (Figure 3.16 (c)). This particle type has previously been monitored in Mexico City air and attributed to incineration emissions (Moffet et al., 2008b). In Paris, the Incineration (Pb-Cl) particles were present at low counts during the campaign but exhibited short sharp peaks in particle number lasting about an hour. These short-lived peaks in particle number are indicative of a local point source, such as incineration or other industrial processes. This particle type presented a broad size distribution centred around 420 nm. The wind dependence of the particle type was mainly to the South East, which can help identify the point source of the emissions. A slight influence of the Western sector was also observed. There are several waste incinerators in Paris with the three closest to measurement sites located to the south, east and south-east along with one further to the west (SVDU, 2014). The location of these waste to energy incineration plants are likely contributors to this particle type and further contribute to the classification of these particles as incineration emissions.

(a) (b)

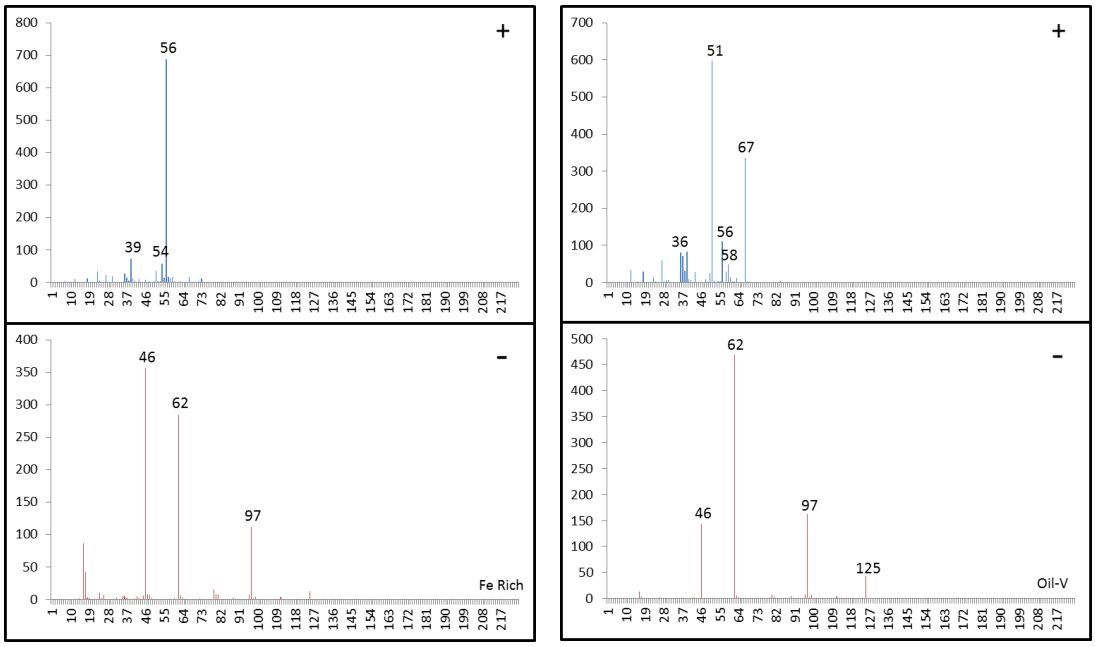

(c)

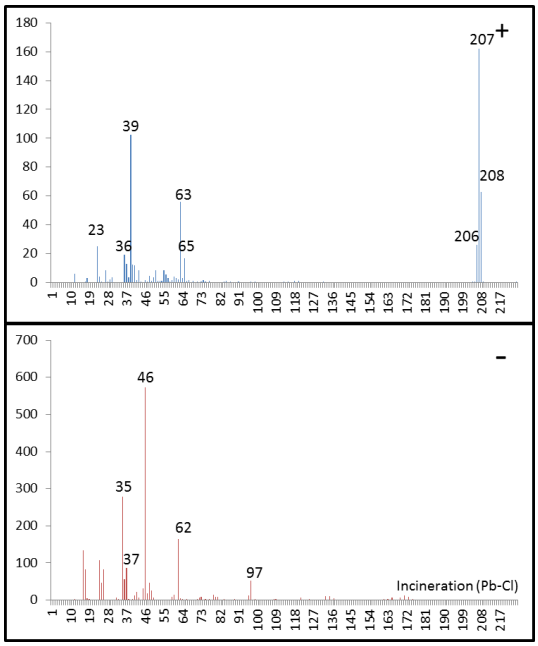

Figure 3.17 Average dual ion mass spectra for (a) Fe-Rich, (b) Oil-V and (c) Incineration (Pb-Cl) with the relative ion intensity shown on the *y*-axis and *m/z* shown on the *x*-axis.

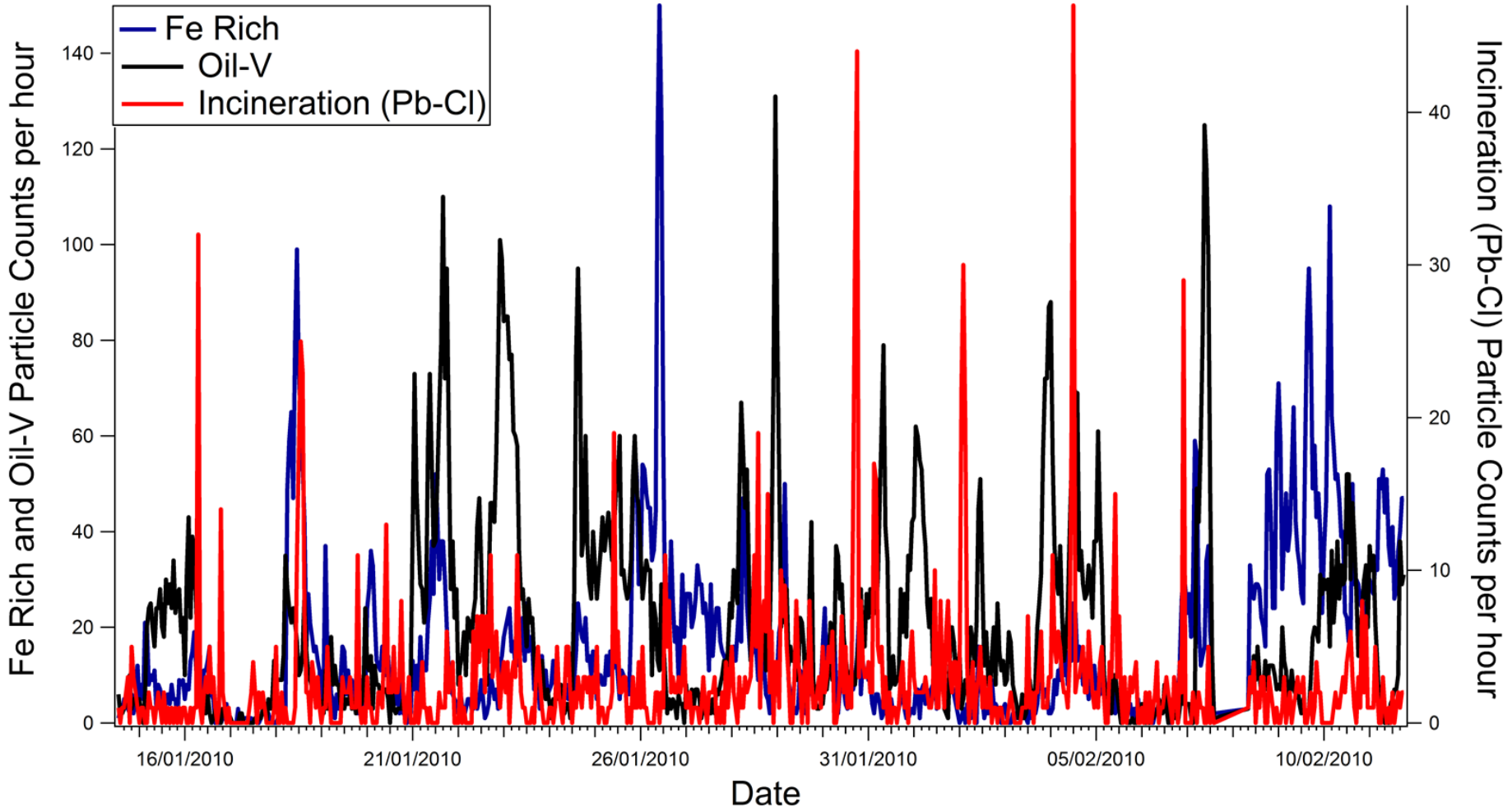

Figure 3.18 Temporal trends of Fe-Rich, Oil-V and Incineration (Pb-Cl) particle types during the MEGAPOLI measurement campaign.

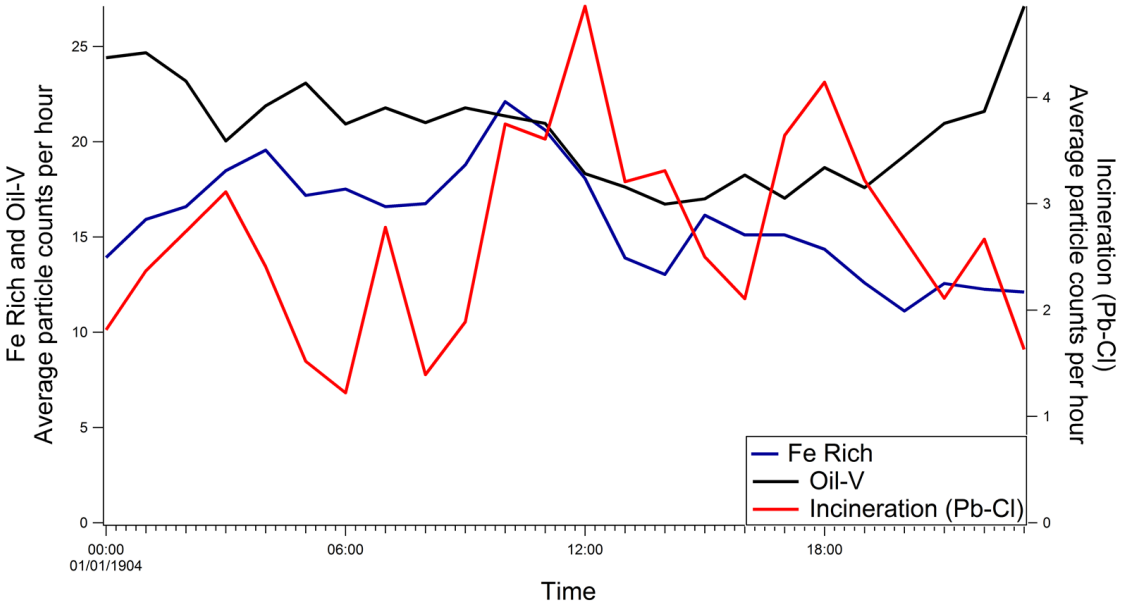

Figure 3.19 Daily trends of Fe-Rich, Oil-V and Incineration (Pb-Cl) particle types during the MEGAPOLI measurement campaign

3.3.1.3 Sea-Salt

Sea-Salt

The particle class identified as Sea-Salt presented an average mass spectrum, shown in Figure 3.19(a), containing the *m/z* signals: 23 $[Na]^+$, 39 [K], 81 $[NaCl_2]^+$ in the positive ion mass spectrum and 16 $[O]^+$ 35 $[Cl]^-$, 46 $[NO_2]^-$, 62 $[NO_3]^-$, 93 $[NaCl_2]^-$, 97 $[HSO_4]^-$, 125 $[H(NO_3)]^-$, 147 $[Na(NO_3)_2]^-$ in the negative ion mass spectrum. All of the signals in the positive ion mass spectrum are associated with sea-salt (Healy et al., 2010; Noble and Prather, 1997). The negative ion mass spectrum shows peaks associated with sea-salt along with nitrate and sulfate indicating that the particles have been processed during transport, with the *m/z* = -125 $(H(NO_3)^-)$ signal being indicative of highly aged particles. This is consistent with transport of particles from the Atlantic to the sampling site in Paris and the temporal profile, shown in Figure 3.20 clearly indicates higher amounts of Sea-Salt particles during the Atlantic air mass intrusions. While the particles were not detected throughout the marine periods, they were found during periods with elevated wind speed. The particle classification as Sea-Salt is further confirmed by the size distribution. It presents a bimodal

distribution and a major mode at a maximum value of 600 nm, which continues to the limit of the ATOFMS AFL inlet (>2500 nm).

3.3.1.4 Aged Traffic

Aged Traffic

The Aged Traffic average mass spectrum is shown in Figure 3.19(b). It contains signals at: 23 $[Na]^+$, 40 $[Ca]^+$, in the positive ion mass spectrum and 46 $[NO_2]^-$, 62 $[NO_3]^-$, 97 $[HSO_4]^-$ in the negative ion mass spectrum. As mentioned in Section 3.3.1.1, sodium and calcium are used as tracers for traffic emissions in ATOFMS mass spectra due to the presence of these elements in lubricating oil (Shields et al., 2007). The identification of this particle type as Aged Traffic was aided by examining the daily trend shown in Figure 3.21; the particle type shows maxima twice during the day at 12:00 and 21:00. Both of the observed maxima occur three hours after those observed for the EC Traffic particles which are, of course, the likely precursors to the Aged Traffic particles. The particles exhibited a size distribution which is larger than the freshly emitted particles with a mode centred at 400 nm. The larger size is due to the processing of the fresh particles and the condensation of secondary species onto the surface of the particles. As indicated in Figure 3.20, the Aged Traffic particles are present throughout the campaign, during both marine and continental air intrusions, suggesting that the particles are locally emitted and not transported to the monitoring site.

(a) (b)

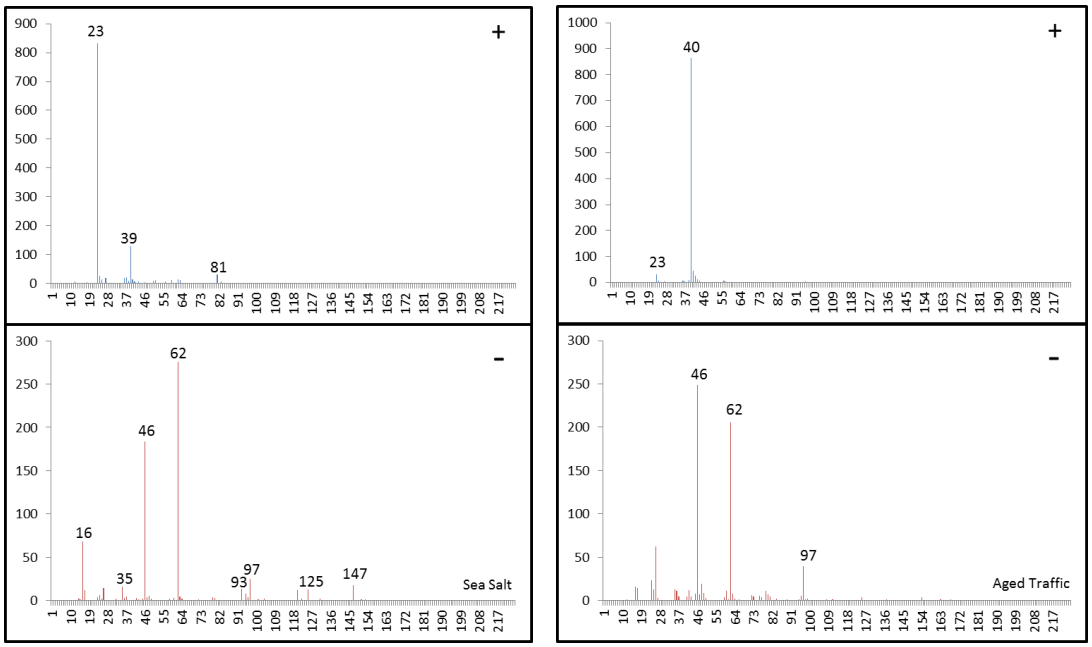

Figure 3.20 Average dual ion mass spectra for (a) Sea-salt and (b) Aged Traffic with the relative ion intensity shown on the *y*-axis and *m/z* shown on the *x*-axis.

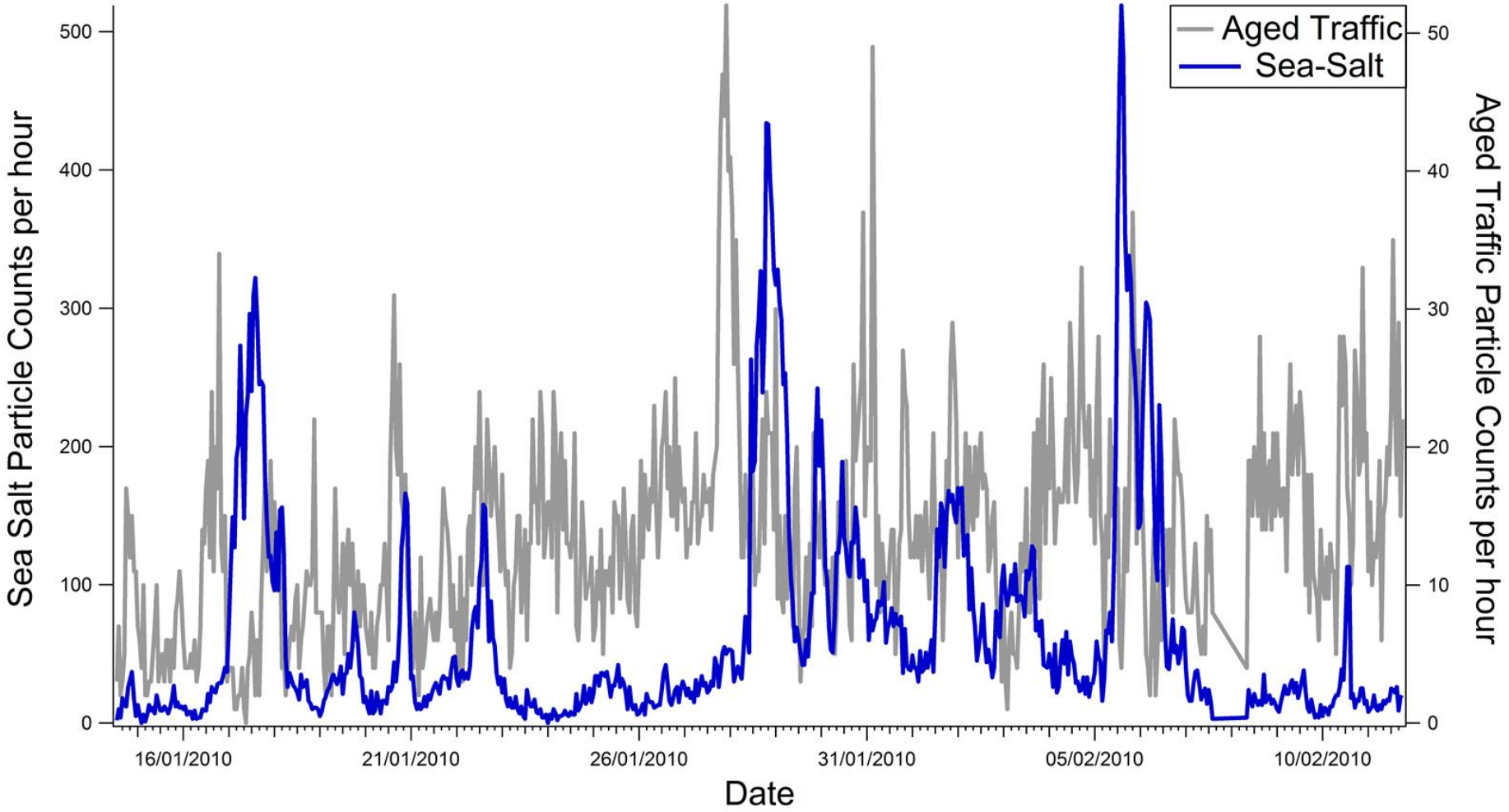

Figure 3.21 Temporal trends of Sea Salt and Aged Traffic particle types during the MEGAPOLI measurement campaign.

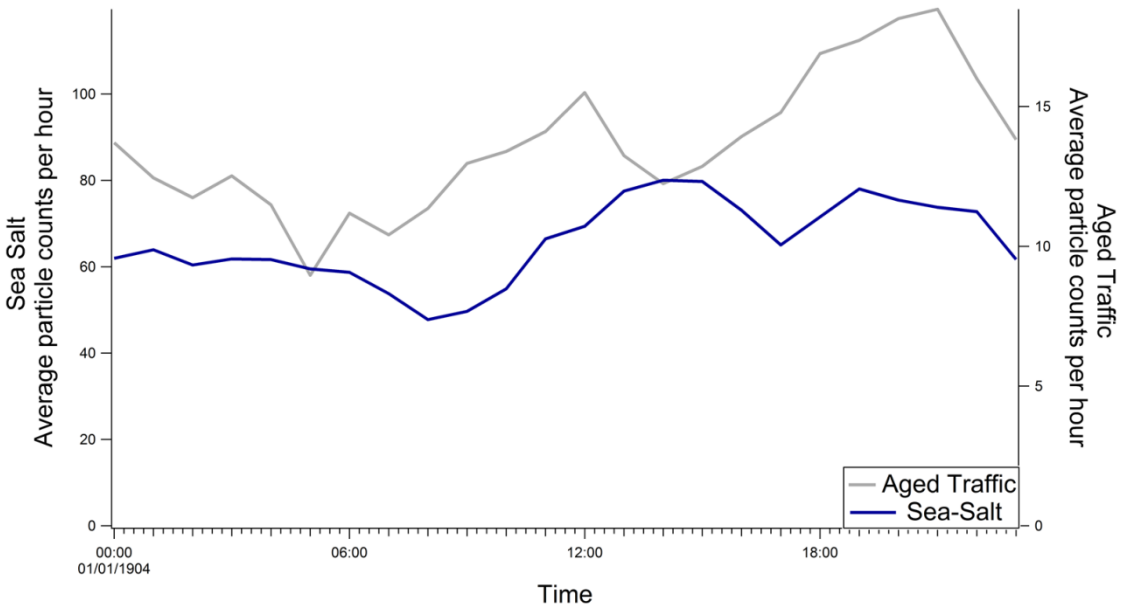

Figure 3.22 Daily trends of Sea Salt and Aged Traffic particle types during the MEGAPOLI measurement campaign.

3.3.1.5 PAH

K-PAH, OC-PAH and Ca-PAH

During the MEGAPOLI campaign three particle types were observed to contain characteristic peaks due to Polycyclic Aromatic Hydrocarbons (PAHs) in their positive mass spectra at *m/z*: 189^+, 202^+, 206^+, 215^+, 228^+, 231^+, 252^+, 276^+, Figure 3.22. Several previous single particle studies have identified PAH particle types in ambient measurements (Dall'Osto et al., 2012; Gross et al., 2005; Oster et al., 2011). Some of the signals have been attributed to specific PAHs e.g., Pyrene and fluoranthene for *m/z* 202, Benzopyrenes, benzofluoranthenes and perylene for *m/z* 252 (Oster et al., 2011). Further to the PAH signals the three particle types contained signals for 46 $[NO_2]^-$, 62 $[NO_3]^-$, 97 $[HSO_4]$ in the negative ion mass spectra. The three particle types were separated due to different species being present in the positive mass spectra as evident in Figure 3.22; K-PAH contained signals for 23 $[Na]^+$ and 39 $[K]^+$, Ca-PAH presented signals for 12 $[C]^+$, 23 $[Na]^+$, 27 $[C_2H_3]^+$, 40 $[Ca]^+$, 96 $[Ca_2O]^+$ and OC-PAH had signals for 12 $[C]^+$, 27 $[C_2H_3]^+$, 39 $[C_3H_3]^+$, 43 $[C_2H_3O]^+$, 63 $[C_5H_3]^+$, 69 $[C_4H_5O]^+$. Both OC-PAH and Ca-PAH are attributed to

traffic emissions as the daily trend in Figure 3.24 shows that both of these particles exhibit maxima during the morning and evening rush hour, similar to EC Traffic. As stated previously the sodium and calcium signals in Ca-PAH are indicative of lubricating oil in traffic emissions (Shields et al., 2007). The OC-PAH is likely due to carbonaceous particles from traffic emissions that have been oxidised as the mass spectrum contains signals at *m/z* = 43 ($[C_2H_3O]^+$) and 69 ($[C_4H_5O]^+$) which are associated with oxidised OC. The K-PAH particle type is attributed to biomass burning as it contains the dominant signal for potassium and also exhibits a daily trend similar to EC Biomass with high levels overnight. All three of the PAH particle types OC-PAH, Ca-PAH and K-PAH were found to have size distributions consistent with a combustion source peaking at 270, 280 and 360 nm respectively.

(a) (b)

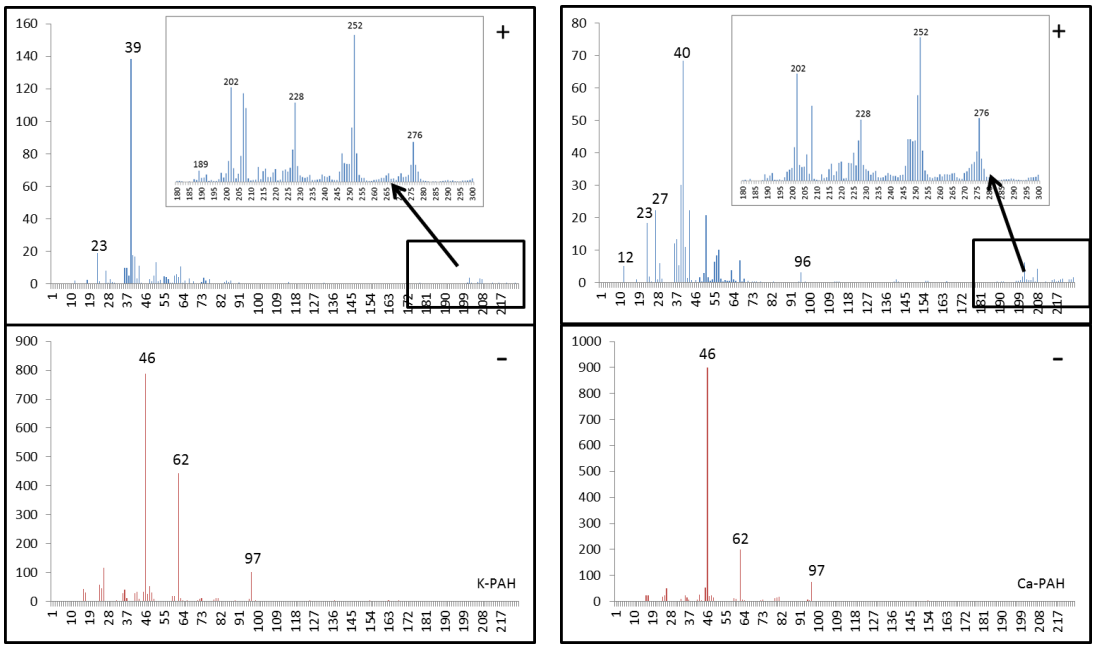

(c)

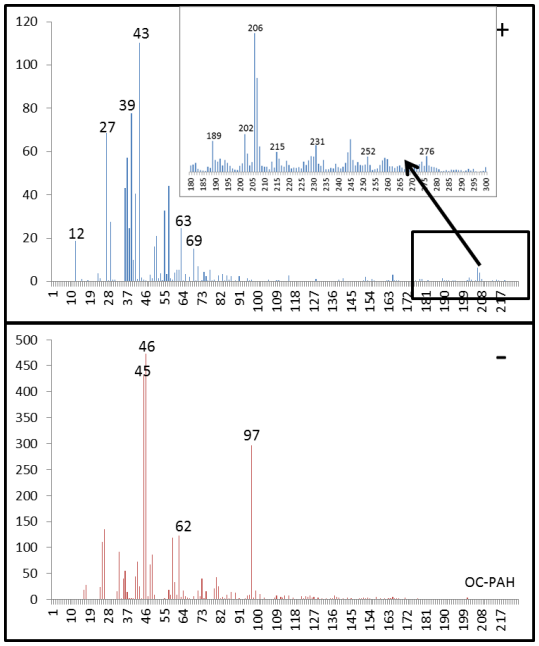

Figure 3.23 Average dual ion mass spectra for (a) K-PAH, (b) Ca-PAH and (c) OC-PAH.

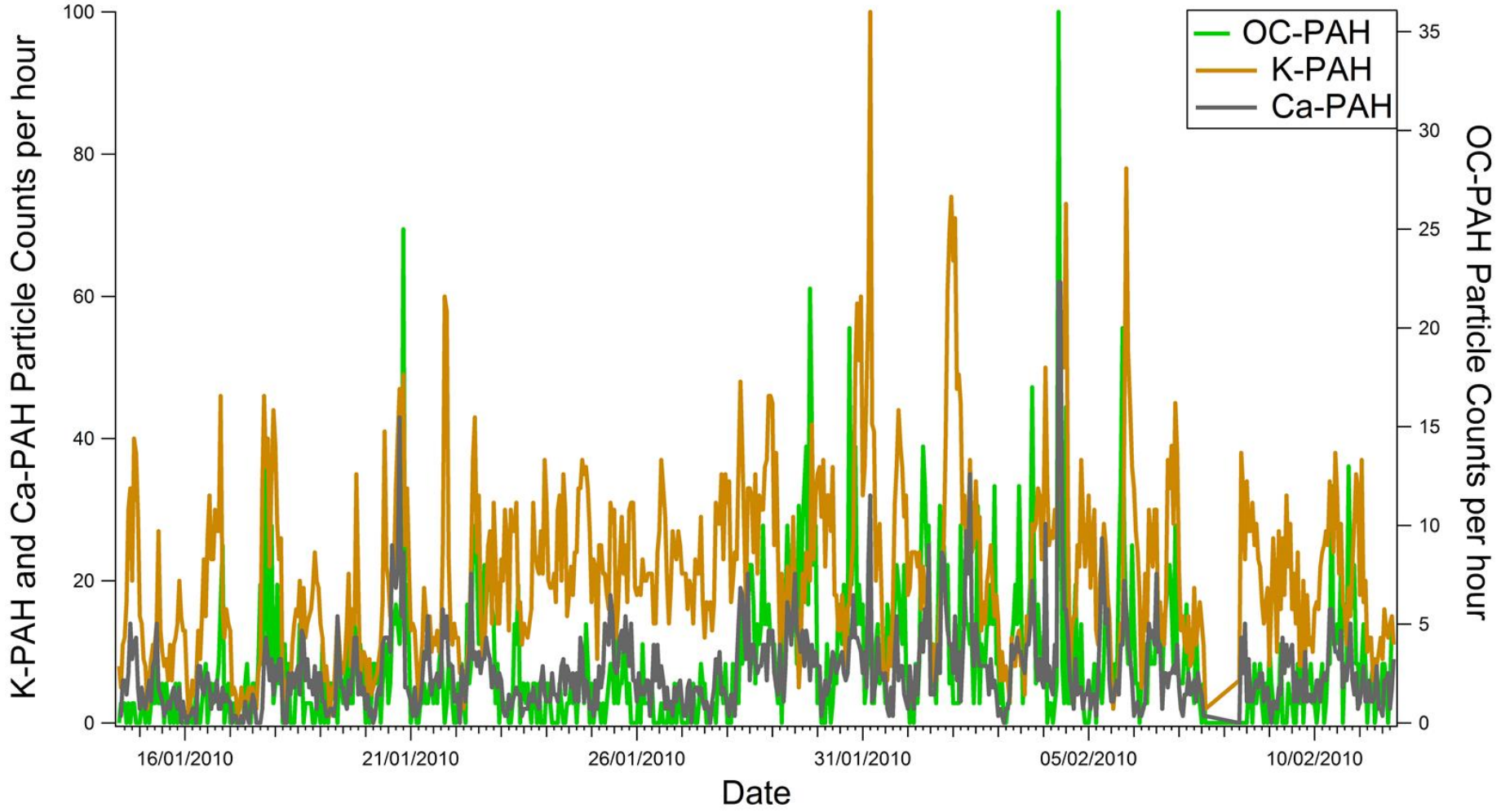

Figure 3.24 Temporal trends of K-PAH, Ca-PAH and OC-PAH particle types during the MEGAPOLI measurement campaign

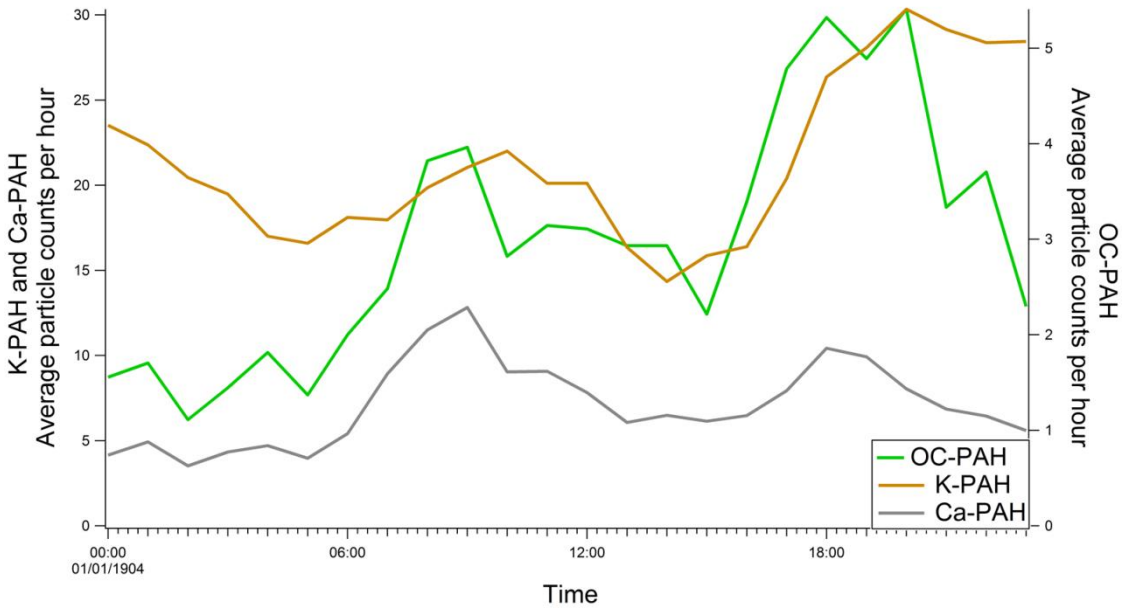

Figure 3.25 Daily trends of K-PAH, Ca-PAH and OC-PAH particle types during the MEGAPOLI measurement campaign

3.3.2 Comparison of ATOFMS with other measurement techniques

The co-location of several quantitative measurement techniques at the LHVP allowed for comparison of the ATOFMS derived particle counts with the mass concentrations determined by Multi-Angle Absorption Photometer (MAAP), Aethalometer and Aerosol Mass Spectrometer (AMS). The direct comparison of this quantitative data with the ATOFMS is not straight-forward and advanced analytical procedures are required to convert ATOFMS counts to mass concentrations. However, the results can be very useful since the ATOFMS data can be used to identify the mixing state of the OA and BC types quantified using the AMS and the Aethalometer. The inability of the ATOFMS to detect particles in a direct quantitative fashion is due to size dependent transmission efficiencies of the AFL, size detection of the lasers in the sizing region and data acquisition issues during instrument "busy time" (Healy et al., 2012; Pratt et al., 2009; Su et al., 2004). Matrix effects associated with the D/I process also inhibit the quantitative detection of different chemical elements in the mass spectra as signal strength detected is not proportional to the concentration of the species present in the particle. (Dall'Osto et al., 2006; McGillicuddy et al., 2014 In Preparation).

The inter-comparisons performed as part of this study directly compared the ATOFMS particle counts to the quantitative MAAP, aethalometer and AMS measurements. However, this ATOFMS data was utilised in other studies and scaled to coincident Twin Differential Mobility Particle Sizer (TDMPS) measurements to provide size resolved mass concentrations of the carbonaceous aerosol by Dr R.M. Healy. (Healy et al., 2013; Healy et al., 2012). The scaling procedure carried out should take into account several of the issues that inhibit the quantitative determination of aerosol concentrations by the ATOFMS alone. These scaled measurements will be discussed here in conjunction with the comparisons carried out as part of this work.

Comparison with MAAP and aethalometer measurements

EC-containing particle types were compared to quantitative BC data obtained using MAAP and aethalometer measurements. The operating principle of the MAAP is described in detail elsewhere, (Petzold and Schönlinner, 2004) but briefly the transmittance and reflectance of BC on a filter is measured at multiple angles and corrections for filter and aerosol scattering are made using a radiative transfer model. (Petzold and Schönlinner, 2004; Andreae and Gelencsér, 2006). Petzold and Schönlinner, (2004) noted a strong correlation between black carbon mass concentration and aerosol light absorption in MAAP measurements. It was also noted that comparison with a reference method resulted in a strong correlation (Petzold and Schönlinner, 2004). The ATOFMS particle types that contain strong signals for Elemental Carbon (EC) (i.e. C_n^+ and C_n^-) are compared to the MAAP BC concentrations. The ATOFMS identified four EC particle types; EC Traffic, EC Biomass, ECOCNO$_X$ and ECOCSO$_X$. These particle counts per hour were summed to produce particle numbers for all EC-containing particles. The temporal profile of MAAP BC and the ATOFMS EC Total is shown in Figure 3.25(a). It can be seen that the two methods do not show strong agreement during the campaign with an R^2 = 0.05. It is observed however, that during the period 15-23 January the ATOFMS response is similar to the MAAP concentration with both techniques presenting coincident increases in concentration or number respectively. For 23-28 January, periods of high concentration were observed in the MAAP data although the ATOFMS particle number shows a clear underestimation. It has been noted

previously that during periods of high particle concentration the ATOFMS can suffer "busy time" wherein the time taken to process the data generated by single particles limits the overall particle detection efficiency. (Su et al., 2004). This detection issue is the likely cause of the undercounting of the particles during this period.

The correlation between the ATOFMS and the ambient concentration is improved by scaling of the ATOFMS counts. The scaling procedure was undertaken by Dr R. M. Healy and involved scaling the ATOFMS counts to the unbiased TDMPS size distributions in order to provide meaningful temporal trends. The scaling was carried out using an assumed density value of 1.5 g cm^{-3}, derived from AMS and MAAP mass concentrations, and assuming all particles are spherical. This analysis resulted in an improved R^2 of 0.68 (Healy et al., 2012). The scaling procedure results in improved correlation as periods with poor particle detection efficiency are accounted for. Several issues are associated with scaling procedure as a single density is used throughout the campaign and all particles are assumed to be spherical. Finally, the quantification approach used provides mass concentrations for particle types rather than individual chemical species meaning that the final scaled mass contains contributions from all species present in the particle. However the scaling undertaken vastly improved the correlation between the ATOFMS and the MAAP measurements as is clear in Figure 3.25 (b) especially during the period affected by ATOFMS "busy time" (Healy et al., 2012).

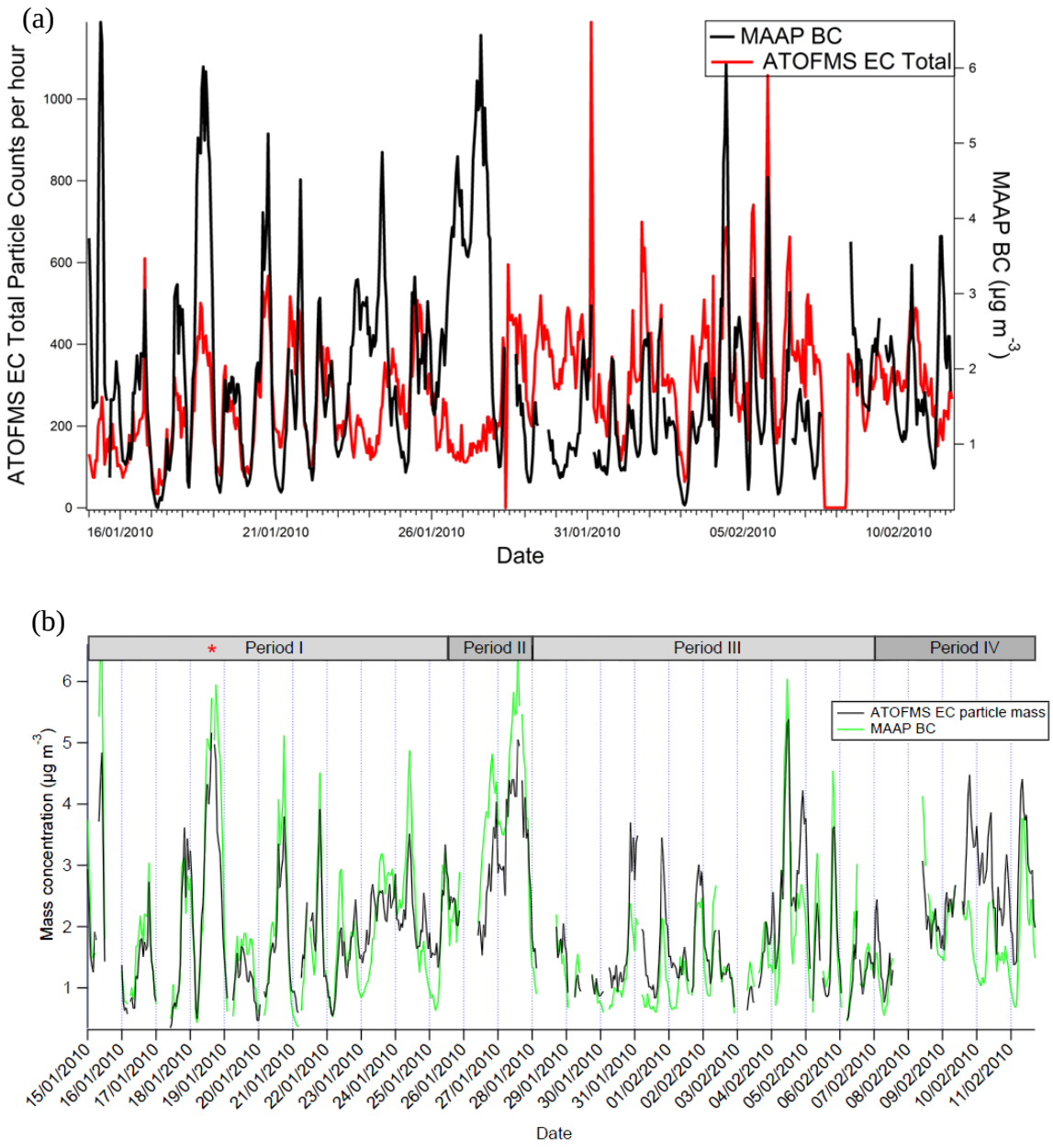

Figure 3.26 Temporal trends of MAAP BC and ATOFMS EC Total (a) Particle counts and (b) scaled counts (Healy et al., 2012)

The presence of an aethalometer at the sampling site during the campaign allowed further investigation of the BC sources, as the instrument allows the separation of the BC component into the fossil fuel derived BC (BC_{ff}) and the biomass burning BC (BC_{bb}). (Crippa et al., 2013b). The aethalometer measures the BC concentration by collecting the particles on a quartz fibre filter; the light attenuation of the collected particles is then measured. A previous study noted that while BC measured using an

Aethalometer correlated well with thermal optical EC measurements, the calculated concentration from the aethalometer was consistently higher (Jeong et al., 2004). During the MEGAPOLI summer campaign Freutel et al. (2013) also noted that aethalometer measurements were consistently higher than concurrent MAAP measurements and calculated a 30% error to be associated with the aethalometer measurements. The ATOFMS EC data was separated into components associated with fossil fuel combustion (EC Traffic, $ECOCNO_X$ and $ECOCSO_X$) and biomass burning (EC Biomass) and then compared to the aethalometer factors. The temporal profiles of these inter-compared factors are shown in Figure 3.26 (a) and (b) respectively. It is clear that the correlation is poor with R^2 of 0.09 and 0.05 found for fossil fuel combustion and biomass burning components respectively. Similar to the MAAP BC comparison, the ATOFMS suffers from clear undercounting during the period of high concentration (23-28 January) because of the "busy time" issue mentioned above. (Su et al., 2004). The temporal profile for both ATOFMS EC traffic and EC biomass, while not responding in a quantitative fashion, does track the ambient concentration of BC_{ff} and BC_{bb} with increases in concentration matched by coincident increases in particle count in the ATOFMS, especially during the period 15-23 January. While the correlation between the two methods is poor they both determine that the BC is mainly due to fossil fuel (85 % by aethalometer and 86 % by ATOFMS particle counts) with biomass burning contributing the smaller fragment (15 % by aethalometer and 14% by ATOFMS particle counts).

The particle counts measured by the ATOFMS were scaled using the same method as for the total EC and compared to the aethalometer factors by Dr R. M. Healy. (Healy et al., 2012). The correlations were greatly improved by the scaling with the R^2 values improving to 0.60 and 0.48 for fossil fuel and biomass burning, respectively. The temporal trend for these scaled ATOFMS counts and the aethalometer factors are shown in Figure 3.27. It is again clear that the scaling procedure improves the correlation by accounting for periods where ATOFMS counts are affected by transmission efficiencies or "busy time". The scaling procedure also led to the conclusion that fossil fuel combustion contributed 88 % to the total BC with biomass burning contributing 12 %. The reason for the slight difference is likely due to the EC particles not being wholly composed of carbon but containing contributions from other internally and externally mixed fragments such

as ammonium, nitrate and sulfate, along with particle classes that contain organic carbon (OC) fragments.

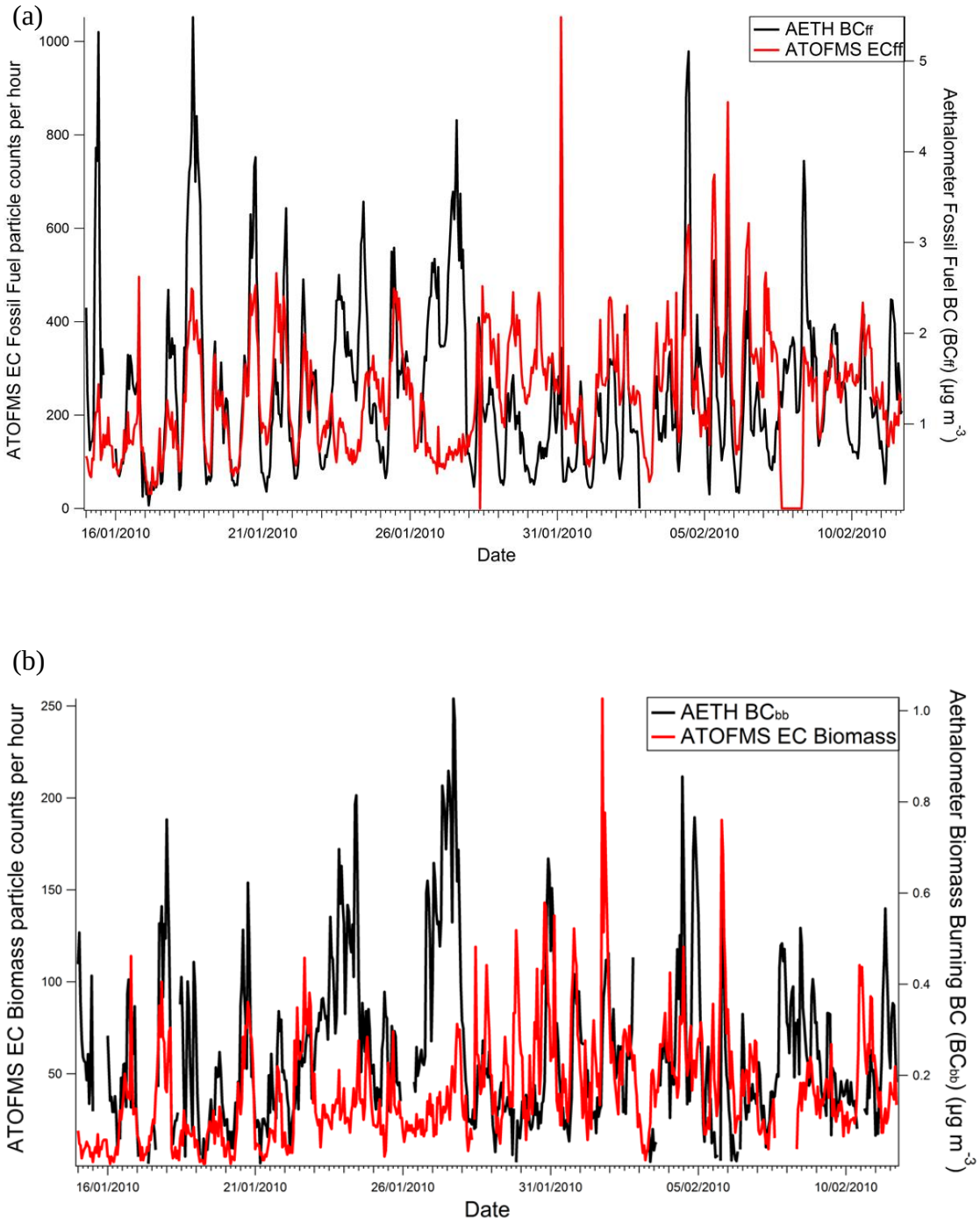

Figure 3.27 Temporal trends of (a) Aethalometer BC fossil fuel fraction and ATOFMS fossil fuel EC particle counts and (b) Aethalometer BC biomass burning fraction and ATOFMS EC Biomass particle counts.

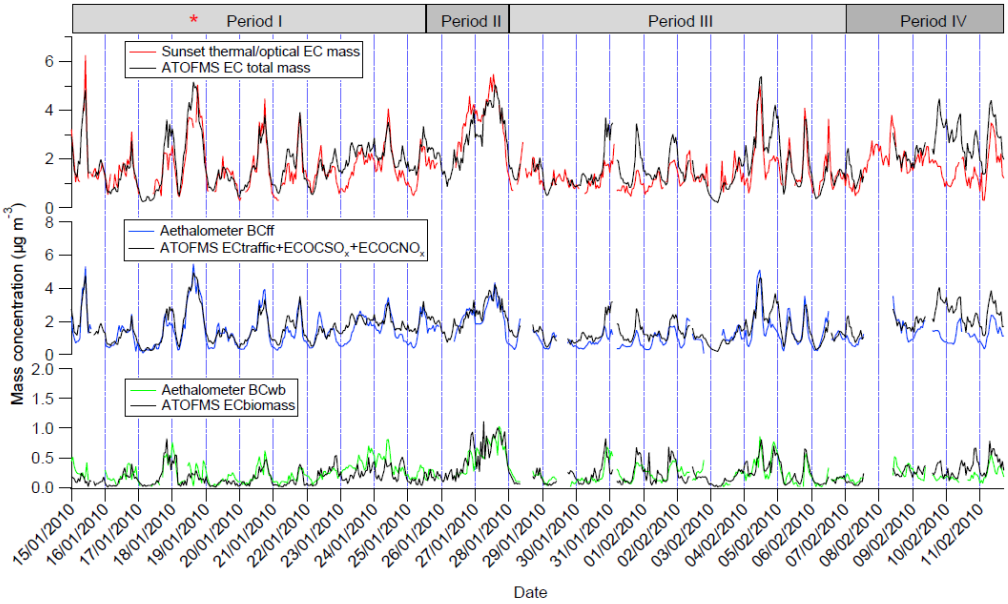

Figure 3.28 Top: Comparison of total scaled hourly ATOFMS EC particle mass concentration and hourly average Sunset thermal/optical EC mass concentration. **Middle:** scaled ATOFMS mass concentration for the sum of EC traffic, ECOCSOx and ECOCNOx compared with hourly average modelled aethalometer BC_{ff} mass concentration. **Bottom:** scaled ATOFMS mass concentration for EC biomass compared with hourly average modelled aethalometer BC_{bb} mass concentration. (Healy et al., 2012).

Finally, after scaling ATOFMS data and establishing good correlations, Healy et al. (2012) used the information to ascertain the relative contributions of local and regional sources to overall BC loading. During the measurement campaign a consistent minimum was observed in the EC size distribution at approximately 400 nm. The smaller mode (<400 nm) followed a clear diurnal profile and were attributed to local emissions while the larger (>400 nm) was associated with continental transport events. Based on these observations it was calculated that local emissions contribute 79% of the scaled ATOFMS EC particle mass, while EC particles attributed to continental transport events contribute 21% of the EC particle mass (Healy et al., 2012)

Comparison with AMS measurements

Aerosol Mass Spectrometer (AMS) measurements were carried out in tandem with the ATOFMS measurements at the LHVP. The AMS measurements were performed using a High-resolution time-of-flight aerosol mass spectrometer (HR-ToF-AMS), (DeCarlo et al., 2006). The source apportionment carried out on the AMS data is detailed elsewhere. (Crippa et al., 2013b). As stated previously the AMS identified 5 factors at the LHVP (HOA, BBOA, COA, OOA and OOA2-BBOA). Comparison of the ATOFMS particle types is beneficial as it can provide mixing state information, which is not provided by the quantitative AMS measurements. Particle types corresponding to four of the AMS factors (HOA, BBOA, OOA and OOA2-BBOA) were observed in the ATOFMS dataset, no corresponding particle class was found for the COA factor. The HOA factor attributed to vehicle emissions, (Crippa et al., 2013b) was compared to the sum of the ATOFMS EC Traffic and ECOCSO$_X$ particle types both of which were associated with fresh and aged vehicle emissions respectively. It is clear from Figure 3.28 that the ATOFMS particle counts follow the trend of the HOA factor well with peaks in number occurring during peaks in concentration, especially during the early part of the campaign. However it was found once again that during the period of increased concentration 23-28 January, the ATOFMS appeared to suffer from the "busy time" causing the ATOFMS to undercount the particles. The comparison of the particle counts and the quantitative HOA factor returned an R^2 of only 0.06 but when the ATOFMS particle types were scaled by Dr R. M. Healy and the OA fragment of these particle types compared to the HOA factor, the R^2 improved to 0.67. (Healy et al., 2013). This comparison shows that the scaling of the ATOFMS data is hugely beneficial and returns semi-quantitative data from the raw particle count data of the ATOFMS. Importantly, this study also suggests that the factor described by the AMS analysis as HOA is composed of two particle types: one associated with freshly emitted exhaust particles and one due to aged vehicle emissions.

The temporal profile of the AMS BBOA factor is compared to the sum of ATOFMS EC Biomass and Fresh Biomass OC particle types in Figure 3.27. Although the correlation between these two is poor (R^2 = 0.14), it is again clear that the ATOFMS particle counts follow the trend of the quantitative measurements, often displaying

coincident peaks in counts and concentration, with the exception again occurring during the "busy time" noted during 23-28 January. Following the scaling procedure the OA fragment of the ATOFMS particle counts correlated against the BBOA factor with $R^2 = 0.56$ (Healy et al., 2013). The comparison of the ATOFMS particle classes and the AMS BBOA fragment supports the identification of the BBOA factor as associated with freshly emitted biomass burning particles. (Crippa et al., 2013b)

While the BBOA factor was determined to be due to fresh biomass emissions, the OOA2-BBOA factor was attributed to aged biomass emissions. (Crippa et al., 2013b). The temporal profile of this factor is compared with the ATOFMS Aged Biomass OC particle type in Figure 3.30. The correlation between these two components was the strongest obtained for the direct comparison of the ATOFMS counts with mass concentrations. An $R^2 = 0.37$ was obtained which shows that these particle types respond in the most quantitative fashion of all those compared. The scaling procedure carried out on the ATOFMS data resulted in an improvement in the correlation to $R^2 = 0.47$, (Healy et al., 2013). While this is not as strong an improvement as observed with other comparisons (Healy et al. 2013) the results can be attributed to discrimination between fresh and aged particles using both techniques. That is, the ATOFMS technique uses particle composition as a measure and AMS uses differences in temporality.

The final AMS factor that was compared with ATOFMS particle counts was the OOA factor, which is attributed to Secondary Organic Aerosol (SOA). (Crippa et al., 2013b). The OOA factor was compared to the sum of particle counts associated with the following five ATOFMS particle types likely comprised of some SOA; $ECOCNO_X$, $OCSO_X$, $OCNO_X$, Amine Rich and Transported Biomass OC. While these particle types are not completely derived from secondary sources, they are likely to contain a significant contribution of secondary species: they are all associated with aged, processed or transported particles. The temporal profile of the OOA factor is compared with the sum of the ATOFMS particle counts in Figure 3.31. The relatively poor correlation of $R^2 = 0.28$ is likely due to the ATOFMS counts being made up of several different particle types, which may not be wholly composed of SOA. The OOA factor was also compared with each of the different particle classes individually, with Amine Rich returning the best correlation of $R^2 =$

0.58. One reason for this good correlation is that both the OOA factor and Amine Rich particle type were strongly associated with the periods influenced by continental air masses. However, the Amine Rich particle type is certainly not the sole contributor to the SOA as the other particle types contain signals for oxidised organic fragments. This is supported by the scaling procedure carried out using the ATOFMS technique, (Healy et al., 2013), where it was found that the combination of the oxidised organic fragments from each of the SOA particle types provided the strongest correlation, $R^2 = 0.81$. Therefore it was determined that each of the particle types ($ECOCNO_X$, $OCSO_X$, $OCNO_X$, Amine Rich and Transported Biomass OC) contribute to the OOA factor i.e. several distinct particle types each contribute to the SOA observed in Paris during the campaign.

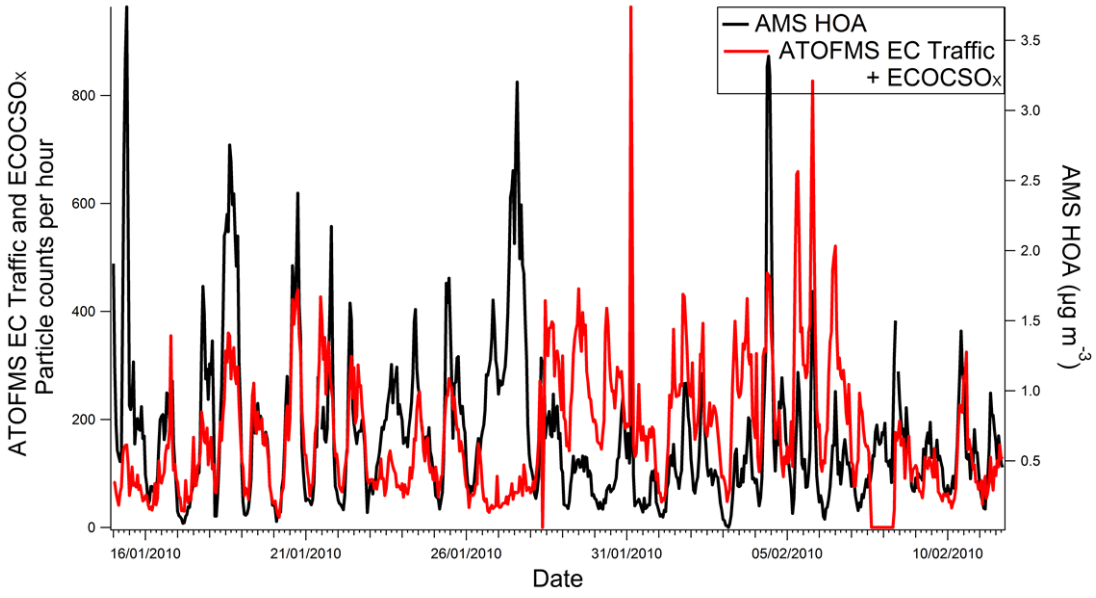

Figure 3.29 Temporal trends of AMS HOA factor and ATOFMS (EC Traffic + $ECOCSO_X$) particle counts during the MEGAPOLI measurement campaign

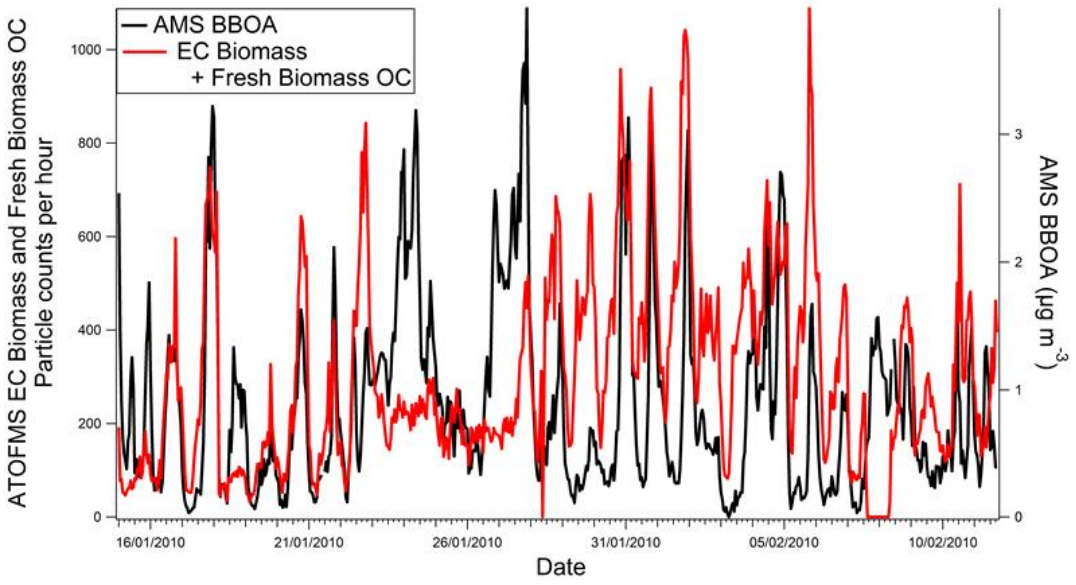

Figure 3.30 Temporal trends of AMS BBOA factor and ATOFMS (EC Biomass + Fresh Biomass OC) particle counts during the MEGAPOLI measurement campaign

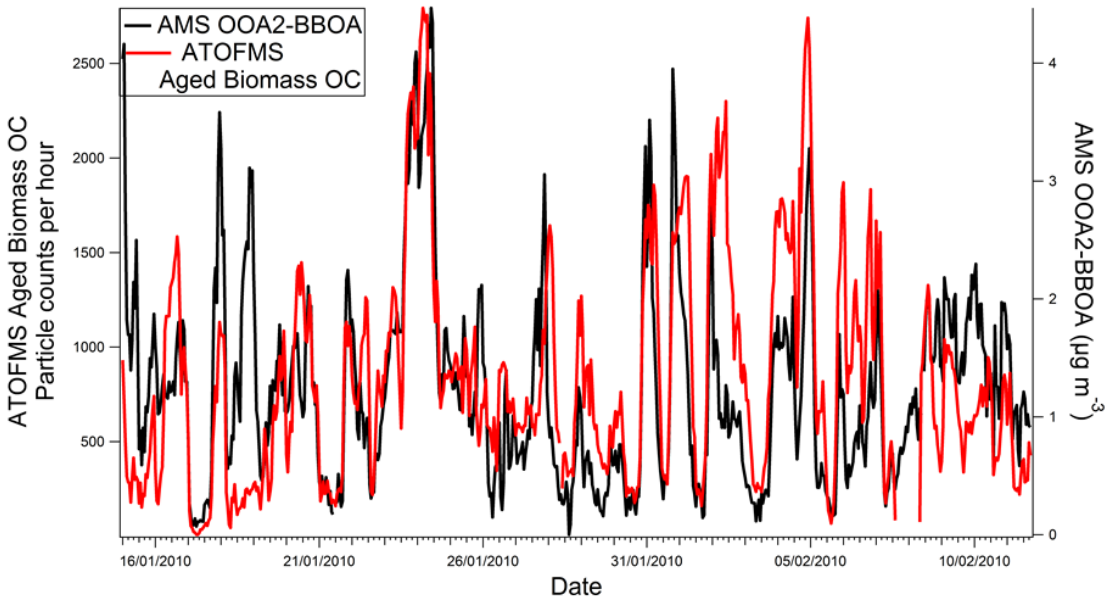

Figure 3.31 Temporal trends of AMS $BBOA_2$ factor and ATOFMS Aged Biomass OC particle types during the MEGAPOLI measurement campaign

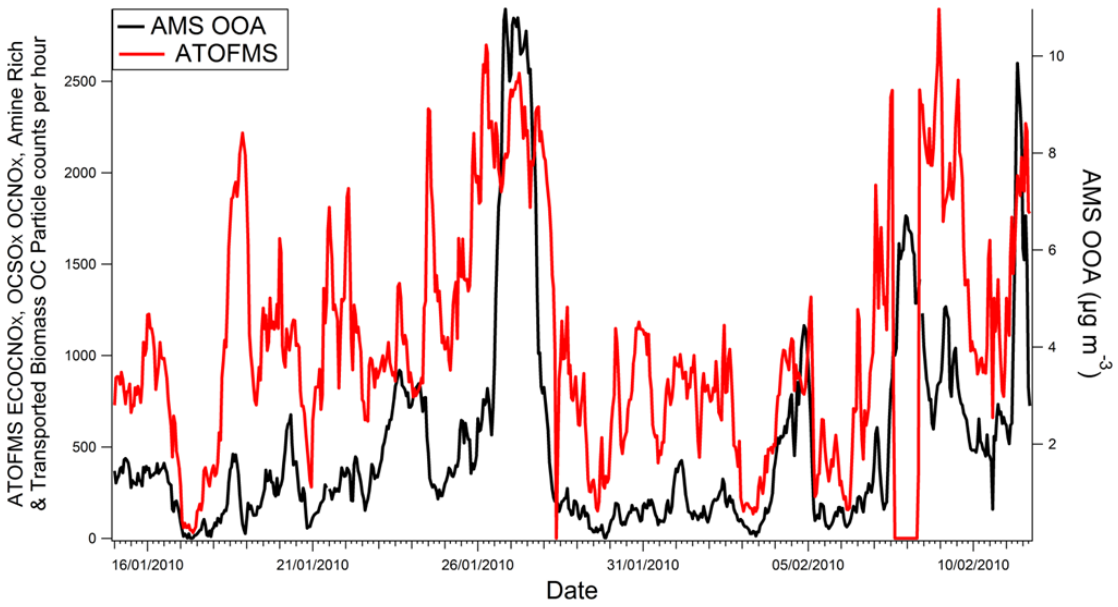

Figure 3.32 Temporal trends of AMS OOA factor and ATOFMS ($ECOCNO_X$ + $OCSO_X$ + $OCNO_X$ + Amine Rich + Transported Biomass OC) Particle Counts

Comparison with PILS-IC and ICP-MS

The ATOFMS spectra obtained during the campaign contained peaks for many metals including K, Na, Ca and Fe among the most abundant. The ATOFMS dataset was therefore also compared with quantitative results obtained using PILS-IC (undertaken by Laboratoire des Sciences du Climat et de l'Environnement (LCSE)) and ICP-MS analysis of 12-hour filter samples (carried out by Laboratoire Chimie Environment – Instrument et Reactivité Atmosphérique (LCE – IRA)). Preparation of the ATOFMS data for this inter-comparison exercise was carried out using the method outlined in a previous study (Snyder et al., 2009). Comparisons were specifically made against the hourly Na, K, Mg and Ca measurements determined by PILS-IC and against the 12 hour Ca, Cr, Cu, Fe, K, Mg, Mn, Na, Ni, Pb, Ti, V and Zn measurements from ICP-MS. Overall the correlations were found to be poor with the strongest relationships found for the 12 hour Ni and Pb concentrations yielding R^2 of 0.60 and 0.43 respectively. All other correlations gave R^2 values less than 0.2 with the majority below 0.1. The reason for the low correlations is related to many factors; transmission efficiency of the AFL, matrix effects associated with particle composition and interference from *m/z* signals associated with organic fragments.

While the comparison carried out on the ATOFMS ion intensity associated with the metal signals in the Paris dataset is small-scale, a much more thorough investigation was carried out on the dataset collected during the SAPUSS measurement campaign in Barcelona, and this is fully discussed in Chapter 5 of this thesis.

3.4 Conclusion

An ATOFMS was deployed at an urban background site in Paris during the MEGAPOLI monitoring campaign held in January and February 2010. The ATOFMS was operated with an Aerodynamic Focusing Lens (TSI AFL 100) and collected a total of 1742992 size-resolved single particle dual ion mass spectra. The particle mass spectra were attributed to 18 particle types which were grouped into 5 general categories. By far the largest category of particles detected and classified was carbonaceous aerosol represented 94% of the total observed. The particles were described as being due to local emissions or transport of aerosols to the city during periods influenced by continental air masses. Locally emitted EC Traffic, EC Biomass, ECOCSO$_X$ and Fresh and aged Biomass OC particle types all exhibited strong diurnal trends and were present throughout the campaign. Particle types determined to be largely due to transportation were: ECOCNO$_X$, OCNO$_X$, OCSO$_X$, Transported Biomass OC and Amine Rich. These particle types did not exhibit a strong diurnal profile and increased particle numbers were clearly detected during continental transport events. Higher particle counts were observed for ECOCSO$_X$, and OCSO$_X$ during a fog event on 18 January 2010, which suggests that these particles may be the result of heterogeneous processing of locally emitted particles, likely from traffic emissions.

Three metal-containing particle types were identified during the measurement campaign; Fe-Rich, Oil-V and Incineration (Pb-Cl). The Fe-Rich particle type was largely attributed to transported industrial emissions as the particle counts were higher during continental air mass intrusions. This particle type has previously been attributed to continentally transported industrial particles in London (Harrison et al., 2012b). The Oil-V particles had mass spectra similar to shipping and heavy oil combustion particles previously classified. (Healy et al., 2009; Pastor et al., 2003). In

this study the Oil-V particle counts increased during marine air masses where the trajectory would bring the air mass over shipping lanes and heavily industrialised areas to the NW of Paris. The Oil-V particle types were also detected during continental air masses, indicating a contribution from oil combustion on the local or regional scale. A particle type characterised by the presence of strong Pb and Cl signals and previously attributed to incineration, (Moffet et al., 2008b) was also observed. These particles were detected in sharp peaks in particle number, indicative of point source emissions of industrial particles.

Sea-Salt particles were detected during Atlantic air mass intrusions and contained signals for highly aged nitrate showing the particles were heavily processed during transport to Paris. Another particle type containing Na but with a stronger signal for Ca, along with nitrate and sulfate was attributed to processed traffic emissions. This particle type – Aged Traffic – displayed a strong diurnal trend with peaks appearing some three hours after morning and evening traffic periods.

The final category of particles classified by the ATOFMS was PAH particle types. Three particles were classified: K-PAH, OC-PAH and Ca-PAH. Both OC-PAH and Ca-PAH were identified as traffic emissions based on their diurnal profiles, which showed strong peaks during the morning and evening rush hour. The K-PAH particle type was attributed to biomass burning due to strong K signals, along with a daily trend similar to EC Biomass and showing high levels overnight.

During the measurement campaign a range of concurrent quantitative analytical measurements were performed and compared to ATOFMS particle types. The ATOFMS showed poor correlations with MAAP. However, the ATOFMS temporal profiles exhibited increases in particle counts coincident with increases in concentration for the aethalometer and AMS measurements of BC and carbonaceous aerosol. During periods with very high ambient particle concentrations the ATOFMS counts showed clear undercounting. The undercounting was due to instrumental issues (busy time). Correlations were greatly improved when the particle counts were scaled and compared with the quantitative measurements. (Healy et al., 2013; Healy et al., 2012). The comparisons between the ATOFMS and AMS were particularly useful as it allowed the further separation of the AMS factors. For example, HOA was found to be composed of two particle types EC Traffic and ECOCSO$_X$.

3.5 References

Andreae, M.O., Gelencsér, A., 2006. Black carbon or brown carbon? The nature of light-absorbing carbonaceous aerosols. Atmospheric Chemistry and Physics 6, 3131-3148.

Angelino, S., Suess, D.T., Prather, K.A., 2001. Formation of aerosol particles from reactions of secondary and tertiary alkylamines: Characterization by aerosol time-of-flight mass spectrometry. Environmental Science & Technology 35, 3130-3138.

Ault, A.P., Moore, M.J., Furutani, H., Prather, K.A., 2009. Impact of emissions from the Los Angeles port region on San Diego air quality during regional transport events. Environmental Science & Technology 43, 3500-3506.

Baklanov, A., Lawrence, M., Pandis, S., Mahura, A., Finardi, S., Moussiopoulos, N., Beekmann, M., Laj, P., Gomes, L., Jaffrezo, J.L., Borbon, A., Coll, I., Gros, V., Sciare, J., Kukkonen, J., Galmarini, S., Giorgi, F., Grimmond, S., Esau, I., Stohl, A., Denby, B., Wagner, T., Butler, T., Baltensperger, U., Builtjes, P., van den Hout, D., van der Gon, H.D., Collins, B., Schluenzen, H., Kulmala, M., Zilitinkevich, S., Sokhi, R., Friedrich, R., Theloke, J., Kummer, U., Jalkinen, L., Halenka, T., Wiedensholer, A., Pyle, J., Rossow, W.B., 2010. MEGAPOLI: concept of multi-scale modelling of megacity impact on air quality and climate. Advances in Science and Research 4, 115-120.

Bessagnet, B., Hodzic, A., Blanchard, O., Lattuati, M., Le Bihan, O., Marfaing, H., Rouil, L., 2005. Origin of particulate matter pollution episodes in wintertime over the Paris Basin. Atmospheric Environment 39, 6159-6174.

Bressi, M., Sciare, J., Ghersi, V., Bonnaire, N., Nicolas, J.B., Petit, J.E., Moukhtar, S., Rosso, A., Mihalopoulos, N., Féron, A., 2013a. A one-year comprehensive chemical characterisation of fine aerosol (PM2.5) at urban, suburban and rural background sites in the region of Paris (France). Atmospheric Chemistry and Physics 13, 7825-7844.

Bressi, M., Sciare, J., Ghersi, V., Mihalopoulos, N., Petit, J.-E., Nicolas, J., Moukhtar, S., Rosso, A., Féron, A., Bonnaire, N., 2013b. Sources and geographical origins of fine aerosols in Paris (France). Atmospheric Chemistry and Physics Discussions 13, 33237-33309.

Crippa, M., Canonaco, F., Slowik, J.G., El Haddad, I., DeCarlo, P.F., Mohr, C., Heringa, M.F., Chirico, R., Marchand, N., Temime-Roussel, B., Abidi, E., Poulain, L., Wiedensohler, A., Baltensperger, U., Prévôt, A.S.H., 2013a. Primary and secondary organic aerosol origin by combined gas-particle phase source apportionment. Atmospheric Chemistry and Physics. 13, 8411-8426.

Crippa, M., DeCarlo, P.F., Slowik, J.G., Mohr, C., Heringa, M.F., Chirico, R., Poulain, L., Freutel, F., Sciare, J., Cozic, J., Di Marco, C.F., Elsasser, M., Nicolas, J.B., Marchand, N., Abidi, E., Wiedensohler, A., Drewnick, F., Schneider, J., Borrmann, S., Nemitz, E., Zimmermann, R., Jaffrezo, J.L., Prévôt, A.S.H., Baltensperger, U., 2013b. Wintertime aerosol chemical composition and source apportionment of the organic fraction in the metropolitan area of Paris. Atmospheric Chemistry and Physics 13, 961-981.

Dall'Osto, M., Booth, M.J., Smith, W., Fisher, R., Harrison, R.M., 2008. A study of the size distributions and the chemical characterization of airborne particles in the vicinity of a large integrated steelworks. Aerosol Science and Technology 42, 981-991.

Dall'Osto, M., Harrison, R.M., 2012. Urban organic aerosols measured by single particle mass spectrometry in the megacity of London. Atmospheric Chemistry and Physics 12, 4127-4142.

Dall'Osto, M., Harrison, R.M., 2006. Chemical characterisation of single airborne particles in Athens (Greece) by ATOFMS. Atmospheric Environment 40, 7614-7631.

Dall'Osto, M., Harrison, R.M., Beddows, D.C.S., Freney, E.J., Heal, M.R., Donovan, R.J., 2006. Single-particle detection efficiencies of aerosol time-of-flight mass spectrometry during the North Atlantic marine boundary layer experiment. Environmental Science & Technology 40, 5029-5035.

Dall'Osto, M., Drewnick, F., Fisher, R., Harrison, R.M., 2012. Real-Time Measurements of Nonmetallic Fine Particulate Matter Adjacent to a Major Integrated Steelworks. Aerosol Science and Technology 46, 639-653.

DeCarlo, P.F., Kimmel, J.R., Trimborn, A., Northway, M.J., Jayne, J.T., Aiken, A.C., Gonin, M., Fuhrer, K., Horvath, T., Docherty, K.S., 2006. Field-deployable, high-resolution, time-of-flight aerosol mass spectrometer. Analytical Chemistry 78, 8281-8289.

Favez, O., Cachier, H., Sciare, J., Le Moullec, Y., 2007. Characterization and contribution to $PM_{2.5}$ of semi-volatile aerosols in Paris (France). Atmospheric Environment 41, 7969-7976.

Favez, O., Cachier, H., Sciare, J., Sarda-Estève, R., Martinon, L., 2009. Evidence for a significant contribution of wood burning aerosols to $PM_{2.5}$ during the winter season in Paris, France. Atmospheric Environment 43, 3640-3644.

Freutel, F., Schneider, J., Drewnick, F., von der Weiden-Reinmüller, S.L., Crippa, M., Prévôt, A.S.H., Baltensperger, U., Poulain, L., Wiedensohler, A., Sciare, J., Sarda-Estève, R., Burkhart, J.F., Eckhardt, S., Stohl, A., Gros, V., Colomb, A., Michoud, V., Doussin, J.F., Borbon, A., Haeffelin, M., Morille, Y., Beekmann, M., Borrmann, S., 2013. Aerosol particle measurements at three stationary sites in the megacity of Paris during summer 2009: meteorology and air mass origin dominate aerosol particle composition and size distribution. Atmospheric Chemistry and Physics. 13, 933-959.

Furutani, H., Jung, J., Miura, K., Takami, A., Kato, S., Kajii, Y., Uematsu, M., 2011. Single-particle chemical characterization and source apportionment of iron-containing atmospheric aerosols in Asian outflow. Journal of Geophysical Research 116, D18204.

Gross, D.S., Atlas, R., Rzeszotarski, J., Turetsky, E., Christensen, J., Benzaid, S., Olson, J., Smith, T., Steinberg, L., Sulman, J., Ritz, A., Anderson, B., Nelson, C., Musicant, D.R., Chen, L., Snyder, D.C., Schauer, J.J., 2010. Environmental chemistry through intelligent atmospheric data analysis. Environmental Modelling & Software 25, 760-769.

Gross, D.S., Barron, A.R., Sukovich, E.M., Warren, B.S., Jarvis, J.C., Suess, D.T., Prather, K.A., 2005. Stability of single particle tracers for differentiating between heavy- and light-duty vehicle emissions. Atmospheric Environment 39, 2889-2901.

Guazzotti, S.A., Suess, D.T., Coffee, K.R., Quinn, P.K., Bates, T.S., Wisthaler, A., Hansel, A., Ball, W.P., Dickerson, R.R., Neususs, C., Crutzen, P.J., Prather, K.A., 2003. Characterization of carbonaceous aerosols outflow from India and Arabia: Biomass/biofuel burning and fossil fuel combustion. Journal of Geophysical Research-Atmospheres 108.

Harrison, R., Beddows, D., Hu, L., Yin, J., 2012a. Comparison of methods for evaluation of wood smoke and estimation of UK ambient concentrations. Atmospheric Chemistry and Physics 12, 8271-8283.

Harrison, R.M., Dall'Osto, M., Beddows, D.C.S., Thorpe, A.J., Bloss, W.J., Allan, J.D., Coe, H., Dorsey, J.R., Gallagher, M., Martin, C., Whitehead, J., Williams, P.I., Jones, R.L., Langridge, J.M., Benton, A.K., Ball, S.M., Langford, B., Hewitt, C.N., Davison, B., Martin, D., Petersson, K.F., Henshaw, S.J., White, I.R., Shallcross, D.E., Barlow, J.F., Dunbar, T., Davies, F., Nemitz, E., Phillips, G.J., Helfter, C., Di Marco, C.F., Smith, S., 2012b. Atmospheric chemistry and physics in the atmosphere of a developed megacity (London): an overview of the REPARTEE experiment and its conclusions. Atmospheric Chemistry and Physics 12, 3065-3114.

Healy, R., Hellebust, S., Kourtchev, I., Allanic, A., O'Connor, I., Bell, J., Healy, D., Sodeau, J., Wenger, J., 2010. Source apportionment of PM 2.5 in Cork Harbour, Ireland using a combination of single particle mass spectrometry and quantitative semi-continuous measurements. Atmospheric Chemistry and Physics 10, 9593-9613.

Healy, R.M., O'Connor, I.P., Hellebust, S., Allanic, A., Sodeau, J.R., Wenger, J.C., 2009. Characterisation of single particles from in-port ship emissions. Atmospheric Environment 43, 6408-6414.

Healy, R.M., Riemer, N., Wenger, J.C., Murphy, M., West, M., Poulain, L., Wiedensohler, A., O'Connor, I.P., McGillicuddy, E., Sodeau, J.R., Evans, G.J., 2014. Single particle diversity and mixing state measurements. Atmospheric Chemistry and Physics 14, 6289-6299.

Healy, R.M., Sciare, J., Poulain, L., Crippa, M., Wiedensohler, A., Prévôt, A.S.H., Baltensperger, U., Sarda-Estève, R., McGuire, M.L., Jeong, C.H., McGillicuddy, E., O'Connor, I.P., Sodeau, J.R., Evans, G.J., Wenger, J.C., 2013. Quantitative determination of carbonaceous particle mixing state in Paris using single-particle mass spectrometer and aerosol mass spectrometer measurements. Atmospheric Chemistry and Physics 13, 9479-9496.

Healy, R.M., Sciare, J., Poulain, L., Kamili, K., Merkel, M., Müller, T., Wiedensohler, A., Eckhardt, S., Stohl, A., Sarda-Estève, R., McGillicuddy, E., O'Connor, I.P., Sodeau, J.R., Wenger, J.C., 2012. Sources and mixing state of size-resolved elemental carbon particles in a European megacity: Paris. Atmospheric Chemistry and Physics 12, 1681-1700.

Jeong, C.-H., Hopke, P.K., Kim, E., Lee, D.-W., 2004. The comparison between thermal-optical transmittance elemental carbon and Aethalometer black carbon measured at multiple monitoring sites. Atmospheric Environment 38, 5193-5204.

Kamilli, K.A., Poulain, L., Held, A., Nowak, A., Birmili, W., Wiedensohler, A., 2014. Hygroscopic properties of the Paris urban aerosol in relation to its chemical composition. Atmospheric Chemistry and Physics 14, 737-749.

Laborde, M., Crippa, M., Tritscher, T., Jurányi, Z., Decarlo, P.F., Temime-Roussel, B., Marchand, N., Eckhardt, S., Stohl, A., Baltensperger, U., Prévôt, A.S.H., Weingartner, E., Gysel, M., 2013. Black carbon physical properties and mixing state in the European megacity Paris. Atmospheric Chemistry and Physics 13, 5831-5856.

Lake, D.A., Tolocka, M.P., Johnston, M.V., Wexler, A.S., 2004. The character of single particle sulfate in Baltimore. Atmospheric Environment 38, 5311-5320.

Lopez, M., Schmidt, M., Delmotte, M., Colomb, A., Gros, V., Janssen, C., Lehman, S.J., Mondelain, D., Perrussel, O., Ramonet, M., Xueref-Remy, I., Bousquet, P., 2013. CO, NOx and 13CO2 as tracers for fossil fuel CO2: results from a pilot study in Paris during winter 2010. Atmospheric Chemistry and Physics 13, 7343-7358.

McGillicuddy, E., Dall'Osto, M., Querol, X., Lucarelli, F., Nava, S., Harrison, R.M., Gross, D., Healy, R.M., Sodeau, J.R., Wenger, J.C., 2014 In Preparation. Comparative Analysis of Metal-Containing Atmospheric Particles in Barcelona using Single Particle Mass Spectrometry and Particle Induced X-ray Emission (PIXE). In Preparation.

McGuire, M., Jeong, C.-H., Slowik, J., Chang, R.-W., Corbin, J., Lu, G., Mihele, C., Rehbein, P., Sills, D., Abbatt, J., 2011. Elucidating determinants of aerosol composition through particle-type-based receptor modeling. Atmospheric Chemistry and Physics 11, 8133-8155.

Moffet, R.C., de Foy, B., Molina, L.T., Molina, M.J., Prather, K.A., 2008a. Measurement of ambient aerosols in northern Mexico City by single particle mass spectrometry. Atmospheric Chemistry and Physics 8, 4499-4516.

Moffet, R.C., Desyaterik, Y., Hopkins, R.J., Tivanski, A.V., Gilles, M.K., Wang, Y., Shutthanandan, V., Molina, L.T., Abraham, R.G., Johnson, K.S., Mugica, V., Molina, M.J., Laskin, A., Prather, K.A., 2008b. Characterization of aerosols containing Zn, Pb, and Cl from an industrial region of Mexico City. Environmental Science & Technology 42, 7091-7097.

Moffet, R.C., Prather, K.A., 2009. In-situ measurements of the mixing state and optical properties of soot with implications for radiative forcing estimates. Proceedings of the National Academy of Sciences 106, 11872-11877.

Noble, C.A., Prather, K.A., 1997. Real-time single particle monitoring of a relative increase in marine aerosol concentration during winter rainstorms. Geophysical Research Letters 24, 2753-2756.

Oster, M., Elsasser, M., Schnelle-Kreis, J., Zimmermann, R., 2011. First field application of a thermal desorption resonance-enhanced multiphoton-ionisation single particle time-of-flight mass spectrometer for the on-line detection of particle-bound polycyclic aromatic hydrocarbons. Analytical and Bioanalytical Chemistry 401, 3173-3182.

Pastor, S.H., Allen, J.O., Hughes, L.S., Bhave, P., Cass, G.R., Prather, K.A., 2003. Ambient single particle analysis in Riverside, California by aerosol time-of-flight mass spectrometry during the SCOS97-NARSTO. Atmospheric Environment 37, 239-258.

Petzold, A., Schönlinner, M., 2004. Multi-angle absorption photometry—a new method for the measurement of aerosol light absorption and atmospheric black carbon. Journal of Aerosol Science 35, 421-441.

Pio, C., Cerqueira, M., Harrison, R.M., Nunes, T., Mirante, F., Alves, C., Oliveira, C., Sanchez de La Campa, A., Artíñano, B., Matos, M., 2011. OC/EC ratio observations in europe: Re-thinking the approach for apportionment between primary and secondary organic carbon. Atmospheric Environment 45, 6121-6132.

Pratt, K.A., Mayer, J.E., Holecek, J.C., Moffet, R.C., Sanchez, R.O., Rebotier, T.P., Furutani, H., Gonin, M., Fuhrer, K., Su, Y., 2009. Development and characterization of an aircraft aerosol time-of-flight mass spectrometer. Analytical Chemistry 81, 1792-1800.

Qin, X., Pratt, K.A., Shields, L.G., Toner, S.M., Prather, K.A., 2012. Seasonal comparisons of single-particle chemical mixing state in Riverside, CA. Atmospheric Environment 59, 587-596.

Rehbein, P.J., Jeong, C.-H., McGuire, M.L., Yao, X., Corbin, J.C., Evans, G.J., 2011. Cloud and fog processing enhanced gas-to-particle partitioning of trimethylamine. Environmental Science & Technology 45, 4346-4352.

Sciare, J., d'Argouges, O., Zhang, Q., Sarda-Estève, R., Gaimoz, C., Gros, V., Beekmann, M., Sanchez, O., 2010. Comparison between simulated and

observed chemical composition of fine aerosols in Paris (France) during springtime: contribution of regional versus continental emissions. Atmospheric Chemistry and Physics 10, 11987-12004.

Shields, L.G., Qin, X.Y., Toner, S.M., Prather, K.A., 2008. Detection of ambient ultrafine aerosols by single particle techniques during the SOAR 2005 campaign. Aerosol Science and Technology 42, 674-684.

Shields, L.G., Suess, D.T., Prather, K.A., 2007. Determination of single particle mass spectral signatures from heavy-duty diesel vehicle emissions for PM2.5 source apportionment. Atmospheric Environment 41, 3841-3852.

Silva, P.J., Liu, D.Y., Noble, C.A., Prather, K.A., 1999. Size and chemical characterization of individual particles resulting from biomass burning of local Southern California species. Environmental Science & Technology 33, 3068-3076.

Skyllakou, K., Murphy, B.N., Megaritis, A.G., Fountoukis, C., Pandis, S.N., 2014. Contributions of local and regional sources to fine PM in the megacity of Paris. Atmospheric Chemistry and Physics 14, 2343-2352.

Snyder, D.C., Schauer, J.J., Gross, D.S., Turner, J.R., 2009. Estimating the contribution of point sources to atmospheric metals using single-particle mass spectrometry. Atmospheric Environment 43, 4033-4042.

Stohl, A., Eckhardt, S., Forster, C., James, P., Spichtinger, N., Seibert, P., 2002. A replacement for simple back trajectory calculations in the interpretation of atmospheric trace substance measurements. Atmospheric Environment 36, 4635-4648.

Stohl, A., Forster, C., Frank, A., Seibert, P., Wotawa, G., 2005. Technical note: The Lagrangian particle dispersion model FLEXPART version 6.2. Atmospheric Chemistry and Physics 5, 2461-2474.

Su, Y.X., Sipin, M.F., Furutani, H., Prather, K.A., 2004. Development and characterization of an aerosol time-of-flight mass spectrometer with increased detection efficiency. Analytical Chemistry 76, 712-719.

SVDU, 2014. http://www.incineration.org/?-Usines-. Syndicat national du traitement et de la Valorisation des Déchets Urbains et assimilés.

Yu, S., Dennis, R.L., Bhave, P.V., Eder, B.K., 2004. Primary and secondary organic aerosols over the United States: estimates on the basis of observed organic carbon (OC) and elemental carbon (EC), and air quality modeled primary OC/EC ratios. Atmospheric Environment 38, 5257-5268.

4 Characterisation of Airborne Single Particles in Barcelona, Spain using ATOFMS

Contents

4.1 Introduction

4.1.1 Barcelona

Barcelona is a city on the north eastern (NE) coast of Spain in the western Mediterranean basin (WMB). According to the local government the city of Barcelona has a population of around 1 600 000 people with the larger Metropolitan Region having a population of just over 4.7 million people. The city is on the Mediterranean Sea and is surrounded by the mountains of the Catalan Coastal Range, with the Llobregat River to the southwest and the Besòs River to the north, Figure 4.1.

Figure 4.1 Map showing the topography of the city of Barcelona and the surrounding region.

4.1.2 Atmospheric monitoring in Barcelona

Numerous atmospheric studies have been carried out within the city of Barcelona and its greater metropolitan area. In an early study, it was found that levels of $PM_{2.5}$ and PM_1 at a kerbside site followed the daily traffic cycle whereas PM_{10} did not (Querol et al., 2001b). Subsequent source apportionment analysis showed that anthropogenic emissions accounted for 54% of PM_{10} and 73% of $PM_{2.5}$ mass, marine aerosol accounted for 4% of PM_{10} and less than 1% of $PM_{2.5}$ while crustal aerosol accounted for 26% of PM_{10} and 8% of the $PM_{2.5}$ fraction. During Saharan dust intrusions, the crustal contribution to PM_{10} rose to 44% and it was also shown that $PM_{2.5}/PM_{10}$ ratios can be used to distinguish pollution events from dust episodes (Querol et al., 2001b). Later, it was found that Saharan dust episodes can result in exceedances of the PM_{10} daily limit value and exhibit a summer maximum and a winter minimum in the WMB (Querol et al., 2009).

In comparison with other European cities, Barcelona has relatively high PM levels (Pérez et al., 2008). This observation has been attributed to high anthropogenic emissions accompanied by a dry warm climate, low dispersive conditions, and high dust levels due to soil re-suspension and Saharan dust intrusions. Pérez et al., (2008) reported that the $PM_{2.5–10}$ fraction mainly consisted of mineral dust (63%), sea-spray (10%), and secondary inorganic aerosols (mostly Na, Ca, K, Mg sulfate and nitrate, 20–25%), while the $PM_{1–2.5}$ fraction contained mineral dust (37%), secondary inorganic aerosols (27%) and carbonaceous matter (14%). The PM_1 fraction was found to mainly contain OM+EC (45%), secondary inorganic aerosols (ammonium nitrate and sulfate, 31%) and a minor contribution from crustal and sea-salt particles (Pérez et al., 2008).

A source apportionment study (PMF) found that road dust re-suspension accounted for 17% of PM_{10}, 8% of $PM_{2.5}$ and <2% of PM_1 respectively at an urban background site in Barcelona (Amato et al., 2009a). The composition of dust sampled directly from the road surface around Barcelona was enriched by many components including OC, EC, Fe, S, Cu, Zn, Mn, Cr, Sb, Sn, Mo, Zr, Hf, Ni, Ba, with the various locations being influenced by different elements, e.g., areas with high levels

of braking displayed increased levels of Cu, Sb, Zn and Mo. Other sites that were enriched with different components were those near construction and road works (Amato et al., 2009b).

The seasonal variation in concentration of metals present in PM collected at an urban measurement site in Barcelona was determined during the "Determination of the sources of atmospheric Aerosols in Urban and Rural Environments in the Western Mediterranean" (DAURE) field measurement campaign (Moreno et al., 2011). For most of the metals identified in the PM_{10} size fraction (Zn, Cu, Sn, Sb, Ti, Pb and Bi), the highest average concentrations were found during the winter. The exceptions were V and Ni which both peaked during the summer. Both vanadium and nickel are often attributed to heavy oil combustion, most notably shipping emissions (Healy et al., 2009). Similarly for $PM_{2.5}$ and PM_1, the winter samples also contained the highest concentrations of Cu, Zn, As, Rb, Cd, Sb, Ta, Ti, Pb and Bi with summer highs being observed for V, Ni Co and Sb. When the daily trend was examined, several metals (Cu, Sb, Sn and Ba) clearly presented a morning and afternoon peak in a pattern that followed road traffic activity. This trend was particularly evident in the coarse fraction which indicates the presence of emissions from road dust re-suspension and mechanical processes associated with traffic. Another group of metals (Ni, Mn and Cr) showed only a morning peak, which was attributed to industrial metallurgical emissions carried in with the morning sea breeze; similar peaks were observed for the finer fraction (Moreno et al., 2011).

As part of the DAURE campaign the elemental and organic carbon content of ambient aerosol was examined by radiocarbon (^{14}C) analysis (Minguillón et al., 2011). This study found that around 90% of the EC and 45% of the OC originated from fossil fuel burning, irrespective of season. The remaining fractions are mainly attributed to biomass burning and biogenic secondary organic aerosol, which is expected to make a significant contribution to OC during summer months. During wintertime 2011 the influence of biomass burning on the city was studied (Viana et al., 2013). It was found that at both an urban background and a residential site there was no evidence of local scale biomass burning, although regional scale biomass burning accounted for 8% of the PM mass measured at both sampling sites. The source apportionment analysis performed during this study identified several

sources: vehicle exhaust (the tracer for this factor being Black Carbon), mineral matter (tracers Ca, K, Al, Fe), sea-spray mixed with contributions from urban dust (tracers Na, Cl, Zn, Fe, Cu), and a factor identified as regional-scale transport of secondary aerosols, characterised by the main tracers S and K, which includes a contribution from regional scale biomass burning.

4.1.3 Solving Aerosol Problems Using Synergistic Strategies (SAPUSS) Campaign

Solving Aerosol Problems Using Synergistic Strategies (SAPUSS) was a measurement campaign carried out in and around the metropolitan area of Barcelona, Spain between 20th September and 20th October 2010.

The SAPUSS campaign is outlined in detail elsewhere (Dall'Osto et al., 2013a). The objectives of SAPUSS were: (i) to study the variability between aerosol concentration and composition within the city; (ii) to study aerosol formation and transformation within the city; (iii) to determine the evolution of fresh particles emitted within the boundary layer; (iv) to examine urban nucleation events; (v) to study the chemical and physical properties of aerosols at both ground level and above the city measured at tower sites; (vi) to quantify the contributions of traffic-related particles at a road site relative to an urban background measurement site; (vii) to apply a receptor model to the collected data to enable source identifications and to measure their contribution to the ambient aerosol concentration in the city.

Figure 4.2 Map of Barcelona with SAPUSS measurement sites marked.

Measurements were carried out at five sites in the city, Figure 4.2; a road site (RS), an urban background site (UB) and two tower sites Torre Mapfre (TM) and Torre Collserola (TC), where the latter was supported by ground-based measurements at the Fabra Observatory (TC_g). The final measurement site was the rural background (RB) station located at Montseny, 50 km north east of the city, which is part of the EUSAAR (European Supersites for Atmospheric Aerosol Research) monitoring network. All the monitoring sites are fully described in the SAPUSS overview paper (Dall'Osto et al., 2013a).

During the SAPUSS measurement campaign continuous atmospheric boundary layer observations were carried out (Pandolfi et al., 2013). The mean ceilometer Surface Mixed Layer (SML) and decoupled residual/convective layer (DRCL) mean heights were found to be 904 ± 273 m above ground level and 1761 ± 363 m above ground level respectively. In general the SML exhibited a diurnal profile with a lower height overnight/early morning and a peak around midday, while the backscatter actually showed a peak at night that was likely due to the higher night-time relative humidity resulting in particle growth. It was also observed that the different air mass intrusions

resulted in different boundary layer conditions. The lowest SML and DRLC were detected during a North African air mass intrusion while the highest were detected during Regional and Atlantic air mass events.

SMPS (Scanning Mobility Particle Sizer) measurements were carried out at four monitoring sites (UB, RS, TC and RB) during SAPUSS. During the campaign the Road Site exhibited the highest particle number concentrations (N) (12890±6300 cm^{-3}) and the Urban Background site provided the second highest N value (10490 ± 5900 cm^{-3}) (Dall'Osto et al., 2013b). It was also observed that the Black Carbon peaks, which were consistent with road traffic at the RS, UB and TM sites, did not peak until late afternoon at the TC site due to the delay in transport of the pollution plume to this site by the sea breeze. Three different particle nucleation events were observed during the campaign. The first was detected at the four sites simultaneously. The second event only occurred at the RB measurement site and coincided with a spike in SO_2 concentration. These nucleation events were found to occur during days with low relative humidity. A final nucleation event was determined to originate within the city and not throughout the region (Dall'Osto et al., 2013b).

Brines et al., (2014) applied *K*-means cluster analysis to particle number concentration (N) data collected by the SMPS instruments. Nine clusters were classified: three "Traffic" clusters (Traffic 1, Traffic 2 and Traffic 3); three Background Pollution clusters (Urban Background 1, Regional Background 1 and Regional Background 2); and three "Special Cases" (Nucleation, Regional Nitrate and Mix). Traffic 1 and 2 clusters were associated with primary vehicle emissions whereas traffic 3 was associated with the evaporation of traffic emissions and represented the highest levels of traffic pollution detected at UB and TC. The Urban Background 1 cluster was the most prevalent type monitored at the four sites and, as expected, occurred most frequently at the UB. The Regional Background 1 cluster was present at all sites except for the RS. It accounted for aged or long range transported aerosols. Regional Background 2 occurred with greater frequency at the RB and was less prevalent closer to the city; this cluster peaked at night. The Nucleation cluster was observed to occur mainly at the UB and TC and was found during intense solar radiation periods and at high ozone concentrations, suggesting

that it is associated with photochemically-driven nucleation events. The Regional Nitrate cluster predominated at TC and RB and was detected mainly at night. The final cluster, Mix, was likely due to a mixture of different sources and was the least defined of the nine in total analysed for the campaign (Brines et al., 2014).

During the campaign source apportionment was performed on the submicron organic aerosol (OA) measured at the RS and UB sites (Alier et al., 2013). Two primary anthropogenic OA components, three secondary OA components and one further component, that was not easily identifiable, were detected. The first of the Primary OA components was termed POA Urban for which traffic is a major contributor, along with some cigarette smoke: it represented 18% of total OC at the UB site. The second Primary component was regional biomass burning (BBOA regional), which accounted for 12% of OA at the UB and was found to be present especially within regional air masses. The Secondary components were; (i) Isoprene SOA, which was detected at similar levels at both sites and peaked during regional air mass events suggesting a regional source, (ii) α-Pinene SOA, which represented 24% of OA at the UB site, (iii) Aged SOA, which represented 18% of OA and was at its lowest levels during periods when North Atlantic air masses were present. The final component was described as "oxidised organic aerosol" of mainly urban origin and was not identified as either primary or secondary in origin, but did represent 10% of the OA at the UB. This component peaked during the day and was more abundant at RS suggesting an urban source for its origin.

Hourly elemental concentrations of $PM_{2.5}$ were determined for Na, Mg, Al, S, Cl, K, Ca, Ti, V, Cr, Mn, Fe, Ni, Cu, Zn, Sr and Pb at both the Urban Background and the Road Site monitoring locations by Particle Induced X-Ray Emission (PIXE) (Dall'Osto et al., 2013c). PIXE measurements were carried out on samples collected using a 'Streaker' sampler. The hourly elemental concentrations indicated that many of the elements were present in similar concentrations at both UB and RS. However, the contribution from elements related to non-combustion traffic sources (Fe and Cu) was elevated at the RS, while at the UB an increased contribution from industrial marker elements (Pb, Zn and Mn) was noted. During North African air masses both sites were found to have elevated levels of Al, Ti, K and Fe, while the North Atlantic air masses showed elevated levels of Zn, Pb, Mn and Cl at both sites. Source

apportionment analysis was performed on the elemental data and 9 PMF factors were classified, namely, Regional Sulfate, Sea-salt, Biomass Burning, Soil Dust, Urban Dust, Brake Dust, Industrial (Zn-Mn), Industrial (Pb-Cl) and Oil Combustion. The PIXE study is discussed further in Chapter 5.

The aim of the study described here as part of the SAPUSS campaign was to deploy an ATOFMS at the UB measurement site in order to provide size-resolved, chemical compositional data for single particles measured in real time. This information was then analysed to provide a description of the different types of particles present in Barcelona and used to address the specific objectives of the SAPUSS campaign described above.

4.2 Methodology

4.2.1 Measurement Site

The location used for the ATOFMS measurements made during SAPUSS was the Urban Background (UB) site (41°23'15'' N, 02°07'05' E) located on the North Western periphery of the city in a small park 6 km from the sea on Carrer de Jordi Girona. It is surrounded mainly by residential areas and several University campuses. The site is 300 m from Diagonal Avenue, which is a road comprising of nine vehicle lanes and two tram lines and is one of the main access roads for Barcelona. During the SAPUSS measurement campaign the avenue had a traffic volume of 62000 vehicles per day with a high of 5100 ± 1700 vehicles per hour during the morning traffic rush hour (Dall'Osto et al., 2013a). The location of the UB site is shown in Figure 4.3. ATOFMS measurements were carried out at the urban background measurement site from 24/09/2010 to 18/10/2010.

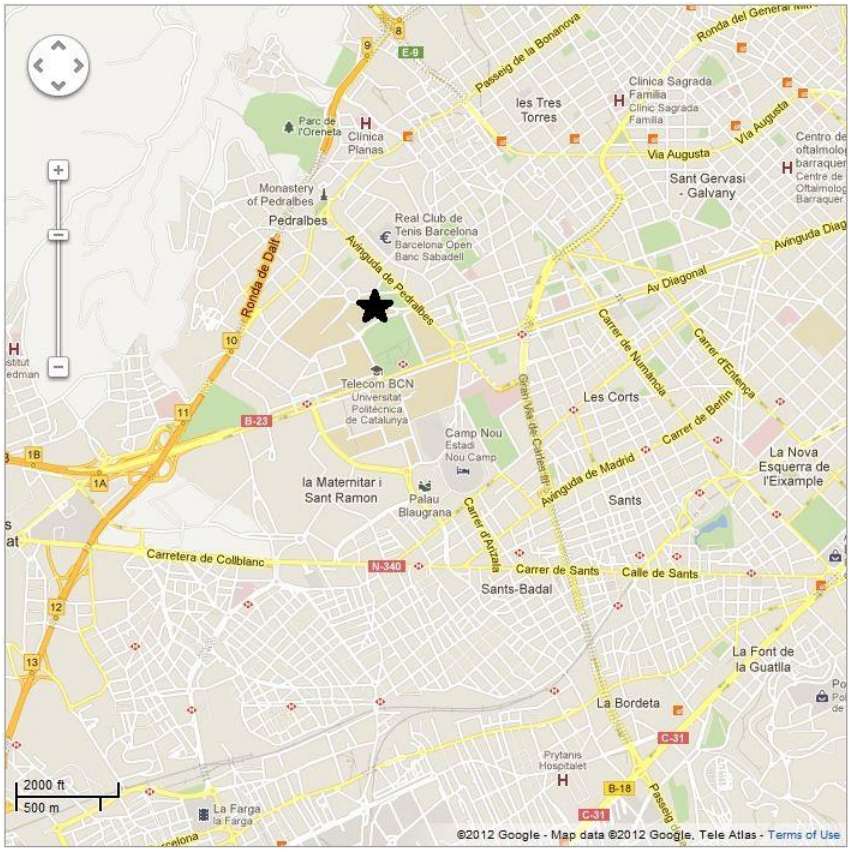

Figure 4.3 Map showing the location of the Urban Background measurement site and the surrounding road network and other infrastructure**.**

4.2.2 ATOFMS deployment

The ATOFMS deployed at the Urban Background measurement site during SAPUSS was a TSI model 3800 incorporating a converging nozzle inlet kindly loaned to University College Cork by Deborah S. Gross of Carleton College MN USA. The operating principle of this ATOFMS is identical to the model deployed in Paris during the MEGAPOLI campaign described in Chapter 3. However, the different inlet systems employed results in different particles being detected: the converging nozzle inlet used here favours the transmission of super-micron particles and crustal and sea-salt particle types are therefore detected with greater efficiency than an ATOFMS operating with an aerodynamic lens inlet. The ATOFMS deployed during the campaign was located in an air-conditioned sampling cabin shown in Figure 4.4. A sampling line comprising of quarter-inch copper tubing, which was protected with

a rain cap, was used to sample ambient aerosols. The final section of the sampling line was composed of a short section of quarter-inch flexible rubber tubing to connect the sampling line to the ATOFMS inlet. The aerosol was sampled at a height of 4 m above ground level. The operating principles of the instrument are described in detail in Chapter 2.

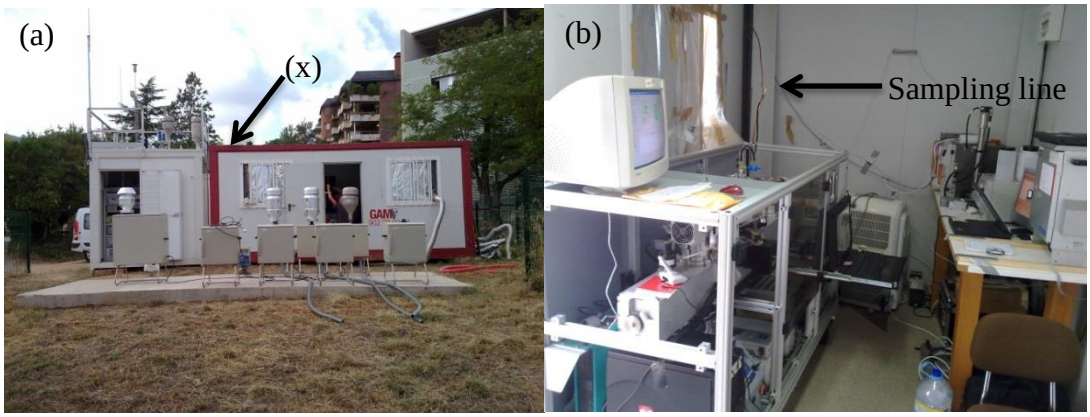

Figure 4.4 (a) The Urban Background measurement site with the ATOFMS inlet marked (x). (b) The ATOFMS inside the container.

During the campaign a total of 326395 size-resolved, single particle mass spectra were collected. The ATOFMS datasets were imported into ENCHILADA (Environmental Chemistry Through Intelligent Atmospheric Data Analysis) (Gross et al., 2010) and 282117 of the single particle mass spectra were analysed using a *K*-Means algorithm (MacQueen, 1967). The resulting clusters were then grouped into 22 particle types.

4.2.3 Meteorology

During the SAPUSS measurement campaign the city of Barcelona was influenced by several air masses with differing origins. The air mass periods were determined by performing HYSPLIT air mass back trajectories (Draxler, 2013) at six hour intervals. Each day was classified based on the origin of the air masses arriving at the site over

the 24-hour period. If the air masses arriving at the site changed source during the 24-hour period then that day was classified as a ‘transition’ day. A full description of the air masses has been outlined previously (Dall'Osto et al., 2013a). In summary, the types of air mass arriving at the site during the campaign were as follows:

Atlantic: 25, 26, 27, 28 September; 05 and 18 October

Regional: 29, 30 September; 01, 14, 15, 16, 17 October

North African West: 03 October

North African East: 07, 08, 09 October

European: 12 October

Transition: 24 September; 02, 04, 06, 10, 11, 13 October.

While some of the particle types are influenced by the origin of the air mass, others that derive from a local source are more linked with wind direction. A range of meteorological parameters were therefore monitored continuously at the UB site including wind speed, wind direction, temperature, relative humidity (Dall'Osto et al., 2013a). During the SAPUSS measurement campaign the average temperature measured at the UB site was 18.7 °C. This value was higher than the temperatures measured at the sites outside the city due to the urban heat island effect associated with the Barcelona metropolitan area (Dall'Osto et al., 2013a). Furthermore the temperature was found to be higher when North African air masses impinged on the city. The highest average wind speeds were observed during the period of the European air mass, with the North African (East) air mass also showing higher than average wind speed. The European air mass was also associated with precipitation (Dall'Osto et al., 2013a).

4.3 Results and Discussion

4.3.1 Particle types determined by ENCHILADA

The collected particle mass spectra were imported into ENCHILADA, a freeware SQL-based ATOFMS data analysis programme developed by Carleton College (Gross et al., 2010). Particle clusters were thereby determined using the *K*-means algorithm with $K = 80$ (a value which was user defined). The 80 particle clusters were examined and then grouped into 22 different particle types described by the dominant species present in the average mass spectrum or by the source of the particle. The detected particle types were subsequently grouped into 9 general categories which contain particle types with similar compositions or sources together: these groups are listed in Table 4.1.

For the purposes of the following discussion, mass spectra, and temporal/daily trends are shown in the body of the text while the particle size distributions and wind roses are included in the Appendix.

General Category	Particle Type	Particle Number	%
Carbonaceous	EC-NIT (aged EC)	79978	28.3
	K-CN	52588	18.6
	K-EC	20861	7.4
	Fresh/Local EC	19117	6.8
	Aged/Transported Biomass	5439	1.9
	Oxidised OC	4786	1.7
	OC NIT	2331	0.8
	K-SUL	2008	0.7
Sea Salt	Sea-Salt	43288	15.3
	Na-EC	2987	1.1
Dust	Saharan Dust	4009	1.4
	Ca Dust	6007	2.1
	Dust	18956	6.7
Heavy Oil Combustion	Oil-V	3388	1.2
Metal Containing	Fe	3824	1.4
	Pb-Cl	720	0.3
	Mn	1359	0.5
	Cu	362	0.1
Vegetative	Veg-KP	9239	3.3
Lubricating Oil	Ca-EC	367	0.1
Amine	Amine 84 (ETS)	395	0.1
PAH	PAH	108	0.0
Total		**282117**	**100.0**

Table 4.1 Particle types determined by ENCHILADA (K-means) analysis of the ATOFMS data collected at the Urban Background (UB) site in Barcelona.

4.3.1.1 Carbonaceous

Carbonaceous aerosol consists of two components: elemental carbon (EC) and organic carbon (OC). EC is directly emitted into the atmosphere due to the incomplete burning of fuels. OC is also directly emitted into the atmosphere but can be formed *in situ*, through gas-to-particle conversions of organic species (Pio et al., 2011; Yu et al., 2004). It is known that carbonaceous aerosol is a large constituent of atmospheric aerosol in Barcelona (Querol et al., 2001a; Querol et al., 2004). During the SAPUSS measurement campaign 9 different particle types were identified as carbonaceous and are discussed below.

EC-NIT

EC-NIT was the most abundant particle type observed during SAPUSS, accounting for 28.3% of the total number of particles detected at the UB site. This particle type was identified as EC-NIT due to the following specific ions observed in the average mass spectrum, Figure 4.5(a); 12 $[C]^+$, 24 $[C_2]^+$, 36 $[C_3]^+$, 48 $[C_4]^+$, 60 $[C_5]^+$, 72 $[C_6]^+$, 84 $[C_7]^+$ in the positive ion mass spectrum and 24 $[C_2]^-$, 36 $[C_3]^-$, 46 $[NO_2]^-$, 48 $[C_4]^-$, 60 $[C_5]^-$, 62 $[NO_3]^-$, 72 $[C_6]^-$, 97 $[HSO_4]^-$ in the negative ion mass spectrum. These peaks are all indicative of EC particles that have undergone some atmospheric processing. Similar particle types have previously been identified in ATOFMS spectra (Healy et al., 2012; Liu et al., 2003; Noble and Prather, 1996), and attributed to combustion, most likely fossil fuel combustion. The designation of this particle type as originating from a combustion process is further strengthened by the size distribution of the particle type, which peaks around 300 – 350 nm (Willeke and Whitby, 1975).

EC-NIT exhibits a diurnal profile (Figure 4.7(a)) with a minimum level apparent during the day (around 12:00-16:00), which increases again overnight. While the daily trend of this particle type does not exhibit a profile associated with local road traffic such a source remains most likely as other sources of EC, such as domestic combustion, are not significant in Barcelona or the WMB at this time of the year (September/October). The temporal profile for EC-NIT is shown in Figure 4.6(a) and includes several periods where particle numbers peaked. The largest of these accumulations occurs at the end of the campaign when the site was influenced by a

regional air mass and stagnant conditions. This suggests that the EC-NIT particle type is associated with local or regional emissions and that these accumulations may also strongly influence the daily trend as the residence time of the particles in the region is increased.

K-CN

The second most abundant particle type detected during the sampling campaign was K-CN, which represented 18.6 % of the total number of particles classified during the campaign. The average mass spectrum for this particle type is shown in Figure 4.5(b) and contains the signals: 36 $[C_3]^+$, 39 $[K]^+$, 41 $[K]^+$ in the positive ion mass spectrum and 26 $[CN]^-$, 36 $[C_3]^-$, 42 $[CNO]^-$ 46 $[NO_2]^-$, 48 $[C_4]^-$, 60 $[C_5]^-$, 62 $[NO_3]^-$, 97 $[HSO_4]^-$ in the negative ion mass spectrum. The large size of the *m/z* 39 peak in the positive mass spectrum suggests that it is due to potassium and not the hydrocarbon fragment $C_3H_3^+$. This conclusion is also confirmed by the presence of the secondary potassium isotope *m/z* 41 in the mass spectrum. The mass spectral features indicate that K-CN is likely due to biomass burning (Silva et al., 1999) (Guazzotti et al., 2003; Moffet et al., 2008a), while Healy et al., (2010) also identified CN fragments along with potassium in mass spectra of particles from biomass burning. The particle type also has a sub-micron size, which peaks around 350-400 nm, a value fairly typical for combustion particles.

This K-CN particle type exhibits a diurnal profile (Figure 4.7(a)) similar to that of K-EC, but not as pronounced. A slight increase in particle number is observed at night, consistent with a biomass burning source. The temporal trend of the K-CN particle type (Figure 4.6(a)) contains peaks in particle numbers at the end of the campaign during regional air mass impingement with stagnant conditions. Hence this trend is very similar to EC-NIT with the correlation between these two particle types being $R^2 = 0.71$. The peak in particle number found during the regional air mass event suggests that the K-CN particle type is also associated with local or regional emissions.

K-EC

The average mass spectrum for this particle type (Figure 4.5(c)) contained peaks 12 $[C]^+$, 36 $[C_3]^+$, 39 $[K]^+$, 48 $[C_4]^+$, 60 $[C_5]^+$, 72 $[C_6]^+$ in the positive ion mass spectrum

and 24 $[C_2]^-$, 36 $[C_3]^-$, 46 $[NO_2]^-$, 48 $[C_4]^-$, 60 $[C_5]^-$, 62 $[NO_3]^-$, 72 $[C_6]^-$, 97 $[HSO_4]^-$ in the negative ion mass spectrum. Therefore this particle type was identified as a biomass burning particle type due to the presence of potassium and elemental carbon fragments in the average mass spectrum similar to those detected and assigned previously (Healy et al., 2010; Healy et al., 2012). The particle size was also indicative of a combustion source with the sub-micron size distribution peaking around 350–400 nm. The 20861 K-EC particles detected during the sampling campaign represented 7.4% of all the classified particles at the Urban Background site.

This particle type exhibits a diurnal profile (Figure 4.7(a)) that shows higher overnight levels and a minimum during the day. Such a trend also suggests that the likely source of these particles is biomass burning. The temporal trend of K-EC is shown in Figure 4.6(a) and again shows a large peak in particle number at the end of the campaign during the regional air mass period associated with stagnant conditions. The temporal profile is strikingly similar to that observed for the EC-NIT type and a correlation of $R^2 = 0.86$ is obtained. As a result, the K-EC particle type is also associated with local or regional emissions.

Fresh/Local EC

A total of 19117 particles identified as fresh/local EC were detected during the measurement campaign. This number represents 6.8% of all the particles classified at the Urban Background site. The particle type displayed an average mass spectrum with peaks for 12 $[C]^+$, 24 $[C_2]^+$, 36 $[C_3]^+$, 39 $[K]^+/[C_3H_3]^+$, 48 $[C_4]^+$, 60 $[C_5]^+$, 72 $[C_6]^+$, 84 $[C_7]^+$, 96 $[C_8]^+$, 108 $[C_9]^+$, 120 $[C_{10}]^+$, 132 $[C_{11}]^+$, 144 $[C_{12}]^+$, 168 $[C_{14}]^+$, 180 $[C_{15}]^+$ in the positive ion mass spectrum and 24 $[C_2]^-$, 36 $[C_3]^-$, 46 $[NO_2]^-$, 48 $[C_4]^-$, 60 $[C_5]^-$, 62 $[NO_3]^-$, 72 $[C_6]^-$, 84 $[C_7]^-$, 96 $[C_8]^-$, 108 $[C_9]^-$, in the negative ion mass spectrum as seen in Figure 4.5 (d). Therefore the particle type was identified as fresh or local EC due to the low level of nitrate, which suggests that the particles are not as highly processed as the EC-NIT type and represent fresher emissions. Furthermore similar particle types have been detected during other ATOFMS measurement campaigns (Liu et al., 2003; Moffet et al., 2008a). The small *m/z* peak at 39 in the positive ion mass spectrum is of low intensity and is thus more indicative

of the hydrocarbon fragment, $C_3H_3^+$. The size distribution peaks around 300-350 nm, which also supports the attribution of this particle type to a combustion source.

The Fresh/Local EC particles exhibit a diurnal profile (Figure 4.7(a)) that shows higher overnight levels with a minimum during the day (12:00 -16:00). The temporal trend observed is shown in Figure 4.6(a), exhibiting a number of peaks in particle number. The largest of them again occurs at the end of the campaign during the regional air mass event. Once again this temporal profile is similar to that found for the EC-NIT particle type and the correlation between these two particle types is R^2 = 0.95. As discussed above, the Fresh/Local EC particle type is also associated with local or regional emissions.

Aged/Transported Biomass

5439 (1.9 %) particles were identified as Aged/Transported Biomass. The average mass spectrum is shown in Figure 4.5(e) and contains the following peaks; 24 $[C_2]^+$ 27 $[C_2H_3]^+$, 36 $[C_3]^+$, 39 $[K]^+$, 41 $[K]^+$, 43 $[C_2H_3O]^+$ 60 $[C_5]^+$, 84 $[C_7]^+$, 132 $[C_{11}]^+$ in the positive ion mass spectrum and 24 $[C_2]^-$, 36 $[C_3]^-$, 46 $[NO_2]^-$, 62 $[NO_3]^-$, 97 $[HSO_4]^-$, 125 $[H(NO_3)]^-$ in the negative ion mass spectrum. The assignment of this particle type to Aged/Transported Biomass is based on the presence of potassium peaks in the positive mass spectrum, the very large nitrate peaks in the negative spectrum, along with and the nitrate fragment $H(NO_3)^-$ which is characteristic of highly aged/processed particles (Dall'Osto et al., 2009). A similar particle type has been previously identified (and attributed to biomass burning) in the MEGAPOLI study performed in Paris (Healy et al., 2013). The particle size also indicates combustion as a source of these particles with a sub-micron size distribution peaking around 300-350 nm. However, a smaller additional mode found around 1.2 μm is suggestive of a possible contribution from crustal particles.

This particle type exhibits a diurnal profile shown in Figure 4.7(b) with higher overnight levels of the particles and a minimum during the day. This trend suggests domestic combustion as the source and supports the assignment of biomass burning to this particle type. It is notable that the Aged/Transported Biomass particle type (Figure 4.6(b)) shows very low particle numbers throughout the campaign but with a large peak at the end of the campaign during the stagnant regional air mass which

resulted in a large accumulation of particles. Higher levels of atmospheric processing and ageing occur during stagnant conditions and this explains the chemical composition of this particle type.

Oxidised OC

This particle type contained peaks for 27 $[C_2H_3]^+$, 37 $[C_3H]^+$, 39 $[C_3H_3]^+$, 43 $[C_2H_3O]^+$, 51 $[C_4H_3]^+$, 55 $[C_3H_3O]^+$, 61 $[C_5H]^+$, 63 $[C_5H_3]^+$, 77 $[C_6H_5]^+$ in the positive ion mass spectrum and 26 $[CN]^-$, 42 $[CNO]^-$ 46 $[NO_2]^-$, 62 $[NO_3]^-$, 80$[SO_3]^-$, 97 $[HSO_4]^-$ in the negative ion mass spectrum as shown in Figure 4.5(f). The presence of the oxidised organic fragments leads to the designated label Oxidised OC. The mass spectrum is similar to that previously reported for other OC particle types originating from traffic emissions (Moffet et al., 2008a; Pastor et al., 2003; Dall'Osto and Harrison, 2012) The particle size distribution of Oxidised OC is much broader than the carbonaceous types discussed above as it extends into the coarse mode. However the major portion of the distribution peaks in the 300-350 nm region. The larger size particles may be due to the condensation of semi-volatile organic compounds onto other particles.

Figure 4.7(b) shows the daily trend for the Oxidised OC particle type which peaks overnight with a maximum at 00:00. A secondary peak in particle number is also observed from 08:00 to 14:00 and is possibly due to the processing of combustion particles. The temporal trend observed for Oxidised OC in Figure 4.6(b) shows that it is present throughout the campaign and does not exhibit the accumulation behaviour at the end of the campaign as observed for the other particle types discussed above. The temporal trend also indicates some sharp peaks in the particles at various times, suggesting local emissions are the source of these particles.

OC-NIT

This particle type has the following peaks in the average mass spectrum (Figure 4.5(g)): 12 $[C]^+$, 23 $[Na]^+$, 24 $[C_2]^+$, 36 $[C_3]^+$, 39 $[C_3H_3]^+$, 48 $[C_4]^+$, 60 $[C_5]^+$, in the positive ion mass spectrum and 46 $[NO_2]^-$, 62 $[NO_3]^-$, 95 $[CH_3SO_3]^-$, $[C_6]^-$, 97 $[HSO_4]^-$ in the negative ion mass spectrum. The identification of this particle type as OC-NIT was mainly based on the presence of *m/z* 39 $[C_3H_3]^+$. This peak was identified as being associated with the hydrocarbon fragment, and not potassium, by

the low intensity absence of a signal at *m/z* 41 due to the potassium isotope. The negative mass spectrum contains some very intense peaks for nitrate but with a small contribution from sulfate. Similar particle types have been identified previously and linked to combustion sources or SOA formation (Healy et al., 2013; Moffet et al., 2008a). The likely source for these particles is combustion with the size distribution also supporting such an assignment involving a sub-micron size distribution exhibiting a peak ~400 nm.

The temporal trend for OC-NIT shown in Figure 4.6(b) generally shows low particle numbers with a pronounced increase during the accumulation period. The daily trend for this particle type peaks at 07:00 with an overnight minimum being apparent. During the day the particles begin to increase again from 18:00 leading to another peak time at 23:00 (Figure 4.7(b)). Fossil fuel combustion, due to heating with some influence from traffic, is the likely source of this particle type judging by the observable daily trend. However this particle type is mainly present during the accumulation period when the daily trend may not be as pronounced.

K-SUL

This particle type contains *m/z* peaks: 12 $[C]^+$, 23 $[Na]^+$, 27 $[C_2H_3]^+$, 36 $[C_3]^+$, 39 $[K]^+$, 41 $[K]^+$, 43 $[C_2H_3O]^+$, 48 $[C_4]^+$, 60 $[C_5]^+$ in the positive ion mass spectrum and 24 $[C_2]^-$ 26 $[CN]^-$, 36 $[C_3]^-$, 42 $[CNO]^-$ 46 $[NO_2]^-$, 62 $[NO_3]^-$, 73 $[C_6H]^-$ /$[CH_3CH_2CHOO]^-$, 80$[SO_3]^-$, 97 $[HSO_4]^-$ in the negative ion mass spectrum. As shown in Figure 4.4(h), the sulfate peaks have much greater intensity than nitrate and this, along with the presence of potassium, leads to the K-SUL classification. The particle type is likely due to combustion sources and has a size distribution peaking around 600 nm. K-SUL is similar to a particle type detected in London and attributed to nitrate-sulfate containing particles originating from long range transport which undergo evaporation of nitrate during daylight hours (Dall'Osto et al., 2009). The daily trend of this particle type in the SAPUSS campaign shown in Figure 4.7(b) may support this hypothesis as it reaches a maximum at 12:00 as the light intensity (for nitrate photolysis) and temperature (for nitrate evaporation) increases. The numbers of this particle type then decreases overnight as the temperature decreases and nitrate condensation can occur.

The temporal profile of this particle type is shown in Figure 4.6(b), which indicates that low counts were detected prior to the European air mass event. The appearance of this peak during the European air mass period suggests that K-SUL is transported into the city, similar to that observed for the same particle type in London (Dall'Osto et al, 2009).

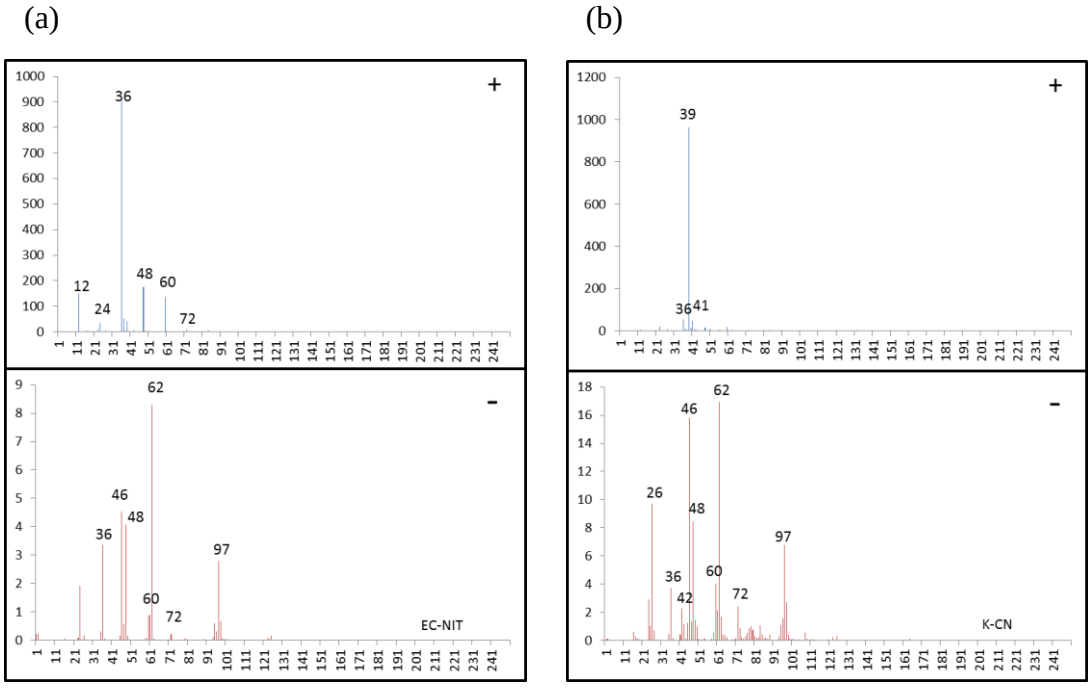

Figure 4.5 Average dual ion mass spectra for (a) EC-NIT, (b) K-CN, (c) K-EC, (d) Fresh/Local EC, (e) Aged/Transported Biomass, (f) Oxidised OC, (g) OC-NIT, (h) K-SUL with the relative ion intensity shown on the *y*-axis and *m/z* shown on the *x*-axis.

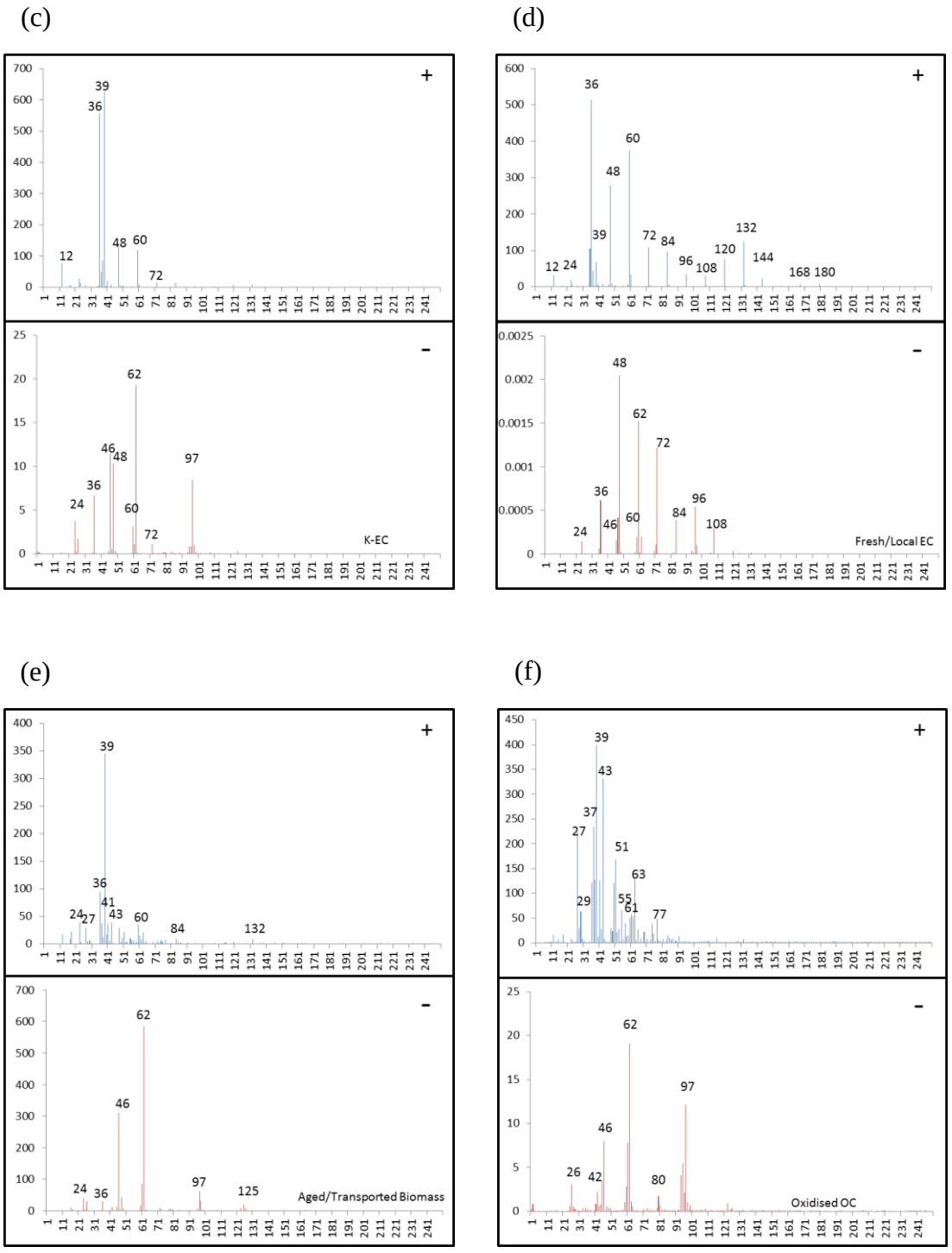

Figure 4.6 Average dual ion mass spectra for (a) EC-NIT, (b) K-CN, (c) K-EC, (d) Fresh/Local EC, (e) Aged/Transported Biomass, (f) Oxidised OC, (g) OC-NIT, (h) K-SUL with the relative ion intensity shown on the *y*-axis and *m/z* shown on the *x*-axis.

(g) (h)

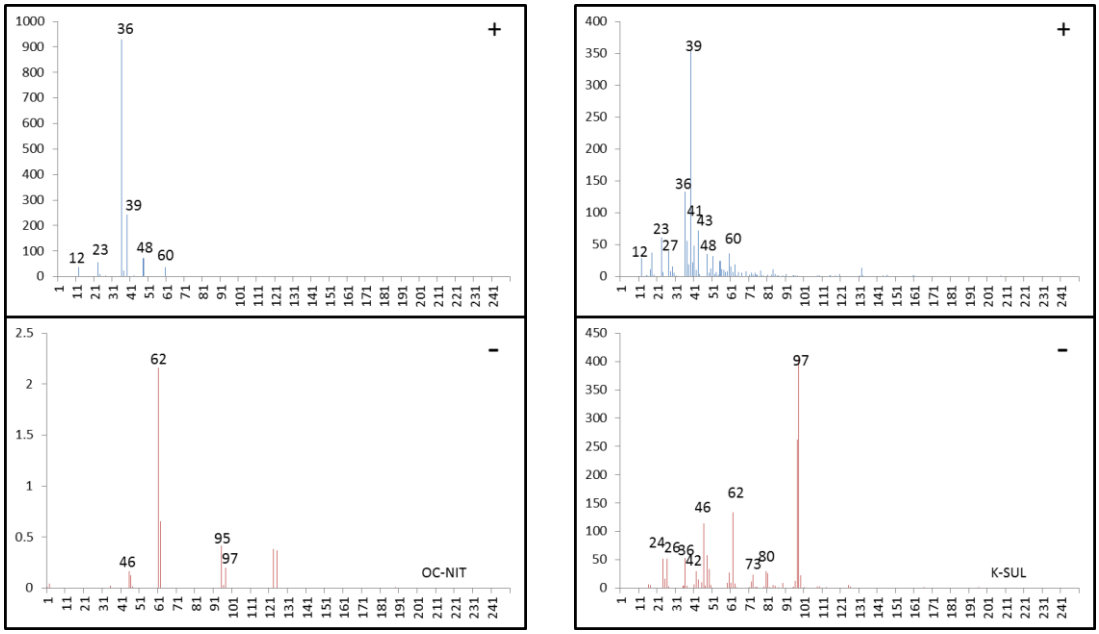

Figure 4.7 Average dual ion mass spectra for (a) EC-NIT, (b) K-CN, (c) K-EC, (d) Fresh/Local EC, (e) Aged/Transported Biomass, (f) Oxidised OC, (g) OC-NIT, (h) K-SUL with the relative ion intensity shown on the *y*-axis and *m/z* shown on the *x*-axis.

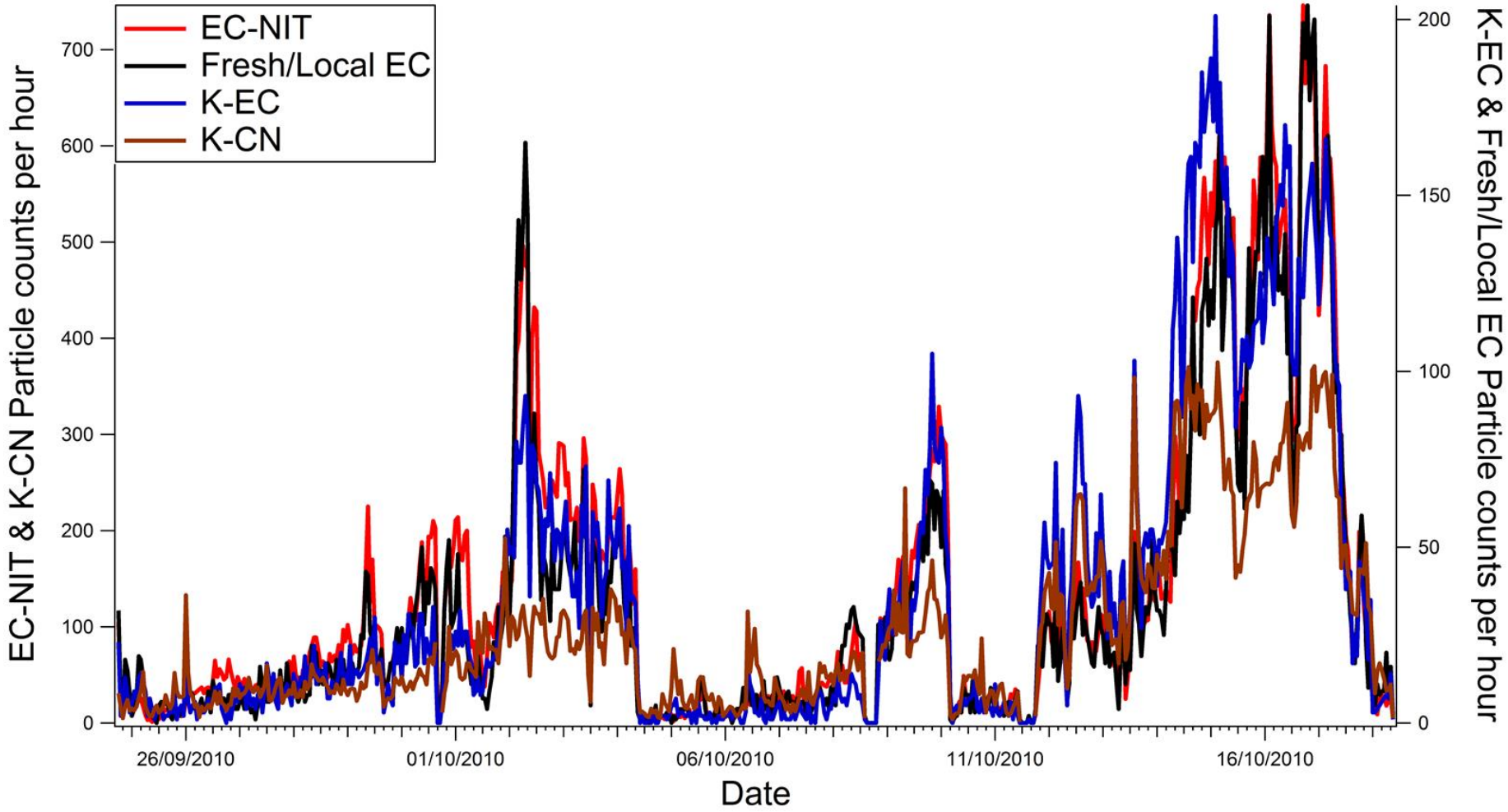

Figure 4.8(a) Temporal trend of EC-NIT, Fresh/Local EC, K-EC and K-CN particle types during the SAPUSS measurement campaign.

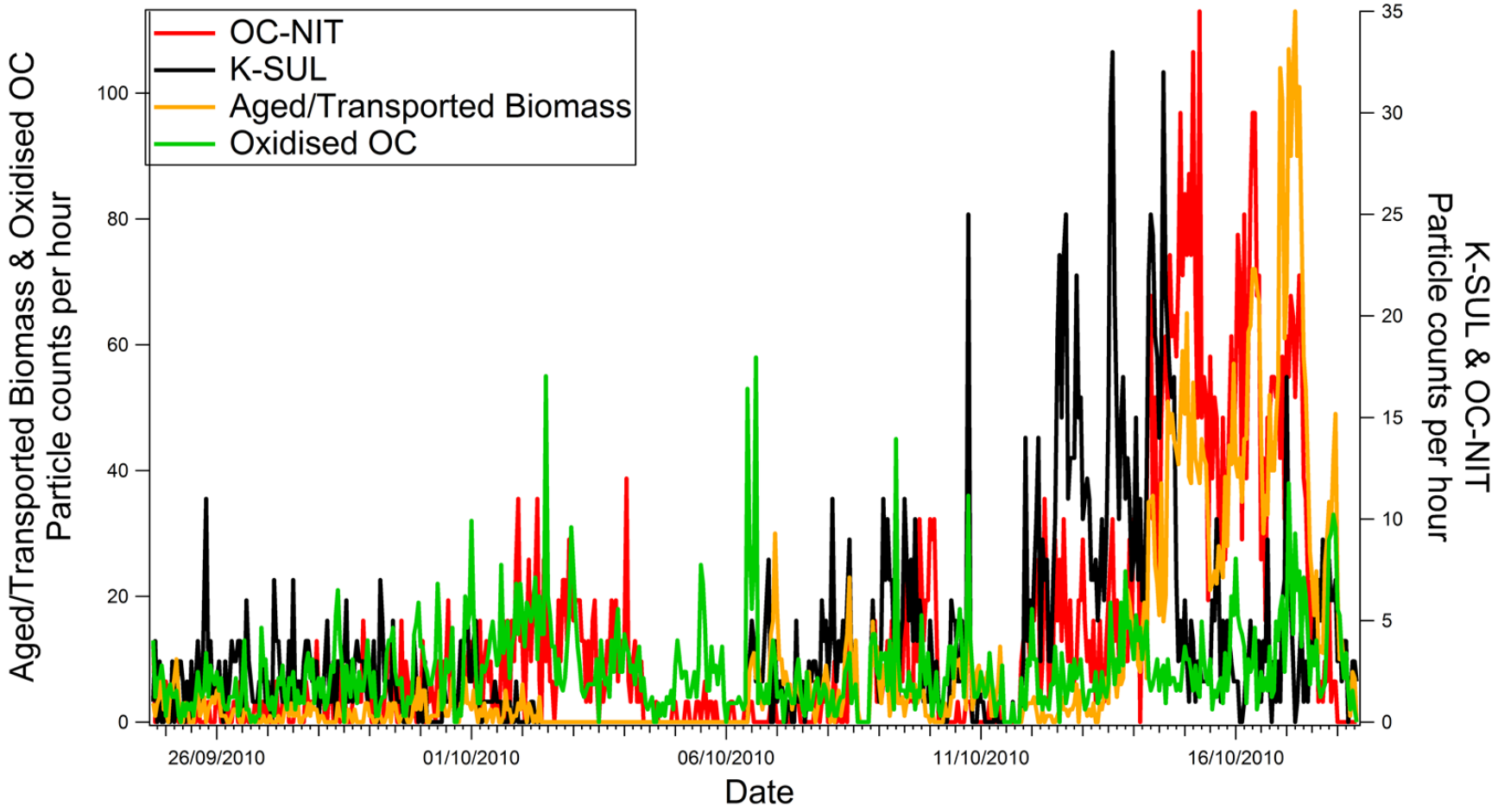

Figure 4.6(b) Temporal trend of OC-NIT, K-SUL, Aged/Transported Biomass and Oxidised OC particle types during the SAPUSS measurement campaign.

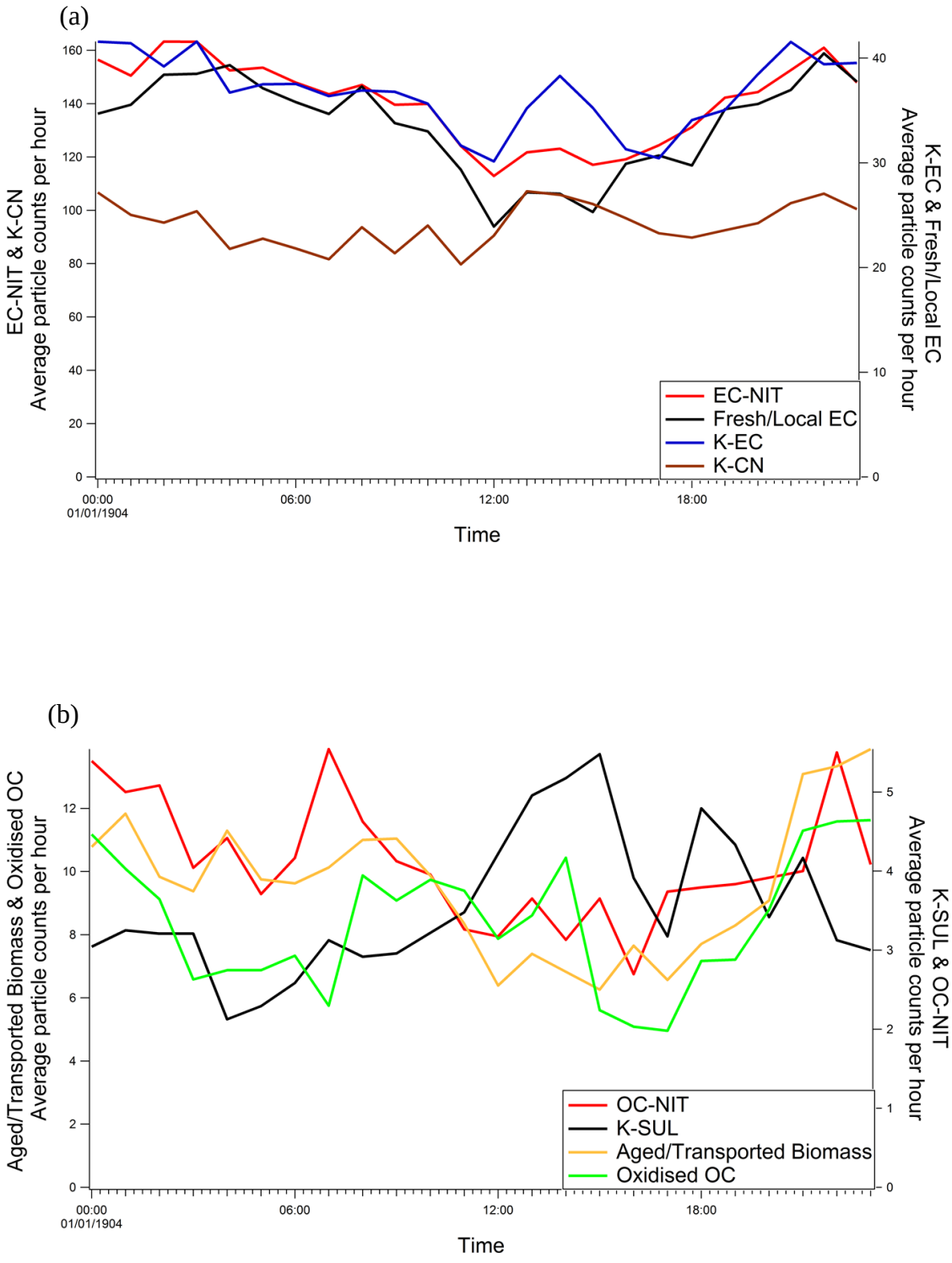

Figure 4.9 Daily trends of; (a) EC-NIT, Fresh/Local EC, K-EC and K-CN; (b) OC-NIT, K-SUL, Aged/Transported Biomass and Oxidised OC particle types during the SAPUSS measurement campaign.

4.3.1.2 Sea-salt

Sea-salt

The particle class identified as sea-salt represented 15.3% (43288) of the particles classified at the UB site during the campaign. This average mass spectrum for this particle type shown in Figure 4.8(a) contains the *m/z* peaks: 23 $[Na]^+$, 24 $[Mg]^+$, 39 $[K]^+$, 41 $[K]^+$, 63 $[Na_2OH]^+$, 81 $[NaCl_2]^+$ in the positive ion mass spectrum and 24 $[C_2]^+$ 35 $[Cl]^-$, 37 $[Cl]^-$, 36 $[C_3]^-$, 46 $[NO_2]^-$, 62 $[NO_3]^-$, 80$[SO_3]^-$, 97 $[HSO_4]^-$ in the negative ion mass spectrum. All of the signals in the positive ion mass spectrum are associated with sea-salt (Healy et al., 2010; Noble and Prather, 1997). The negative ion mass spectrum shows peaks for *m/z* associated with sea-salt but also nitrate and sulfate peaks indicating that these particles have been processed to some degree during transport to the measurement site. The ENCHILADA analysis did not allow the identification of different particle classes for fresh and aged sea-salt as all the clusters of sea-salt showed some degree of processing. This particle type has a bimodal size distribution with the major mode peaking around 1.1 µm and a smaller mode around 2.1-2.2 µm.

The daily trend for the sea-salt particle type (Figure 4.10) shows a peak in particle number at midday, likely associated with the sea breeze carrying air from the sea across the city and into the greater Barcelona region (Moreno, 2011). The wind rose for this particle type also shows a clear influence from the direction of the Mediterranean. Figure 4.9 shows the Sea-salt particle number peaks during periods when the air masses passed over the Mediterranean Sea (7-10 October) or Atlantic Ocean (5-6 October).

Na-EC

The average mass spectrum for the Na-EC particle type is shown in Figure 4.8(b) and contains peaks 12 $[C]^+$, 23 $[Na]^+$, 24 $[C_2]^+$ $[Mg]^+$, 36 $[C_3]^+$, 39 $[K]^+$, 60 $[C_5]^+$ in the positive ion mass spectrum and 24 $[C_2]^-$, 36 $[C_3]^-$, 46 $[NO_2]^-$, 48 $[C_4]^-$, 60 $[C_5]^-$, 62 $[NO_3]^-$, 72 $[C_6]^-$, 97 $[HSO_4]^-$ in the negative ion mass spectrum. The reason for the designation of this particle type as Na-EC is due to the intensity of the peak for sodium evident in the average mass spectrum. Previously Na-EC particle types have been identified as industrial emissions from incineration or refuse burning (Moffet et

al., 2008a). The daily profile for Na-EC is shown in Figure 4.10 exhibits a noticeable drop in particle number from 12:00 to 20:00. Although industrial emissions are a possible source of this particle type, they are much larger than typical combustion particles, with a bimodal distribution peaking around 1.2 µm and 1.8 µm. The Na-EC particles also increased in number during periods when the air masses arriving at the measurement site had travelled across the sea in a manner similar to the Sea-salt particle type (Figure 4.9). The match in temporal profile with Sea-salt suggests that the Na-EC particle could be due to a carbonaceous coating on sea-salt particles. This assertion is supported by both mass spectral and particle size data.

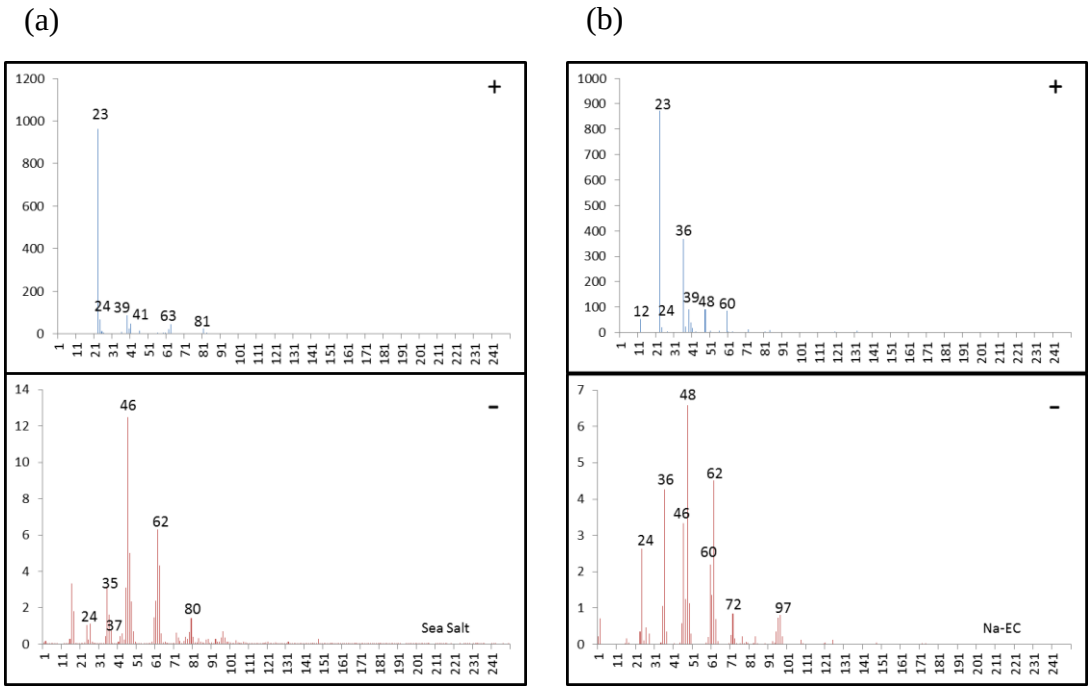

Figure 4.10 Average dual ion mass spectra for (a) Sea-salt and (b) Na-EC with the relative ion intensity shown on the *y*-axis and *m/z* shown on the *x*-axis.

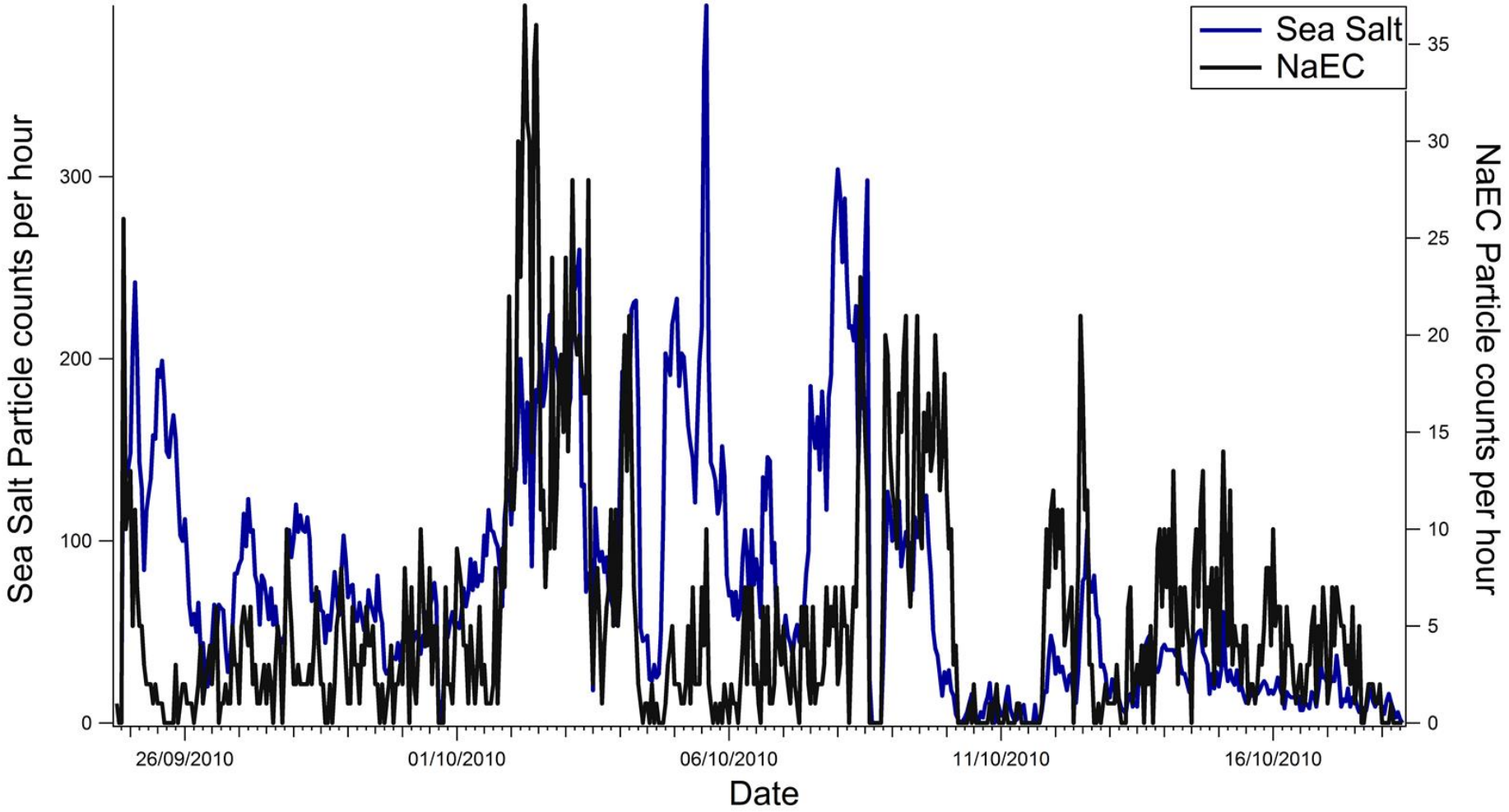

Figure 4.11 Temporal trend of Sea-salt and Na-EC particle types during the SAPUSS measurement campaign.

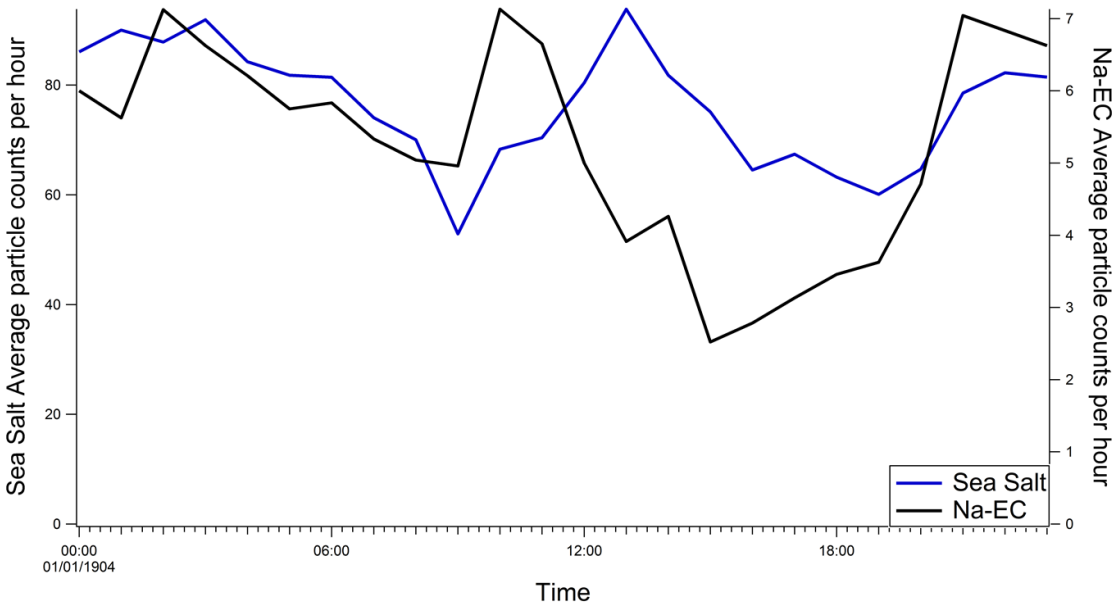

Figure 4.12 Daily trends of Sea-salt and Na-EC particle types during the SAPUSS measurement campaign.

4.3.1.3 Dust

Saharan Dust

The average mass spectrum for the particle type identified as Saharan Dust is shown in Figure 4.11(a). It comprises the peaks: 23 $[Na]^+$, 24 $[Mg]^+$, 27 $[Al]^+$, 39 $[K]^+$, 40 $[Ca]^+$, 48 $[Ti]^+$, 54 $[Fe]^+$, 56 $[Fe]^+$ $[CaO]^+$, 64 $[TiO]^+$, 206 $[Pb]^+$ in the positive ion mass spectrum and 16 $[O]^-$, 35 $[Cl]^-$, 37 $[Cl]^-$, 46 $[NO_2]^-$, 62 $[NO_3]^-$ in the negative ion mass spectrum. The size distribution is centred in the coarse mode suggesting a crustal source. The metals present in the positive ion mass spectrum have previously been associated with Saharan dust (Dall'Osto et al., 2010). The temporal trend of this particle type, as shown in Figure 4.12, indicates that there was a peak in number between 8-10 October, when a North African air mass influenced the sampling site (Dall'Osto et al., 2013a). The numbers of these particles were found to be very low during the rest of the campaign leading to this particle type being unambiguously identified as Saharan Dust.

Ca Dust

The Ca Dust particle type mass spectrum is shown in Figure 4.11(b). The average spectrum contains the peaks: 23 $[Na]^+$, 27 $[Al]^+$, 39 $[K]^+$, 40 $[Ca]^+$, 56 $[Fe]^+$ $[CaO]^+$, 96 $[Ca_2O]^+$ in the positive ion mass spectrum and 46 $[NO_2]^-$, 62 $[NO_3]^-$, 63 $[PO_2]^-$, 79 $[PO_3]^-$, 98 $[SO_4]^-$ in the negative ion mass spectrum. This particle type was seen mainly in the coarse mode and was present up to the limiting size of the sampling inlet, which suggests a crustal source. The identification of this particle type as Ca Dust is based on the presence of a very strong Ca signal at *m/z* 40 along with other Ca species in the positive ion mass spectrum at 56 and 96. The presence of phosphate fragments in the negative ion mass spectrum also suggests a crustal source (Dall'Osto et al., 2010). The temporal trend of the particle type is shown in Figure 4.12 and indicates that it is present throughout the campaign, although peaking during the North African air mass event suggesting that it is also present in the Saharan dust. The particle type was also observed in greater number during the North African (West) air mass period of 3-4 October although there was no peak in the Saharan Dust class at this time. This suggests that the Ca Dust particle type contains a large contribution to its particle numbers from Saharan dust along with local crustal sources.

Dust

The Dust particle type mass spectrum is shown in Figure 4.11(c), and contains the peaks: 23 $[Na]^+$, 27 $[Al]^+$, 39 $[K]^+$, 40 $[Ca]^+$, 56 $[Fe]^+$ $[CaO]^+$, 64 $[TiO]^+$ $[Zn]^+$ in the positive ion mass spectrum. The negative ion mass spectrum for this particle type is cluttered but it does contain peaks for 17 $[OH]^-$, 63 $[PO_2]^-$, 79 $[PO_3]^-$, 98 $[SO_4]^-$ alongside nitrate and sulfate contributions that are indistinct, possibly due to mis-calibration or because this particle type likely represents many crustal sources. The dust particle type was observed throughout the campaign suggesting a contribution from local crustal sources. The particle sizes are in the coarse mode, and extend up to the limit of the inlet. The size distribution shows distinct modes suggesting that this particle type originates from several crustal sources.

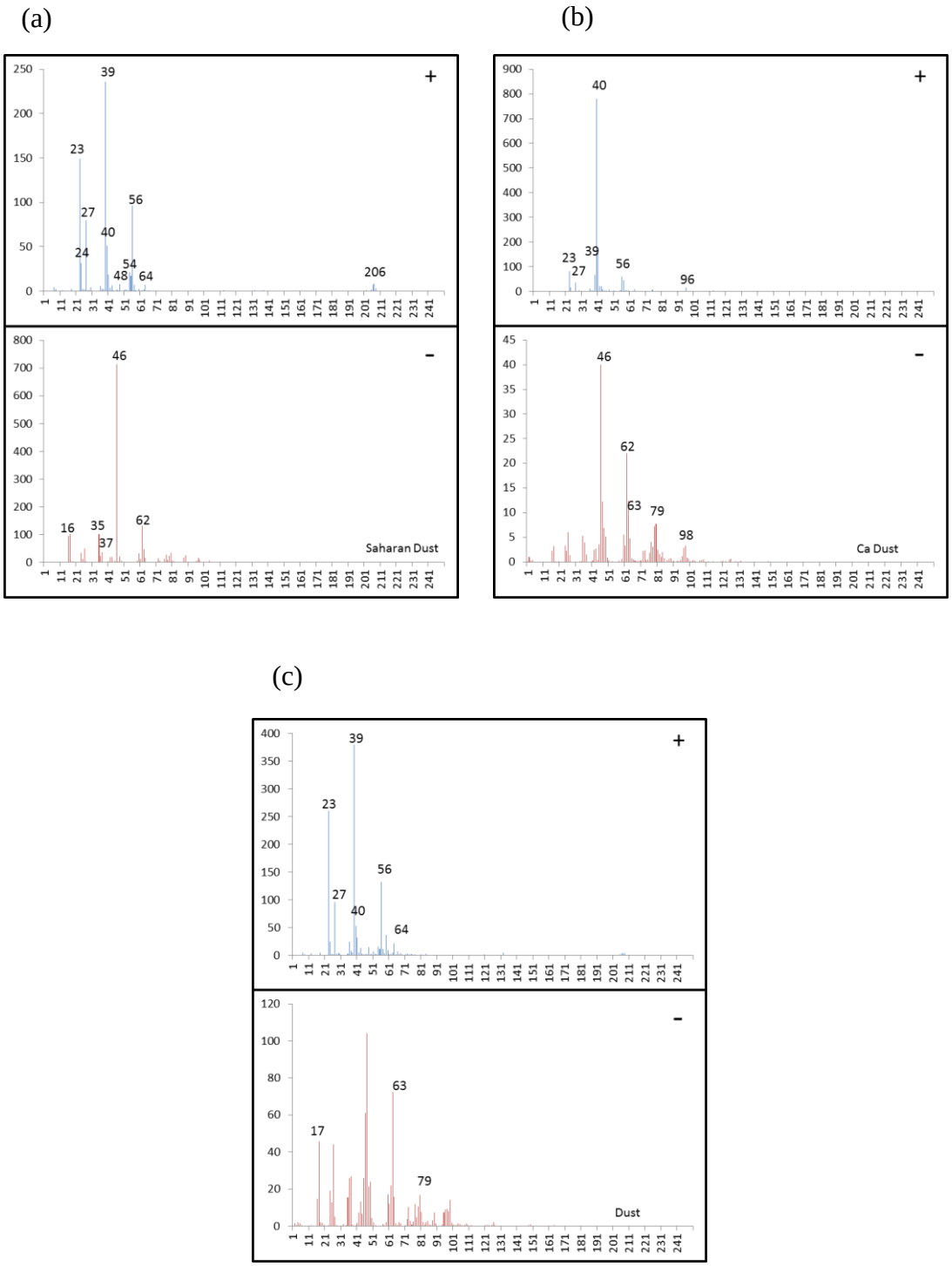

Figure 4.13 Average dual ion mass spectra for (a) Saharan Dust, (b) Ca Dust and (c) Dust with the relative ion intensity shown on the *y*-axis and *m/z* shown on the *x*-axis.

.

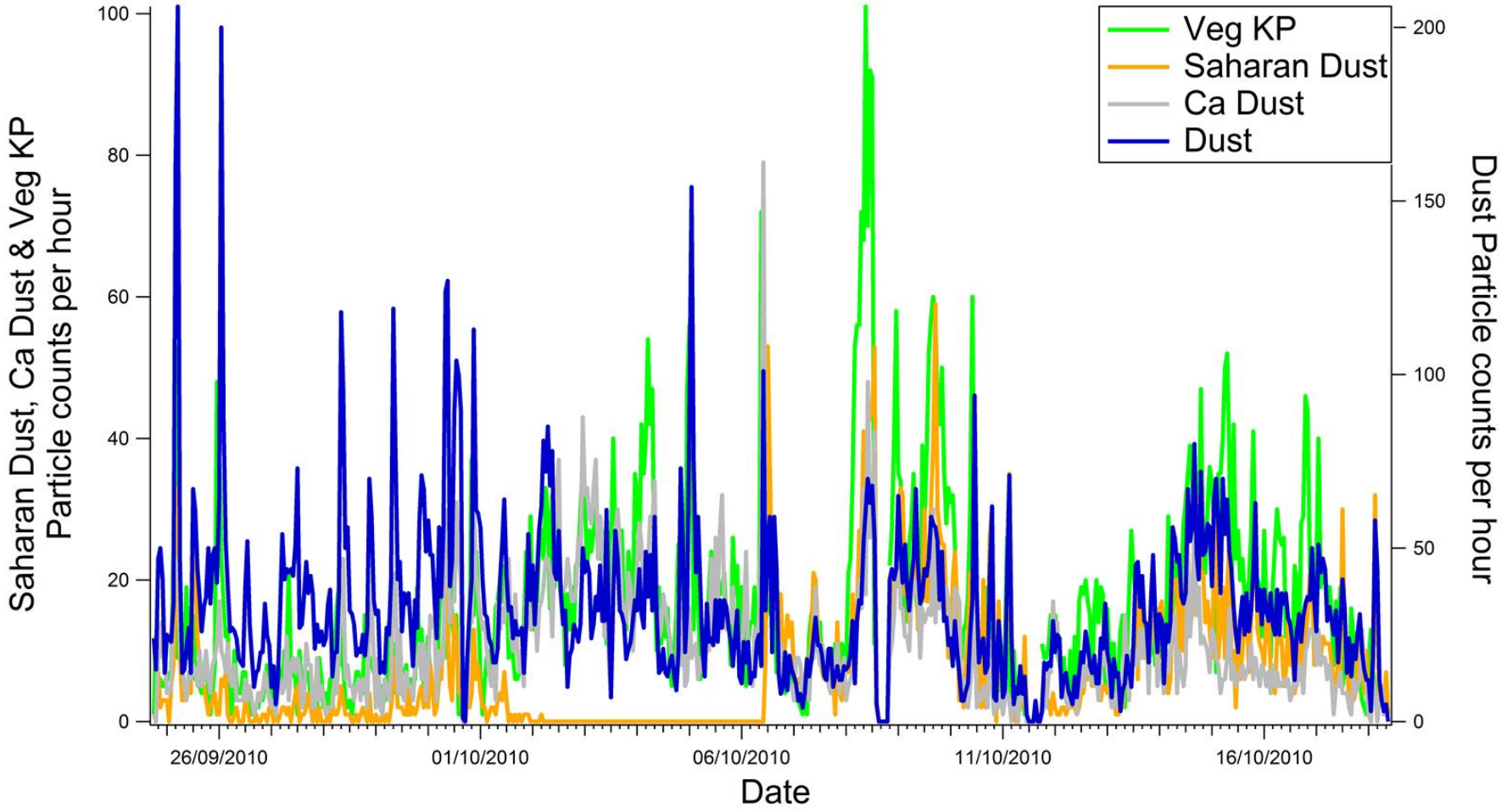

Figure 4.14 Temporal trend of Saharan Dust, Ca Dust and Dust particle types during the SAPUSS measurement campaign (Veg-KP included for comparison purposes).

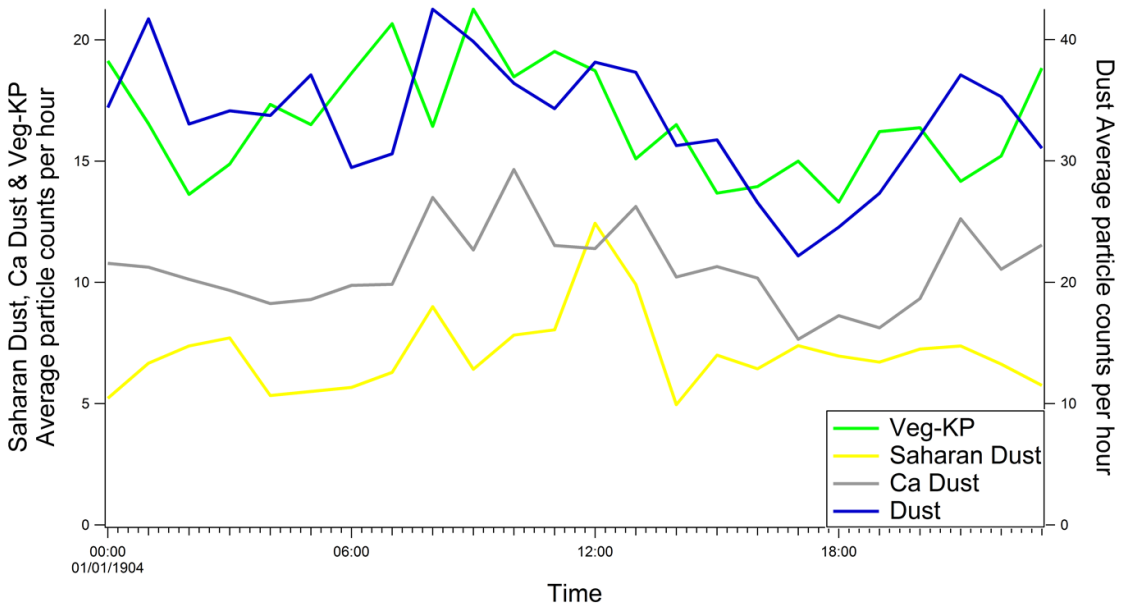

Figure 4.15 Daily trends of Saharan Dust, Ca Dust and Dust particle types during the SAPUSS measurement campaign (Veg-KP included for comparison purposes).

4.3.1.4 Vegetative

Veg-KP

This particle type contains the *m/z* peaks: 23 $[Na]^+$, 27 $[Al]^+$, 39 $[K]^+$, 41 $[K]^+$, 56 $[Fe]^+$ in the positive ion mass spectrum and 26 $[CN]^-$, 35 $[Cl]^-$, 42 $[CNO]^-$, 46 $[NO_2]^-$, 62 $[NO_3]^-$, 63 $[PO_2]^-$, 79 $[PO_3]^-$, 97 $[HSO_4]^-$ in the negative ion mass spectrum. The particle type contains very strong phosphate peaks as shown in Figure 4.14. Vegetative particle (spores) mass spectra contain similar peaks (K, Na, CN, CNO and phosphate fragments) (Fergenson et al., 2004). Figure 4.12 shows that this particle type occurs during the Saharan dust period when the sampling site was under the influence of a North African (East) air mass. Culturable, bioaerosol-based bacteria and fungi have previously been detected during Saharan dust intrusions (Prospero et al., 2005), while aerosolised microorganisms and pollen have also been found in Saharan dust (Kellogg and Griffin, 2006). These studies therefore support the designation made here for the Veg-KP particle type to originate from vegetative sources associated with Saharan dust intrusions during the campaign. Finally, it should be noted that the Veg-KP particle type presents a very similar average mass

spectrum to the K-CN type discussed above. K-means analysis was unable to differentiate the particle types and they had to be separated on the basis of their measured size distributions, which are noticeably larger for Veg-KP (see Appendix).

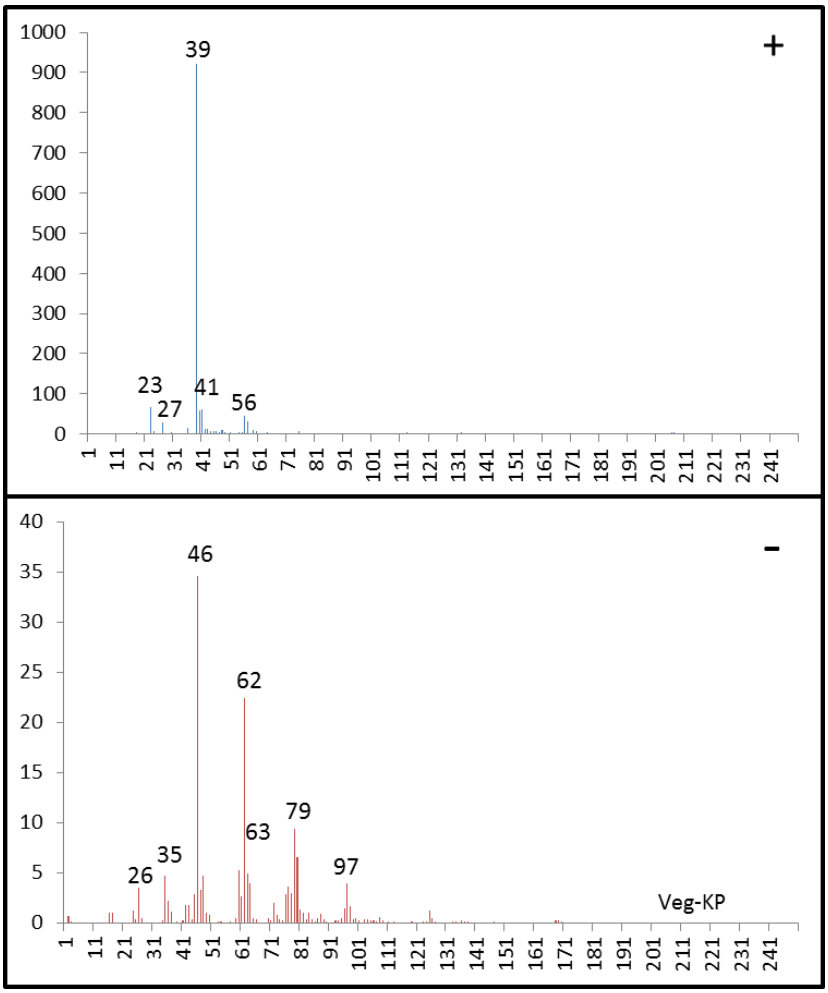

Figure 4.16 Average dual ion mass spectrum of the Veg-KP particle type with the relative ion intensity shown on the *y*-axis and *m/z* shown on the *x*-axis.

4.3.1.5 Heavy Oil Combustion

Oil V

The Oil-V particle type contains peaks for: 36 $[C]^+$, 51 $[V]^+$, 56 $[Fe]^+$, 58 $[Ni]^+$, 67 $[VO]^+$ in the positive ion mass spectrum and 36 $[C]^-$, 46 $[NO_2]^-$, 48 $[C_4]^-$, 62 $[NO_3]^-$,

72 $[C_6]^-$, 95 $[CH_3SO_3]$, 97 $[HSO_4]^-$ in the negative ion mass spectrum. This particle type has previously been attributed to heavy oil combustion in California (Pastor et al., 2003) and Baltimore (Lake et al., 2004) and more specifically as shipping-related emissions in Cork (Healy et al., 2009). In the latter study it was found that the shipping particle type contained high levels of sulfate in the negative mass spectrum and no contribution from nitrate. This was explained by the fact that sampling was performed very close to the shipping berths, thus limiting time for uptake of nitrate via atmospheric processing. In contrast, the Oil V particles observed during SAPUSS also contained a large contribution from nitrate along with sulfate, indicating that they were processed during transport from the source to the sampling site. The particle size supports the designation of a combustion source with the size distribution peaking around 300-350 nm. The wind rose for this particle type does show dependence on the direction of the port, however this sector also contains the city itself and large industrial areas near the port. For these reasons this particle type is attributed to general heavy oil combustion but not specifically due to shipping activity. The Oil V particle type peaks in number on 3-4 October (Figure 4.16) during the North African (West) air mass. During this period, the air mass passes over the port area and could pick up particulate emissions from shipping and industrial activity.

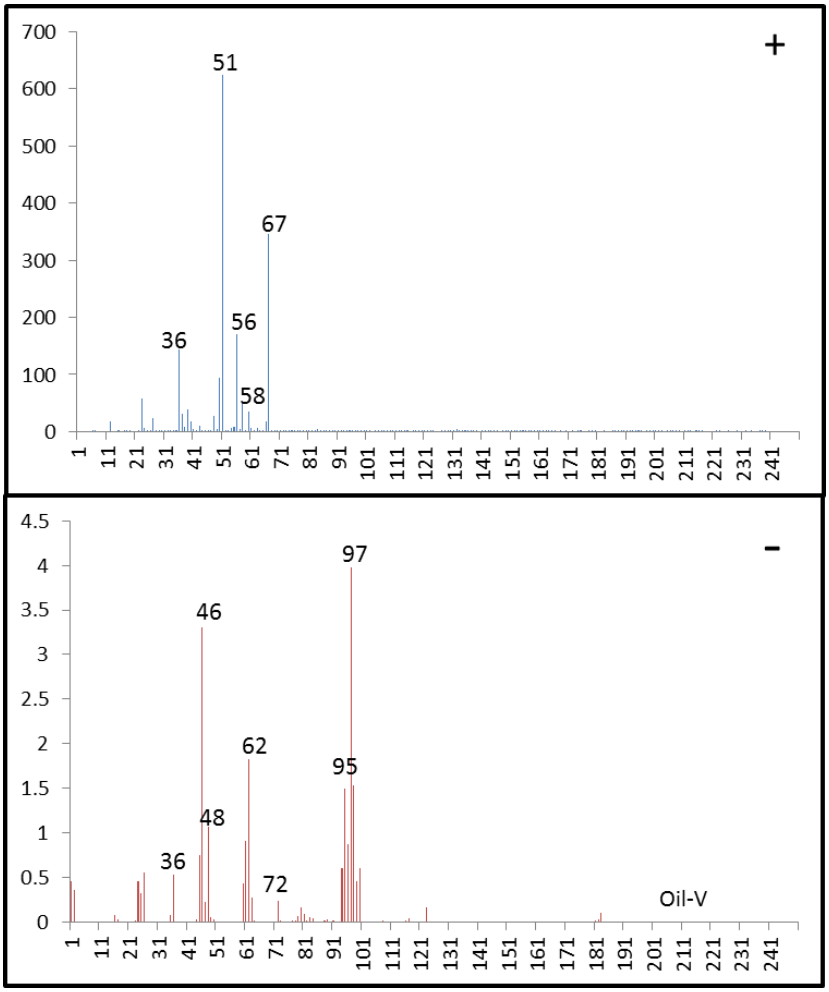

Figure 4.17 Average dual ion mass spectrum for Oil-V particle type with the relative ion intensity shown on the *y*-axis and *m/z* shown on the *x*-axis.

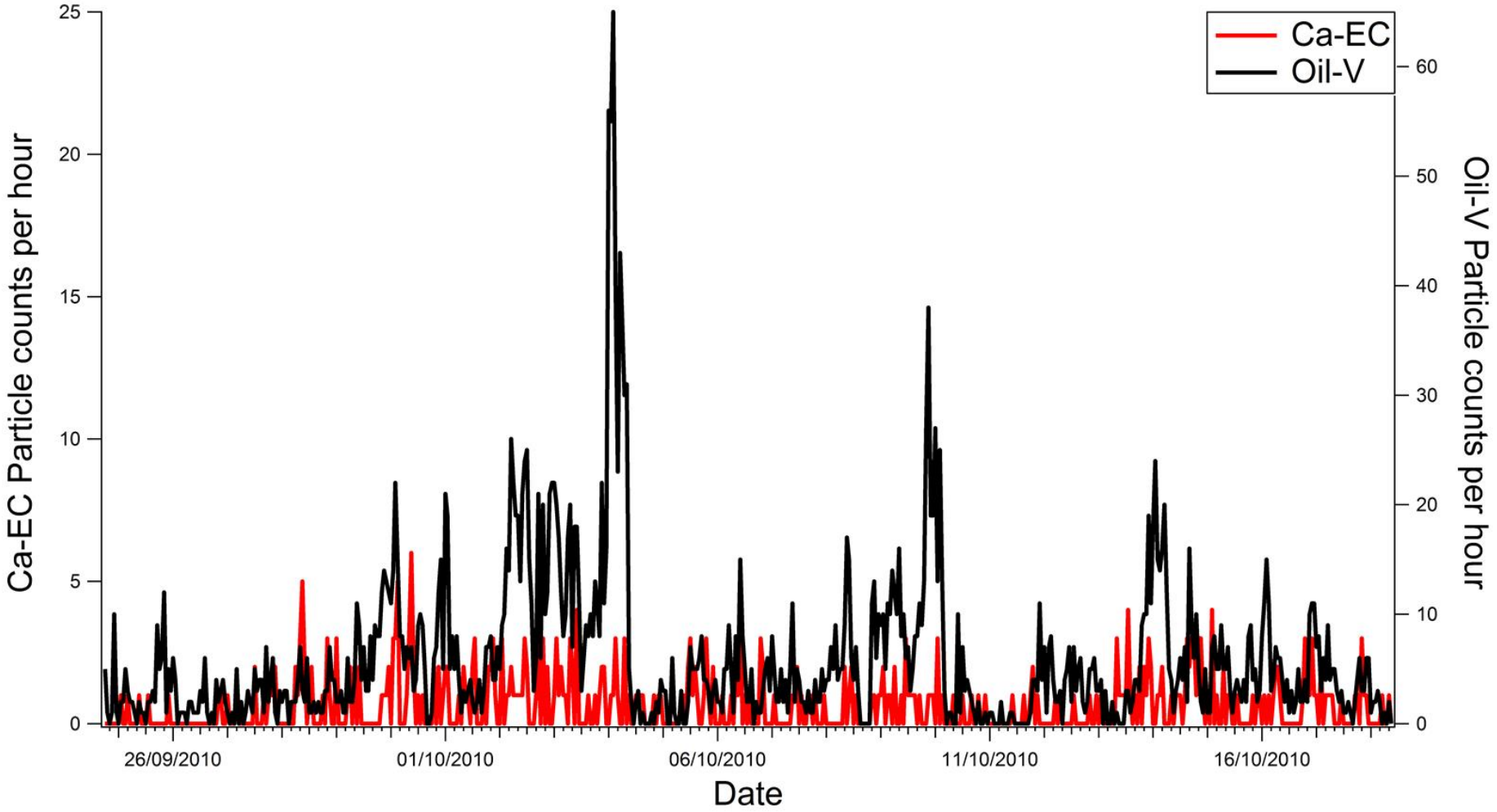

Figure 4.18 Temporal trend of Oil-V and Ca-EC particle types during the SAPUSS measurement campaign.

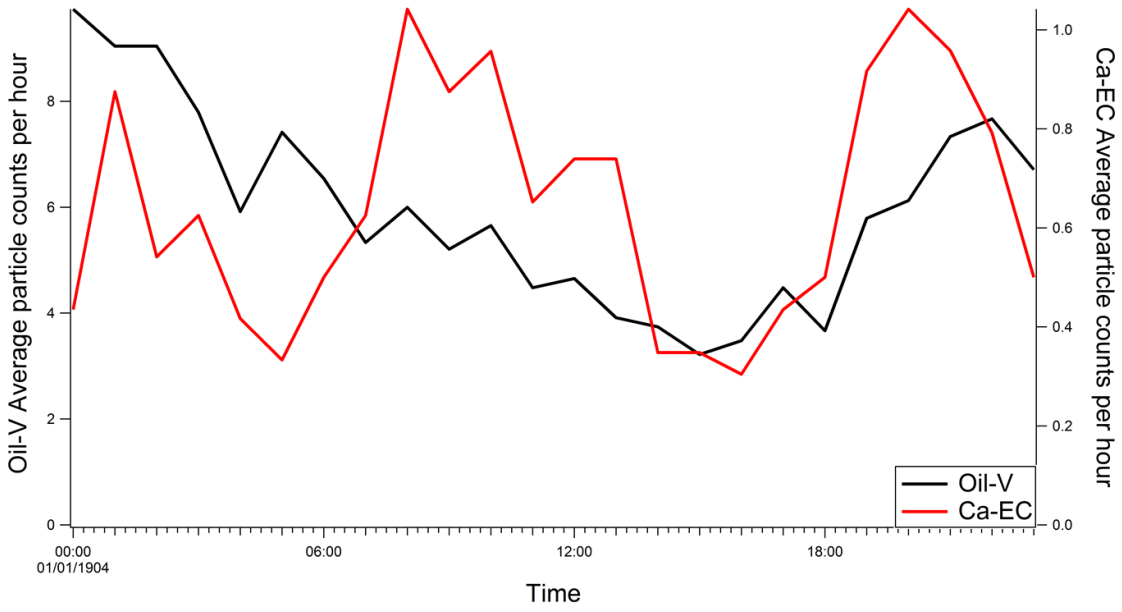

Figure 4.19 Daily trends of Oil-V and Ca-EC particle types during the SAPUSS measurement campaign.

4.3.1.6 Lubricating Oil

Ca-EC

The average mass spectrum for the Ca-EC particle type is shown in Figure 4.18 and contains peaks as follows: 12 $[C]^+$, 24 $[C_2]^+$, 36 $[C_3]^+$, 40 $[Ca]^+$, 48 $[C_4]^-$, 60 $[C_5]^+$ in the positive ion mass spectrum and 24 $[C_2]^-$, 36 $[C_3]^-$, 46 $[NO_2]^-$, 48 $[C_4]^-$, 60 $[C_5]^-$, 62 $[NO_3]^-$, 72 $[C_6]^-$, 97 $[HSO_4]^-$ in the negative ion mass spectrum. This particle type has been identified previously and is associated with vehicle emissions, particularly lubricating oil (Healy et al., 2010; Spencer et al., 2006). The number of particles monitored is low (Figure 4.16), which is unexpected due to the proximity of the sampling site to the Avenue Diagonal. On the other hand, the wind-dependence for this particle was found to be associated with the direction of the Avenue Diagonal, which supports the traffic-based identification. The daily trends are shown in Figure 4.17, which indicates major peaks in the morning and the evening during the traffic rush hour. Interestingly, a peak also appears overnight, which is unlikely due to traffic. However analysis of the size distribution shows some coarse particles to be

present in the particle type, which may represent interference from dust, thereby leading to this observation.

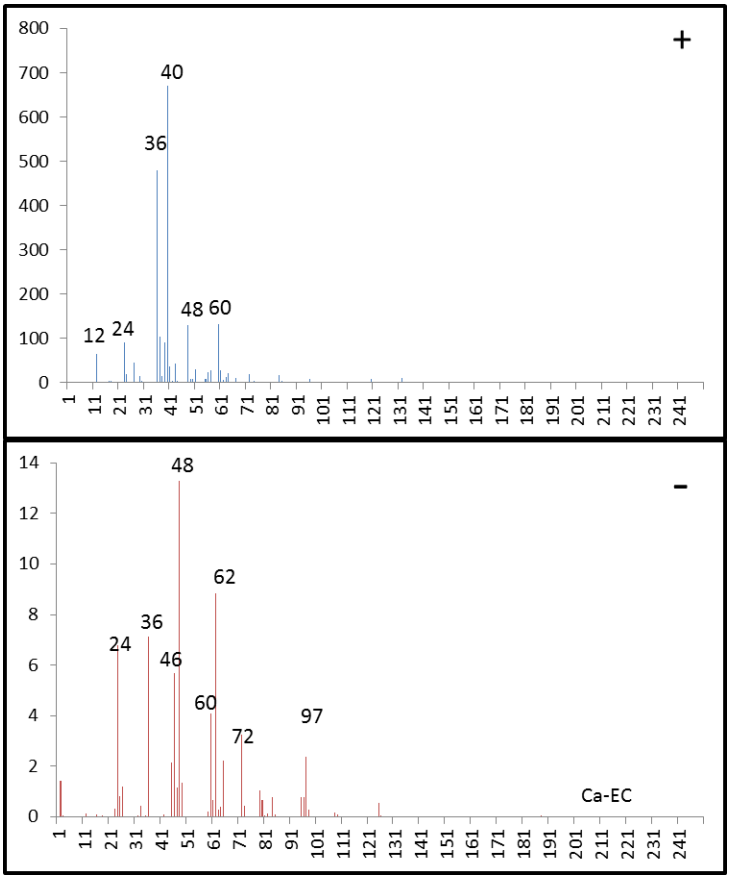

Figure 4.20 Average dual ion mass spectrum of Ca-EC particle type with the relative ion intensity shown on the *y*-axis and *m/z* shown on the *x*-axis.

4.3.1.7 Metal-Containing

Fe

The Fe particle type contains peaks for: 23 $[Na]^+$, 36 $[C_3]^+$, 39 $[K]^+$, 51 $[V]^+$, 54 $[Fe]^+$, 56 $[Fe]^+$, 67 $[VO]^+$ in the positive ion mass spectrum and 46 $[NO_2]^-$, 62 $[NO_3]^-$, 97 $[HSO_4]^-$ in the negative ion mass spectrum, Figure 4.19 (a). Particles with similar composition have previously been identified (Dall'Osto et al., 2008; Furutani et al., 2011) and attributed to industrial activities, such as steelmaking (Dall'Osto et al., 2008). Furthermore a similar Fe-containing particle has been detected and attributed to the long range transport of industrial particles (Harrison et al., 2012).

The size distribution of the Fe particle type observed in this campaign is centred in the fine mode which rules out crustal materials as the source and suggests they are of industrial origin. As shown in Figure 4.20, low numbers of the Fe particle type were observed for most of the campaign but increased at the end when the regional air mass influenced the city and stagnant conditions prevailed. This indicates that the particles probably originate from a regional source and are transported to the city during this period, although the possibility that they are produced locally and accumulate under the stagnant conditions cannot be ruled out.

Pb-Cl and Mn

These two particle types are industrial emissions that are observed together with short sharp peaks in particle number. Examination of their temporal trends (Figure 4.20) shows the co-incident nature of their detection, with $R^2 = 0.6$ which would be stronger if the relative intensities of the peaks in number during these events was consistent.

The average mass spectrum for the Pb-Cl type contains peaks as follows: 23 $[Na]^+$, 39 $[K]^+$, 55 $[Mn]^+$, 56 $[Fe]^+$, 64 $[Zn]^+$, 113 $[K_2Cl]^+$, 115 $[K_2Cl]^+$, 206 $[Pb]^+$, 207 $[Pb]^+$, 208 $[Pb]^+$ in the positive ion mass spectrum and 35 $[Cl]^-$, 46 $[NO_2]^-$, 62 $[NO_3]^-$, 80 $[SO_3]^-$, 97 $[HSO_4]^-$ in the negative ion mass spectrum, Figure 4.19 (b). This particle type has previously been detected in Mexico City and identified as incineration emissions (Moffet et al., 2008b).

The Mn particle type average mass spectrum contains peaks for: 23 $[Na]^+$, 39 $[K]^+$, 55 $[Mn]^+$, 56 $[Fe]^+$ in the positive ion mass spectrum and 16 $[O]^-$, 35 $[Cl]^-$, 46 $[NO_2]^-$, 62 $[NO_3]^-$ in the negative ion mass spectrum, Figure 4.19 (c). The largest and most distinguishing feature of the mass spectrum is the peak observed at *m/z* 55 due to Mn, which has previously been associated with industrial emissions (Prati et al., 2000).

Both particle types were shown to exhibit similar wind dependencies. The peaks in the temporal trend occur during Atlantic and Regional air masses and during the transition period. These results suggest that the local wind direction is responsible for the transport of these particles to the sampling site rather than the origins of the air mass. The point source nature of these emissions is further confirmed by the co-

incident detection of the Pb-Cl types in short sharp peaks at the other city sites monitored during the SAPUSS campaign (Dall'Osto et al. In Preparation; Dall'Osto et al., 2013c). The daily trends of these particle types are also very similar (Figure 4.21) and show an increase in particle number during night-time.

Cu

The Cu particle type was detected with very low number and it can be seen from the daily and temporal and daily trends shown in Figures 4.20 and 4.21 that this behaviour makes it difficult to determine a likely or unambiguous source. However, the particle size distribution is mainly in the fine mode, peaking around 350 nm, which is suggestive of a combustion source. It has been reported that Cu detected in Barcelona during SAPUSS originates from brake wear (Dall'Osto et al., 2013c). The results indicate that this particle source was also associated with barium, iron and zinc. The ATOFMS mass spectrum reported here contained peaks as follows: 23 $[Na]^+$, 27$[Al]^-$ 39 $[K]^+$, 51 $[V]^+$, 63 $[Cu]^+$, 65 $[Cu]^+$, 126 $[Cu_2]^+$, 128 $[Cu_2]^+$, 208 $[Pb]^+$ in the positive ion mass spectrum and 35 $[Cl]^-$, 46 $[NO_2]^-$, 48 $[C_4]^-$, 62 $[NO_3]^-$, 97 $[HSO_4]^-$ in the negative ion mass spectrum, Figure 4.19 (d). The spectrum does not contain barium or iron peaks and so this particle type is likely associated with fuel combustion or industrial emissions.

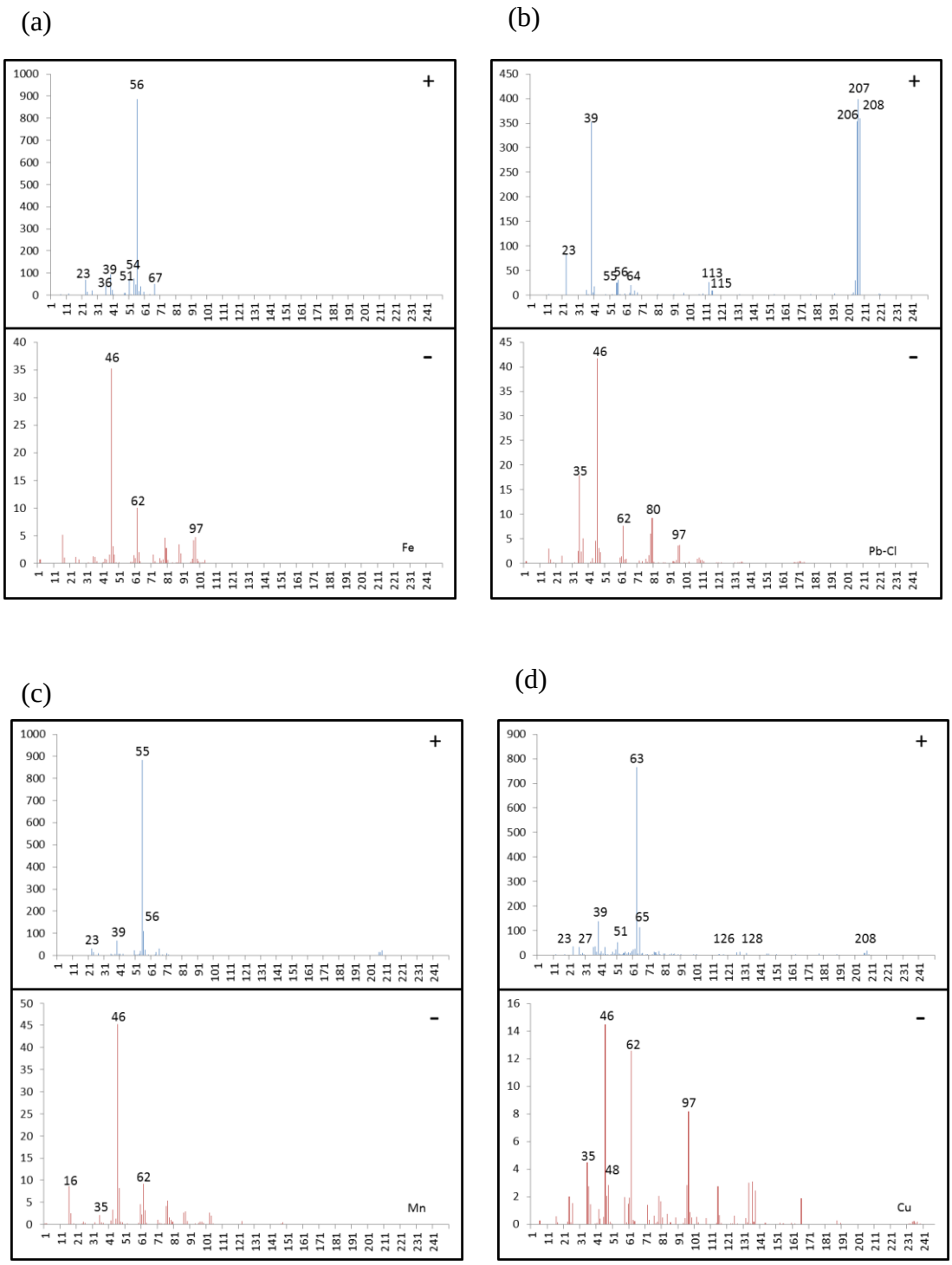

Figure 4.21 Average dual ion mass spectra for (a) Fe, (b) Pb-Cl, (c) Mn and (d) Cu with the relative ion intensity shown on the *y*-axis and *m/z* shown on the *x*-axis.

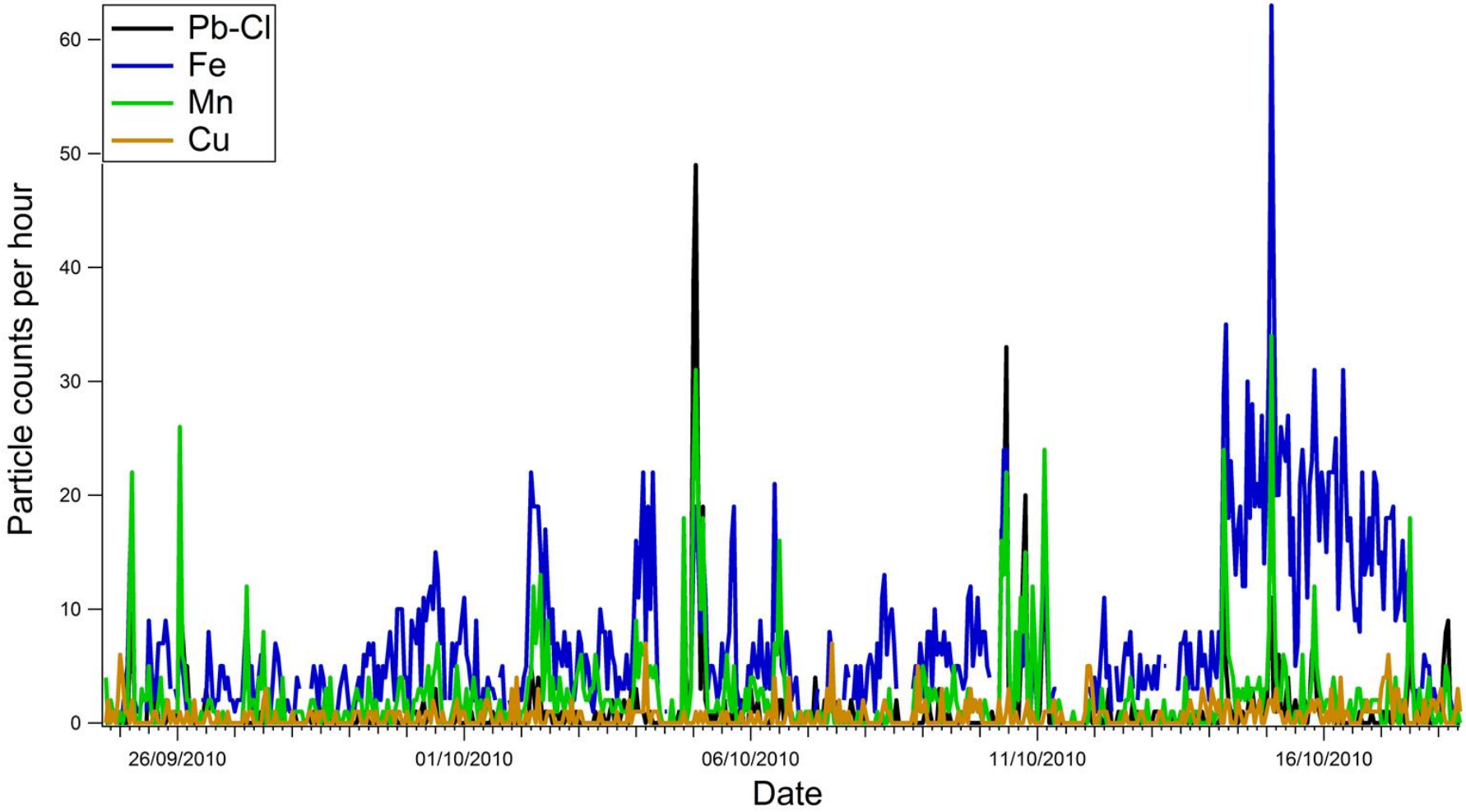

Figure 4.22 Temporal trend of Fe, Pb-Cl, Mn and Cu particle types during the SAPUSS measurement campaign.

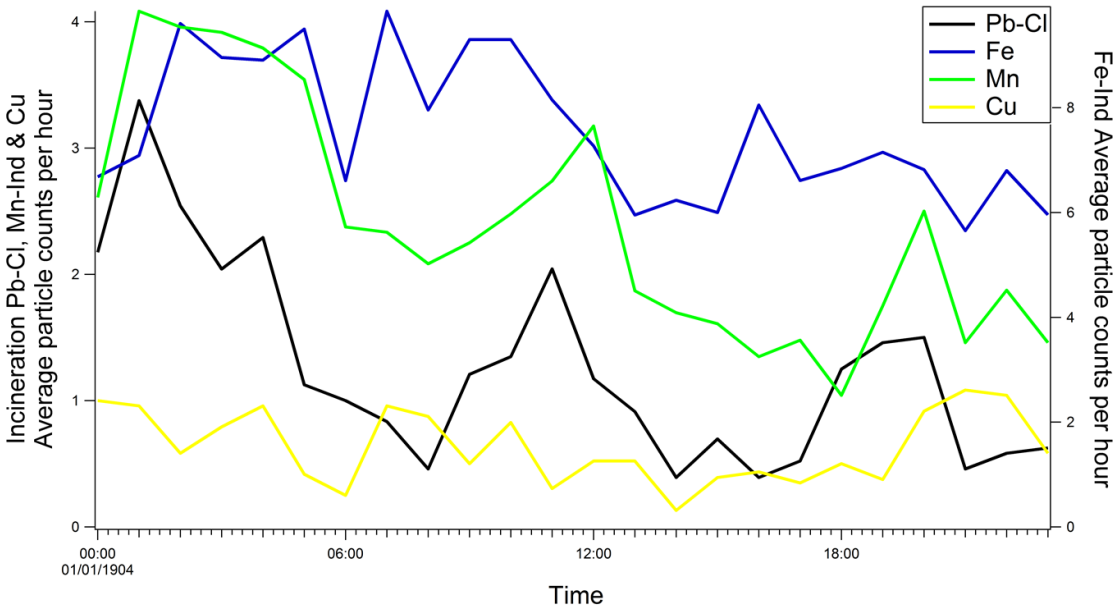

Figure 4.23 Daily trends of Fe, Pb-Cl, Mn and Cu particle types during the SAPUSS measurement campaign.

4.3.1.8 Amine

Amine 84 (ETS)

The Amine 84 (ETS) particle type mass spectrum is shown in Figure 4.22. It contains unique peaks in the positive mode due to nicotine (*m/z* 161) and its methyl-pyrrole fragment (*m/z* 84), as well as other features at 39 $[K]^+$, 51 $[C_4H_3]^+$, 58 $[C_2H_5NHCH_2]^+$. The negative ion mass spectrum is noisy and does not contain any clear peaks. This particle type has been previously detected by ATOFMS and identified as Environmental Tobacco Smoke (ETS) (Dall'Osto et al., 2007). The particles monitored in this study were found to have a sub-micron size distribution peaking around 350 nm, which suggests a combustion source. The temporal and daily trends are not useful in assisting in the identification of the source due to the low particle numbers detected (Figure 4.24 and 4.25).

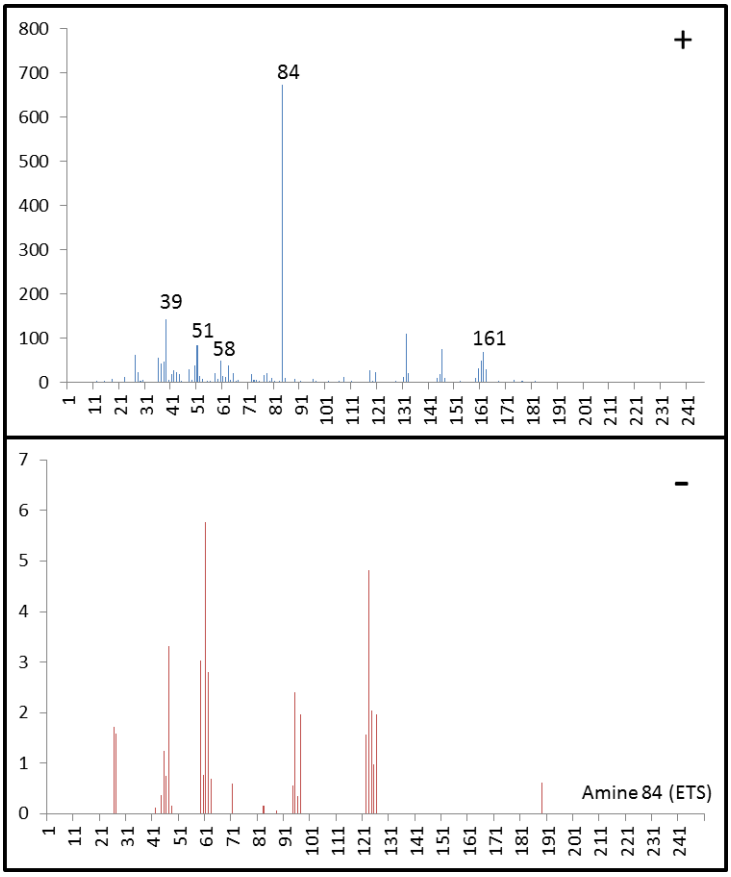

Figure 4.24 Average dual ion mass spectrum of Amine 84 (ETS) particle type with the relative ion intensity shown on the *y*-axis and *m/z* shown on the *x*-axis.

4.3.1.9 PAH

PAH

The average mass spectrum for the PAH particle type contains the following main peaks: 178^+, 189^+, 202^+, 215^+, 216^+, 220^+, 252^+ in the positive ion mass spectrum and 46 $[NO_2]^-$, 62 $[NO_3]^-$, 97 $[HSO_4]$ in the negative ion mass spectrum, which is of poor quality. Previous single particle studies have identified PAHs in ambient particles and attributed some of the signals to specific PAHs e.g., Phenanthrene and anthracene 178^+, Pyrene and fluoranthene 202^+, C3-phenanthrene 220^+, Benzopyrenes, benzofluoranthenes and perylene 252^+ (Dall'Osto et al., 2012; Gross et al., 2005; Oster et al., 2011). Only 108 PAH particles were detected during the whole measurement campaign and the particle counts are thus too low for decent

temporal trends to be established, although the daily trend does show morning and evening peaks suggesting that the particles are due to traffic emissions.

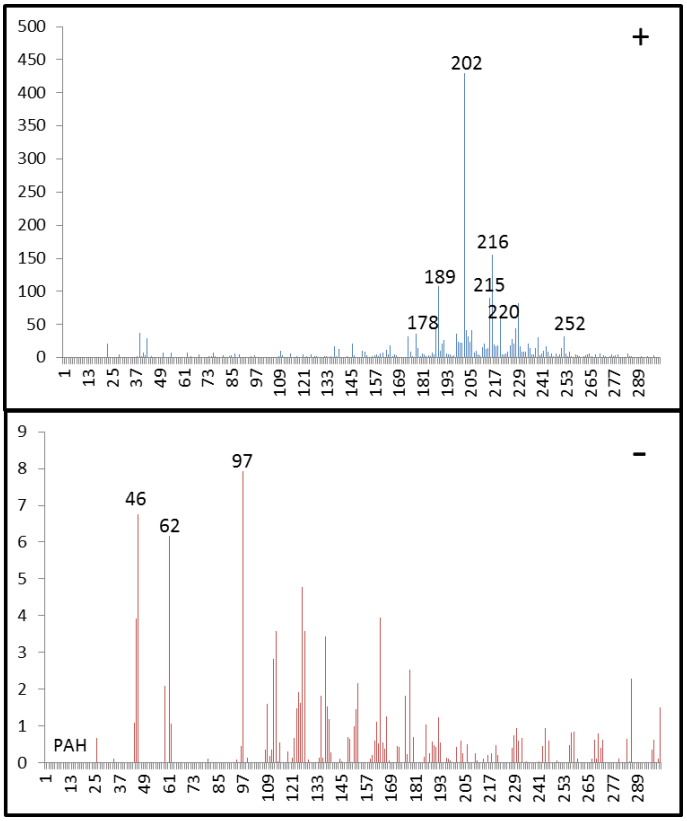

Figure 4.25 Average dual ion mass spectrum of the PAH particle type with the relative ion intensity shown on the *y*-axis and *m/z* shown on the *x*-axis.

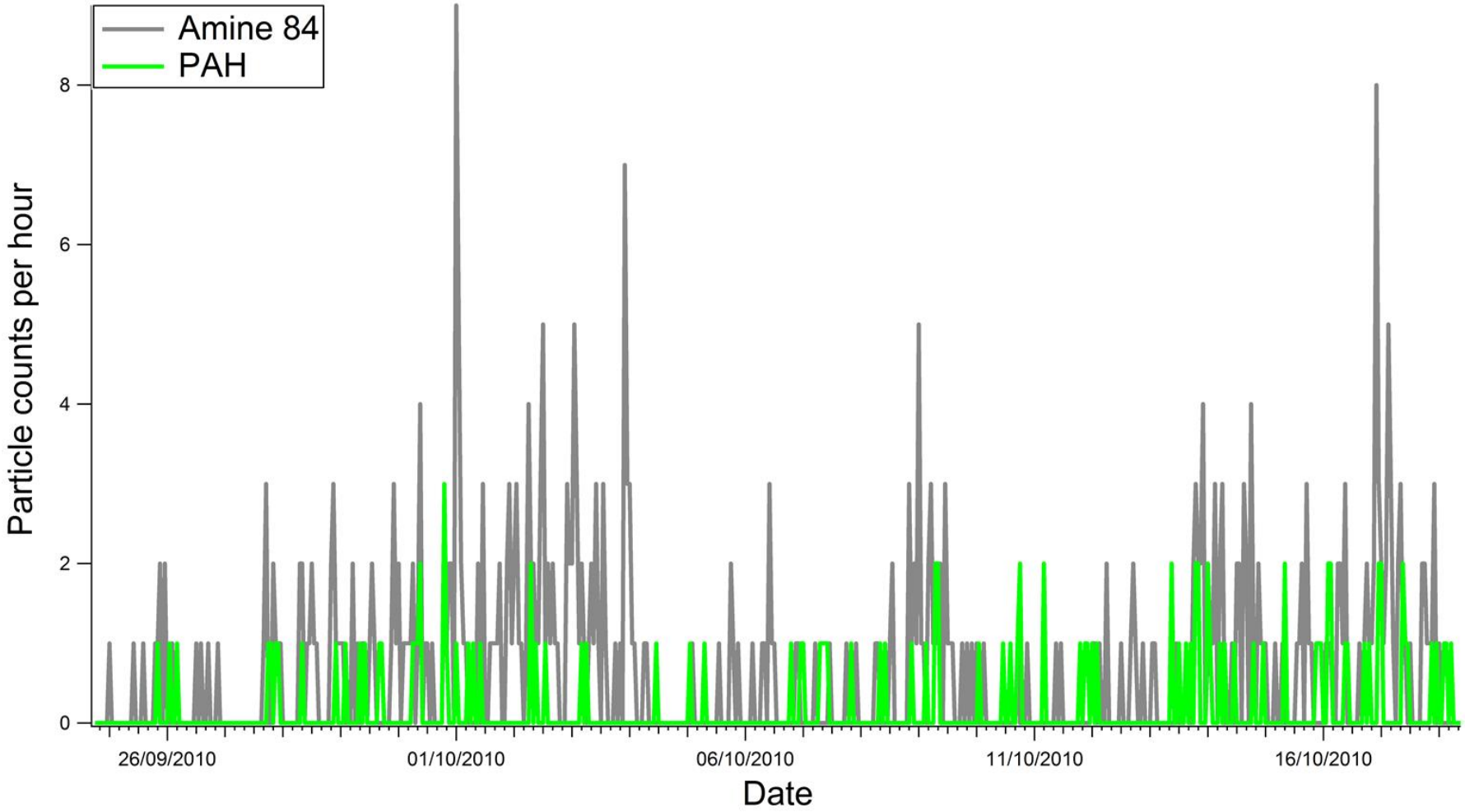

Figure 4.26 Temporal trend of Amine 84 (ETS) and PAH particle types during the SAPUSS measurement campaign.

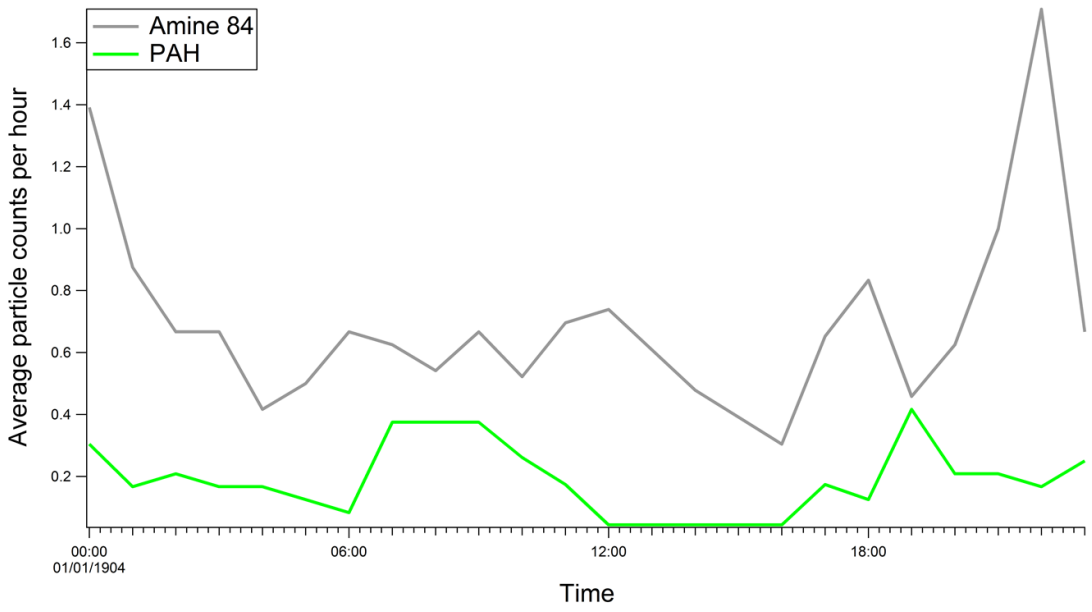

Figure 4.27 Daily trends of Amine 84 (ETS) and PAH particle types during the SAPUSS measurement campaign.

4.3.2 Comparison of ENCHILADA and YAADA

The ATOFMS data collected during the SAPUSS measurement campaign was analysed using two different techniques. Firstly, as outlined in the previous section the data was treated by using the *K*-Means algorithm in the ENCHILADA programme. However the data was also analysed by the ART-2a algorithm using the YAADA data analysis programme (Dall'Osto et al. In Preparation) to enable an inter-comparison of the two techniques to be made.

The procedures for performing the ENCILADA analysis are outlined in Section 4.3.1. For the YAADA (ART-2a) analysis, the following parameters were used: learning rate 0.05, vigilance factor 0.85, and 20 iterations (Dall'Osto et al. In Preparation). This resulted in 14 particle types being identified, which are discussed in greater detail below. A summary of the particle types detected by both analysis methods is provided in Table 4.2.

The first thing to note from Table 4.2 is that the number of particles classified using the *K*-means analysis was larger than the number classified using ART-2a. This difference is most likely due to the user input to the analysis (Giorio et al., 2012; Rebotier and Prather, 2007). For example, the user might discard clusters that may represent a very small fraction of the analysed particles, resulting in fewer particles being included in the final analysis. In Section 4.2.2 it was indicated that the total number of dual ion mass spectra collected by the ATOFMS at the UB site during the campaign was 326395, while the final number of particles classified by ENCHILADA analysis was 282117 (representing 86.4% of total particles) and 221139 (67.8% of total particles) with YAADA analysis. The reason that lower numbers of particles are classified is due to the removal of spectra that contain no discernible peaks or those which are noisy.

ENCHILADA Analysis			YAADA Analysis		
Particle Type	**Particle Number**	**%**	**Particle Type**	**Particle Number**	**%**
EC-NIT (aged EC)	79978	28.3	EC-Aged-R	76,678	35
Fresh/Local EC	19117	6.8			
K-CN	52588	18.6	EC-Aged-L	52,074	24
			K-CN	2,778	1.3
Aged/Transported Biomass	5439	1.9	LRT-NIT	9,982	4.6
K-SUL	2008	0.7	LRT-SUL	6,635	3
Sea-Salt	43288	15.3	NaCl	31,853	15
			NaCl-NIT	8,166	3.7
Saharan Dust	4009	1.4	Soil-Saharan	2,842	1.3
Ca Dust	6007	2.1	Soil-Ca	2,482	0.9
Oil-V	3388	1.2	Oil-V	1,875	0.9
Fe	3824	1.4	Fe	5,564	2.5
Pb-Cl	720	0.3	Pb	382	0.2
Veg-KP	9239	3.3	Veg-KP	3,897	1.7
K-EC	20861	7.4	Loc-NIT	15,931	7.3
Oxidised OC	4786	1.7			
OC NIT	2331	0.8			
Na-EC	2987	1.1			
Dust	18956	6.7			
Mn	1359	0.5			
Cu	362	0.1			
Ca-EC	367	0.1			
Amine 84 (ETS)	395	0.1			
PAH	108	0			
Total	**282117**	**100**	**Total**	**221,139**	**100**

Table 4.2 Particle types detected at the Urban Background site during the SAPUSS campaign determined by ENCHILADA and ART-2a.

The main reason for the difference in the number of particle types produced is that the YAADA analysis only returned 3 particle types representing less than 1% of the total number of particles classified whereas in the ENCHILADA returned 8. Such particle types represent only a small portion of the total particles detected, and therefore are of little statistical importance. However they are often retained in analyses because they may provide interesting information about chemical composition and specific sources. The lower number of particle types from the

YAADA analysis is most likely due to user inputs to the analysis and not the ART-2a algorithm, as a previous study determined that both methods gave similar results (Giorio et al., 2012). A more detailed examination of the particle types detected by YAADA shows that the ART-2a analysis did not identify the following particle types classified by the *K*-means analysis: Oxidised OC, OC-NIT, Na-EC, Dust, Mn, Cu, Ca-EC, Amine 84 (ETS) and PAH. In summary all of these particle types do not present distinct mass spectra in the ART-2a treatment.

All of the particle types detected during the campaign were compared and the correlations between them are shown in Table 4.3. It is clear that many of the more abundant particle types show strong correlations between the ENCHILADA and YAADA methods and these particle types will be discussed in detail below. Interestingly, the OC-NIT and Mn *K*-means particle classes do show some correlation with the ART-2a particle types despite not having a corresponding particle type in the ART-2a. However, it seems that these relationships are based on similar temporal trends rather than similarities in composition. For example Mn has a coincident temporality with Pb-Cl and OC-NIT is associated with several carbonaceous particle types, namely, EC-NIT, K-EC, K-CN and Fresh/Local EC. The behaviour also represents the reason for several of the carbonaceous particle types having strong correlations, as was discussed previously in Section 4.3.1.1. Nonetheless, many of the particle types detected using *K*-means correlate with the particle types classified using ART-2a analysis. These particle types exhibit similar average particle mass spectra, suggesting that they were successfully classified by both methods.

Particle classes Art-2a & ENCHILADA		Particle types determined using ART-2a (YAADA)														
		EC-AGED-L	EC-AGED-R	LRT-NIT	Loc-NIT	LRT-SUL	NaCl-NIT	NaCl	NaCl+ NaCl-NIT	Fe	Pb	K-CN	Soil-Saharan	Soil-Ca	Oil-V	Veg-KP
Particle types determined using K-means (ENCHILADA)	EC-NIT	0.79	0.98	0.75	0.65	0.01	0.05	0.02	0.03	0.43	0.00	0.48	0.02	0.00	0.03	0.02
	K-CN	0.87	0.71	0.63	0.76	0.23	0.03	0.05	0.07	0.36	0.00	0.77	0.04	0.01	0.00	0.05
	K-EC	0.89	0.85	0.66	0.70	0.11	0.05	0.04	0.05	0.44	0.00	0.66	0.02	0.00	0.01	0.03
	Fresh/Local EC	0.74	0.92	0.80	0.70	0.02	0.04	0.03	0.05	0.38	0.00	0.50	0.02	0.00	0.01	0.02
	Aged/Transported Biomass	0.48	0.50	0.85	0.90	0.02	0.01	0.09	0.08	0.25	0.00	0.46	0.02	0.04	0.01	0.04
	Oxidised OC	0.09	0.07	0.04	0.06	0.00	0.03	0.00	0.00	0.06	0.00	0.03	0.00	0.06	0.04	0.00
	OC-NIT	0.71	0.73	0.67	0.69	0.06	0.04	0.05	0.06	0.39	0.00	0.58	0.02	0.01	0.00	0.03
	K-SUL	0.12	0.02	0.01	0.10	0.74	0.00	0.08	0.04	0.01	0.00	0.35	0.07	0.07	0.02	0.04
	Sea Salt	0.02	0.04	0.10	0.11	0.05	0.24	0.83	0.88	0.00	0.01	0.12	0.04	0.21	0.08	0.00
	Na-EC	0.12	0.13	0.00	0.00	0.01	0.00	0.20	0.09	0.05	0.01	0.01	0.12	0.17	0.24	0.01
	Saharan Dust	0.06	0.06	0.05	0.22	0.06	0.08	0.03	0.00	0.14	0.02	0.16	0.50	0.05	0.00	0.52
	Ca Dust	0.06	0.03	0.01	0.00	0.01	0.00	0.27	0.21	0.12	0.00	0.01	0.07	0.61	0.22	0.01
	Dust	0.04	0.03	0.01	0.02	0.00	0.01	0.02	0.02	0.18	0.17	0.01	0.07	0.03	0.02	0.11
	Oil-V	0.11	0.10	0.00	0.00	0.00	0.02	0.11	0.06	0.13	0.01	0.00	0.01	0.27	0.91	0.00
	Fe	0.48	0.44	0.40	0.42	0.00	0.02	0.01	0.02	0.71	0.11	0.27	0.01	0.00	0.02	0.10
	Pb-Cl	0.00	0.01	0.00	0.00	0.01	0.00	0.02	0.01	0.05	0.75	0.00	0.00	0.00	0.00	0.12
	Mn	0.03	0.00	0.00	0.01	0.01	0.01	0.02	0.01	0.25	0.71	0.00	0.00	0.01	0.01	0.12
	Cu	0.05	0.04	0.05	0.07	0.00	0.00	0.00	0.00	0.03	0.00	0.05	0.01	0.00	0.01	0.01
	Veg-KP	0.16	0.12	0.04	0.08	0.01	0.00	0.07	0.06	0.14	0.01	0.07	0.28	0.05	0.09	0.13
	Ca-EC	0.04	0.05	0.01	0.01	0.00	0.01	0.01	0.00	0.05	0.00	0.01	0.00	0.10	0.03	0.00
	Ca Dust +CaEC	0.06	0.03	0.01	0.00	0.01	0.00	0.26	0.20	0.13	0.00	0.01	0.07	0.61	0.22	0.01
	Amine 84 (ETS)	0.10	0.11	0.04	0.04	0.00	0.01	0.00	0.00	0.04	0.01	0.02	0.00	0.04	0.05	0.00
	PAH	0.01	0.01	0.01	0.02	0.00	0.00	0.01	0.01	0.01	0.00	0.02	0.00	0.01	0.00	0.01

Table 4.3 Correlations (R^2) between particle types determined by ENCHILADA and ART-2a analyses. Correlations ≥ 0.9 marked in green, ≥ 0.8 marked in blue, ≥ 0.7 marked in orange and ≥ 0.5 marked in yellow**.**

Carbonaceous

K-means analysis identified 8 carbonaceous particle types, while the ART-2a only classified 6 carbonaceous types. Both methods found that the greatest contribution by number were particle types containing EC.

The *K*-means EC-NIT and ART-2a EC-Aged-R particle types presented very similar average mass spectra and were detected with a similar number by both analysis methods. The temporal trend for the particle types (Figure 4.26) shows that they are coincident, with a very high R^2 of 0.98. It is therefore very clear that the EC-NIT and EC-Aged-R particle types are identical and that the two analytical methods are in excellent agreement.

The particle type identified by *K*-means as Fresh/Local EC also shows a strong correlation with EC-Aged-R with $R^2 = 0.92$. This is not surprising since Fresh/Local EC also has a strong correlation with the EC-NIT particle type. As mentioned previously, the EC-NIT particle type is attributed to the processing of Fresh/Local EC type particles. It is also possible that some of the Fresh/Local EC particles may be included in the EC-Aged-R particle type as the level of processing present in all of the particles makes it difficult to separate the fresh, processed and aged particle classes.

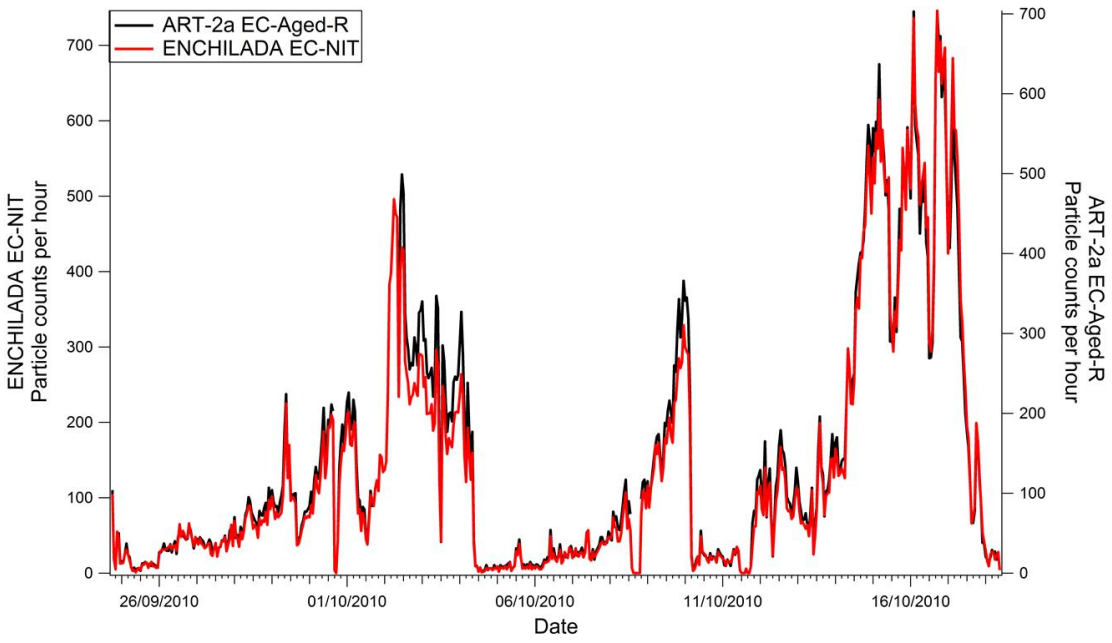

Figure 4.28 Temporal trends of EC-NIT determined by ENCHILADA and EC-Aged-R determined by ART-2a.

K-means analysis classified a particle type identified as K-CN which was found to correlate well with several ART-2a particle types. Firstly K-CN correlates with the ART-2a type also identified as K-CN, with R^2 = 0.77. The particle types also presented very similar mass spectra. However while *K*-means identified 52588 particles as K-CN, ART-2a only identified 2788. The reason for the difference may be related to the correlation between the *K*-means K-CN and other ART-2a particle types. For example, the *K*-means K-CN correlates with ART-2a EC-Aged-L with R^2 = 0.87. These two types have very similar positive mass spectra but the EC-Aged-L type presents a blank negative mass spectrum, which prevents the identification of the particle type as K-CN as the signals associated with CN are in the negative ion mass spectrum. This difference in mass spectra is likely due to the difference in the normalising procedure used by both methods. For this reason it is probable that the EC-Aged-L class contains particles that the *K*-means included in the K-CN class due to the presence of a discernable negative ion mass spectrum.

The EC-Aged-L particle type was also found to correlate well (R^2 = 0.89) with another *K*-means particle type; K-EC. Both present similar positive mass spectra

and, as discussed above, this relationship may be due to the lack of a negative mass spectrum in the EC-Aged-L preventing the attribution of the class specifically and therefore, it may contain particles identified as several specific particle types by *K*-means.

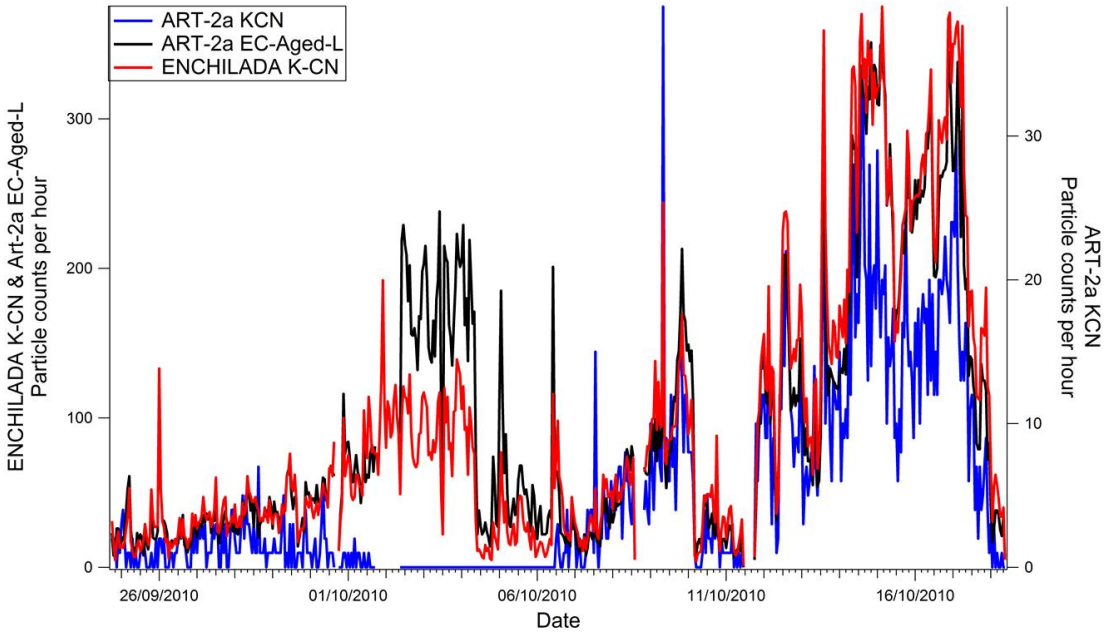

Figure 4.29 Temporal trends of K-CN determined by ENCHILADA and EC-Aged-L and K-CN determined by ART-2a.

The average mass spectrum for the ART-2a particle type classified as LRT-NIT contains the following peaks: 24 $[C_2]^+$ 27 $[C_2H_3]^+$, 36 $[C_3]^+$, 39 $[K]^+$, 48 $[C_4]^+$ 60 $[C_5]^+$, 72 $[C_6]^+$,84 $[C_7]^+$ in the positive mode and 46 $[NO_2]^-$, 62 $[NO_3]^-$, 60 $[C_5]^-$, 97 $[HSO_4]^-$ in the negative mode. The average mass spectrum is similar to the particle type identified by *K*-means as Aged/Transported Biomass and these two types exhibit a similar temporal profile (Figure 4.28), with R^2 = 0.85. Although the average particle mass spectra are not wholly similar, they were determined to be classifications of the same particles. The mass spectra differ mainly in the strength of the K^+ signal at *m/z* 39 which is dominant in the Aged/Transported Biomass but only present as a weak signal in the LRT-NIT mass spectrum. Previously Giorio et al., (2012) noted that *K*-means and ART-2a analyses sometimes presented the same

particle types with small differences in the average mass spectra. It was also found that the *K*-means appeared to produce a higher ion intensity for potassium in the data analysis. The large potassium peak in the Aged/Transported Biomass mass spectrum is the main reason for the description as biomass burning, with the presence of $[H(NO_3)]^-$ *m/z* = 125 identifying the particle as being aged or transported, This description is consistent with the label for the ART-2a class, LRT-NIT, as being the result of long-range transport of aged combustion particles.

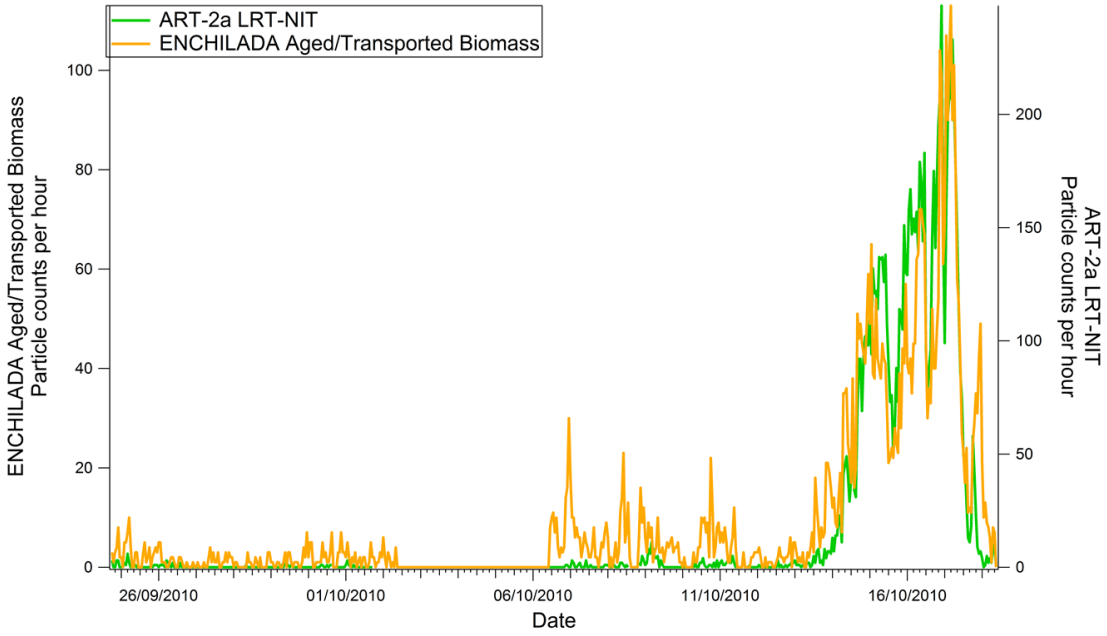

Figure 4.30 Temporal trends of Aged/Transported Biomass determined by ENCHILADA and LRT-NIT determined by ART-2a.

The K-SUL (*K*-means) and LRT SUL (ART-2a) types were found to correlate well with an $R^2 = 0.74$. The temporal trend for these two particle types is very similar and shows a large increase in number at the end of the campaign, Figure 4.29. Both particle types present very similar mass spectra with peaks for potassium, sulphate, nitrate and carbon fragments with *m/z* =97 $[HSO_4]^-$ as the dominant peak in the negative mass spectra. Despite these similarities, the number of particles classified by the two methods is quite different – with 6635 particles for LRT-SUL and 2008 for K-SUL. This discrepancy may be due to the inclusion of K-SUL particles in

other *K*-means particle types that contain potassium and sulfate in their average mass spectra. While there is a difference in the number of particles detected by both analytical methods, the similarity of the mass spectra and the correlation of the temporal trends suggest that these two classes correspond to the same particle type.

It is proposed that the LRT-SUL and LRT-NIT particle types are related (Dall'Osto et al. In Preparation), with the LRT-NIT particles undergoing loss of their nitrate coating during the day leaving the core which is composed of LRT-SUL. This suggests that the LRT-NIT particles may be associated with biomass burning emissions as the LRT-SUL contains a large potassium peak. This also supports the previous identification of Aged/Transported Biomass and LRT-NIT particle types being due to the same source.

It can be seen from Table 4.3 that the relationships between the carbonaceous particle types are complicated by the fact that each type correlates with several other carbonaceous types identified using the other method. The likely reason for this is that many of the carbonaceous particle types occur with a similar temporality. Furthermore, some of the particle types contain components associated with other types as is the case with EC-Aged-L, K-CN and K-EC.

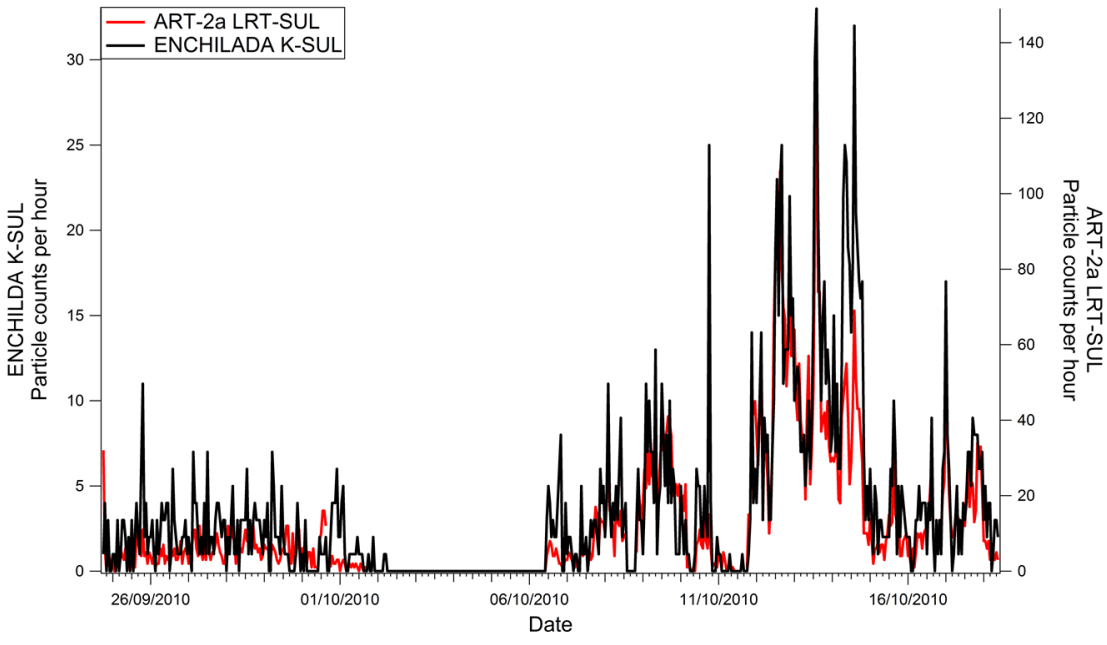

Figure 4.31 Temporal trends of K-SUL determined by ENCHILADA and LRT-SUL determined by ART-2a.

Sea-salt

Both analyses classified sea-salt particle types. *K*-means classified one particle type as Sea-salt while ART-2a detected two different particle types attributed to Sea-salt: NaCl, a particle type representing fresh sea-salt emissions and NaCl-NIT, a particle type identified as aged sea-salt with a larger contribution from nitrate signals to the average mass spectrum and diminished contribution from chloride. A correlation with R^2 = 0.88 was found when the *K*-means Sea-salt particle type was compared with the sum of the two ART-2a types. A similar number of sea-salt particles were detected by both methods with *K*-means classifying 43288 particles and ART-2a classifying 40019 particles as being associated with sea-salt. These findings suggest that both of the analysis methods detected sea-salt type particles in similar numbers during the campaign and Figure 4.30 shows that the particles were detected with a similar temporal profile. The inability of the *K*-means analysis to distinguish fresh and aged sea-salt may be due to all of the sea-salt particles being processed to some degree as they were transported from the sea across the city to the sampling site.

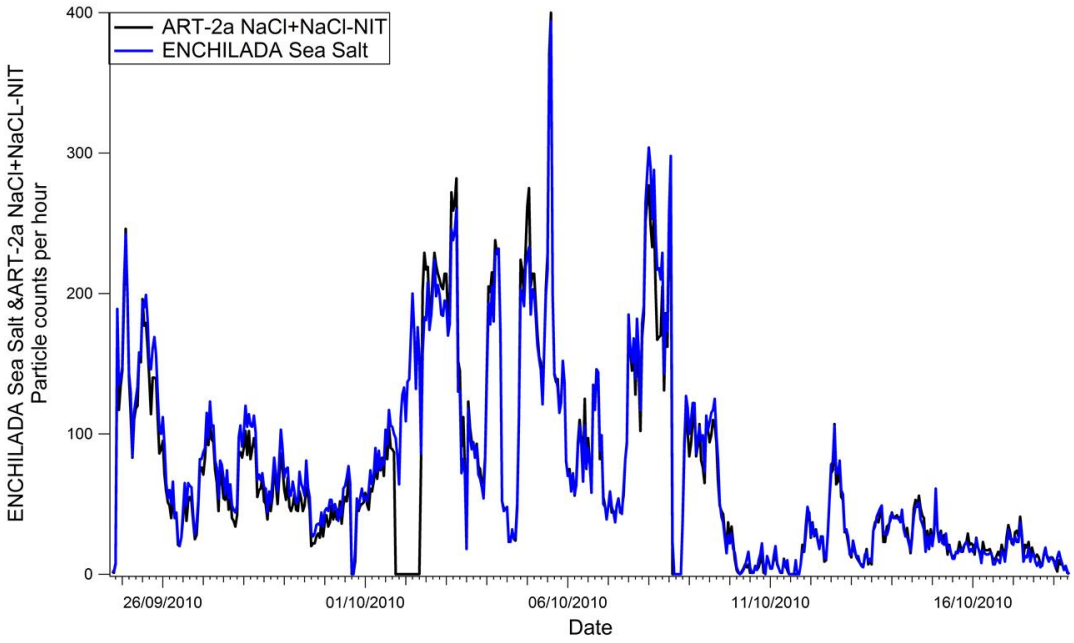

Figure 4.32 Temporal trends of Sea-salt determined by ENCHILADA and the sum of NaCl and NaCl-NIT determined by ART-2a.

Oil-V

Both *K*-means and ART-2a analysis presented particle types with similar positive mass spectra that are identified as Oil-V. The ART-2a type did not yield a negative ion spectrum, while the *K*-means type has one with low ion intensity. Figure 4.31 shows that the temporal profile of these two particle type follows, with R^2 = 0.91. Thus, both methods clearly detect this particle type with a similar temporality, however, *K*-means analysis classified almost twice as many Oil-V particles. The reason for this is likely due to the user input to the ART-2a analysis, as discussed previously.

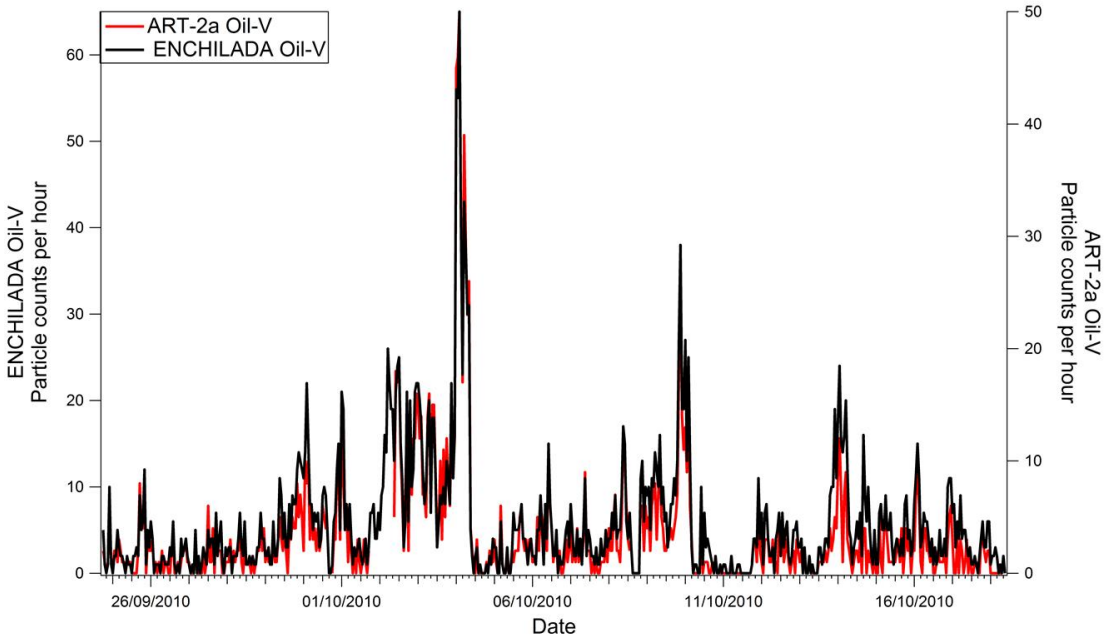

Figure 4.33 Temporal trends of Oil-V determined by ENCHILADA and Oil-V determined by ART-2a**.**

Pb-Cl

The Pb-Cl particle type was detected by both methods, with the *K*-means classifying 720 particles and the ART-2a analysis identifying 382 particles. The correlation between the two particle types is very good (R^2 = 0.75) and the temporal trend

shown in Figure 4.32 indicates that the particle types originate from short-lived emissions. While the peaks in particle number are coincident, the ratio of the peaks in number for the two classes is somewhat variable, and is likely due to the different number of the particles identified as Pb-Cl by the two analysis methods.

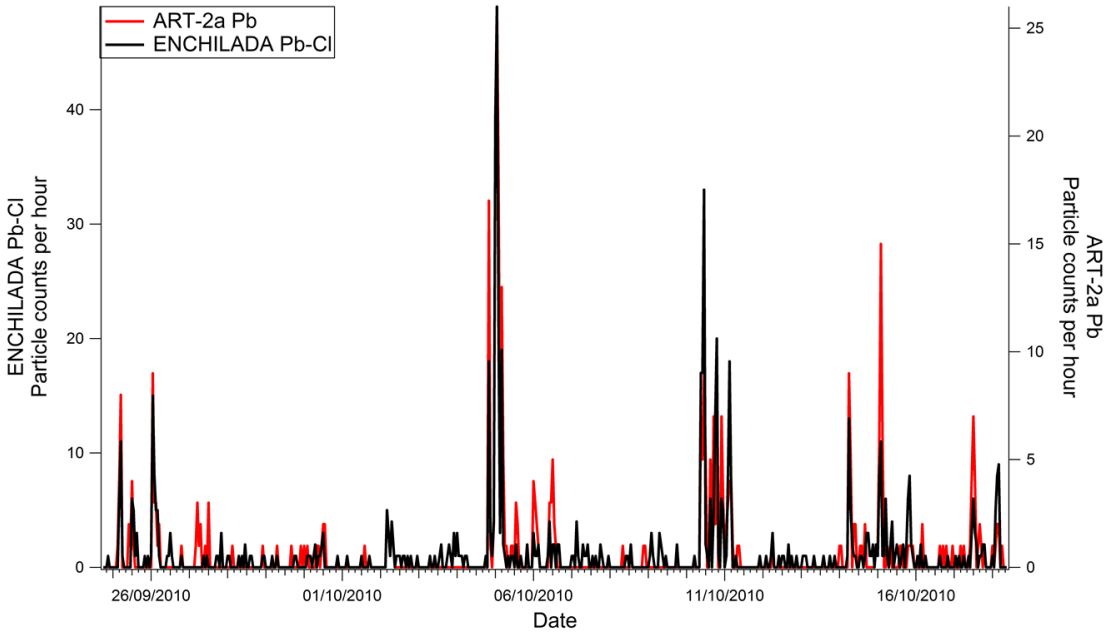

Figure 4.34 Temporal trends of Pb-Cl determined by ENCHILADA and Pb determined by ART-2a.

Fe

The Fe particle types identified by both methods are very similar in relation to mass spectra and correlate well R^2 = 0.71. *K*-means identified 3388 particles as Fe while ART-2a analysis classified 5564 particles as Fe. Figure 4.33 shows that the two particle types present very similar temporal profiles, with only a short period from 2-4 October showing a noticeable difference in the temporal trend.

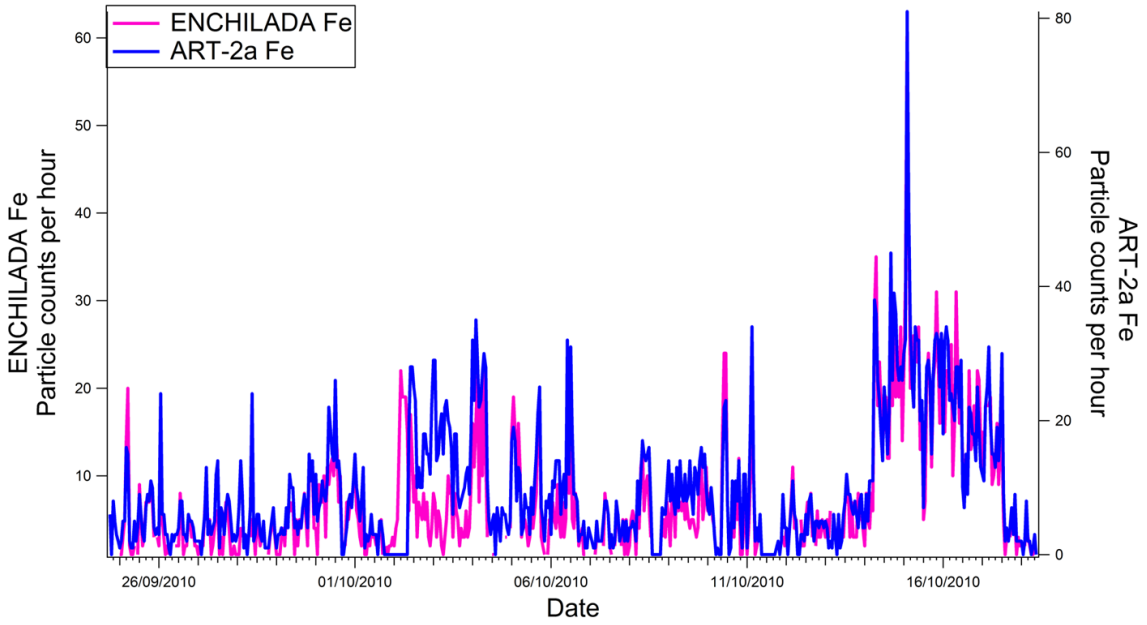

Figure 4.35 Temporal trends of Fe determined by ENCHILADA and Fe determined by ART-2a.

4.4 Conclusion

An ATOFMS operating with a converging nozzle inlet was successfully deployed at the urban background (UB) monitoring site in Barcelona during the SAPUSS measurement campaign held in September and October 2010. A total of 326395 size-resolved single particle dual ion mass spectra were collected during the campaign.

The collected particles were analysed using the *K*-means algorithm which resulted in 282117 of the particles being classified as specific particle types. Overall 22 particle types were identified and grouped into 9 categories. The largest category was carbonaceous which contained 8 of the particle types classified. Many of the carbonaceous aerosols exhibited similar temporal trends with most particle types (EC-NIT, K-CN, K-EC, Fresh/Local EC, Aged/Transported Biomass and OC-NIT) exhibiting maxima at the end of the campaign, when the city was influenced by a regional air mass and experienced stagnant weather conditions. Oxidised OC was found to be present throughout the campaign. It did not increase in contribution during the stagnation period and the daily trend of these particles suggests that they originated from the processing of combustion particles. The final carbonaceous type

was identified as K-SUL, which peaked during the European air mass event suggesting that long range transport was the source.

Sea-salt particles were detected throughout the campaign and peaked during periods where the air masses travelled over the Atlantic or Mediterranean Sea. The daily trend displayed an increase in particle number in the early afternoon coincident with sea breezes blowing inland from the Mediterranean Sea direction. Another particle type exhibiting large peaks for sodium in the mass spectra was identified as Na-EC and based on size, composition and temporal trend was attributed to sea-salt particles possibly coated by carbonaceous material.

Three dust types were detected during the campaign. The first was identified as Saharan dust, which was found to maximise during a North African (East) air mass event. Other particle types that maximised during this period included Veg-KP, the source of which is likely associated with the transport of biogenic particles that are known to accompany Saharan dust impingement. Both Ca-Dust and the Dust particle types were detected throughout the campaign and although they were at a maximum during the North African air mass events, the presence of these particles throughout the campaign suggests a local source.

The ATOFMS also detected some specific metal-containing particles such as Oil-V, which likely originate from shipping emissions or heavy oil combustion. Two further particle types, Pb-Cl and Mn, were detected as coincident, short-sharp contributions and determined to be related to industrial emissions. Similarly Fe was attributed to industrial emission sources.

A number of classes associated with low numbers of particle counts were identified. This experimental difficulty restricted the detailed identification of their sources. However inspection of their average mass spectra could be used to qualitatively identify them as Cu (attributed to a combustion or industrial source) and Ca-EC (due to road traffic). Amine 84 (ETS) was determined to be due to tobacco smoking. The PAH particles collected are likely to be due to traffic emissions.

The data collected at the UB was also analysed using ART-2a (Dall'Osto et al. In Preparation) and this data analysis was compared to the *K*-means analysis carried out. *K*-means classified more particles and identified more particle types. However,

it was found that for Aged/Transported Biomass, K-SUL, Oil-V, Fe, Pb-Cl, Ca Dust, Saharan Dust and sea-salt there were clear correlations with particles determined using ART-2a. While there was a complicated relationship for carbonaceous particle types, similar particle classifications were found for EC-NIT, K-CN, K-EC and Fresh/Local EC. The differences found between the two analysis methods were found to be mainly due to user inputs. However, it was found that, especially for carbonaceous particles, the differences in the data treatment resulted in different average mass spectra and was likely due to the approach each method uses to normalise the spectra prior to analysis.

4.5 References

Alier, M., van Drooge, B.L., Dall'Osto, M., Querol, X., Grimalt, J.O., Tauler, R., 2013. Source apportionment of submicron organic aerosol at an urban background and a road site in Barcelona (Spain) during SAPUSS. Atmospheric Chemistry and Physics 13, 10353-10371.

Amato, F., Pandolfi, M., Escrig, A., Querol, X., Alastuey, A., Pey, J., Perez, N., Hopke, P.K., 2009a. Quantifying road dust resuspension in urban environment by Multilinear Engine: A comparison with PMF2. Atmospheric Environment 43, 2770-2780.

Amato, F., Pandolfi, M., Viana, M., Querol, X., Alastuey, A., Moreno, T., 2009b. Spatial and chemical patterns of PM10 in road dust deposited in urban environment. Atmospheric Environment 43, 1650-1659.

Brines, M., Dall'Osto, M., Beddows, D.C.S., Harrison, R.M., Querol, X., 2014. Simplifying aerosol size distributions modes simultaneously detected at four monitoring sites during SAPUSS. Atmospheric Chemistry and Physics 14, 2973-2986.

Dall'Osto, M., Beddows, D., Gielt, J., Harrison, R., McGillicuddy, E.J., Wenger, J., Alastuey, A., Querol, X., On the simultaneous deployment of single particle mass spectrometry at an urban background and a road site during SAPUSS. In Preparation.

Dall'Osto, M., Booth, M.J., Smith, W., Fisher, R., Harrison, R.M., 2008. A study of the size distributions and the chemical characterization of airborne particles in the vicinity of a large integrated steelworks. Aerosol Science and Technology 42, 981-991.

Dall'Osto, M., Harrison, R.M., 2012. Urban organic aerosols measured by single particle mass spectrometry in the megacity of London. Atmospheric Chemistry and Physics 12, 4127-4142.

Dall'Osto, M., Harrison, R., Coe, H., Williams, P., Allan, J., 2009. Real time chemical characterization of local and regional nitrate aerosols. Atmospheric Chemistry and Physics 9, 3709-3720.

Dall'Osto, M., Harrison, R.M., Charpantidou, E., Loupa, G., Rapsomanikis, S., 2007. Characterisation of indoor airborne particles by using real-time aerosol mass spectrometry. Science of the Total Environment 384, 120-133.

Dall'Osto, M., Querol, X., Alastuey, A., Minguillon, M.C., Alier, M., Amato, F., Brines, M., Cusack, M., Grimalt, J.O., Karanasiou, A., Moreno, T., Pandolfi, M., Pey, J., Reche, C., Ripoll, A., Tauler, R., Van Drooge, B.L., Viana, M., Harrison, R.M., Gietl, J., Beddows, D., Bloss, W., O'Dowd, C., Ceburnis, D., Martucci, G., Ng, N.L., Worsnop, D., Wenger, J., Mc Gillicuddy, E., Sodeau, J., Healy, R., Lucarelli, F., Nava, S., Jimenez, J.L., Gomez Moreno, F., Artinano, B., Prévôt, A.S.H., Pfaffenberger, L., Frey, S., Wilsenack, F., Casabona, D., Jiménez-Guerrero, P., Gross, D., Cots, N., 2013a. Presenting SAPUSS: Solving Aerosol Problem by Using Synergistic Strategies in Barcelona, Spain. Atmospheric Chemistry and Physics 13, 8991-9019.

Dall'Osto, M., Querol, X., Alastuey, A., O'Dowd, C., Harrison, R.M., Wenger, J., Gómez-Moreno, F.J., 2013b. On the spatial distribution and evolution of ultrafine particles in Barcelona. Atmospheric Chemistry and Physics 13, 741-759.

Dall'Osto, M., Querol, X., Amato, F., Karanasiou, A., Lucarelli, F., Nava, S., Calzolai, G., Chiari, M., 2013c. Hourly elemental concentrations in PM2.5 aerosols sampled simultaneously at urban background and road site during

SAPUSS – diurnal variations and PMF receptor modelling. Atmospheric Chemistry and Physics 13, 4375-4392.

Dall'Osto, M., Drewnick, F., Fisher, R., Harrison, R.M., 2012. Real-Time Measurements of Nonmetallic Fine Particulate Matter Adjacent to a Major Integrated Steelworks. Aerosol Science and Technology 46, 639-653.

Dall'Osto, M., Harrison, R.M., Highwood, E.J., O'Dowd, C., Ceburnis, D., Querol, X., Achterberg, E.P., 2010. Variation of the mixing state of Saharan dust particles with atmospheric transport. Atmospheric Environment 44, 3135-3146.

Draxler, R.R.R., G.D. , 2013. HYSPLIT (HYbrid Single-Particle Lagrangian Integrated Trajectory) Model access via NOAA ARL READY Website (http://ready.arl.noaa.gov/HYSPLIT.php). NOAA Air Resources Laboratory, Silver Spring, MD.

Fergenson, D.P., Pitesky, M.E., Tobias, H.J., Steele, P.T., Czerwieniec, G.A., Russell, S.C., Lebrilla, C.B., Horn, J.M., Coffee, K.R., Srivastava, A., Pillai, S.P., Shih, M.T.P., Hall, H.L., Ramponi, A.J., Chang, J.T., Langlois, R.G., Estacio, P.L., Hadley, R.T., Frank, M., Gard, E.E., 2004. Reagentless detection and classification of individual bioaerosol particles in seconds. Analytical Chemistry 76, 373-378.

Furutani, H., Jung, J., Miura, K., Takami, A., Kato, S., Kajii, Y., Uematsu, M., 2011. Single-particle chemical characterization and source apportionment of iron-containing atmospheric aerosols in Asian outflow. Journal of Geophysical Research 116, D18204.

Giorio, C., Tapparo, A., Dall'Osto, M., Harrison, R.M., Beddows, D., Di Marco, C., Nemitz, E., 2012. Comparison of three techniques for analysis of data from an Aerosol Time-of-Flight Mass Spectrometer. Atmospheric Environment 61, 316-326

Gross, D.S., Atlas, R., Rzeszotarski, J., Turetsky, E., Christensen, J., Benzaid, S., Olson, J., Smith, T., Steinberg, L., Sulman, J., Ritz, A., Anderson, B.,

Nelson, C., Musicant, D.R., Chen, L., Snyder, D.C., Schauer, J.J., 2010. Environmental chemistry through intelligent atmospheric data analysis. Environmental Modelling & Software 25, 760-769.

Gross, D.S., Barron, A.R., Sukovich, E.M., Warren, B.S., Jarvis, J.C., Suess, D.T., Prather, K.A., 2005. Stability of single particle tracers for differentiating between heavy- and light-duty vehicle emissions. Atmospheric Environment 39, 2889-2901.

Guazzotti, S.A., Suess, D.T., Coffee, K.R., Quinn, P.K., Bates, T.S., Wisthaler, A., Hansel, A., Ball, W.P., Dickerson, R.R., Neususs, C., Crutzen, P.J., Prather, K.A., 2003. Characterization of carbonaceous aerosols outflow from India and Arabia: Biomass/biofuel burning and fossil fuel combustion. Journal of Geophysical Research-Atmospheres 108, 4485, doi:10.1029/2002JD003277, D15.

Harrison, R.M., Dall'Osto, M., Beddows, D.C.S., Thorpe, A.J., Bloss, W.J., Allan, J.D., Coe, H., Dorsey, J.R., Gallagher, M., Martin, C., Whitehead, J., Williams, P.I., Jones, R.L., Langridge, J.M., Benton, A.K., Ball, S.M., Langford, B., Hewitt, C.N., Davison, B., Martin, D., Petersson, K.F., Henshaw, S.J., White, I.R., Shallcross, D.E., Barlow, J.F., Dunbar, T., Davies, F., Nemitz, E., Phillips, G.J., Helfter, C., Di Marco, C.F., Smith, S., 2012. Atmospheric chemistry and physics in the atmosphere of a developed megacity (London): an overview of the REPARTEE experiment and its conclusions. Atmospheric Chemistry and Physics 12, 3065-3114.

Healy, R., Hellebust, S., Kourtchev, I., Allanic, A., O'Connor, I., Bell, J., Healy, D., Sodeau, J., Wenger, J., 2010. Source apportionment of PM 2.5 in Cork Harbour, Ireland using a combination of single particle mass spectrometry and quantitative semi-continuous measurements. Atmospheric Chemistry and Physics 10, 9593-9613.

Healy, R., Sciare, J., Poulain, L., Kamili, K., Merkel, M., Müller, T., Wiedensohler, A., Eckhardt, S., Stohl, A., Sarda-Esteve, R., 2012. Sources and mixing state of size-resolved elemental carbon particles in a European megacity: Paris. Atmospheric Chemistry and Physics 12, 1681-1700.

Healy, R.M., O'Connor, I.P., Hellebust, S., Allanic, A., Sodeau, J.R., Wenger, J.C., 2009. Characterisation of single particles from in-port ship emissions. Atmospheric Environment 43, 6408-6414.

Healy, R.M., Sciare, J., Poulain, L., Crippa, M., Wiedensohler, A., Prévôt, A.S.H., Baltensperger, U., Sarda-Estève, R., McGuire, M.L., Jeong, C.H., McGillicuddy, E., O'Connor, I.P., Sodeau, J.R., Evans, G.J., Wenger, J.C., 2013. Quantitative determination of carbonaceous particle mixing state in Paris using single-particle mass spectrometer and aerosol mass spectrometer measurements. Atmospheric Chemistry and Physics 13, 9479-9496.

Kellogg, C.A., Griffin, D.W., 2006. Aerobiology and the global transport of desert dust. Trends in Ecology & Evolution 21, 638-644.

Lake, D.A., Tolocka, M.P., Johnston, M.V., Wexler, A.S., 2004. The character of single particle sulfate in Baltimore. Atmospheric Environment 38, 5311-5320.

Liu, D.Y., Wenzel, R.J., Prather, K.A., 2003. Aerosol time-of-flight mass spectrometry during the Atlanta Supersite Experiment: 1. Measurements. Journal of Geophysical Research-Atmospheres 08, 8426, doi:10.1029/2001JD001562, D7.

MacQueen, J., 1967. Some methods for classification and analysis of multivariate observations, Proceedings of the fifth Berkeley symposium on mathematical statistics and probability. California, USA, p. 14.

Minguillón, M., Perron, N., Querol, X., Szidat, S., Fahrni, S., Alastuey, A., Jimenez, J., Mohr, C., Ortega, A., Day, D., 2011. Fossil versus contemporary sources of fine elemental and organic carbonaceous particulate matter during the DAURE campaign in Northeast Spain. Atmospheric Chemistry and Physics 11, 12067-12084.

Moffet, R.C., de Foy, B., Molina, L.T., Molina, M.J., Prather, K.A., 2008a. Measurement of ambient aerosols in northern Mexico City by single particle mass spectrometry. Atmospheric Chemistry and Physics 8, 4499-4516.

Moffet, R.C., Desyaterik, Y., Hopkins, R.J., Tivanski, A.V., Gilles, M.K., Wang, Y., Shutthanandan, V., Molina, L.T., Abraham, R.G., Johnson, K.S., Mugica, V., Molina, M.J., Laskin, A., Prather, K.A., 2008b. Characterization of aerosols containing Zn, Pb, and Cl from an industrial region of Mexico City. Environmental Science & Technology 42, 7091-7097.

Moreno, T., Querol, X., Alastuey, A., Reche, C., Cusack, M., Amato, F., Pandolfi, M., Pey, J., Richard, A., Prévôt, A., 2011. Variations in time and space of trace metal aerosol concentrations in urban areas and their surroundings. Atmospheric Chemistry and Physics 11, 9415-9430.

Moreno, T.Q., X. Alastuey, A. Reche, C. Cusack, M. Amato, F. Pandolfi, M. Pey, J. Richard, A. Prévôt, A. S. H. Furger, M. Gibbons, W., 2011. Variations in time and space of trace metal aerosol concentrations in urban areas and their surroundings. Atmospheric Chemistry and Physics 11, 9415- 9430.

Nielsen, T., Jørgensen, H.E., Larsen, J.C., Poulsen, M., 1996. City air pollution of polycyclic aromatic hydrocarbons and other mutagens: occurrence, sources and health effects. Science of the Total Environment 189, 41-49.

Noble, C.A., Prather, K.A., 1996. Real-time measurement of correlated size and composition profiles of individual atmospheric aerosol particles. Environmental Science & Technology 30, 2667-2680.

Noble, C.A., Prather, K.A., 1997. Real-time single particle monitoring of a relative increase in marine aerosol concentration during winter rainstorms. Geophysical Research Letters 24, 2753-2756.

Oster, M., Elsasser, M., Schnelle-Kreis, J., Zimmermann, R., 2011. First field application of a thermal desorption resonance-enhanced multiphoton-ionisation single particle time-of-flight mass spectrometer for the on-line detection of particle-bound polycyclic aromatic hydrocarbons. Analytical and bioanalytical chemistry 401, 3173-3182.

Pandolfi, M., Martucci, G., Querol, X., Alastuey, A., Wilsenack, F., Frey, S., O'Dowd, C.D., Dall'Osto, M., 2013. Continuous atmospheric boundary layer

observations in the coastal urban area of Barcelona during SAPUSS. Atmospheric Chemistry and Physics 13, 4983-4996.

Pastor, S.H., Allen, J.O., Hughes, L.S., Bhave, P., Cass, G.R., Prather, K.A., 2003. Ambient single particle analysis in Riverside, California by aerosol time-of-flight mass spectrometry during the SCOS97-NARSTO. Atmospheric Environment 37, 239-258.

Pérez, N., Pey, J., Querol, X., Alastuey, A., López, J.M., Viana, M., 2008. Partitioning of major and trace components in PM10–PM2.5–PM1 at an urban site in Southern Europe. Atmospheric Environment 42, 1677-1691.

Pio, C., Cerqueira, M., Harrison, R.M., Nunes, T., Mirante, F., Alves, C., Oliveira, C., Sanchez de La Campa, A., Artíñano, B., Matos, M., 2011. OC/EC ratio observations in europe: Re-thinking the approach for apportionment between primary and secondary organic carbon. Atmospheric Environment 45, 6121-6132.

Prati, P., Zucchiatti, A., Lucarelli, F., Mandò, P.A., 2000. Source apportionment near a steel plant in Genoa (Italy) by continuous aerosol sampling and PIXE analysis. Atmospheric Environment 34, 3149-3157.

Prospero, J.M., Blades, E., Mathison, G., Naidu, R., 2005. Interhemispheric transport of viable fungi and bacteria from Africa to the Caribbean with soil dust. Aerobiologia 21, 1-19.

Querol, X., Alastuey, A., Rodriguez, S., Plana, F., Mantilla, E., Ruiz, C.R., 2001a. Monitoring of PM10 and PM2.5 around primary particulate anthropogenic emission sources. Atmospheric Environment 35, 845-858.

Querol, X., Alastuey, A., Rodriguez, S., Plana, F., Ruiz, C.R., Cots, N., Massagué, G., Puig, O., 2001b. PM10 and PM2.5 source apportionment in the Barcelona Metropolitan area, Catalonia, Spain. Atmospheric Environment 35, 6407-6419.

Querol, X., Alastuey, A., Viana, M.M., Rodriguez, S., Artiñano, B., Salvador, P., Garcia do Santos, S., Fernandez Patier, R., Ruiz, C.R., de la Rosa, J.,

Sanchez de la Campa, A., Menendez, M., Gil, J.I., 2004. Speciation and origin of PM10 and PM2.5 in Spain. Journal of Aerosol Science 35, 1151-1172.

Querol, X., Pey, J., Pandolfi, M., Alastuey, A., Cusack, M., Pérez, N., Moreno, T., Viana, M., Mihalopoulos, N., Kallos, G., Kleanthous, S., 2009. African dust contributions to mean ambient PM10 mass-levels across the Mediterranean Basin. Atmospheric Environment 43, 4266-4277.

Rebotier, T.P., Prather, K.A., 2007. Aerosol time-of-flight mass spectrometry data analysis: A benchmark of clustering algorithms. Analytica Chimica Acta 585, 38-54.

Silva, P.J., Liu, D.Y., Noble, C.A., Prather, K.A., 1999. Size and chemical characterization of individual particles resulting from biomass burning of local Southern California species. Environmental Science & Technology 33, 3068-3076.

Spencer, M.T., Shields, L.G., Sodeman, D.A., Toner, S.M., Prather, K.A., 2006. Comparison of oil and fuel particle chemical signatures with particle emissions from heavy and light duty vehicles. Atmospheric Environment 40, 5224-5235.

Viana, M., Reche, C., Amato, F., Alastuey, A., Querol, X., Moreno, T., Lucarelli, F., Nava, S., Cazolai, G., Chiari, M., Rico, M., 2013. Evidence of biomass burning aerosols in the Barcelona urban environment during winter time. Atmospheric Environment 72, 81-88.

Willeke, K., Whitby, K.T., 1975. Atmospheric aerosols: size distribution interpretation. Journal of the Air Pollution Control Association 25, 529-534.

Yu, S., Dennis, R.L., Bhave, P.V., Eder, B.K., 2004. Primary and secondary organic aerosols over the United States: estimates on the basis of observed organic carbon (OC) and elemental carbon (EC), and air quality modeled primary OC/EC ratios. Atmospheric Environment 38, 5257-5268.

5 Comparative Analysis of Metal-Containing Atmospheric Particles in Barcelona using ATOFMS and Particle Induced X-ray Emission (PIXE)

Contents

5.1 Introduction

Metals present in atmospheric particulate matter have both natural and anthropogenic origin. Natural sources of metals in the atmosphere include volcanic activity and wind-blown dust, while anthropogenic sources include industrial processes, traffic emissions, incineration and fossil fuel combustion (Allen et al., 2001; Querol et al., 2002). It is known that exposure to particulate matter has adverse effects on human health (Pope and Dockery, 2006; U.S.EPA, 2009) and also that a number of metals are potentially toxic (Kelly and Fussell, 2012).

Traditionally the metal component of atmospheric aerosols has been measured using off-line methods, whereby particles are collected onto a substrate and later analysed using techniques such as Inductively Coupled Plasma- Mass Spectrometry (ICP-MS) (Moreno, 2011; Pratt and Prather, 2012a). Although these methods can quantitatively determine the concentration of individual metals in particulate matter, sufficient mass is usually required for analysis, which results in sampling times as long as 12 or 24 hours. The off-line techniques therefore typically suffer from poor time resolution and cannot detect short-lived emissions. This problem has been recently overcome to a certain extent with the combined use of a rotating impactor and analytical techniques such as x-ray fluorescence (XRF) and Particle induced X-ray Emission (PIXE) which allow elemental concentrations to be determined with hourly temporal resolution (Bukowiecki et al., 2005; Calzolai et al., 2008; Chiari et al., 2005). Although these developments improve the study of specific short-lived events they do not provide information on the mixing state or size distribution of metals in the particles, which is useful for source identification purposes.

The interest in measuring the mixing state of individual aerosol particles led to the development of single particle mass spectrometers, such as the Aerosol Time of Flight Mass Spectrometer (ATOFMS). The ATOFMS provides size resolved single particle dual ion mass spectra of particles in the size range 100-3000 nm, thus enabling characterisation of the primary composition of single particles, e.g., elemental/organic carbon and transition metals, along with determination of secondary species, such as nitrate and sulfate (Gard et al., 1997; Prather et al., 1994). The ATOFMS has proven to be a very useful tool for analysis of atmospheric

particles and has been successfully deployed in numerous locations world-wide (Pratt and Prather, 2012b). The technique utilizes laser desorption/ionization which is influenced by particle size, morphology and chemical composition and these well-documented matrix effects can limit its ability to quantitatively determine the concentration of individual chemical species (Pratt and Prather, 2009; Reilly et al., 2000). Nevertheless, the ATOFMS is one of a small number of instruments that can be used as a real time method for the determination of metals within atmospheric aerosols and several previous studies have compared these measurements with quantitative techniques. Dall'Osto et al., (2008) compared metal particle types identified using the ATOFMS with size segregated measurements of metals contained in aerosol samples collected using a Micro-Orifice Uniform-Deposit Impactor (MOUDI). The comparison was found to be very beneficial in identifying both the size distribution and the chemical composition of particles emanating from an integrated steelworks. Dall'Osto et al., (2006) also compared ATOFMS single particle data collected at Mace Head in Ireland with quantitative off-line measurements of Na^+, K^+, Mg^+, and Cl^- to assist in the determination of the major particle types observed during the NAMBLEX campaign. Moffet et al., (2008) compared ATOFMS and PIXE measurements for particles containing Zn, Pb and Cl detected in Mexico City during the MILAGRO campaign to show that they originated from industrial waste incineration.

In the most detailed study of this type, Snyder et al., (2009) showed that the ATOFMS ion signals for a number of metals exhibited a semi-quantitative relationship with daily average concentrations determined using XRF. In particular, good correlations were obtained for calcium, potassium and lead, however, the inter-comparison was not so successful for most other metals. While this study demonstrated the potential of the ATOFMS for providing quantitative measurements, the use of 24 h average values is of limited value in monitoring short-lived emissions, which can be important sources of metal-containing particles (D'Alessandro et al., 2003). These short-lived events may also be beneficial for comparisons between the ATOFMS and quantitative techniques as they typically exhibit a strong increase in concentration of metals to well above the limits of detection. The matrix effect associated with ATOFMS may also be reduced, leading to an improved correlation between the on-line and off-line measurements.

In the work reported in this Chapter, an in-depth analysis of ATOFMS and PIXE data was performed to evaluate the suitability of the ATOFMS for the quantitative determination of metals in atmospheric particles at high time resolution. The data was collected as part of the SAPUSS field measurement campaign carried out in Barcelona, Spain (Dall'Osto et al., 2013b). The hourly elemental concentrations determined by PIXE were used to identify the following aerosol sources; regional sulfur, aged sea-salt, sea-salt, biomass burning, soil dust, urban dust, brake dust, industrial smelters, industrial combustion and oil combustion (Dall'Osto et al., 2013c). The ATOFMS data collected during the campaign has been used to identify a number of particle types, which are described fully by (Dall'Osto et al. In Preparation). Here, a detailed investigation into the metals detected by ATOFMS during the SAPUSS campaign and the results of a comparative analysis with the PIXE dataset are presented. New information on the mixing state and size distribution of metals in the particles is obtained and the ability of ATOFMS to quantitatively determine the metal content in atmospheric particles is fully explored.

5.2 Methods

5.2.1 Measurement Sites

The measurement sites used for the inter-comparison between the ATOFMS and PIXE were the Urban Background (UB) site and the Road Site (RS), which are ca. 3 km apart and are described fully elsewhere (Dall'Osto et al., 2013b). The UB measurement site was located on the North Western periphery of the city in a small park 6 km from the sea. It is mainly surrounded by residential areas and several University campuses. The site is 300 m from Diagonal Avenue, one of the main access roads for Barcelona. The RS site was situated in the car park of the Escola de Ingeniería Técnica Industrial on C\ Urgell. The streets surrounding the institute form a street canyon. Instruments at the RS were all located inside three vans parked about 4 metres from the kerb. At both of the sampling sites an ATOFMS and a streaker sampler were deployed. Data was collected during the SAPUSS measurement campaign encompassing the period 27/09/2010 12:00:00 to 16/10/2010 23:00:00. This accounted for the period when the ATOFMS and PIXE instrumentation was operational at the UB and RS measurement sites.

5.2.2 ATOFMS

The ATOFMS (TSI model 3800, incorporating a converging nozzle inlet) at the UB measurement site was located in an air-conditioned sampling cabin and employed a quarter inch copper sampling line at 4 m above ground level with a rain cap. The ATOFMS (TSI model 3800 fitted with an aerodynamic lens TSI model AFL 100) at the RS was housed in an air conditioned van and sampling was conducted 4 m above ground level using a $PM_{2.5}$ sampling head and quarter inch stainless steel tubing. The operating principles of both instruments are described in detail in Chapter 2 and elsewhere (Gard et al., 1997; Su et al., 2004).

The ATOFMS datasets were imported into YAADA (Yet Another ATOFMS Data Analyzer) and the single particle mass spectra were grouped using the adaptive resonance theory neural network, ART-2a algorithm (Song et al., 1999). The analysis resulted in the generation of 18 particle types at RS and 14 at UB, with 10 of these types common to both sites (Dall'Osto et al. In Preparation).

5.2.3 PIXE

The samples for PIXE analysis were collected using streaker samplers. The streaker sampler, which is described in detail elsewhere (Prati et al., 1998) is composed of a rotating impaction surface which has an Effective Cut Diameter (ECD) of 2.5 µm at a flow rate of 1 l/min. Air flows over a Kapton film where coarse particles (2.5 µm < D_{ae} < 10 µm) are deposited. The particles with D_{ae} < 2.5 µm are impacted onto a Nuclepore filter positioned on the impaction stage. The impaction stage and the filter rotate around a common axis which allows for time resolved information to be collected. The streaker samplers were located at both the UB and RS measurement sites during the campaign to collect fine particulate matter. PIXE analyses were performed on the fine fraction of these samples with 3 MeV protons from the 3 MV Tandetron accelerator of the LABEC laboratory of INFN in Florence, with the external beam set-up described elsewhere (Chiari et al., 2005; Dall'Osto et al., 2013c) The proton beam (30–80 nA) scanned the streak in steps corresponding to 1 h of aerosol sampling. Hourly concentrations were determined for the following elements: Na, Mg, Al, P, S, Cl, K, Ca, Ti, V, Cr, Mn, Fe, Ni, Cu, Zn, Sr and Pb. The detection limits for the PIXE analysis were about 10 ng m^{-3} for elements with low Z (elements from Na to V) and 1 ng m^{-3} for elements with medium-high Z (elements from Cr to Pb) (Prati et al., 2000). PIXE measurements have previously been found to compare well with XRF and ICP-AES (Calzolai et al., 2008; Menzel et al., 2002; Traversi et al., 2014).

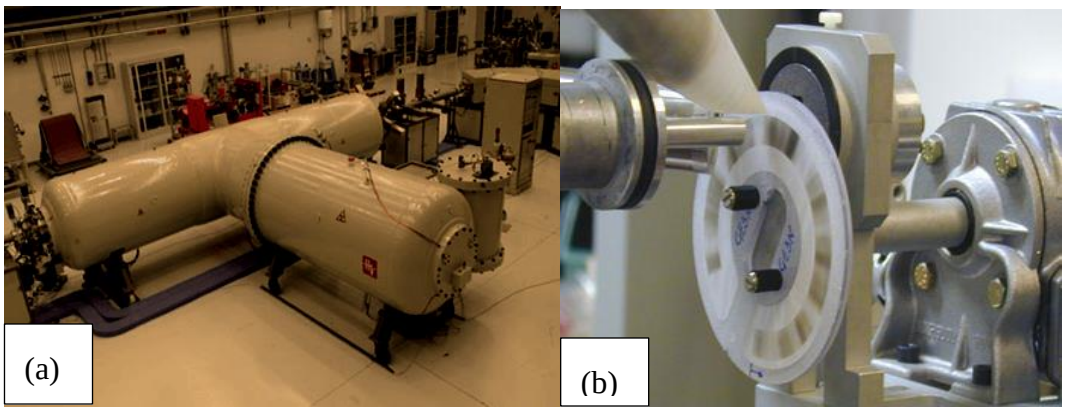

Figure 5.1 (a) Accelerator for PIXE analysis of samples and (b). PIXE measurement of a Nuclepore filter collected using a streaker sampler.

5.3 Results and Discussion

5.3.1 Ion Identification and Validation

The ATOFMS dataset was interrogated for all of the metal species identified by PIXE (Na, Mg, Al, K, Ca, Ti, V, Cr, Mn, Fe, Ni, Cu, Zn, Sr and Pb). The first step in the treatment of the ATOFMS data involved identification of appropriate mass-to-charge ratios (*m/z*) for the metals of interest (identifying ion) and the identification of a second *m/z* for the metals of interest to be used for validation purposes (confirmatory ion). The approach taken was similar to that employed by Snyder et al., (2009) where the identifying ion was typically the *m/z* corresponding to the most abundant isotope of the metal of interest and the confirmatory ion was another isotope of the metal, e.g., the identifying and confirmatory ions selected for potassium were *m/z* 39 and 41 respectively. In cases where no abundant second isotope exists or where a contribution from another ion with the same *m/z* (isobaric interference) was expected, a metal oxide was used as the confirmatory ion. For several metals, two confirmatory ions were used, e.g., for vanadium, *m/z* 67 (VO) was used as an additional confirmatory ion for vanadium (*m/z* 51) as the second most abundant isotope of V *m/z* 50 has a relative abundance of just 0.25%. The ion intensities for identifying and confirmatory ions were compared and the *m/z* was considered representative of the metal if a good correlation was obtained ($R^2 > 0.50$).

The list of identifying and confirmatory ions for the metals is shown in Table 5.1, along with the R^2 values obtained from correlation plots of the ion intensity. It can be seen that several of the metals present good correlations between identifying and confirmatory ions including; calcium, iron, lead, potassium and zinc, thus validating the selected ions. Some other metals present somewhat poorer correlations including copper, nickel and titanium. The reason for the poor correlation between the identifying and confirmatory ion is likely due to isobaric interference, e.g. due to the presence of a hydrocarbon fragment with the same *m/z*. For example, common organic fragments are observed at *m/z* 50 and 63 (Gross et al., 2005; Silva and Prather, 2000) which directly interfere with the ion signals for V and Cu, respectively. This explains the weak correlation between the vanadium isotopes at *m/z* 51 and 50, however, the correlation is significantly improved when VO (*m/z* 67)

was used as the confirmatory ion. The comparison with the metal oxide was less successful for other metals including aluminium, calcium, iron and titanium, again likely due to isobaric interferences. For example the *m/z* for calcium oxide is also the *m/z* for the dominant isotope of Fe. Similarly, *m/z* 64 is the major ion for both zinc and titanium oxide. The weak correlation between Al and its oxide is likely due to interference from the oxidised organic carbon fragment $[(CH_3)CO]^+$ (*m/*z = 43) while the aluminium signal *m/z* 27 is associated with both aluminium and the hydrocarbon fragment $[C_2H_3]^+$ (Silva and Prather, 2000).

The ion identification and validation procedure thus confirmed that the ATOFMS could potentially provide semi-quantitative information for the following metals: calcium, iron, lead, potassium, vanadium and zinc. Interestingly, Snyder et al. (2009) also identified these same metals (with the exception of vanadium) as suitable for quantification on an ATOFMS dataset obtained in St Louis, IL. The procedure was less successful for a number of the other metals, again in accord with previous work (Snyder et al., 2009), while correlations could not be obtained for manganese and sodium due to the absence of a suitable confirmatory ion.

Element	Identifying Ion (m/z)	Confirmatory Ion (m/z)	R^2
Aluminium	27	43 (AlO)	0.23
Calcium	40	44	0.52
	40	56 (CaO)	0.38
Chromium	52	53	0.38
Copper	63	65	0.01
Iron	56	54	0.81
	56	72 (FeO)	0.26
Lead	208	207	0.87
Magnesium	24	25	0.41
Manganese	55	n/a	
Nickel	58	62	0.01
Potassium	39	41	0.72
Sodium	23	n/a	
Titanium	48	46	0.07
	48	64 (TiO)	0.00
Vanadium	51	50	0.30
	51	67 (VO)	0.87
Zinc	64	66	0.67

Table 5.1 Validation of metal ion signals from ATOFMS using identifying and confirmatory ion (where available). All identifying ions are the most abundant isotope of that metal and the confirmatory ion is another isotope or the metal oxide.

5.3.2 Size distribution of metal ion signal within ATOFMS dataset

Information on the size distribution of metals in atmospheric particles is important for elucidating sources and also evaluating potential health effects (Pöschl, 2005). The ATOFMS can provide such information and the dataset was therefore interrogated for the presence of metals using the identifying ions. The ion signal was split into four size bins, 0 to 700 nm, 700 to 2100 nm, 1400 to 2100 and 2100 to 2800 nm, which were selected on the basis of the overall size range of particles seen by the ATOFMS at the UB site (Dall'Osto et al. In Preparation). The percentage of

the ion signal for each metal within each of the size bins is shown in Table 5.2. From the distribution it can be seen that Na (*m/z* 23), Al (*m/z* 27) and Ti (*m/z* 48) are located mainly in the larger size bins, which indicates that, as expected, these metals originate from sea-salt or crustal sources. Magnesium is also present in sea-salt and crustal materials, however, *m/z* 24 is present in similar amounts in all size bins suggesting that the C_2^+ peak in EC-containing particles is a source of interference, particularly in the smallest size bin. This is confirmed by the distribution of ion intensity for the second magnesium isotope at *m/z* 25, which has a very low value in the 0-700 nm size bin, and shows a similar pattern to that seen for sodium (*m/z* 23). Calcium (*m/z* 40) is another crustal element which is expected to be mainly present in the larger size bins. However, calcium is also present in lubricating oil used in motor vehicles and is often detected by ATOFMS along with combustion particles, (Dall'Osto et al., 2013a; Suess and Prather, 2002). This latter source therefore most likely accounts for the higher than expected ion intensity observed in the 0-700 nm size range. Pb (*m/z* 207), V (*m/z* 51), Cr (*m/z* 52), Zn (*m/z* 66), Cu (*m/z* 63) and Mn (*m/z* 55) are all located predominantly in the smaller size bins, consistent with general observations that these metals originate from combustion and industrial-type sources (Calvo et al., 2013; Healy et al., 2009; Moffet et al., 2008). Several elements (K (*m/z* 39), Fe (*m/z* 56), Ca (*m/z* 40)) are seen across all the size bins suggesting that these elements are present in both combustion and crustal sources.

Element (*m/z*)	ATOFMS size bins			
	0-700 nm	**700-1400 nm**	**1400-2100 nm**	**2100-2800 nm**
Aluminium (27)	17	35	31	16
Calcium (40)	23	31	29	18
Chromium (52)	66	25	6	3
Copper (63)	74	19	5	2
Iron (56)	38	34	20	9
Lead (208)	36	56	6	1
Lead (208 and 207)	42	51	6	1
Magnesium (24)	21	26	32	22
Magnesium (25)	6	27	37	29
Manganese (55)	43	38	4	15
Nickel (58)	54	22	14	10
Potassium (39)	53	28	13	7
Potassium (41)	38	26	21	15
Sodium (23)	10	30	34	26
Titanium (48)	17	45	27	11
Vanadium (51)	86	11	2	0
Zinc (64 and 66)	41	47	9	2

Table 5.2 Proportion (in %) of ion signal located in different size bins.

5.3.3 ATOFMS-PIXE inter-comparison across entire campaign

The ability of ATOFMS to quantitatively determine metals in particles observed during the SAPUSS campaign has been evaluated by examining the relationship between ion intensity and the hourly average concentrations obtained by PIXE. Correlations between ATOFMS ion intensity and PIXE elemental concentration observed at the UB site are listed in Table 5.3. The R^2 values were determined over the whole size range of the ATOFMS and also for the four size bins outlined above. The best overall correlations (R^2 of 0.5 or greater) were observed for aluminium, manganese and lead, as shown in Figure 5.2 (a-c). The main previous quantitative

ATOFMS study ignored aluminium because the ion signal was assumed to contain significant interference due to the hydrocarbon fragment $C_2H_3^+$ (Snyder et al., 2009). In contrast, this study shows that the correlation between the PIXE signal for Al and *m/z* 27 is good. However; this observation is likely due to the influence of aluminium-rich particles from Saharan dust impacting on the measurement site during the campaign (Dall'Osto et al., 2013b). Indeed, the R^2 values obtained for the larger size bins are much better than for the 0-700 nm range where interference from hydrocarbon fragments is expected to be at its highest. Both manganese and lead are associated with industrial emissions and the temporality of the ATOFMS and PIXE signals for these elements exhibit spikes characteristic of short-lived emissions from point sources. The temporal profile for Mn is shown in Figure 5.3 and clearly highlights the advantage of sampling at high time resolution.

Several other metals, such as iron, (Figure 5.2 (d)) titanium and zinc, exhibit correlations with an R^2 of 0.3 or greater. While these correlations are not very strong they may be of some use with deeper investigation, especially if the comparison is further tuned: for example, examining the relationship between the ATOFMS and PIXE during selected meteorological periods or investigating relationships between particle types and PIXE, as discussed below.

For some of the metals the correlation found was poor, possibly due to the PIXE data containing many gaps. An example of this can be seen in the vanadium correlation where the ATOFMS presents an ion signal that is present throughout the campaign but the PIXE data contains large gaps that will affect their relationship for this element.

Element	0-700 nm	700-1400 nm	1400-2100 nm	2100-2800 nm	Overall
Aluminium	0.00	0.69	0.36	0.28	0.62
Calcium	0.00	0.00	0.08	0.08	0.04
Chromium	0.00	0.01	0.00	0.01	0.00
Copper	0.09	0.01	0.00	0.01	0.10
Iron	0.12	0.32	0.13	0.17	0.36
Lead	0.30	0.57	0.63	0.12	0.61
Magnesium	0.01	0.05	0.08	0.06	0.09
Manganese	0.43	0.52	0.09	0.03	0.50
Nickel	0.03	0.00	0.01	0.02	0.06
Potassium	0.04	0.14	0.22	0.11	0.16
Sodium	0.00	0.16	0.09	0.05	0.15
Titanium	0.00	0.35	0.20	0.00	0.37
Vanadium	0.01	0.00	0.01	0.00	0.01
Zinc	0.19	0.35	0.00	0.01	0.35

Table 5.3 Initial correlations (R^2) for ATOFMS ion intensity of the identifying ion with PIXE mass concentrations located in different size bins and also for the total ATOFMS size range**.**

The correlations between the PIXE and ATOFMS data across the different size bins were also investigated and are shown in Table 5.3. In general, the best correlations were observed in the size bins which contained the highest proportion of the ion intensity. For example, the strongest correlations for aluminium and titanium were in the second and third size bins, indicating that crustal material is the major source of particles containing these metals. The best correlations for manganese and zinc were obtained in the first and second size bins, which corresponds to the presence of smaller particles likely produced from industrial emissions. The only noticeable exception is lead, where the best correlation was observed for the 1400-2100 size range, even though it represents only 6% of the total signal for the identifying ion. It is of note that the first and second bins, which contain the major portion of the ion intensity, also present strong correlations.

In this study, a good degree of quantitative agreement between ATOFMS and PIXE was only observed for a small number of metals. Results of similar quality were obtained when comparing ATOFMS peak area with 24 h-averaged elemental concentration data as determined by XRF (Snyder et al., 2009). However, in contrast to this study, strong quantitative relationships (no R^2 values reported) were observed for calcium and potassium, while lead displayed a poor correlation. The same type of ATOFMS was utilized in both studies and differences in instrumental performance can thus be ruled out (Snyder et al., 2009). Hence the most likely explanation for the observed difference is matrix effects due to differences in chemical composition of the particles measured at the two sites. Other factors of note include the occurrence of the metals in both datasets and the relative sensitivity of the PIXE and XRF techniques. In order to make a more direct comparison with the work of Snyder et al. the ATOFMS and PIXE data were averaged over 6, 12 and 24 hours to see if the correlations improved. For most elements, the correlations obtained for 6 hour averaging were not significantly different but good improvements were obtained for aluminium, manganese, titanium and zinc, with R^2 of 0.72, 0.69, 0.54 and 0.57 respectively. Extending the averaging time to 12 or 24 hours produced mixed results, with some elements showing a marked improvement (Al with $R^2 = 0.90$, Zn with $R^2 = 0.66$) but others showed a notable dis-improvement (Ca, Mn, Na). Thus, no clear advantage in extending the averaging time is obvious, especially since the benefits of the hourly time resolution are lost.

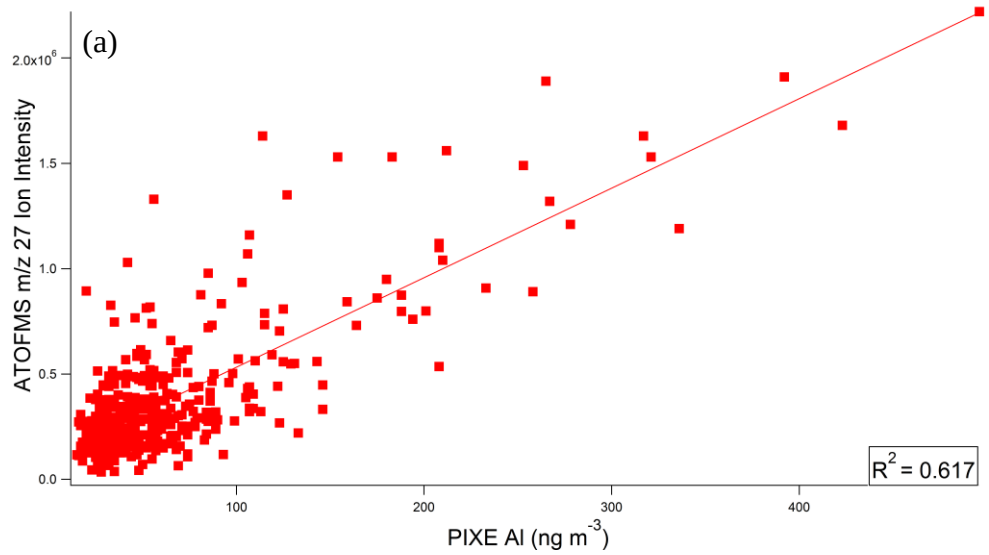
(a)
2.0x10^6
1.5
1.0
0.5
0.0
ATOFMS m/z 27 Ion Intensity
100
200
300
400
PIXE Al (ng m^-3)
R^2 = 0.617

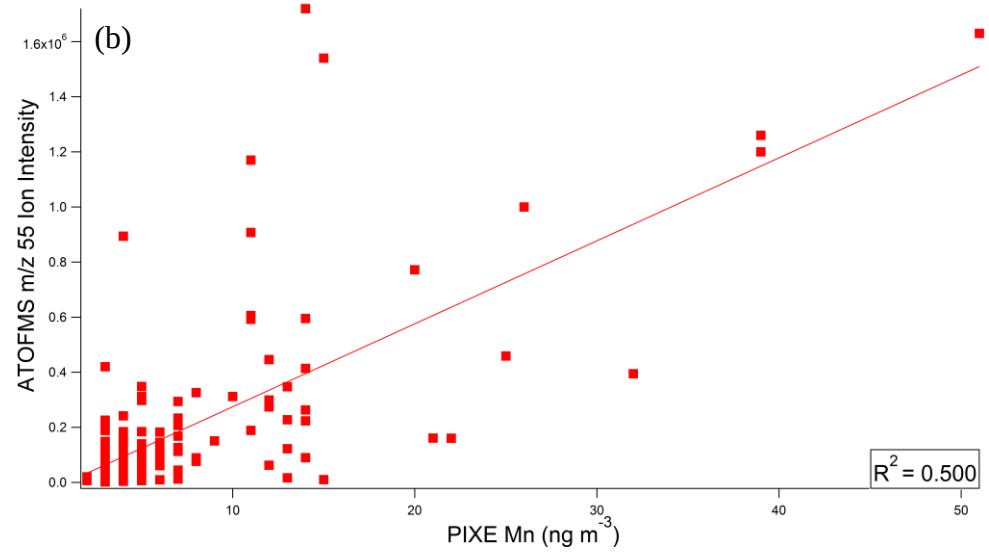
(b)
1.6x10^6
1.4
1.2
1.0
0.8
0.6
0.4
0.2
0.0
ATOFMS m/z 55 Ion Intensity
10
20
30
40
50
PIXE Mn (ng m^-3)
R^2 = 0.500

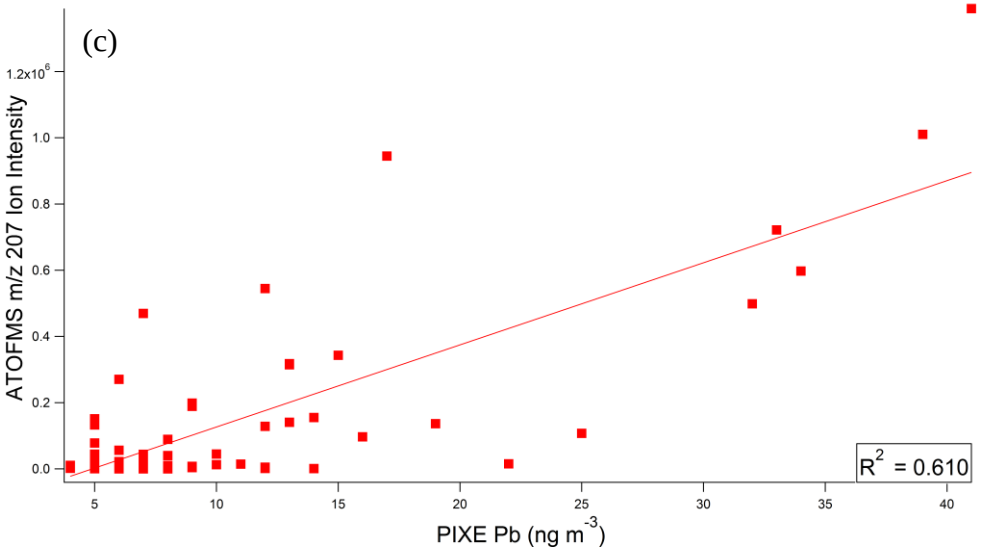
(c)
1.2x10^6
1.0
0.8
0.6
0.4
0.2
0.0
ATOFMS m/z 207 Ion Intensity
5
10
15
20
25
30
35
40
PIXE Pb (ng m^-3)
R^2 = 0.610

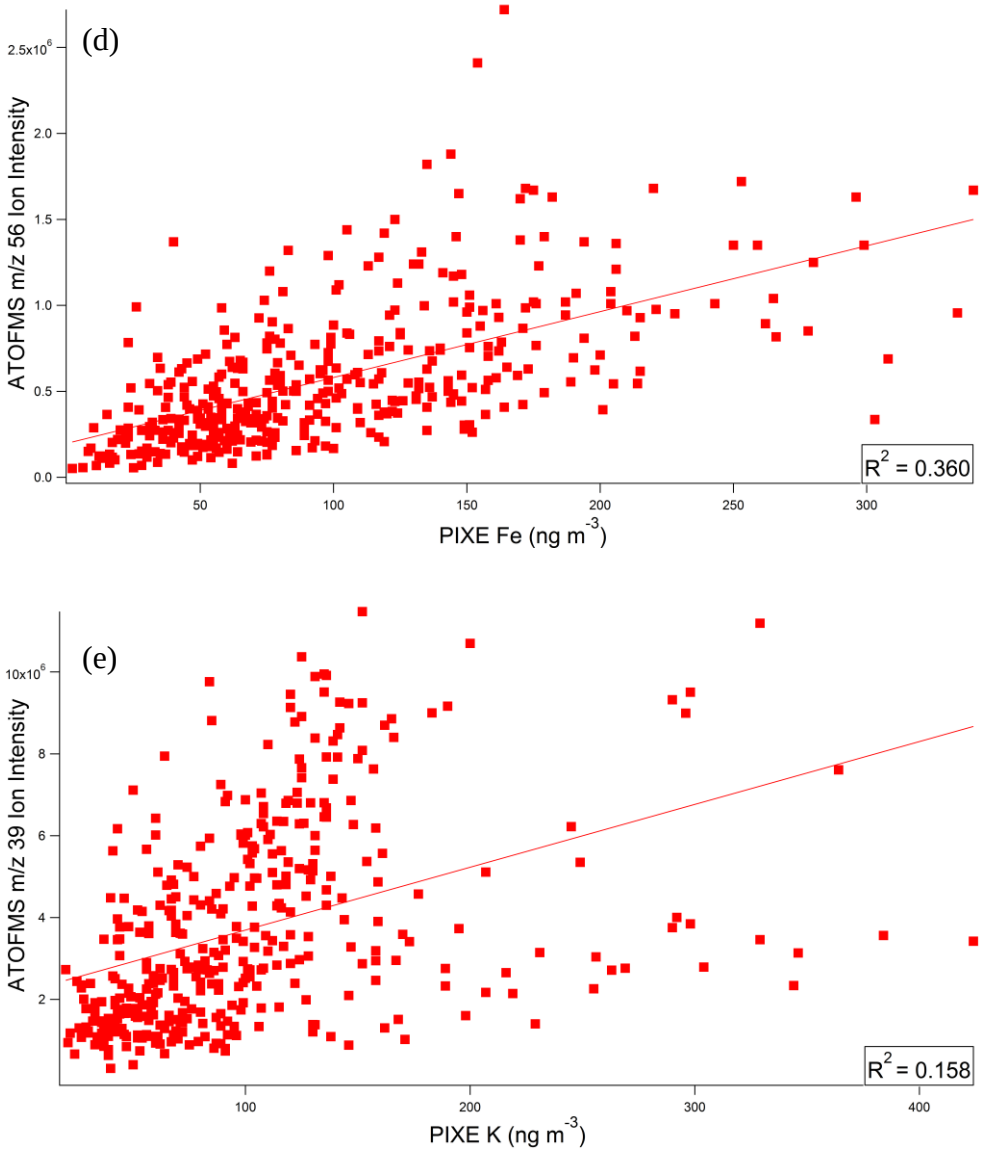

Figure 5.2 Correlations between ATOFMS Ion Intensity and PIXE mass concentrations for the following: (a) Aluminium (m/z 27), (b) Manganese (m/z 55), (c) Lead (m/z 207), (d) Iron (m/z 56) and (e) Potassium (m/z 39).

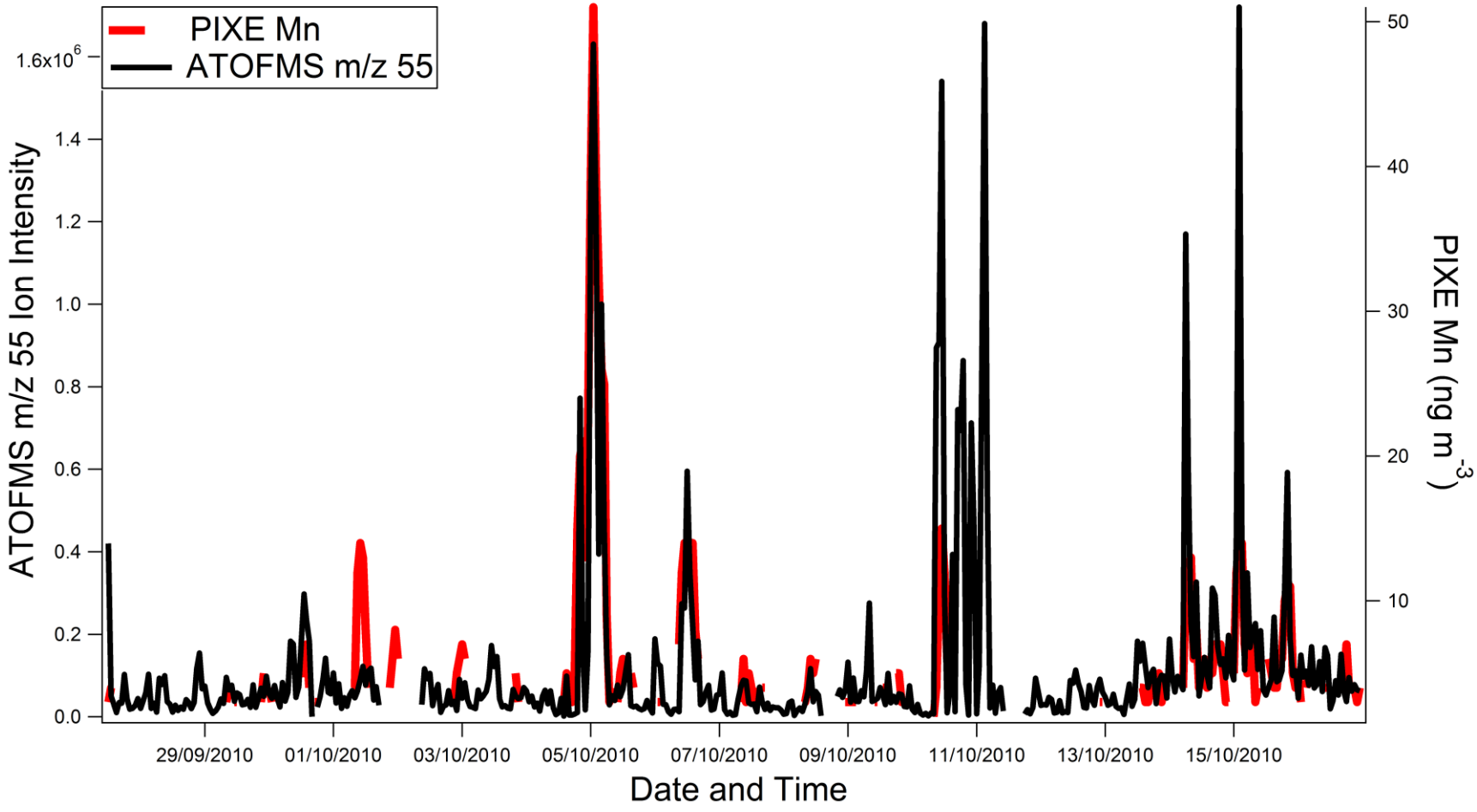

Figure 5.3 Temporal trends of both ATOFMS m/z 55 Ion Intensity and PIXE mass concentrations for Mn during the campaign

5.3.4 ATOFMS-PIXE inter-comparisons made during specific air mass events

During the measurement campaign the UB site was influenced by air masses originating from several different regions including the Atlantic Ocean, North Africa and Regional Europe (Dall'Osto et al., 2013b). Since particle composition is affected by the origin and path of air masses, the changes in ATOFMS and PIXE correlations were examined during the different meteorological regimes. The results are shown in Table 5.4 and indicate that the quantitative relationship for many of the metals varies greatly.

When the site was influenced by an Eastern North African air mass (North African 2) the aluminium correlation improved to $R^2 = 0.73$. During this period and in the Transition period immediately afterwards, the site was influenced by a particle type rich in aluminium, silicon and titanium, identified as Saharan dust (Dall'Osto et al. In Preparation). The correlation for aluminium did not improve during the North African 1 air mass as the particles originating from this area of the Western Sahara were found not to be rich in aluminium.

The strongest correlation found for calcium during the campaign was during the period designated Transition 3. At this time the correlation between ATOFMS ion signals and the PIXE concentration improves to $R^2 = 0.54$ and corresponds to an observed increase in the particle counts of the Soil-Ca particle type which has peaks associated with Ca, Na, Mg and K (Dall'Osto et al. In Preparation). The Soil-Ca particle type was also abundant during the North African 1 air mass but the Ca correlation is not good during this period, possibly due to processing or ageing of the particles, thus causing a matrix effect affecting the calcium signal detected by the ATOFMS.

During the Atlantic 2 air mass the R^2 values for manganese, lead and zinc all improved. This period corresponds to the highest counts of the ATOFMS Pb particle type which contains internally mixed Pb and Zn along with Na, Fe, K, nitrate and chloride (Dall'Osto et al. In Preparation). These elements have been previously associated with waste incineration (Moffet et al., 2008) and the Pb particle type detected here is also observed in short sharp events which suggest point source

emissions. The reason for the improved metal correlations during this period is likely due to the Atlantic air mass passing over industrialised zones picking up these emissions as they travel to the measurement site. While the Pb-Cl particle type average mass spectrum does not contain a clear peak for manganese, the temporal trend shows that both the ATOFMS ion signal at *m/z* 55 and the PIXE concentration increase measured during this period as shown in Figure 5.3. Manganese is associated with industrial emissions and the peak in the concentration of Mn during this period suggests that the air mass passed over an industrial zone.

While the overall correlation for sodium is very poor the correlation improved to R^2 = 0.92 during the Transition 2 period. During this period the air masses influencing the site change, however the local wind is very strongly associated with the WNW direction, corresponding to the incoming Atlantic air mass. The influx of sea-salt particles associated with marine air is likely the main reason for the improved correlation during this period.

The ATOFMS-PIXE correlation for iron improves during a number of different air mass periods. Iron is present in many of the particle types (Fe, Soil-Sahara, Soil-Ca, Pb, Oil-V) detected during the campaign and the nature of the correlation and matrix effects is likely very complicated. Nevertheless, the improved correlations can be attributed, at least in part, to the enhanced occurrence of certain particle types during specific periods, e.g. during the North African 2 air mass event where the Soil-Sahara particle type was prevalent.

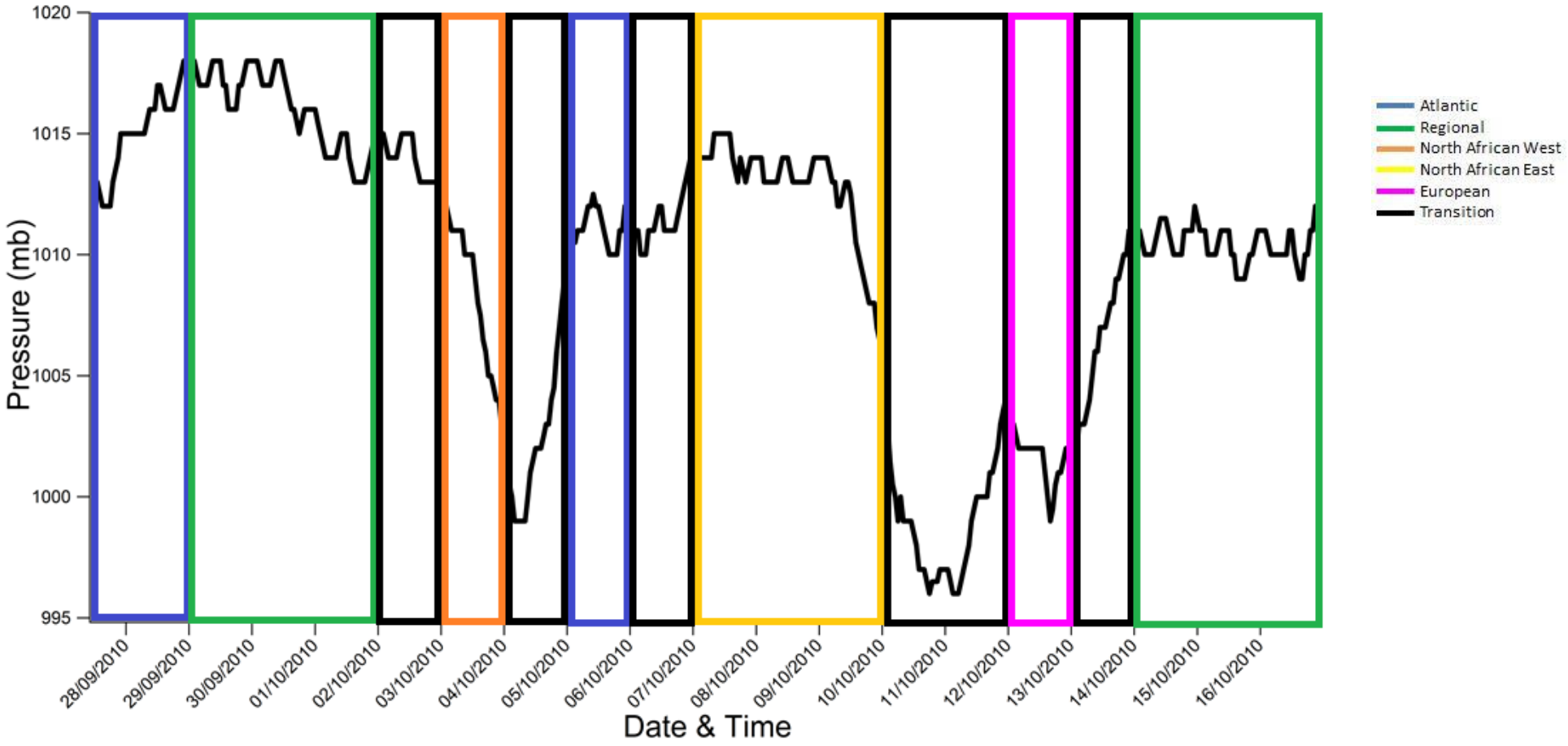

Figure 5.4 Atmospheric pressure (mb) profile obtained during the SAPUSS campaign plotted alongside air mass origins.

Air Mass	Overall	Atlantic 1	Regional 1	Transition 1	North African 1	Transition 2	Atlantic 2	Transition 3	North African 2	Transition 4	European	Transition 5	Regional 2
Local wind		Stagnant S	Stagnant E/ESE	Stagnant	Stagnant	WNW	Stagnant SW/SSW	Stagnant S	NE to E	W/WNW NE/ENE	NE/ENE	NE/ENE	NNW to WNW
Aluminium	0.62	0.01	0.25	0.24	0.06	0.00	0.18	0.37	0.73	0.60	0.37	0.28	0.17
Calcium	0.04	0.25	0.40	0.17	0.00	0.05	0.04	0.54	0.16	0.01	0.05	0.42	0.03
Iron	0.36	0.64	0.51	0.37	0.00	0.55	0.68	0.42	0.55	0.66	0.14	0.65	0.17
Lead	0.61	n/a	0.01	0.11	0.05	0.11	0.92	0.05	0.08	0.56	n/a	n/a	0.05
Magnesium	0.09	0.01	0.00	0.31	0.02	0.40	0.18	0.12	0.15	0.09	0.01	0.24	0.00
Manganese	0.50	0.08	0.04	0.02	0.18	0.32	0.89	0.47	0.03	0.48	0.02	0.14	0.42
Nickel	0.06	0.08	0.09	0.16	0.01	0.02	0.02	0.02	0.05	0.08	0.00	0.19	0.09
Potassium	0.16	0.04	0.01	0.44	0.00	0.00	0.31	0.25	0.56	0.04	0.03	0.59	0.45
Sodium	0.15	0.06	0.03	0.05	0.00	0.92	0.46	0.33	0.23	0.03	0.03	0.46	0.27
Titanium	0.37	0.15	0.21	n/a	0.21	0.44	0.10	0.00	0.32	n/a	n/a	n/a	0.34
Vanadium	0.01	n/a	0.05	0.04	0.01	n/a	n/a	n/a	0.27	n/a	n/a	n/a	0.08
Zinc	0.35	0.19	0.11	0.13	0.00	0.36	0.88	0.24	0.02	0.43	0.10	0.01	0.31

Table 5.4 Different correlations obtained during the different air mass events that influenced the measurement site during the SAPUSS campaign. Correlations with $R^2 \leq 0.50$ are shown in shaded boxes.

5.3.5 ATOFMS-PIXE inter-comparison within particle types

ART-2a Classes	Metals (*m/z*)
Soil-Sahara	Aluminium (27)
Soil-Ca and Soil-Sahara	Calcium (40)
Fe, Soil-Sahara, Soil-Ca, Pb, Oil-V	Iron (56)
Pb	Lead (207)
NaCl, NaCl-NIT, Soil-Ca, Soil-Sahara	Magnesium (24)
Pb, Fe, Oil-V	Manganese (55)
Fe, Pb	Nickel (58)
EC-Aged-L, K-CN, LRT-SUL Loc-NIT, Pb, Soil-Sahara, Veg-KP	Potassium (39)
NaCl, NaCl-NIT, Soil-Ca, Soil-Sahara, Fe, Pb, Oil-V, Veg-KP	Sodium (23)
Soil-Ca, Soil-Sahara	Titanium (48)
Oil-V, Fe	Vanadium (51)
Pb	Zinc (64)

Table 5.5 ART-2a classes queried for metal signals. Selected based on average spectra containing an ion signal for the ion of interest.

All results presented so far have been based on interrogating the whole ATOFMS dataset. However, some useful information may be obtained from examining the relationship between the mass concentrations measured by PIXE and the ion intensity of the metal located *within* the individual particle types (Dall'Osto et al. In Preparation). Specifically, this type of analysis could be beneficial for identifying matrix effects associated with the ATOFMS detection of different particle types.

The 14 particle types obtained by using the ART-2a analysis on the ATOFMS dataset collected at the UB site are listed in Table 5.5, along with the metals clearly present in the average mass spectra. The analysis was performed by determining the proportion of the metal ion signal within each of the selected particle types. The results are presented in Table 5.6 and show that many of the metals are present in several particle types. A peak for potassium is seen in 5 different particle types but it was found that the signal for *m/z* 39 can be mainly attributed to two particle types,

EC-Aged-L and Loc-NIT, which contain just over half of the total ion signal for the whole campaign. The calcium signal (*m/z* 40) is observed in both dust particle types, Soil-Ca and Soil-Sahara, which account for 37% of the total *m/z* 40 ion signal for the campaign. The Oil-V particle type is responsible for 37% of the V (*m/z* 51) ion signal, while 39% of signal for Fe (*m/z* 56) comes from the long-range transport of Fe detected during the accumulation period at the end of the campaign.

40% of the total signal associated with lead is in the ART-2a cluster called, Pb, suggesting that a large proportion of the lead detected by the ATOFMS during the campaign was associated with one specific particle type that is dominated by lead. Similarly a large proportion (66%) of the ion signal *m/z* 23 is attributed to the NaCl and Na-NIT particle types, indicating that the greater proportion of sodium measured by the ATOFMS during the campaign is from sea-salt. However, for magnesium (another metal associated with sea-salt), only 27% of the signal of *m/z* 24 can be ascribed to the sea-salt particle types but this is likely an underestimation of the total signal, as EC also contributed to the *m/z* 24 signal because of the presence of the C_2^+ ion. Finally, although aluminium was only found in one particle type, it contributed a mere 4% of the ion signal (*m/z* 27). This may be due to interference from the hydrocarbon fragment $C_2H_3^+$, as mentioned above.

The ion intensities of the various metals found within the different particle types was also compared with mass concentrations determined by PIXE; the corresponding R^2 values are listed in Table 5.6. Several metals show improved correlations when compared to the overall ATOFMS dataset. The R^2 for Mn increased from 0.50 for the whole ATOFMS dataset to 0.73 when comparing PIXE with the ATOFMS ion signal for *m/z* 55 in the Pb particle type as shown in Figure 5.5. Similarly zinc shows an improvement when its ion intensity is interrogated within a single class (Pb) from R^2 = 0.35 to 0.52. This shows that the ion intensity of these metals within the Pb class corresponds to a greater extent, compared to the overall signal, with the concentration of the metals as measured by PIXE. This process was also found to provide the best correlation for potassium, with R^2 = 0.42 when the ion signal for *m/z* 39 within the Loc-NIT particle type was correlated with the PIXE. However, quantification of potassium by ATOFMS is complicated due to its presence in many of the particle types and the matrix effects associated with them.

Element	*m/z*	Art 2a class	% of total signal	R^2
Aluminium	27	Soil-Sahara	4	0.45
Calcium	40	Soil-Ca	20	0.04
		Soil-Sahara	17	0.06
Iron	56	Soil-Ca	2	0.00
		Fe	39	0.12
		Pb	1	0.17
		Soil-Sahara	2	0.15
		Oil-V	1	0.00
Lead	207	Pb	40	0.29
Magnesium	24	Ca	1	0.00
		Na-NIT	16	0.01
		NaCl	11	0.07
		Soil-Sahara	1	0.07
Manganese	55	Pb	29	0.73
		V	0	0.01
		Fe	59	0.03
Potassium	39	EC-Aged-L	29	0.23
		K-CN	3	0.08
		Veg-KP	2	0.15
		LRT-Sul	6	0.00
		Loc-NIT	22	0.42
		Pb	0	0.00
		Soil-Sahara	0	0.22
Sodium	23	Soil-Ca	1	0.00
		Fe	1	0.00
		Veg-KP	1	0.01
		Na-NIT	41	0.05
		NaCl	25	0.09
		Pb	0	0.20
		Soil-Sahara	1	0.17
		V	0	0.00
Titanium	48	Soil-Ca	6	0.00
		Soil-Sahara	5	0.02
Vanadium	51	Fe	7	0.01
		Oil-V	37	0.03
Zinc	64	Pb		0.52

Table 5.6 Proportion of selected metals within specific ART-2a clusters. In other words, this represents the % of the total signal of a specific m/z in an ART-2a particle type. For example, 40% of the total signal of m/z 208 is in the ART-2a cluster termed Pb.

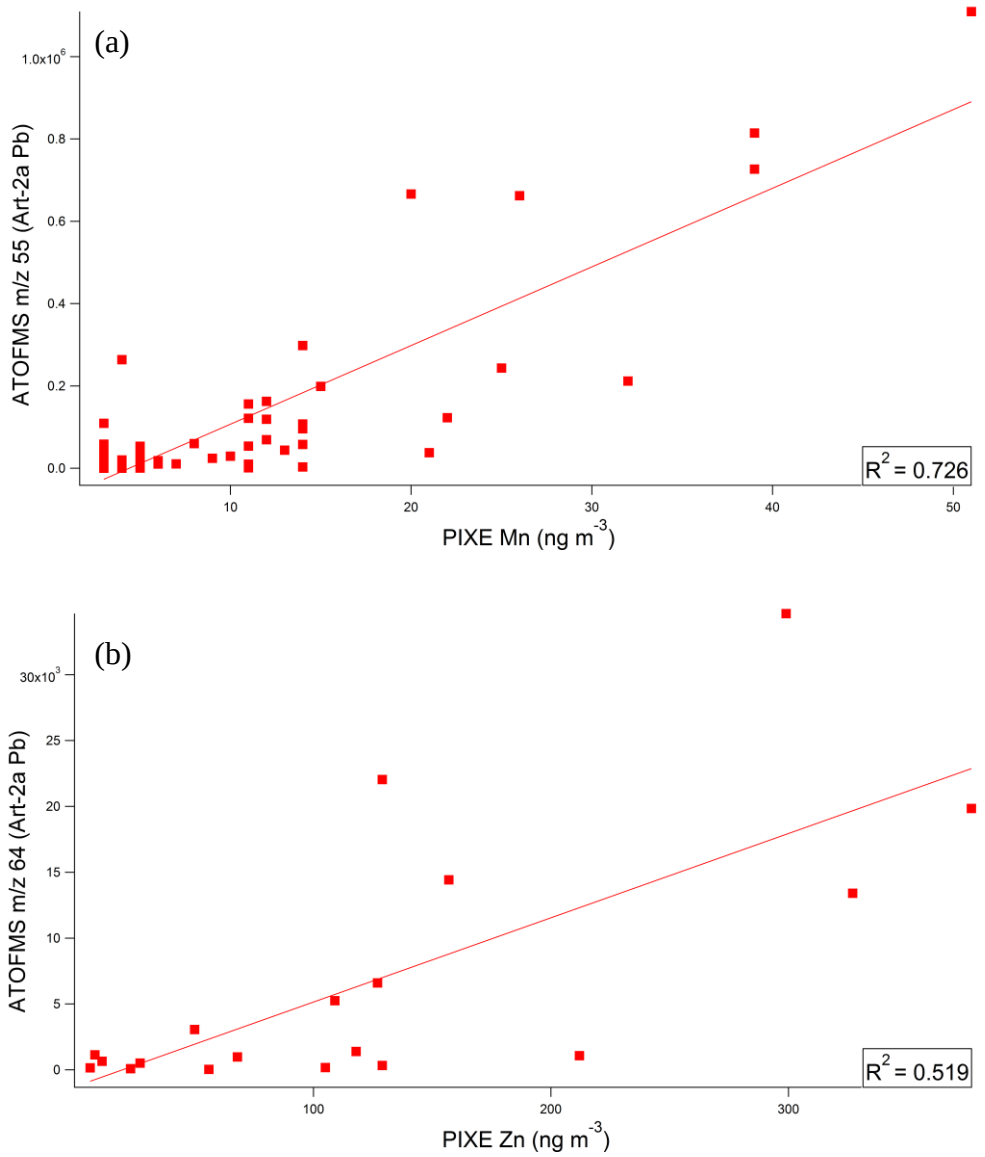

Figure 5.5 Correlations between PIXE and ATOFMS Ion Intensity within ART-2a Pb Class for (a) Manganese (m/z 55) and (b) Zinc (m/z 64)

Further analysis of the matrix effects was carried out by examining the relationship between the overall ATOFMS ion intensity and the PIXE mass concentration, with the ion intensity within the particle class of interest super-imposed using a colour scale. For example, the aluminium ATOFMS ion intensity and PIXE mass correlation is shown in Figure 5.6(a), where the colour-scale indicates the ion intensity within the Soil-Sahara particle type. The plot shows that the ion intensity within the Saharan dust particles follows both the overall ion intensity and the mass

concentration, suggesting that there is no matrix effect associated with this particle type and the ion intensity for aluminium within this particle type is directly related to the quantity of aluminium within the particle. In contrast, the ATOFMS appears to overstate the contribution of calcium in the same Soil-Sahara type as shown in Figure 5.6(b). This observation indicates that matrix effects can be highly dependent on the metal being analysed in the particle. However, the ATOFMS does not have a matrix effect associated with detection of Ca in the Soil-Ca particle type (Figure 5.6(c)), indicating that the mixing state of the metal also affects the quantitative aspect of the measurement.

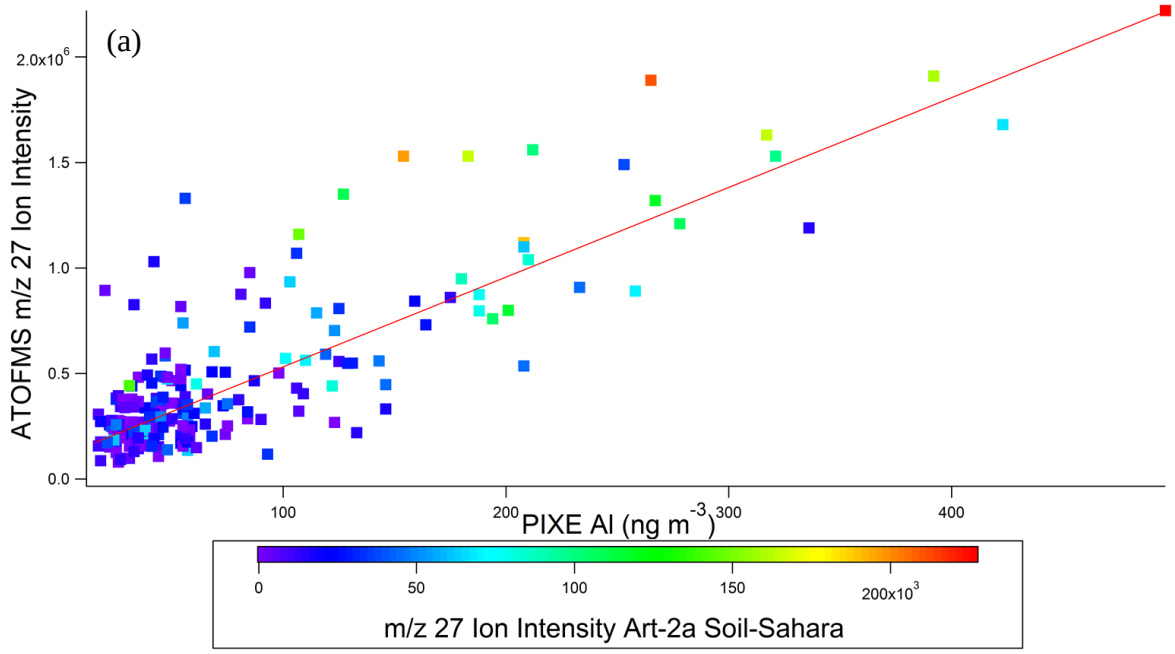

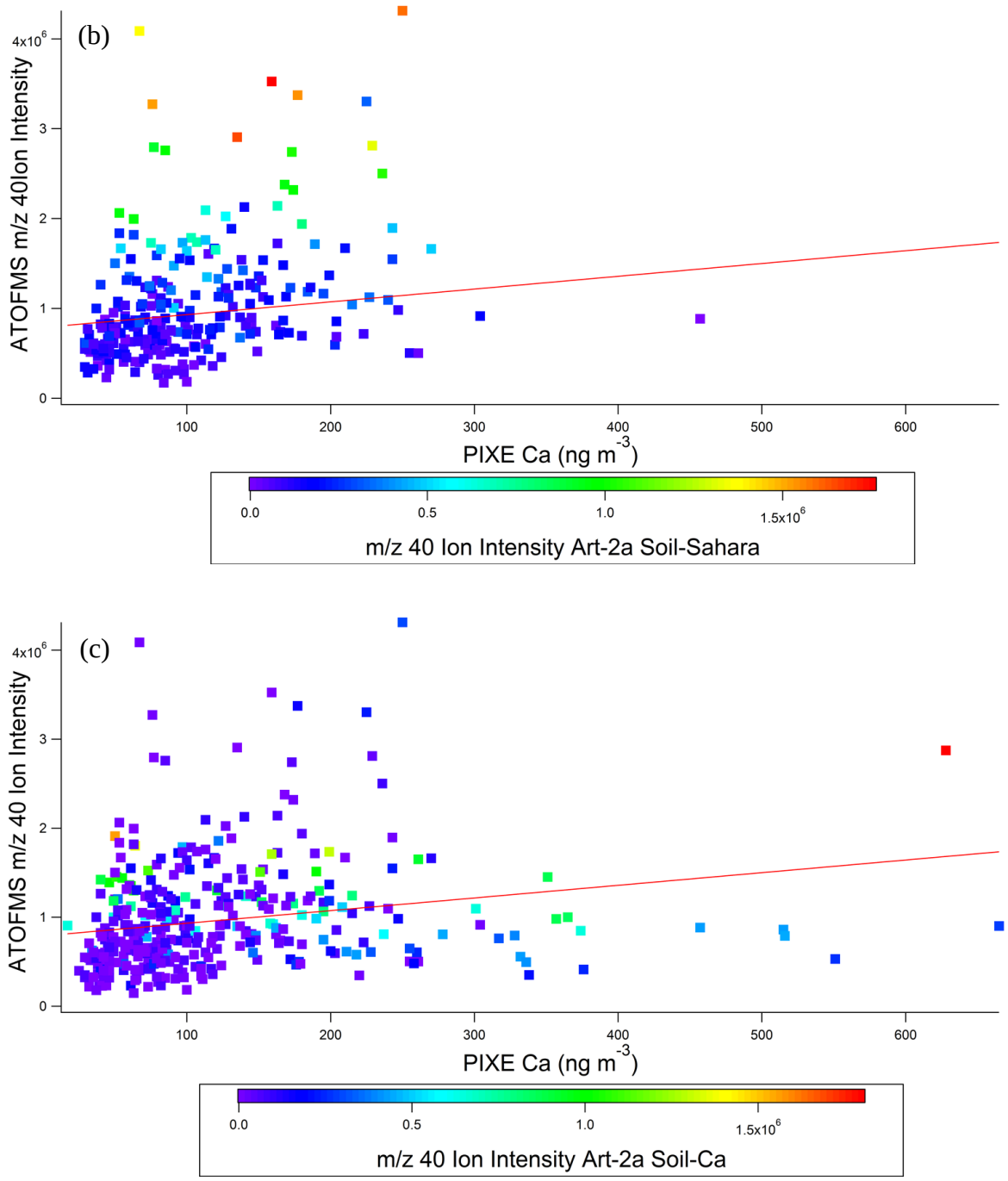

Figure 5.6 (a) Comparison between hourly integrated ATOFMS ion intensities for m/z 27 and PIXE Al. (Third factor (colour scale) m/z 27 Ion Intensity from ART-2a Soil-Sahara class). (b) Comparison of hourly integrated ATOFMS ion intensities m/z 40 and PIXE Ca. (Third factor (colour scale) m/z 40 Ion Intensity from within ART-2a Soil-Sahara class). (b) Comparison of hourly integrated ATOFMS ion intensities m/z 40 and hourly PIXE Ca concentrations. (Third factor (colour scale) m/z 40 Ion Intensity from within ART-2a Soil-Ca class).

As stated previously, the initial ATOFMS-PIXE correlations obtained for potassium were poor. However, the correlation plot shown in Figure 5.2(e) shows some distinct parts, which possibly indicate the presence of several different relationships within the correlation. Therefore these relationships were investigated in more detail and summarised as the colour scale plots shown in Figure 5.7. Three distinct areas exist in the plot. The first area includes a contribution associated with all the particle types investigated. The second is shown clearly in Figure 5.7(a) and is related to the highest intensity of the loc-NIT particle type; this area also shows a contribution from Soil-Sahara and Veg-KP particle types. The final correlation is shown in Figure 5.7(b) and is due to the EC-Aged-L particle type only. This latter area of the plot suggests that there is a matrix effect associated with this type of particle, which suppresses the amount of potassium detected by the ATOFMS. This relationship shows the highest concentration of potassium detected by PIXE during the whole campaign but the ATOFMS ion intensity does not match the high concentration. This investigation shows that potassium clearly presents complex behaviour with matrix effects that vary with chemical composition and particle type, which greatly complicates the ATOFMS-PIXE comparison.

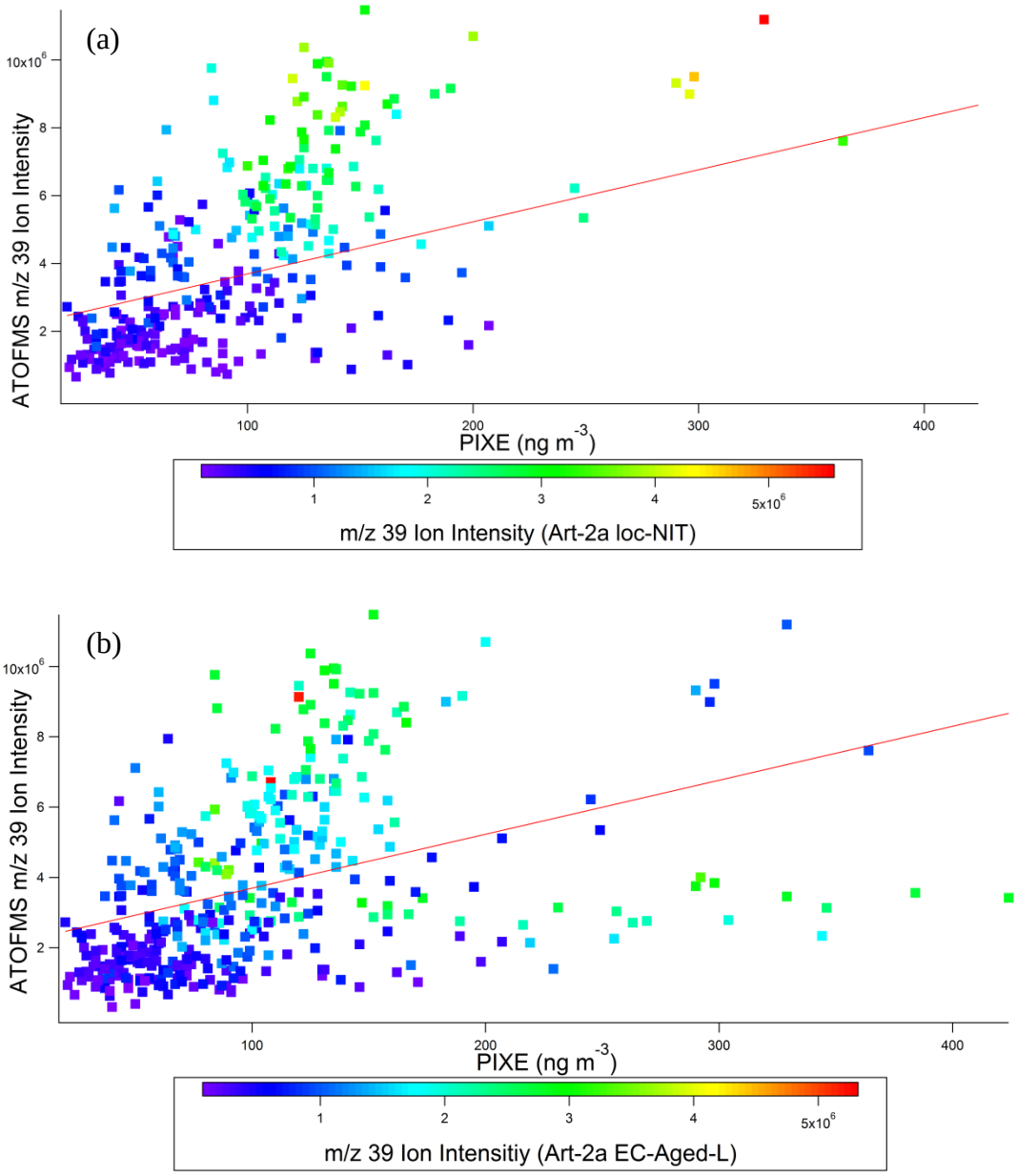

Figure 5.7 Comparison of hourly integrated ATOFMS ion intensities for m/z 39 with hourly PIXE K concentrations. (a) Third factor (colour scale) m/z 39 Ion Intensity from within ART-2a EC-Aged-L class. (b) Third factor (colour scale) m/z 39 Ion Intensity from within ART-2a Loc-NIT class.

Other metals were investigated using the same type of comparisons. Figure 5.8(a) shows a plot of ATOFMS ion intensity and PIXE concentration for iron with the colour scale showing the ion intensity within the Art-2a Fe particle type. The ATOFMS appears to overstate the iron contribution due to ART-2a Fe and when the

highest ion intensity is observed for this particle type, it does not coincide with the highest concentration of iron measured by PIXE. However Figure 5.8(b) shows that this effect is not apparent for the iron associated with the Soil-Sahara particle type. Such analysis suggests that there is an effect due to the differences in mixing state of iron in the particles. The ART-2a Fe class is the particle type that is associated with the highest proportion of iron measured by the ATOFMS and this result shows that the overall signal obtained by the ATOFMS is strongly influenced by this one particle type. It was observed that sodium and calcium, similar to iron were found to overestimate the metal contribution from specific particle types. The ATOFMS overestimates the sodium contribution from the sea-salt particle types along with the calcium contribution from the Soil-Ca particle type.

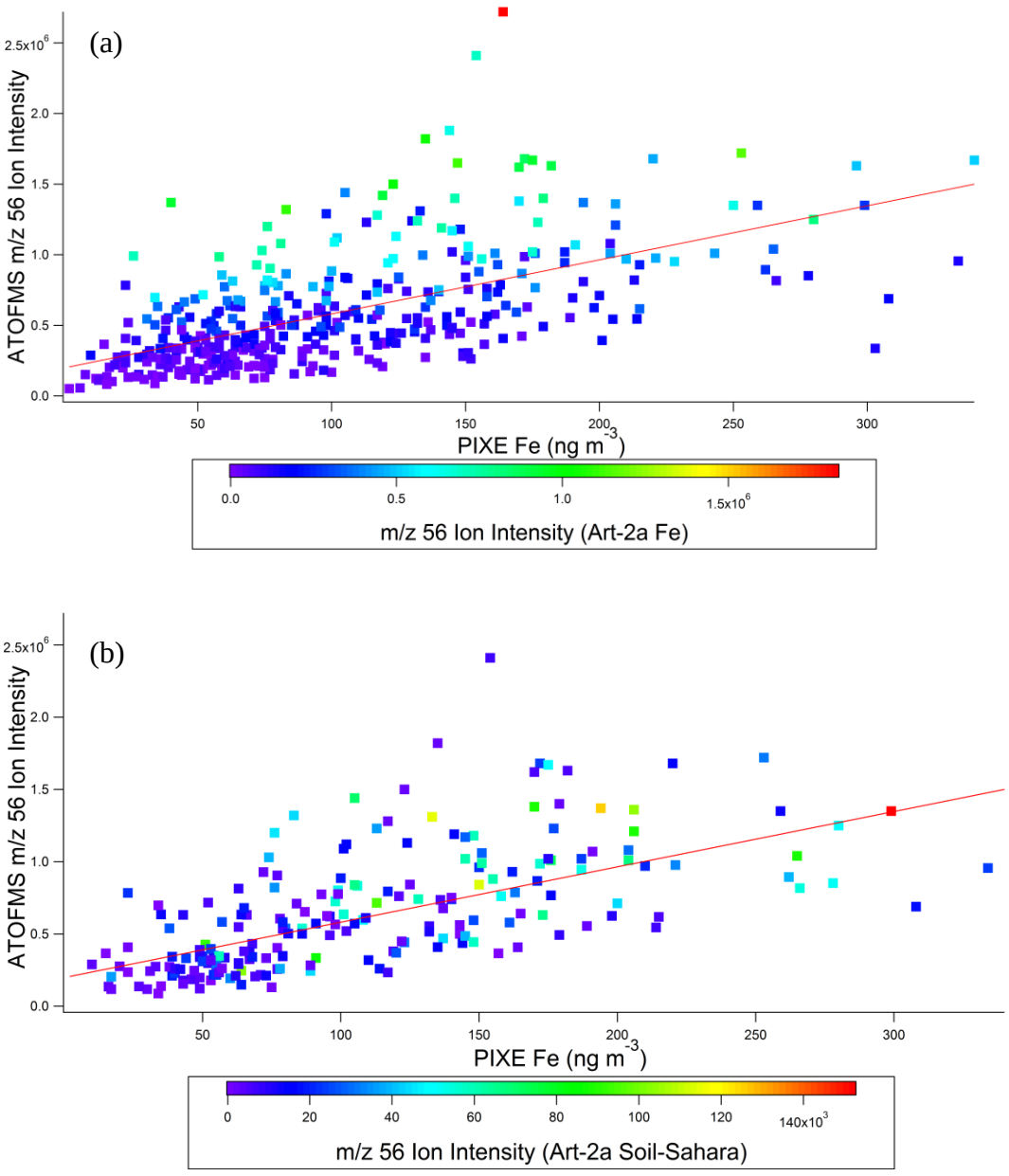

Figure 5.8 Comparison of hourly integrated ATOFMS ion intensities for m/z 56 with hourly PIXE Fe concentrations. (a) Third factor (colour scale) m/z 56 Ion Intensity from within ART-2a Fe class. (b) Third factor (colour scale) m/z 56 Ion Intensity from within ART- 2a Sahara class.

5.3.6 Ion Intensity correlations with PMF factors

The 1-hr resolution PIXE $PM_{2.5}$ aerosol mass data was used in source apportionment studies which resulted in identification of nine PMF factors attributed to different aerosol sources (Dall'Osto et al., 2013c). These PMF factors have also been included in the ATOFMS-PIXE inter-comparison performed here to examine if it results in improved correlations. Such an analysis may also be beneficial in discovering the mixing state of the metals associated with these PMF factors.

Figure 5.9 shows correlations obtained between the PMF factors and the ATOFMS data. It can be seen from the plots that both the titanium and aluminium present very strong correlations with the PMF soil factor. This result shows that the ATOFMS is capable of detecting the aluminium and titanium associated with soil particles (including the contribution from Saharan dust) in a manner that tracks concentrations. Manganese presents a good correlation with the PMF industrial factor.

Finally this analysis also benefits from an investigation of the matrix effects associated with the ATOFMS data. While the correlation between the ATOFMS ion intensity and PIXE mass for titanium was not very strong it can be seen that the correlation between the ATOFMS ion intensity and the PMF soil factor is quite strong. This result suggests that while the ATOFMS may not detect all titanium trends quantitatively it does respond to the presence of titanium from soil type emissions in a more quantitative fashion.

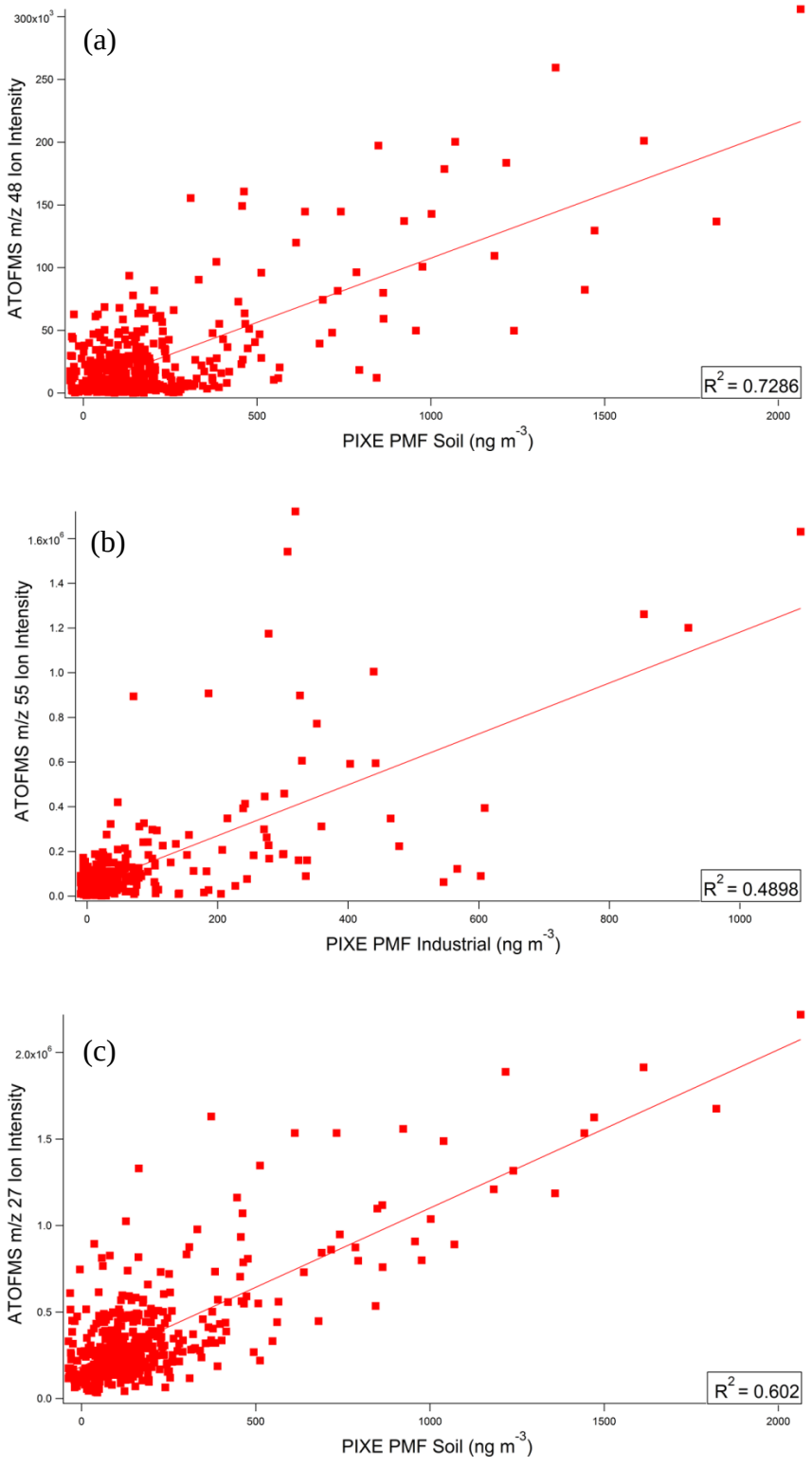

Figure 5.9 Correlations between ATOFMS Ion Intensity and PIXE PMF factors for the following; (a) Titanium (m/z 48) and PMF Soil factor, (b) Manganese (m/z 55) and PMF Industrial factor and (c) Aluminium (m/z 27) and PMF Soil factor

5.3.7 Comparison of ATOFMS operating with AFL inlet and PIXE

The ATOFMS dataset obtained at the RS site was also examined for a range of metals using the same approach as detailed above and compared with PIXE measurements of elemental concentrations at the same site. For aluminium it can be seen from the plot shown in Figure 5.10(a) that there are two clear trends in the relationship between the ATOFMS ion signal and the PIXE mass concentrations. The first is marked in blue and contains the correlation between the PIXE aluminium concentration and the appropriate ATOFMS ion signal. The second relationship marked in red represents the interference from the presence of the hydrocarbon fragment $C_2H_3^+$, which also has its ion signal at *m/z* = 27^+. In this section of the relationship the ATOFMS ion signal increases but the PIXE concentration does not respond in a similar fashion. In other words the increased ion intensity observed for the ATOFMS data does not originate with an increase in the concentration of the ambient aluminium levels. The colour scale added to the correlation in Figure 5.10(a) is the PMF soil factor which is the factor associated with the aluminium-rich Saharan dust (Dall'Osto et al., 2013c). The results again show two clear relationship sections with the area marked in blue containing a strong association with the soil factor and the area marked in red showing no association with the soil factor. In fact the soil factor is the major source of aluminium detected during the campaign. When the ATOFMS *m/z* 27 ion signal and the PIXE concentration were examined for just the period of the Saharan dust intrusion (7-9 October) the correlation improves to R^2=0.34.

The temporal trend shown in Figure 5.10(b) indicates that the ATOFMS signal relationship with the concentration changes over the course of the campaign and the presence of the OC fragment, $C_2H_3^+$, may be the largest reason for the difference between the two trends.

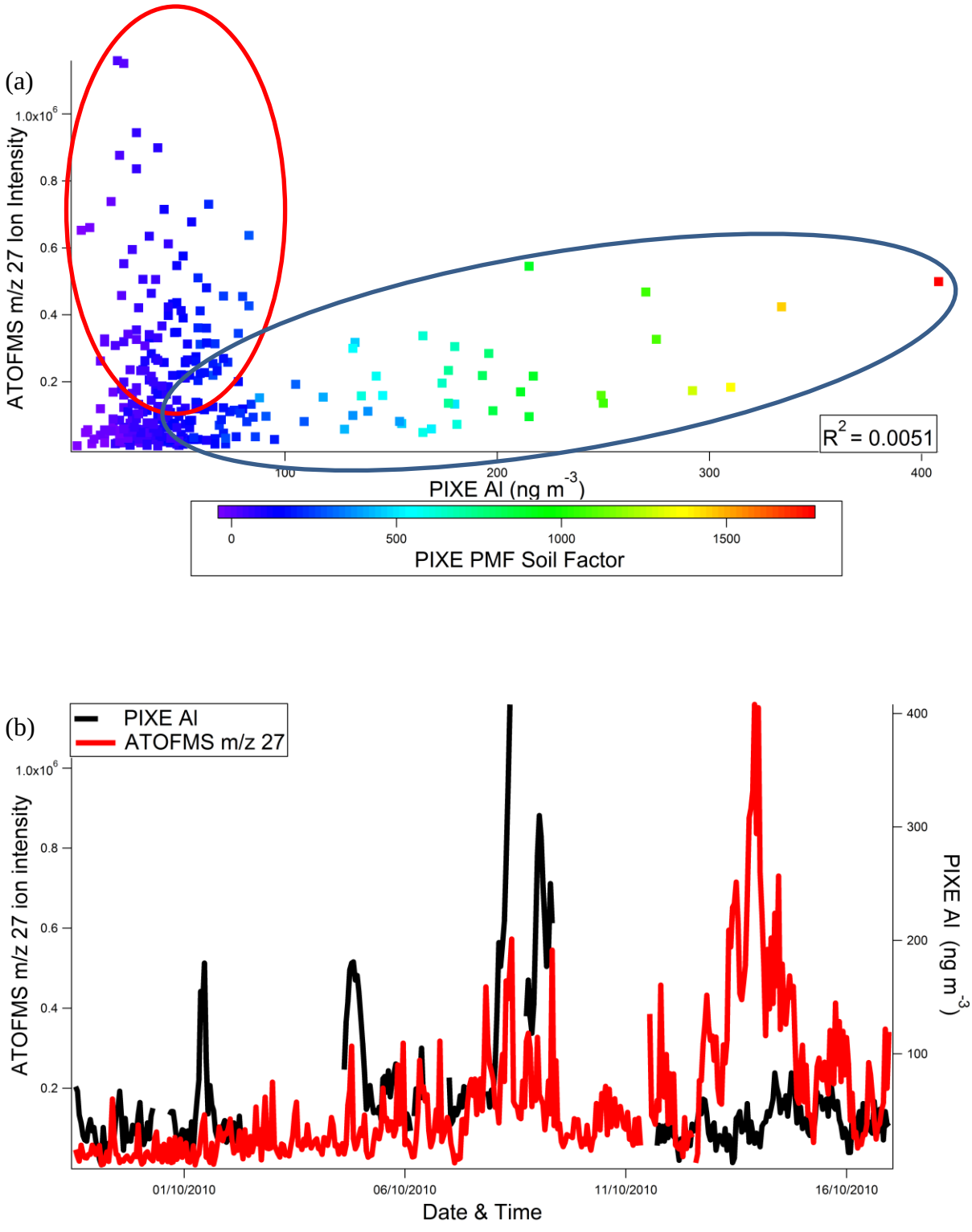

Figure 5.10 (a) Comparison of hourly integrated ATOFMS ion intensities for m/z 27 with hourly PIXE Al concentrations. Third factor (colour scale) PIXE PMF soil factor. (b)Temporal trends of both ATOFMS m/z 27 Ion Intensity and PIXE mass concentrations for Al during the campaign

The ATOFMS-PIXE plot for iron (Figure 5.11(a)) also shows two distinct relationships. The first is marked in blue and contains the actual concentration of the iron present during the campaign measured with PIXE. The second relationship marked in red is one that follows the stronger ATOFMS signal and the ART-2a Fe particle class but not with the actual concentration of iron. This suggests that the ATOFMS has an associated matrix effect in its response to the quantity of iron present in particle. It can be seen that the ATOFMS clearly overestimates the presence of iron in the ART-2a Fe particle type while the ATOFMS response for other particles containing iron underestimates the actual quantity of iron present.

Figure 5.11(b) shows the temporal profile of the PIXE iron concentration and the ATOFMS ion signal. A change in relationship between the two trends is observed during the regional stagnation at the end of the campaign. Prior to the stagnation the PIXE is the dominant trend but this relationship changes with the ATOFMS signal becoming dominant. During the stagnation an increase in the Fe particle type was observed in the ATOFMS data. As noted above the ATOFMS overestimates the quantity of iron in this particle type leading to the large increase in ion intensity altering the relationship.

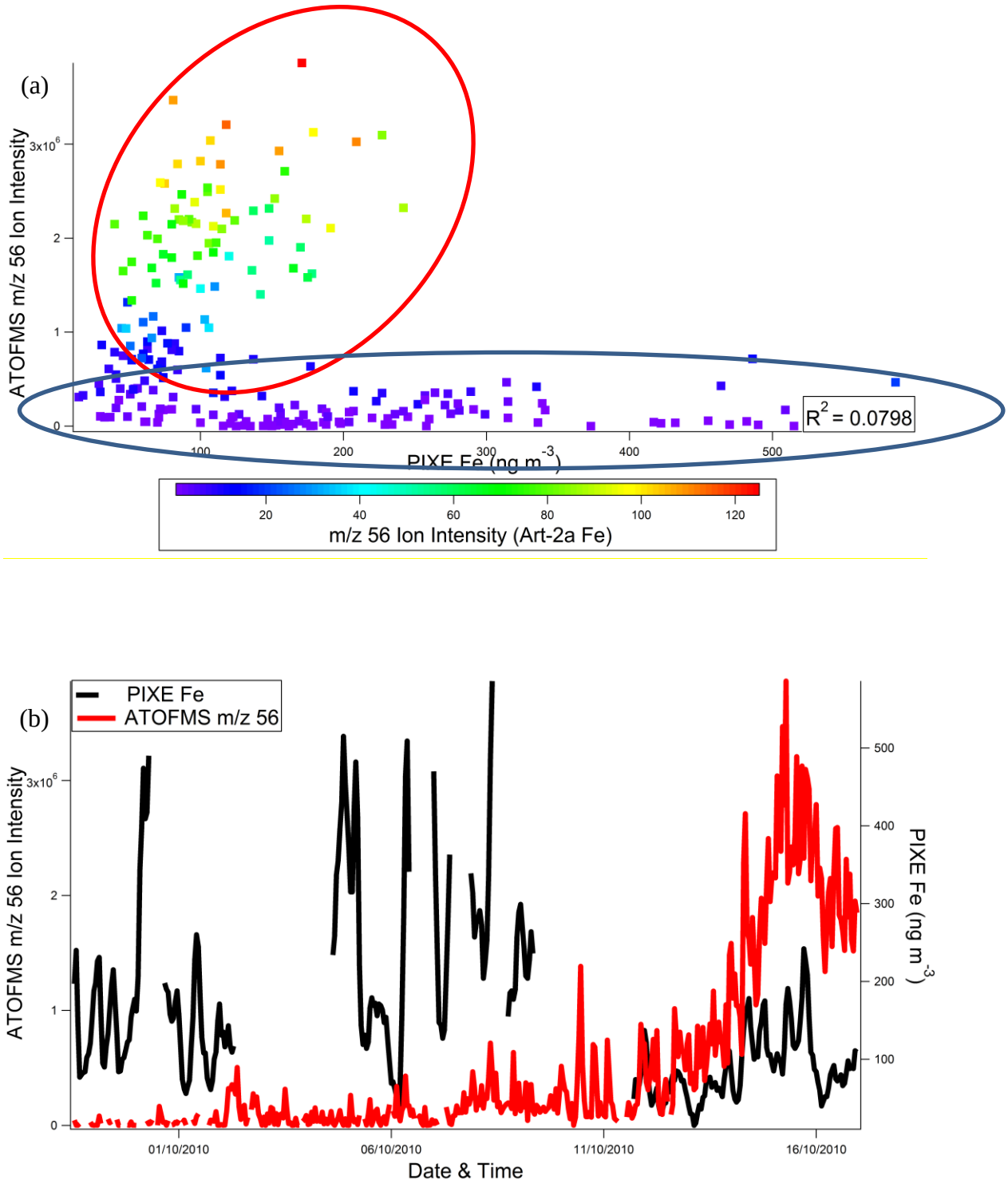

Figure 5.11 (a). Comparison between hourly integrated ATOFMS ion intensities for m/z 56 and hourly PIXE Fe concentrations. Third factor (colour scale) m/z 56 Ion Intensity (ART-2a Fe) (b) Temporal trends of both ATOFMS m/z 56 Ion Intensity and PIXE mass concentration for Fe during the campaign

Element (*m/z*)	R^2
Aluminium (27)	0.01
Copper (63)	0.05
Iron (56)	0.08
Lead (208)	0.02
Magnesium (24)	0.02
Manganese (55)	000
Nickel (58)	0.06
Potassium (39)	0.01
Sodium (23)	0.00
Titanium (48)	0.07
Vanadium (51)	0.00
Zinc (64 and 66)	0.00

Table 5.7 Correlation between PIXE concentration and ATOFMS ion intensity measured at the road site using the ATOFMS 3800 operating with AFL 100

During this analysis it quickly became apparent that the correlations between ATOFMS and PIXE were very poor, Table 5.7. The highest was R^2 =0.08 for Fe. The poor correlations are most likely due to the type of ATOFMS that was located at RS, which employed an aerodynamic focusing lens in the sampling region of the instrument. The aerodynamic lens has a high detection efficiency for smaller particles (Su et al., 2004) such as those produced by combustion. Many of the carbonaceous fragments have the same *m/z* as those of many metals, thus causing isobaric interference. The transmission efficiency of the AFL also results in only a small portion of super-micron particles being sampled and so this aspect of the collection process results in dust and sea-salt particles not being analysed. Hence a large fraction of metal-containing particles were not sampled efficiently, thereby resulting in any correlation with the quantitative measurements being compromised.

5.4. Conclusions

This work shows that the ATOFMS is a very powerful technique for characterising the mixing state of metal-containing particles which is not measurable using off-line techniques. The ATOFMS was found to respond strongly to ambient concentrations of several metals, namely, aluminium, lead, manganese and zinc. However, it was found that matrix effects associated with the detection of different elements can be significant, which makes the *quantitative* determination of metal concentrations difficult. ATOFMS is still very useful for monitoring short-lived emissions of particles. In contrast conventional filter measurements provide no information on these often important events. Hence while the quantification of UB and RS data was problematic due to the matrix effects associated with the particles it was found that when the data was analysed under certain conditions (e.g. during specific air masses or when monitoring specific particle or emission types like industrial emissions vs general background/ambient) the quantifications improved.

The quantitative performance of the ATOFMS clearly improved for certain metals under specific meteorological conditions. This finding may be due to specific particle types associated with the differing air mass origins or to increases in concentration of specific particle type during the event itself. For example during the NAF air mass the aluminium correlation showed an improvement due to the influence of Saharan dust. Similarly the improvement in the correlations observed for Mn, Zn and Pb are due to the sampling location being influenced by specific particles (Pb particle type). During these periods the enhanced occurrence of certain particle types can improve the observed correlations as any detection efficiencies associated with the quantification of trace metals by PIXE may be accounted for. Further, the ATOFMS ion signal may be improved as the domination of a specific particle type results in matrix effects being removed from the sampling.

It was also found that the ATOFMS which uses a converging nozzle inlet detects the presence of metals in particles more effectively than the one fitted with an aerodynamic focussing lens (AFL). Differences in the operating procedures of the two instruments are the likely cause of the observed difference in the detection of metals. The lens ATOFMS favours the detection of sub-micron particles and is

dominated by combustion aerosols, resulting in the ion signal for the metals of interest being interfered with by *m/z* fractions associated with organic fragments. The nozzle inlet favours the detection of super-micron particles and therefore the interference associated with organic fragments is not as problematic.

5.5 References

Allen, A.G., Nemitz, E., Shi, J.P., Harrison, R.M., Greenwood, J.C., 2001. Size distributions of trace metals in atmospheric aerosols in the United Kingdom. Atmospheric Environment 35, 4581-4591.

Bukowiecki, N., Hill, M., Gehrig, R., Zwicky, C.N., Lienemann, P., Hegedüs, F., Falkenberg, G., Weingartner, E., Baltensperger, U., 2005. Trace Metals in Ambient Air: Hourly Size-Segregated Mass Concentrations Determined by Synchrotron-XRF. Environmental Science & Technology 39, 5754-5762.

Calvo, A.I., Alves, C., Castro, A., Pont, V., Vicente, A.M., Fraile, R., 2013. Research on aerosol sources and chemical composition: Past, current and emerging issues. Atmospheric Research 120–121, 1-28.

Calzolai, G., Chiari, M., Lucarelli, F., Mazzei, F., Nava, S., Prati, P., Valli, G., Vecchi, R., 2008. PIXE and XRF analysis of particulate matter samples: an inter-laboratory comparison. Nuclear Instruments and Methods in Physics Research Section B: Beam Interactions with Materials and Atoms 266, 2401-2404.

Chiari, M., Lucarelli, F., Mazzei, F., Nava, S., Paperetti, L., Prati, P., Valli, G., Vecchi, R., 2005. Characterization of airborne particulate matter in an industrial district near Florence by PIXE and PESA. X-Ray Spectrometry 34, 323-329.

D'Alessandro, A., Lucarelli, F., Mandò, P.A., Marcazzan, G., Nava, S., Prati, P., Valli, G., Vecchi, R., Zucchiatti, A., 2003. Hourly elemental composition and

sources identification of fine and coarse PM10 particulate matter in four Italian towns. Journal of Aerosol Science 34, 243-259.

Dall'Osto, M., Beddows, D., Gielt, J., Harrison, R., McGillicuddy, E.J., Wenger, J., Alastuey, A., Querol, X., On the simultaneous deployment of single particle mass spectrometry at an urban background and a road site during SAPUSS. In Preparation.

Dall'Osto, M., Booth, M.J., Smith, W., Fisher, R., Harrison, R.M., 2008. A study of the size distributions and the chemical characterization of airborne particles in the vicinity of a large integrated steelworks. Aerosol Science and Technology 42, 981-991.

Dall'Osto, M., Harrison, R.M., Beddows, D.C.S., Freney, E.J., Heal, M.R., Donovan, R.J., 2006. Single-particle detection efficiencies of aerosol time-of-flight mass spectrometry during the North Atlantic marine boundary layer experiment. Environmental Science & Technology 40, 5029-5035.

Dall'Osto, M., Ovadnevaite, J., Ceburnis, D., Martin, D., Healy, R., O'Connor, I., Kourtchev, I., Sodeau, J., Wenger, J., O'Dowd, C., 2013a. Characterization of urban aerosol in Cork city (Ireland) using aerosol mass spectrometry. Atmospheric Chemistry and Physics 13, 4997-5015.

Dall'Osto, M., Querol, X., Alastuey, A., Minguillon, M.C., Alier, M., Amato, F., Brines, M., Cusack, M., Grimalt, J.O., Karanasiou, A., Moreno, T., Pandolfi, M., Pey, J., Reche, C., Ripoll, A., Tauler, R., Van Drooge, B.L., Viana, M., Harrison, R.M., Gietl, J., Beddows, D., Bloss, W., O'Dowd, C., Ceburnis, D., Martucci, G., Ng, N.L., Worsnop, D., Wenger, J., Mc Gillicuddy, E., Sodeau, J., Healy, R., Lucarelli, F., Nava, S., Jimenez, J.L., Gomez Moreno, F., Artinano, B., Prévôt, A.S.H., Pfaffenberger, L., Frey, S., Wilsenack, F., Casabona, D., Jiménez-Guerrero, P., Gross, D., Cots, N., 2013b. Presenting SAPUSS: Solving Aerosol Problem by Using Synergistic Strategies in Barcelona, Spain. Atmospheric Chemistry and Physics 13, 8991-9019.

Dall'Osto, M., Querol, X., Amato, F., Karanasiou, A., Lucarelli, F., Nava, S., Calzolai, G., Chiari, M., 2013c. Hourly elemental concentrations in PM 2.5

aerosols sampled simultaneously at urban background and road site during SAPUSS–diurnal variations and PMF receptor modelling. Atmospheric Chemistry and Physics 13, 4375-4392.

Gard, E., Mayer, J.E., Morrical, B.D., Dienes, T., Fergenson, D.P., Prather, K.A., 1997. Real-time analysis of individual atmospheric aerosol particles: Design and performance of a portable ATOFMS. Analytical Chemistry 69, 4083-4091.

Gross, D.S., Barron, A.R., Sukovich, E.M., Warren, B.S., Jarvis, J.C., Suess, D.T., Prather, K.A., 2005. Stability of single particle tracers for differentiating between heavy- and light-duty vehicle emissions. Atmospheric Environment 39, 2889-2901.

Healy, R.M., O'Connor, I.P., Hellebust, S., Allanic, A., Sodeau, J.R., Wenger, J.C., 2009. Characterisation of single particles from in-port ship emissions. Atmospheric Environment 43, 6408-6414.

Kelly, F.J., Fussell, J.C., 2012. Size, source and chemical composition as determinants of toxicity attributable to ambient particulate matter. Atmospheric Environment 60, 504-526.

Menzel, N., Schramel, P., Wittmaack, K., 2002. Elemental composition of aerosol particulate matter collected on membrane filters: A comparison of results by PIXE and ICP-AES. Nuclear Instruments and Methods in Physics Research Section B: Beam Interactions with Materials and Atoms 189, 94-99.

Moffet, R.C., Desyaterik, Y., Hopkins, R.J., Tivanski, A.V., Gilles, M.K., Wang, Y., Shutthanandan, V., Molina, L.T., Abraham, R.G., Johnson, K.S., Mugica, V., Molina, M.J., Laskin, A., Prather, K.A., 2008. Characterization of aerosols containing Zn, Pb, and Cl from an industrial region of Mexico City. Environmental Science & Technology 42, 7091-7097.

Moreno, T.Q., X. Alastuey, A. Reche, C. Cusack, M. Amato, F. Pandolfi, M. Pey, J. Richard, A. Prévôt, A. S. H. Furger, M. Gibbons, W., 2011. Variations in

time and space of trace metal aerosol concentrations in urban areas and their surroundings. Atmospheric Chemistry and Physics 11, 9415- 9430.

Pope, C.A., Dockery, D.W., 2006. Health Effects of Fine Particulate Air Pollution: Lines that Connect. Journal of the Air & Waste Management Association 56, 709-742.

Pöschl, U., 2005. Atmospheric Aerosols: Composition, Transformation, Climate and Health Effects. Angewandte Chemie International Edition 44, 7520-7540.

Prather, K.A., Nordmeyer, T., Salt, K., 1994. Real-time characterization of individual aerosol-particles using time-of-flight mass-spectrometry. Analytical Chemistry 66, 1403-1407.

Prati, P., Zucchiatti, A., Tonus, S., Lucarelli, F., Mandò, P.A., Ariola, V., 1998. A testing technique of streaker aerosol samplers via PIXE analysis. Nuclear Instruments and Methods in Physics Research Section B: Beam Interactions with Materials and Atoms 136–138, 986-989.

Prati, P., Zucchiatti, A., Lucarelli, F., Mandò, P.A., 2000. Source apportionment near a steel plant in Genoa (Italy) by continuous aerosol sampling and PIXE analysis. Atmospheric Environment 34, 3149-3157.

Pratt, K.A., Prather, K.A., 2009. Real-Time, Single-Particle Volatility, Size, and Chemical Composition Measurements of Aged Urban Aerosols. Environmental Science & Technology 43, 8276-8282.

Pratt, K.A., Prather, K.A., 2012a. Mass spectrometry of atmospheric aerosols—Recent developments and applications. Part I: Off-line mass spectrometry techniques. Mass Spectrometry Reviews 31, 1-16.

Pratt, K.A., Prather, K.A., 2012b. Mass spectrometry of atmospheric aerosols—Recent developments and applications. Part II: On-line mass spectrometry techniques. Mass Spectrometry Reviews 31, 17-48.

Querol, X., Alastuey, A., Rosa, J.d.l., Sánchez-de-la-Campa, A., Plana, F., Ruiz, C.R., 2002. Source apportionment analysis of atmospheric particulates in an

industrialised urban site in southwestern Spain. Atmospheric Environment 36, 3113-3125.

Reilly, P.T.A., Lazar, A.C., Gieray, R.A., Whitten, W.B., Ramsey, J.M., 2000. The elucidation of charge-transfer-induced matrix effects in environmental aerosols via real-time aerosol mass spectral analysis of individual airborne particles. Aerosol Science and Technology 33, 135-152.

Silva, P.J., Prather, K.A., 2000. Interpretation of mass spectra from organic compounds in aerosol time-of-flight mass spectrometry. Analytical Chemistry 72, 3553-3562.

Snyder, D.C., Schauer, J.J., Gross, D.S., Turner, J.R., 2009. Estimating the contribution of point sources to atmospheric metals using single-particle mass spectrometry. Atmospheric Environment 43, 4033-4042.

Song, X.H., Hopke, P.K., Fergenson, D.P., Prather, K.A., 1999. Classification of single particles analyzed by ATOFMS using an artificial neural network, ART-2A. Analytical Chemistry 71, 860-865.

Su, Y.X., Sipin, M.F., Furutani, H., Prather, K.A., 2004. Development and characterization of an aerosol time-of-flight mass spectrometer with increased detection efficiency. Analytical Chemistry 76, 712-719.

Suess, D.T., Prather, K.A., 2002. Reproducibility of single particle chemical composition during a heavy duty diesel truck dynamometer study. Aerosol Science and Technology 36, 1139-1141.

U.S.EPA, 2009. EPA U.S. Integrated Science Assessment for Particulate Matter (Final Report). U.S. Environmental Protection Agency, Washington, DC, EPA/600/R-08/139F, 2009.

6. Summary

During this study an Aerosol Time of Flight Mass Spectrometer (ATOFMS) was deployed at two urban background locations in Paris and Barcelona as part of the MEGAPOLI and SAPUSS monitoring campaigns respectively. The ATOFMS provided the size-resolved chemical composition of atmospheric single particles in the size range 100 to 3000 nm in real-time. The single particle information collected was then analysed by application of the *K*-means algorithm in order to generate a list of particle types influencing the monitoring sites during sampling. The particle types identified during these campaigns were used to determine the nature and origins of particles at the urban locations to investigate local and regional particle sources and the influence of regional transport on PM composition in urban areas.

In Paris the ATOFMS was operated with an Aerodynamic Focusing Lens (TSI AFL 100) and collected a total of 1742992 size-resolved single particle dual ion mass spectra. 1686229 of the particles were attributed to 18 particle types: EC Biomass, Fresh Biomass OC, Aged Biomass OC, ECOCSOx, ECOCNOx, OCNOx, OCSOx, Transported Biomass OC, Amine Rich, Fe-Rich, Oil-V, Incineration (Pb-Cl), Sea Salt, Aged Traffic, K-PAH, OC-PAH and Ca-PAH. These particle types were grouped into 5 general categories: Carbonaceous, Metal Containing, Sea-Salt, Aged Traffic and PAH.

In Barcelona an ATOFMS which incorporated a converging nozzle inlet was deployed and collected a total of 326395 size-resolved single particle dual ion mass spectra. 282117 of these particles were divided into 22 particle types: EC Traffic, EC-NIT (aged EC), K-CN, K-EC, Fresh/Local EC, Aged/Transported Biomass, Oxidised OC, OC NIT, K-SUL, Sea-Salt, Na-EC, Saharan Dust, Ca Dust, Dust, Oil-V, Fe, Pb-Cl, Mn, Cu, Veg-KP, Ca-EC, Amine 84 (ETS) and PAH. These particle types were grouped into 9 general categories Carbonaceous, Sea Salt, Dust, Heavy Oil Combustion, Metal Containing, Vegetative, Lubricating Oil, Amine and PAH.

At both of the measurement sites, carbonaceous particles were found to dominate with 94% and 66% of the classified particles being attributed to carbonaceous aerosol in Paris and Barcelona respectively. In Paris the carbonaceous particles were described as being due to local or transported emissions. Locally emitted EC Traffic, EC Biomass, $ECOCSO_X$ and Fresh and Aged Biomass OC particle types all exhibited strong diurnal trends and were present during all meteorological regimes. $ECOCNO_X$, $OCNO_X$, $OCSO_X$, Transported Biomass OC and Amine Rich did not exhibit a strong diurnal profile and were detected with increased particle numbers during continental transport events and were therefore attributed to the transport of emissions to the site. Higher particle counts were observed for $ECOCSO_X$, and $OCSO_X$ during a fog event on 18 January 2010, which suggests that these particles may be the result of heterogeneous processing of locally emitted particles. In Barcelona; EC-NIT, K-CN, K-EC, Fresh/Local EC, Aged/Transported Biomass and OC-NIT all exhibited similar trends with a maxima occurring at the end of the campaign, during a period of stagnant weather where local and regional emissions dominated. Oxidised OC was found to be present throughout the campaign. It did not increase in contribution during the stagnation period and the daily trend of these particles suggests that they originated from the processing of combustion particles. During a European air mass event K-SUL particles were observed suggesting that long range transport is also a source of carbonaceous particles in Barcelona.

During both campaigns sea-salt particles were detected, however unsuprisingly given its coastal location, a greater proportion of classified particles in Barcelona were sea-salt with 15.3% as opposed to 2.79% of particles observed in Paris. Both sites showed increased sea-salt counts during periods influenced by marine air masses. In Barcelona an afternoon peak was also observed which coincided with sea breezes.

At both measurement sites several metal-containing particle types were identified; Fe-Rich, Oil-V and Incineration (Pb-Cl). The Fe-Rich particle type was largely attributed to industrial emissions and, particularly in Paris, to transported industrial emissions as the particle counts were higher during continental air mass intrusions. The Oil-V particles presented mass spectra similar to shipping and heavy oil combustion particles classified in previous studies. In Barcelona the particles showed a dependence on the direction of the port, while in Paris the Oil-V particle counts

increased during marine air masses where the trajectory would bring the air mass over shipping lanes and heavily industrialised areas to the NW of Paris along with some contribution during continental air masses. A particle type characterised by the presence of strong Pb and Cl signals, labelled Pb-Cl, was identified during both campaigns and based on previous studies, attributed to incineration. These particles were detected with sharp peaks in particle number, indicative of point source emissions of industrial particles. In Barcelona, an Mn-containing particle type was also detected at the same time as the Pb-Cl containing particles and thus linked to industrial emissions.

In Paris three PAH-containing particle types were classified: K-PAH, OC-PAH and Ca-PAH. Both OC-PAH and Ca-PAH were identified as traffic emissions with the K-PAH particle type attributed to biomass burning. In Barcelona one PAH containing type was identified which was attributed to traffic emissions.

The differences in the operating principle of the instrument deployed in Barcelona allowed the detection of dust particles as the nozzle favours the transmission of super-micron particles. Three dust types were detected during the campaign. The first was identified as Saharan dust, which was found to maximise during a North African (East) air mass event. Other particle types that maximised during this period included Veg-KP, the source of which is likely associated with the transport of biogenic particles that are known to accompany Saharan dust intrusions. Both Ca-Dust and the Dust particle types were detected throughout the campaign and although they were at a maximum during the North African air mass events, the presence of these particles throughout the campaign suggests a local source.

In Barcelona a number of classes associated with low numbers of particle counts were identified: Cu (attributed to a combustion or industrial source) and Ca-EC (due to road traffic) and Amine 84 (ETS). This amine type was attributed to tobacco smoke. In Paris a final particle type presenting low particle counts was determined to be due to the aging of traffic emissions as it displayed a strong diurnal trend with peaks appearing some three hours after morning and evening rush hour peaks.

The ATOFMS data collected during both campaigns was compared to concurrent quantitative measurements. In Paris ATOFMS particle types were compared with

MAAP, aethalometer and AMS measurements. The ATOFMS particle counts showed poor correlations with the quantitative methods, however, the ATOFMS temporal profiles exhibited increases in particle counts coincident with increases in concentration of BC and carbonaceous aerosol. ATOFMS undercounting was observed during periods with very high ambient concentrations, which was attributed to an instrumental issue (busy time). Scaling the ATOFMS particle counts greatly improved the measured correlations.

In Barcelona the metal signals within ATOFMS mass spectra were compared to hourly elemental concentrations determined by PIXE measurements. The ATOFMS was found to respond strongly to ambient concentrations of several metals, namely, aluminium, lead, manganese and zinc. However, matrix effects associated with the detection of different elements were found to be significant, making the *quantitative* determination of metal concentrations difficult. The quantitative performance of the ATOFMS improved for certain metals under specific meteorological conditions. This improvement was likely due to the enhanced occurrence of certain particle types during these periods improving the ATOFMS ion signal as the domination of a specific particle type results in matrix effects being removed from the sampling. The ATOFMS operating with a converging nozzle inlet was found to detect the presence of metals in particles more effectively than the one fitted with an AFL. This was attributed to differences in the operating procedures of the two instruments. The AFL ATOFMS increases the transmission of sub-micron particles and therefore has bias towards smaller combustion aerosols, resulting in the ion signal for the metals of interest being interfered with by *m/z* fractions associated with organic fragments. The nozzle inlet increases the transmission of super-micron particles and therefore the interference associated with organic fragments is not as problematic. The comparison of the ATOFMS with PIXE shows that the ATOFMS is a very powerful technique for characterising the mixing state of metal-containing particles which is not measurable using off-line techniques. ATOFMS measurements are useful for monitoring short-lived emissions of particles, information which not available using traditional off-line filter measurements. Overall, while it was found that the quantification of metals using ATOFMS is problematic due to the matrix effects associated with different particles, it was found that when the data was analysed under certain conditions (e.g. during specific air masses or when monitoring specific

particle or emission types like industrial emissions vs general background/ambient) the quantifications improved.

Different ATOFMS analysis techniques were examined in order to determine if the particle types classified by different analysis techniques were comparable. *K*-means analysis classified more particles and identified more particle types. However, it was found that for Aged/Transported Biomass, K-SUL, Oil-V, Fe, Pb-Cl, Ca Dust, Saharan Dust and sea-salt there were clear correlations with particles determined using ART-2a. While there was a complicated relationship for carbonaceous particle types, similar particle classifications were found for EC-NIT, K-CN, K-EC and Fresh/Local EC. The differences found between the two analysis methods were found to be mainly due to user inputs. However, it was found that, especially for carbonaceous particles, the differences in the data treatment resulted in different average mass spectra and was likely due to the approach each method uses to normalise the spectra prior to analysis.

Overall this work demonstrates that the ATOFMS is a very useful technique in the determination of the size resolved chemical composition of single particles in real-time. In fact the ATOFMS remains one of the few instruments capable of providing this information. While the data provided by the ATOFMS is not quantitative, the benefit of the technique is that it enables identification of the different particle types influencing the measurement site and also the mixing state of the particle - information not provided by other techniques. Several issues were observed with ATOFMS measurements. Firstly matrix effects are apparent where the degree of ionisation, and hence the strength of the signal for a certain species depends strongly on the chemical composition. Secondly, during periods of very high concentration the ATOFMS can suffer from "busy time" where the time taken to process the data generated by single particles limits the overall particle detection efficiency. Nevertheless, scaling the ATOFMS data to unbiased sizing measurements can be used to account for several of the sampling issues associated with ATOFMS measurements and can provide semi-quantitative information from the particle type data.

Appendix 1 (Chapter 3)

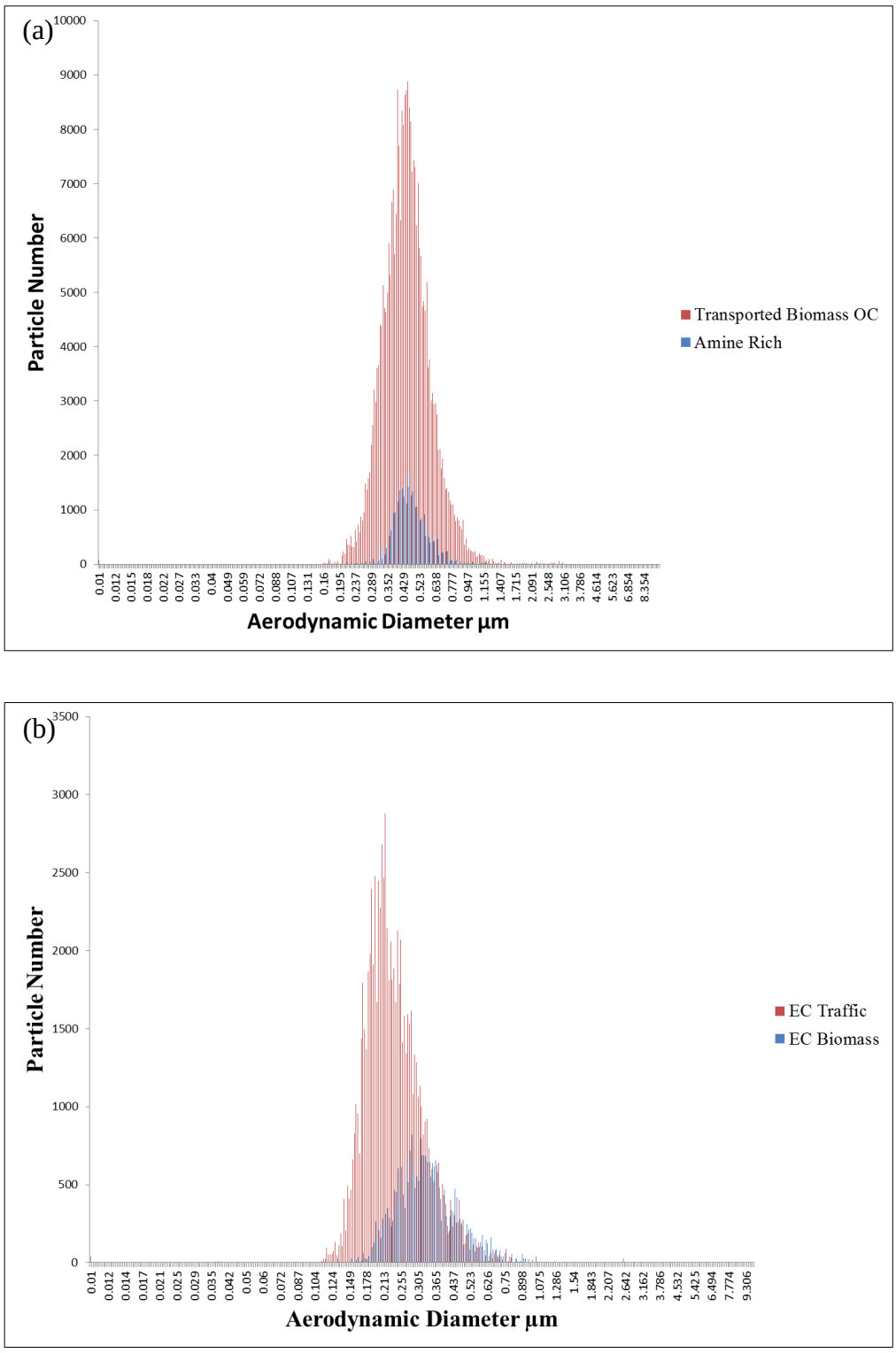

Figure A1.1 Size distribution of (a) Transported Biomass OC and Amine Rich and (b) EC Traffic and EC Biomass particle types Identified in Paris during MEGAPOLI.

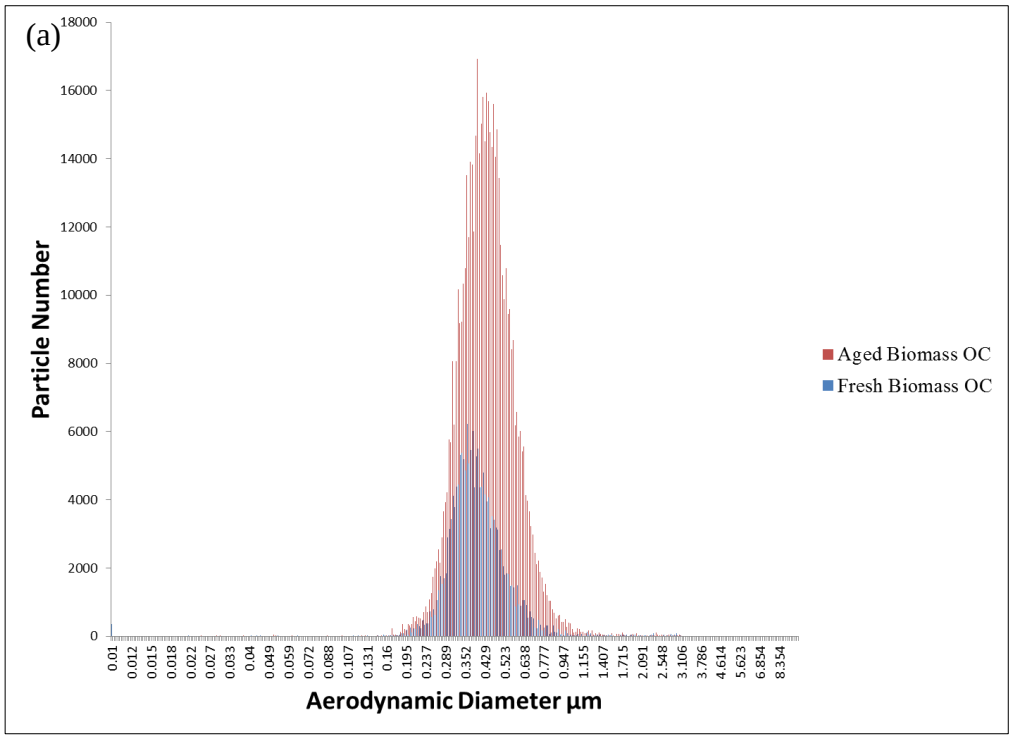

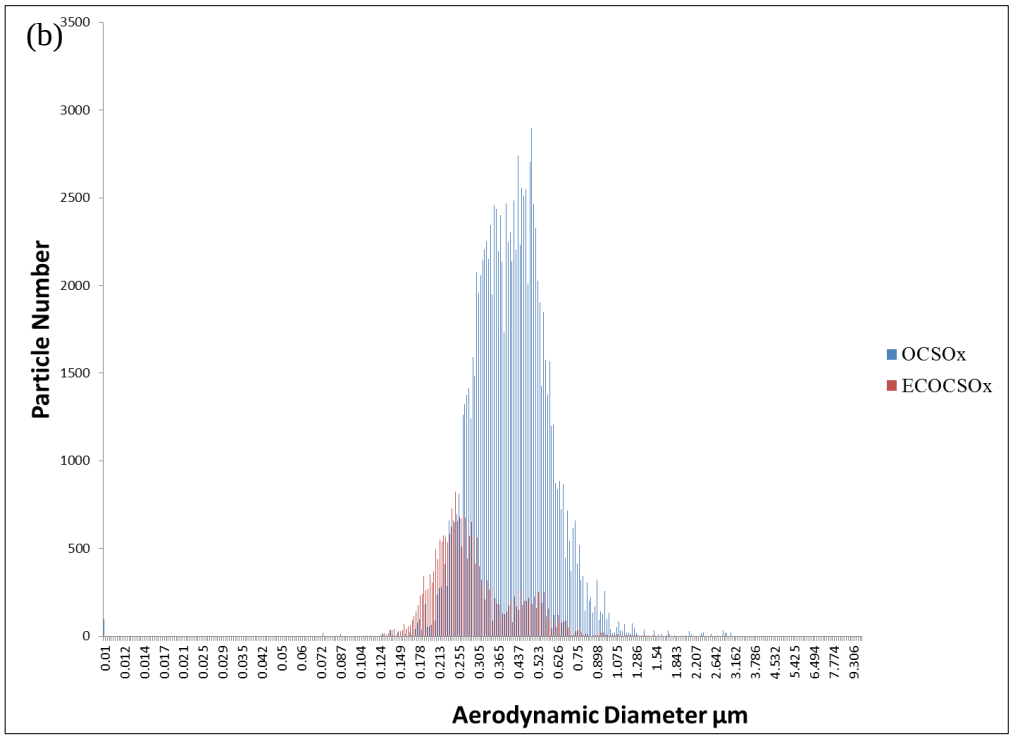

Figure A1.2 Size distribution of (a) Aged Biomass OC and Fresh Biomass OC and (b) $OCSO_X$ and $ECOCSO_X$ particle types Identified in Paris during MEGAPOLI.

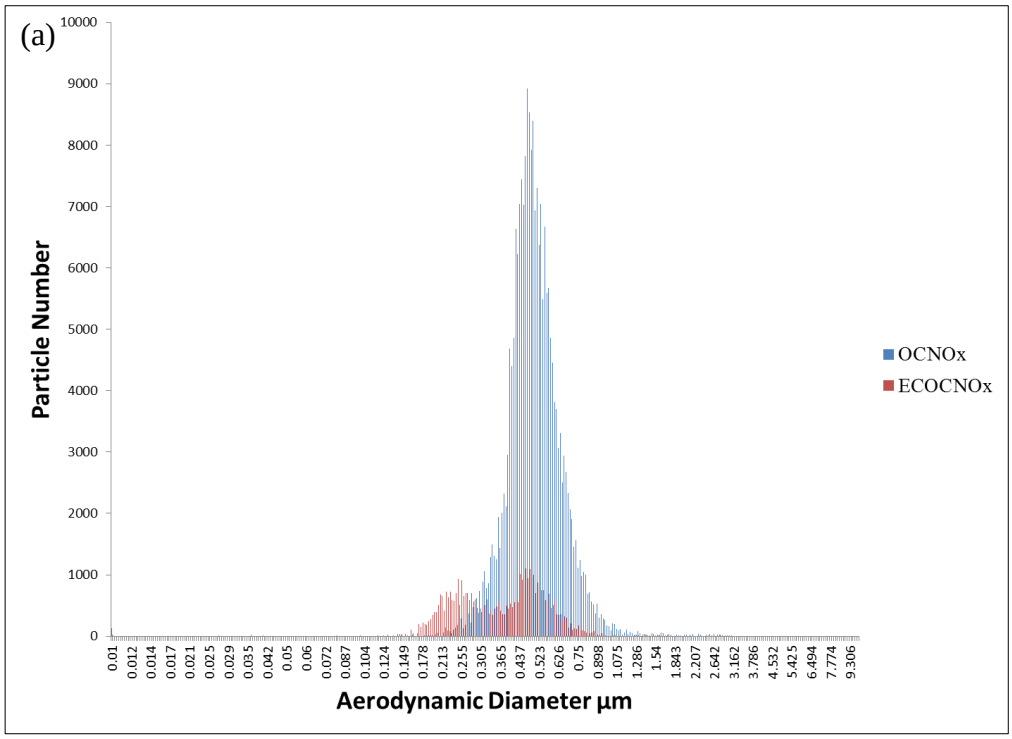

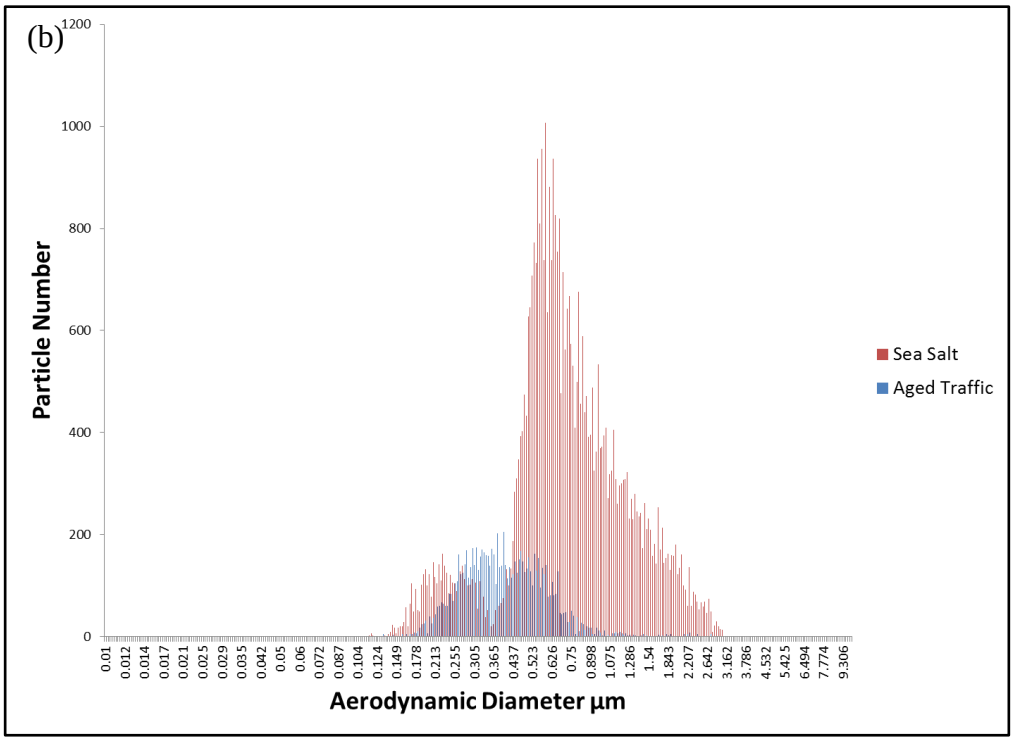

Figure A1.3 Size distribution of (a) $OCSO_X$ and $ECOCSO_X$ and (b) Sea-Salt and Aged Traffic particle types Identified in Paris during MEGAPOLI.

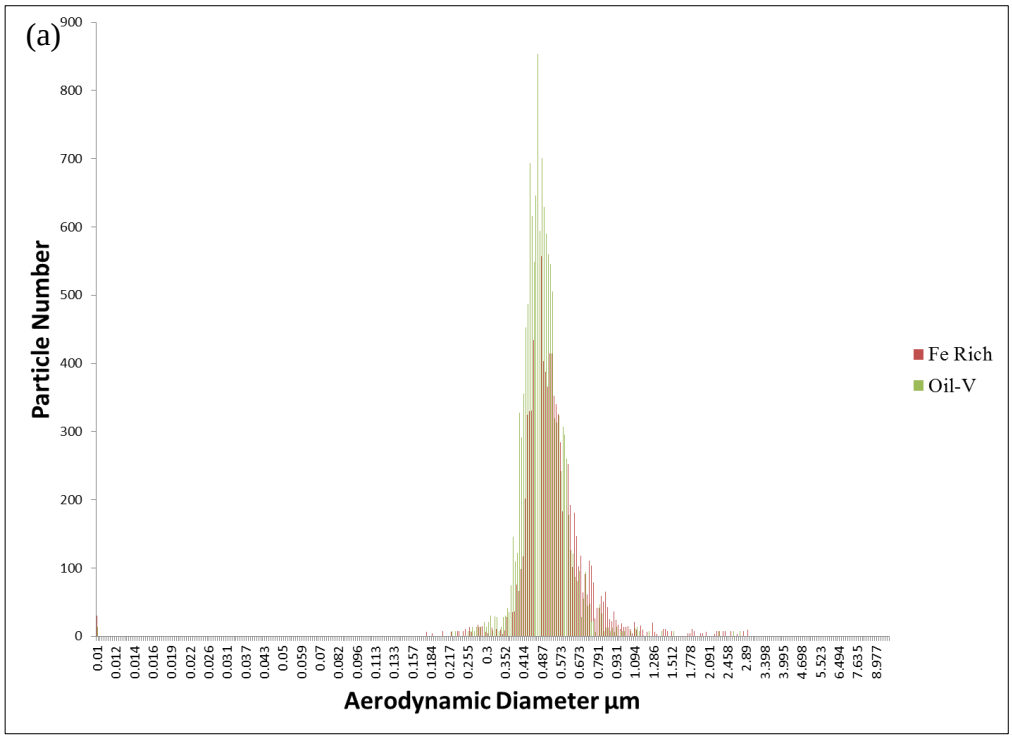

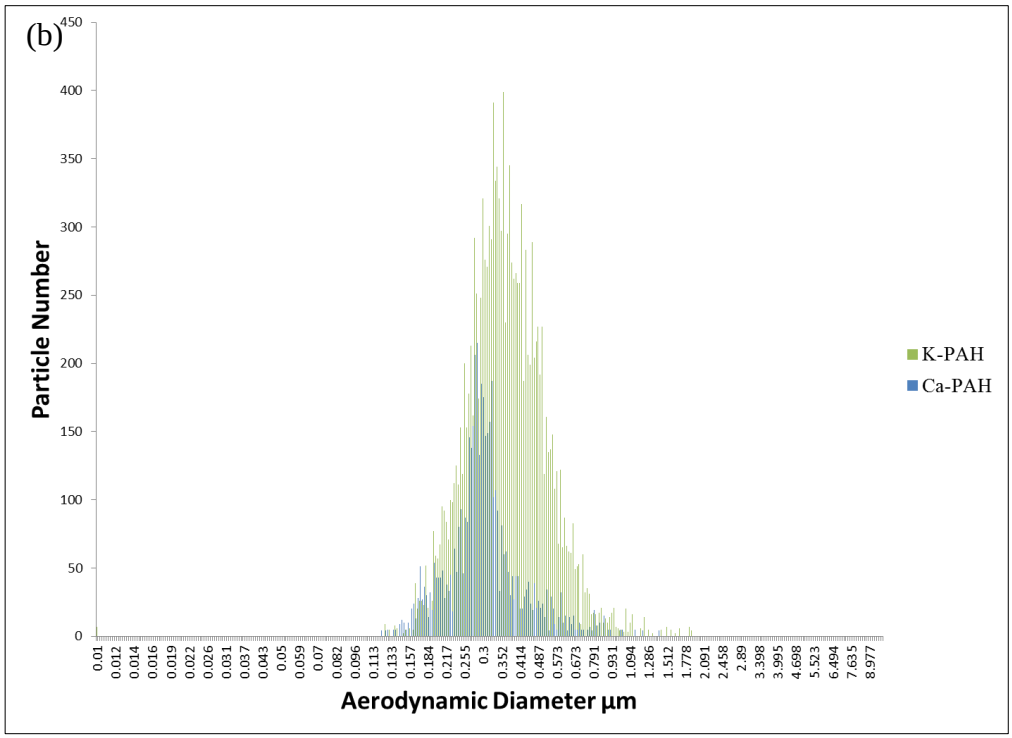

Figure A1.4 Size distribution of (a) Fe Rich and Oil-V and (b) K-PAH and Ca-PAH particle types Identified in Paris during MEGAPOLI.

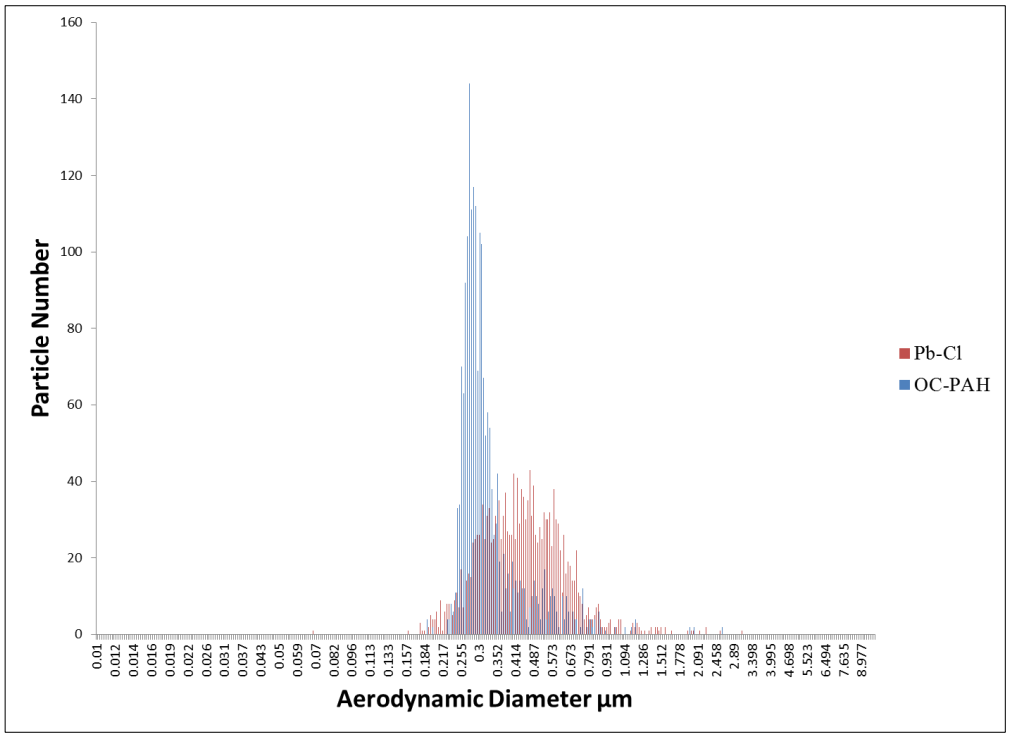

Figure A1.5 Size distribution of Pb-Cl and OC-PAH particle types Identified in Paris during MEGAPOLI.

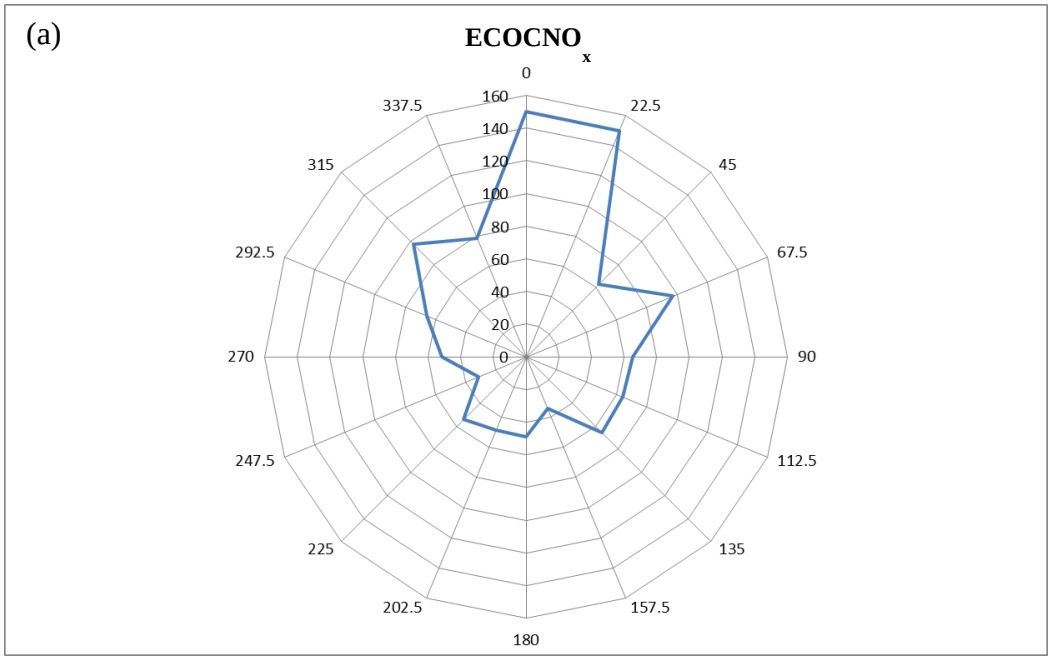

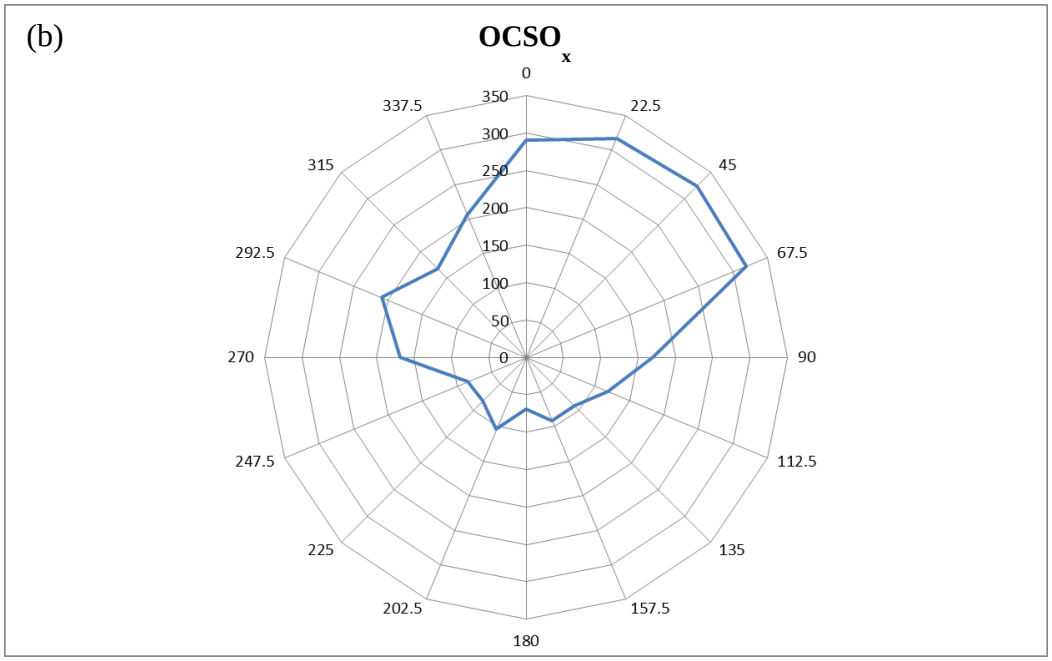

Figure A1.6 Wind dependence of (a) $ECOCNO_X$ and (b) $OCSO_X$ particle types observed during MEGAPOLI in Paris.

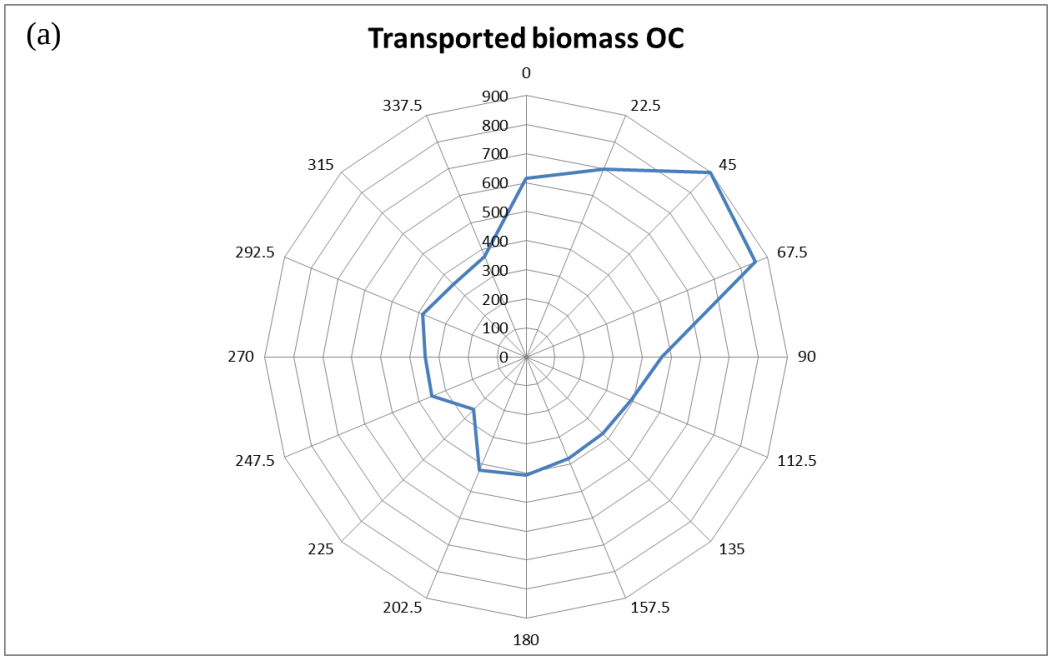

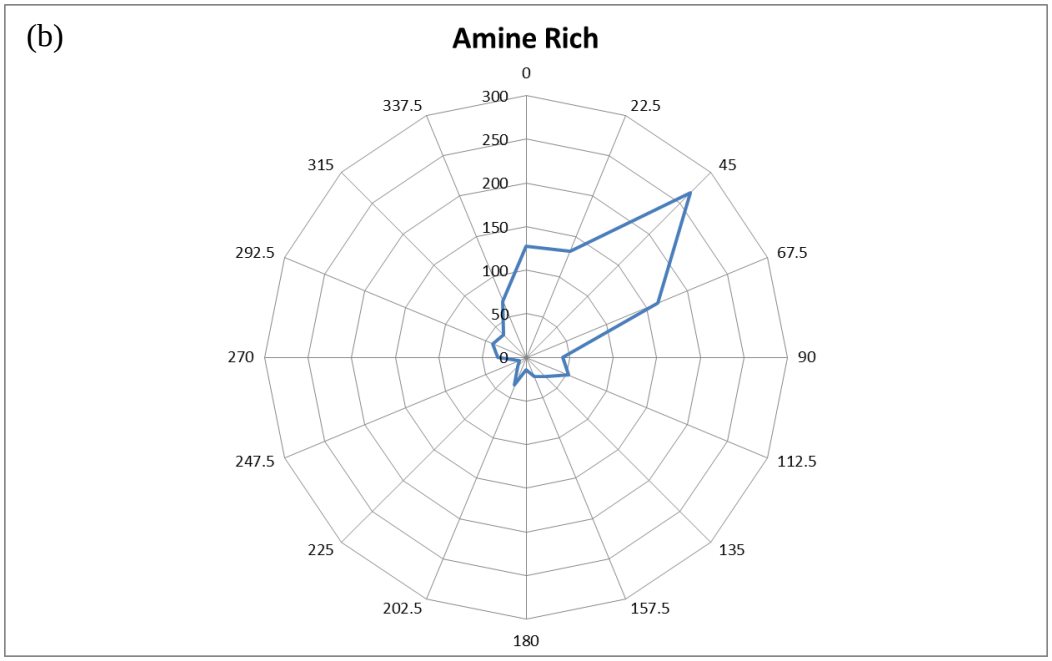

Figure A1.7 Wind dependence of (a) Transported Biomass OC and (b) Amine Rich particle types observed during MEGAPOLI in Paris.

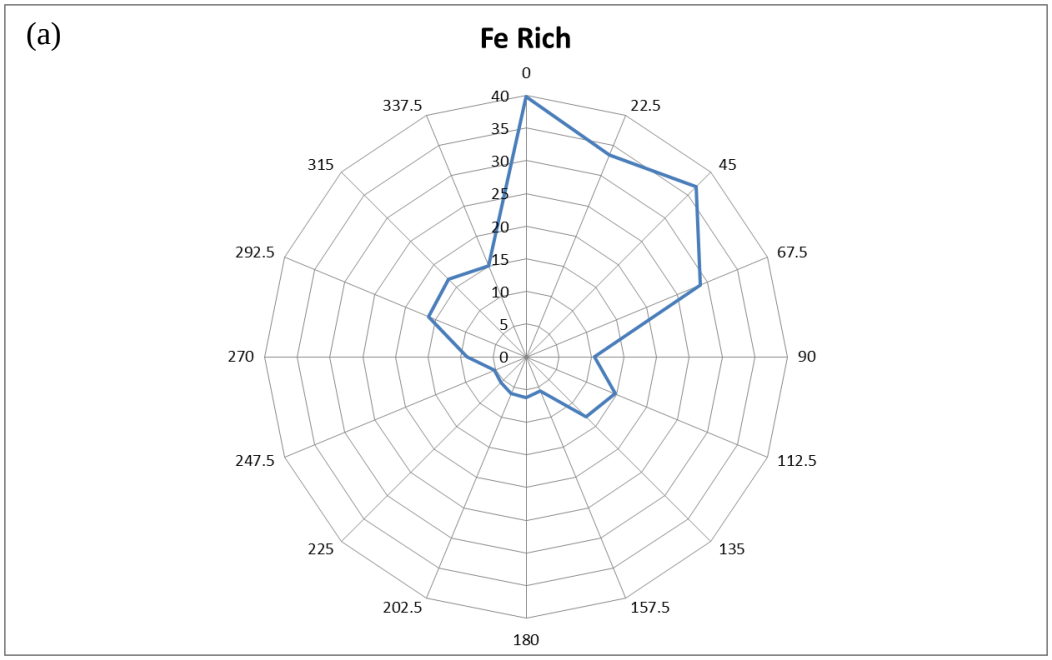

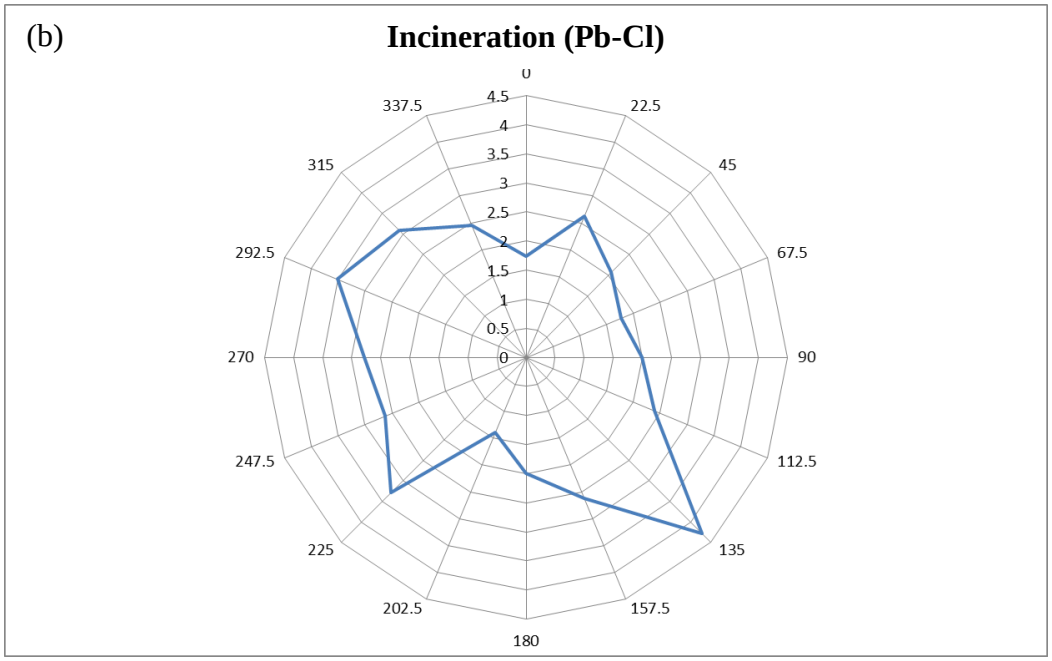

Figure A1.8 Wind dependence of (a) Fe Rich and (b) Incineration (Pb-Cl) particle types observed during MEGAPOLI in Paris.

Appendix 2 (Chapter 4)

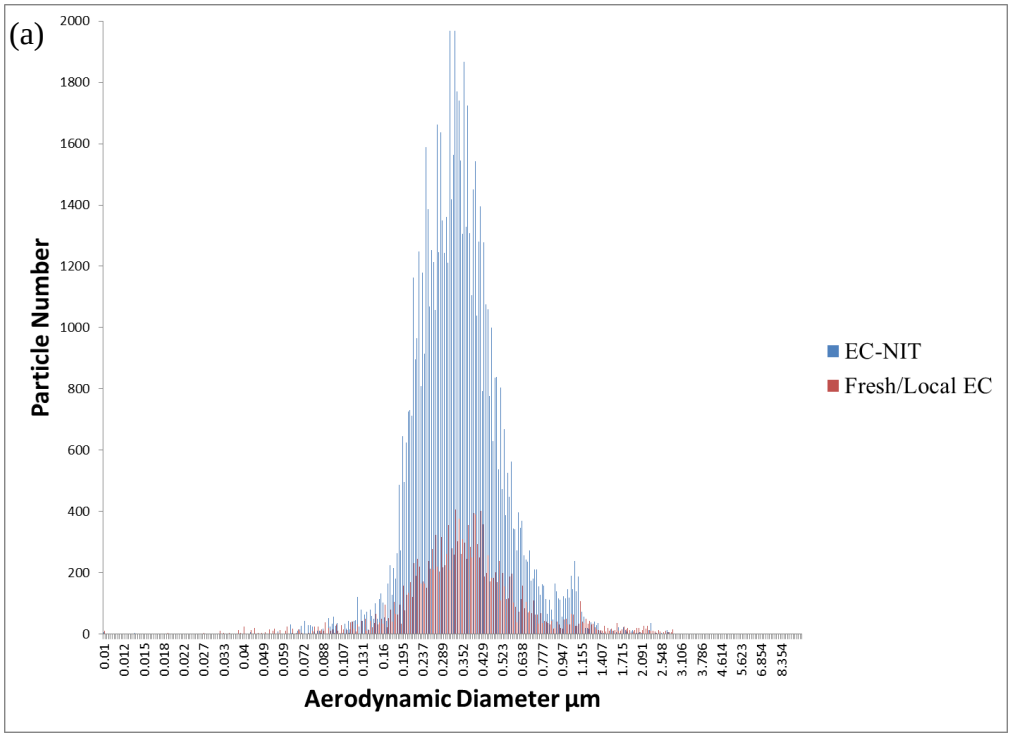

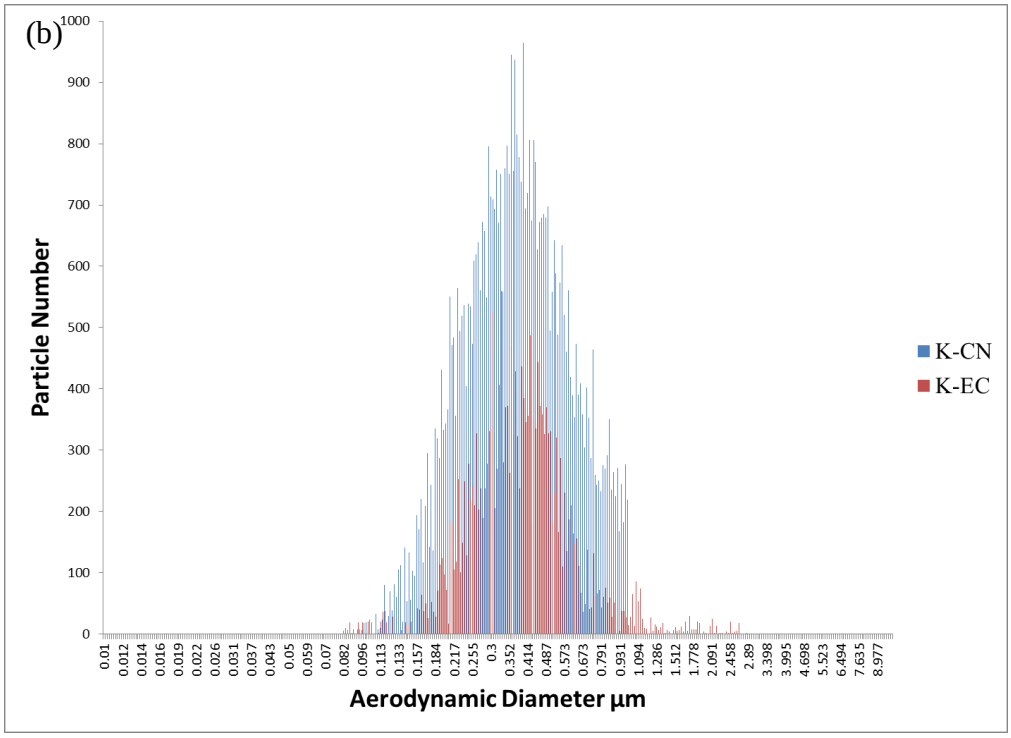

Figure A2.1 Size distribution of (a) EC-NIT and Fresh/Local EC and (b) K-CN and K-EC particle types Identified in Barcelona during SAPUSS.

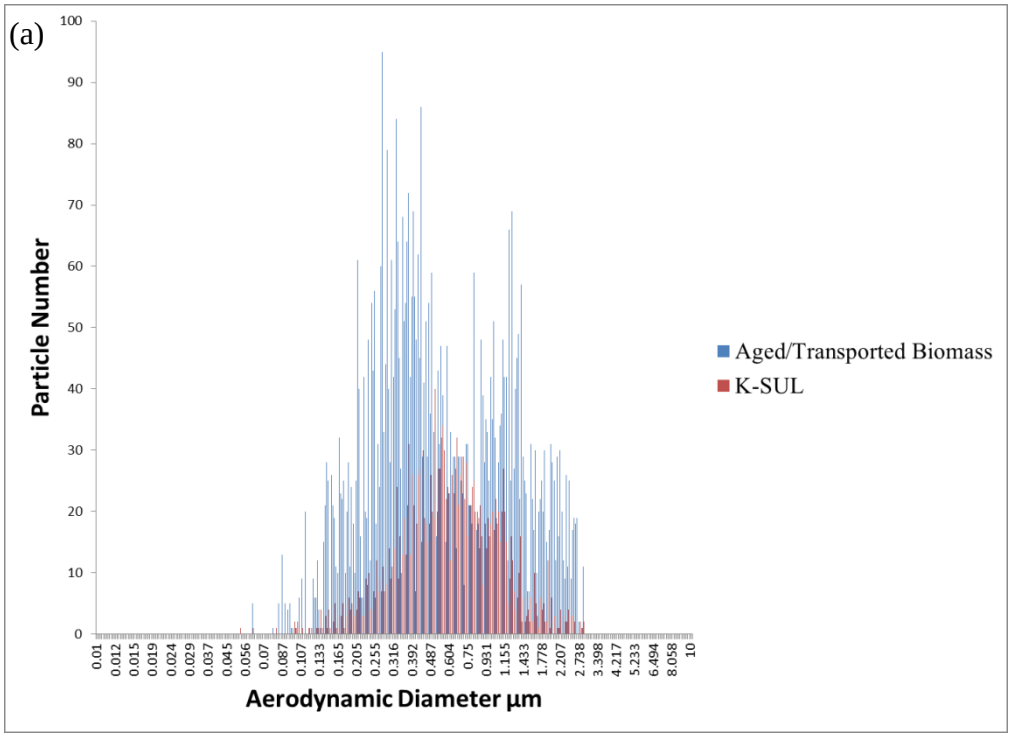

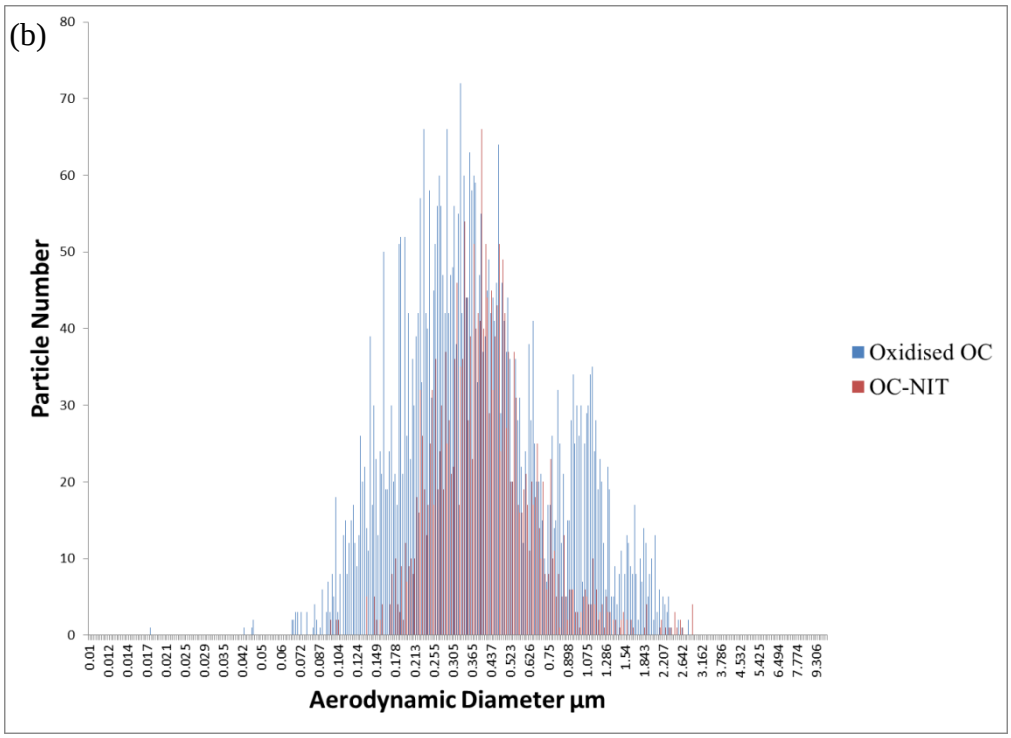

Figure A2.2 Size distribution of (a) Aged/Transported Biomass and K-SUL and (b) Oxidised OC and OC-NIT particle types Identified in Barcelona during SAPUSS.

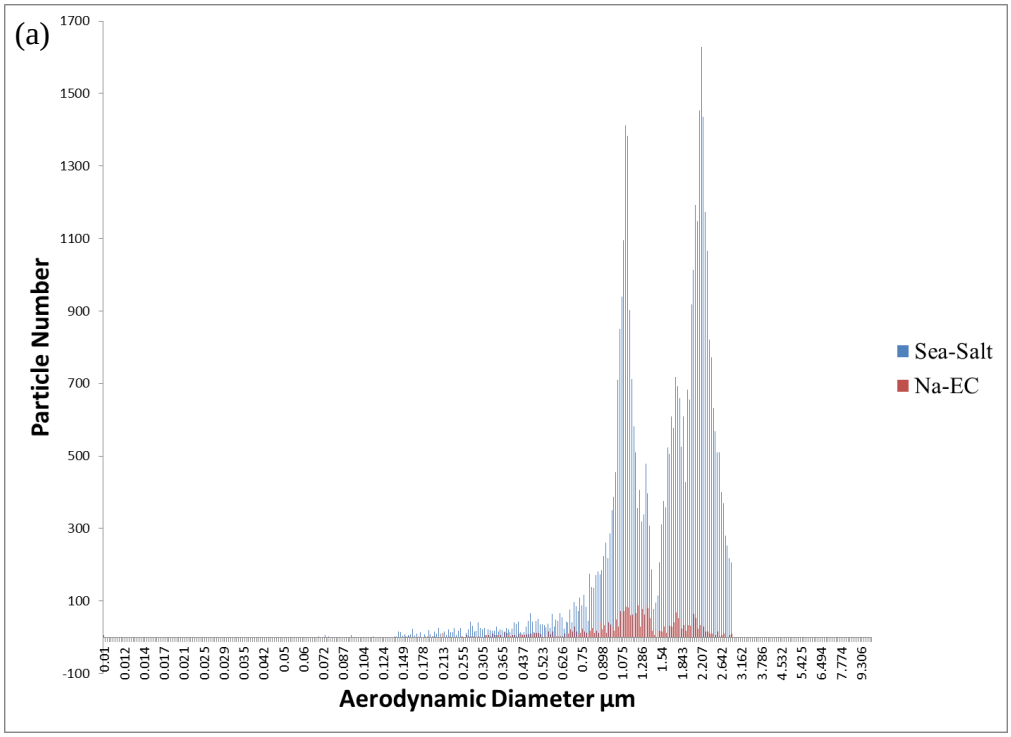

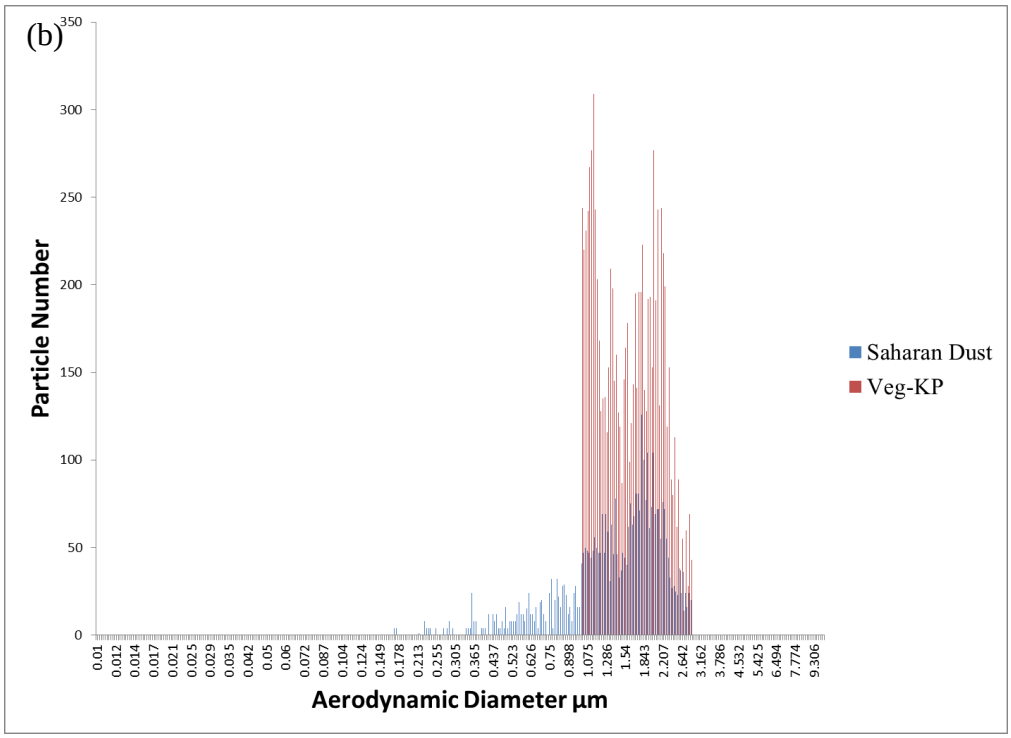

Figure A2.3 Size distribution of (a) Sea-Salt and Na-EC and (b) Saharan Dust and Veg-KP particle types Identified in Barcelona during SAPUSS.

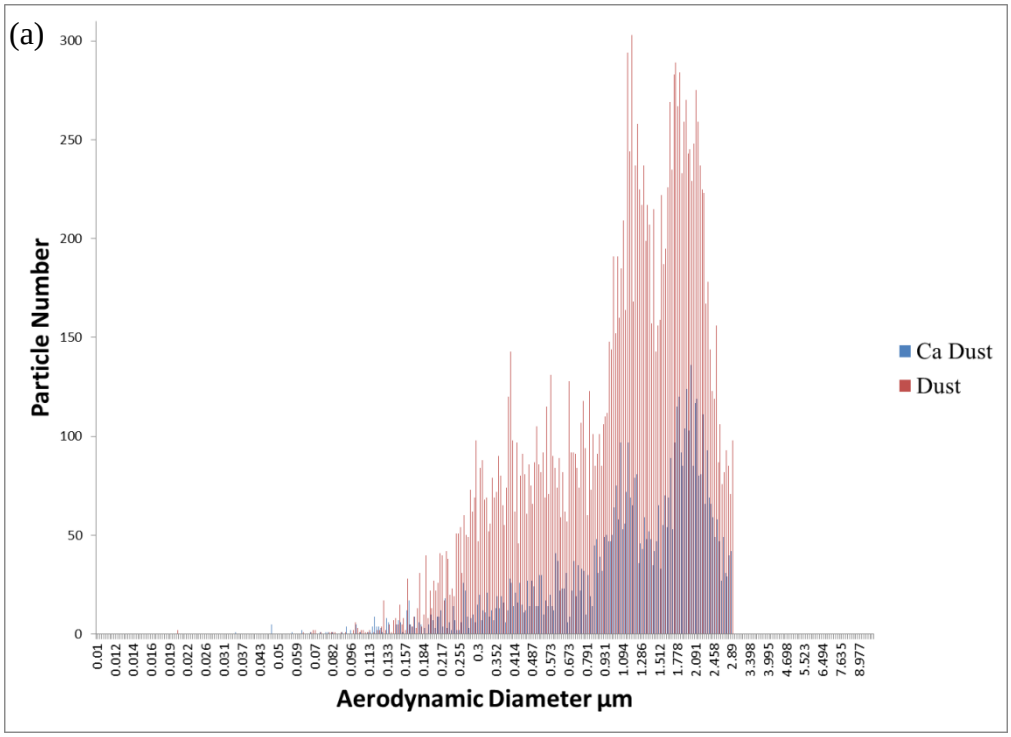

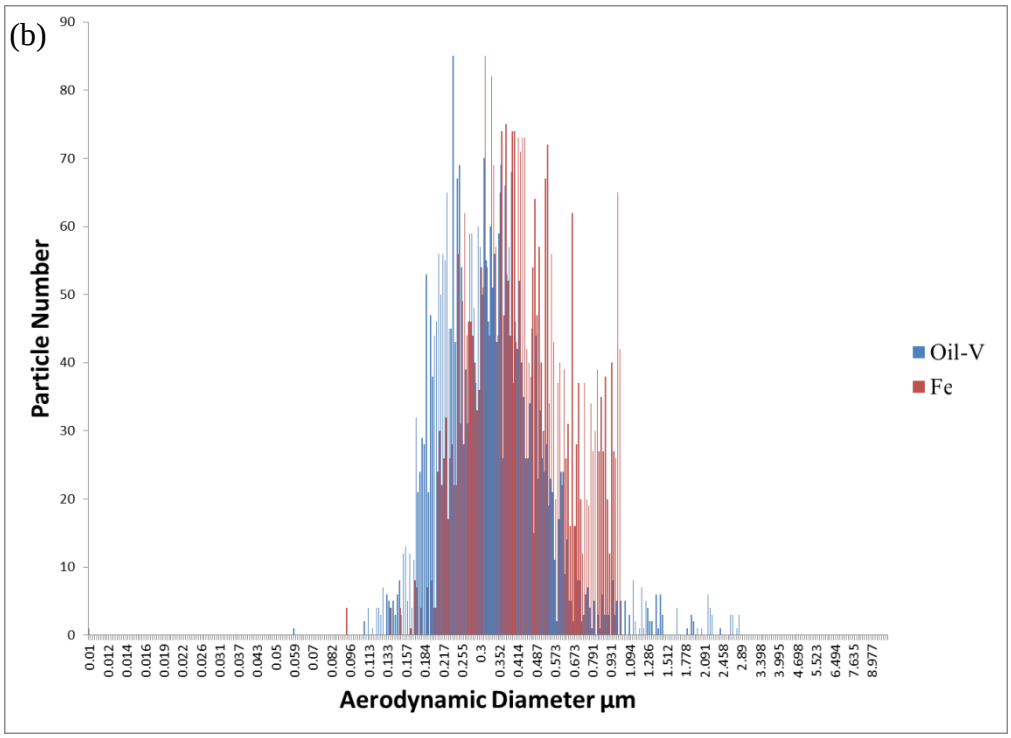

Figure A2.4 Size distribution of (a) Ca Dust and Dust and (b) Oil-V and Fe particle types Identified in Barcelona during SAPUSS.

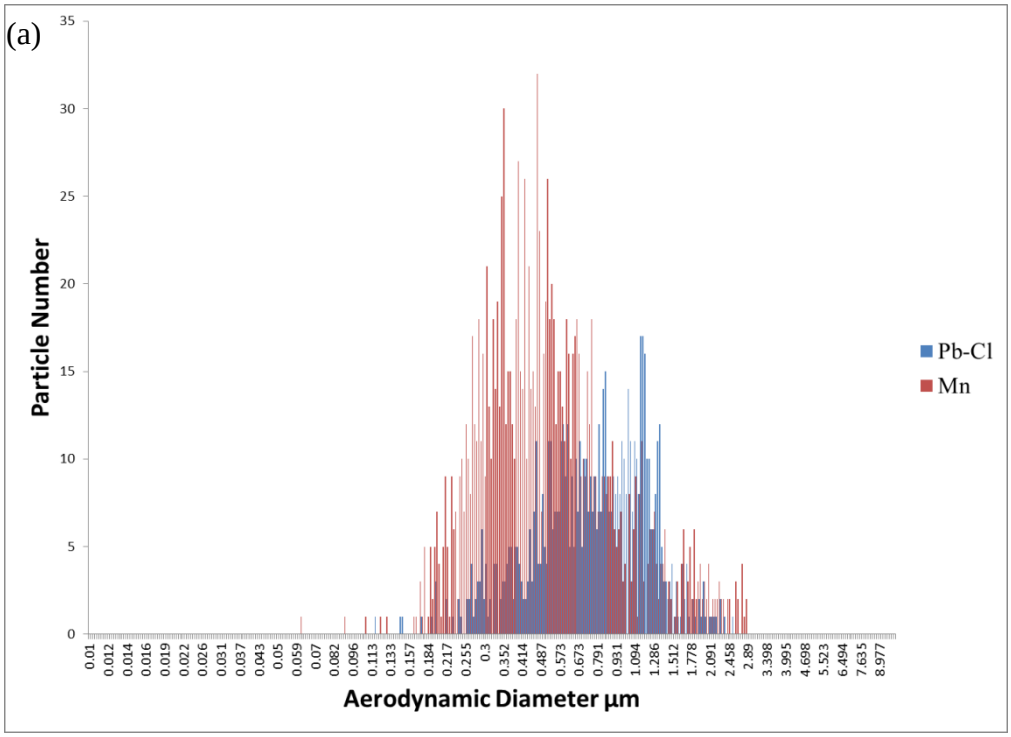

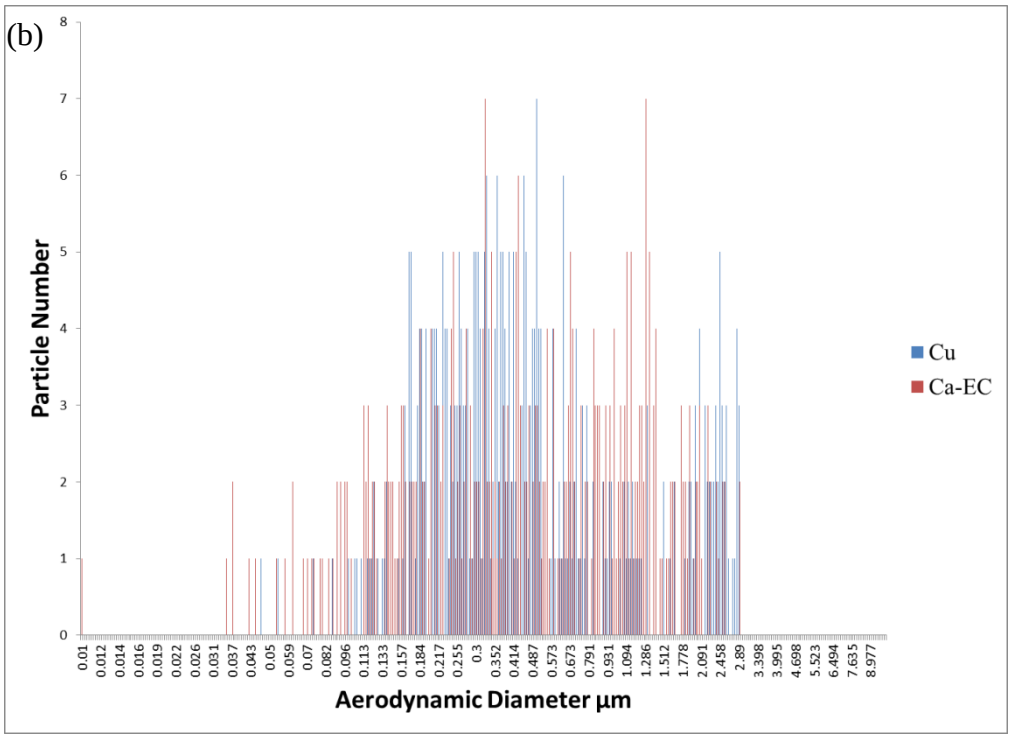

Figure A2.5 Size distribution of (a) Pb-Cl and Mn and (b) Cu and Ca-EC particle types Identified in Barcelona during SAPUSS.

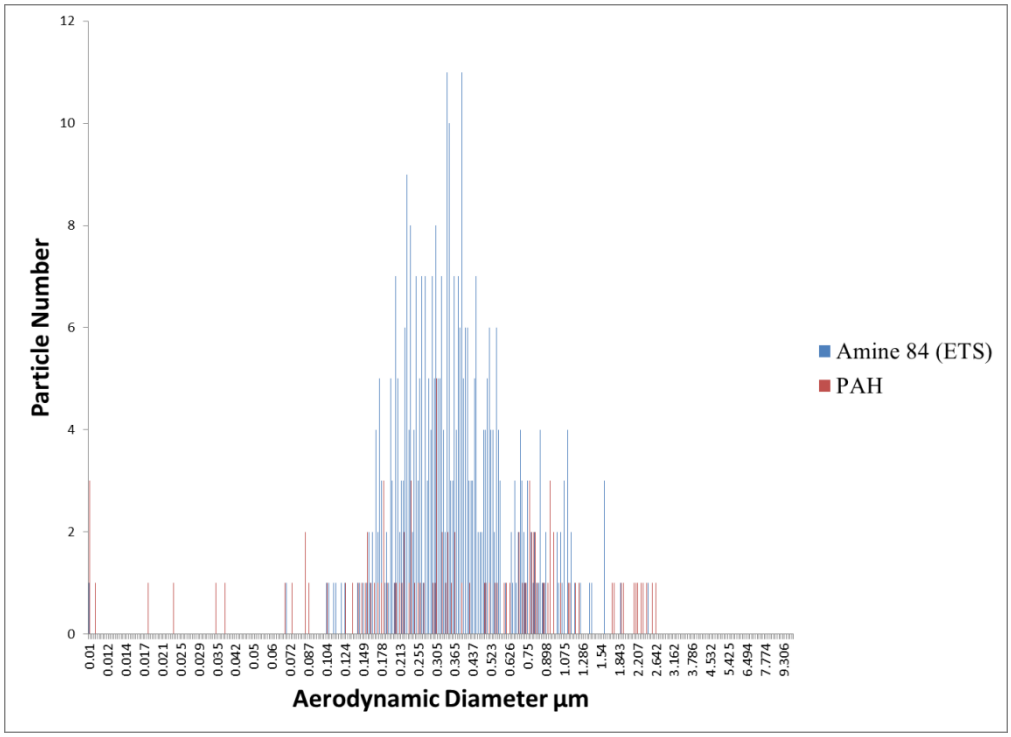

Figure A2.6 Size distribution of Amine 84 and PAH particle types Identified in Barcelona during SAPUSS.

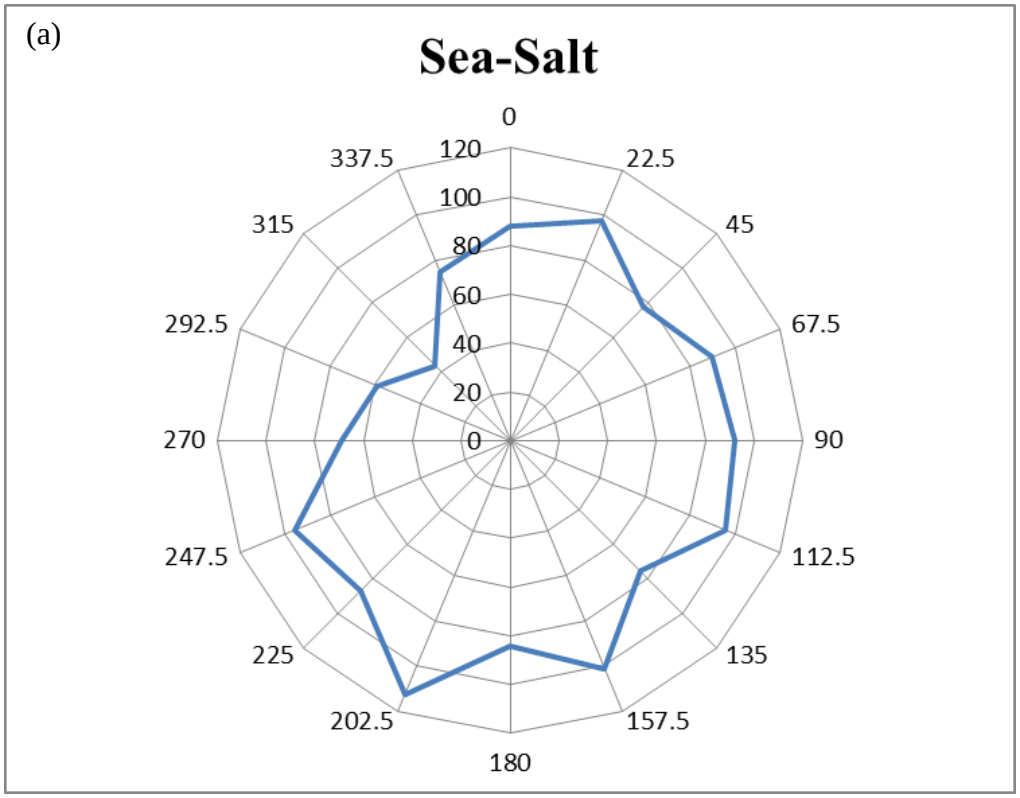

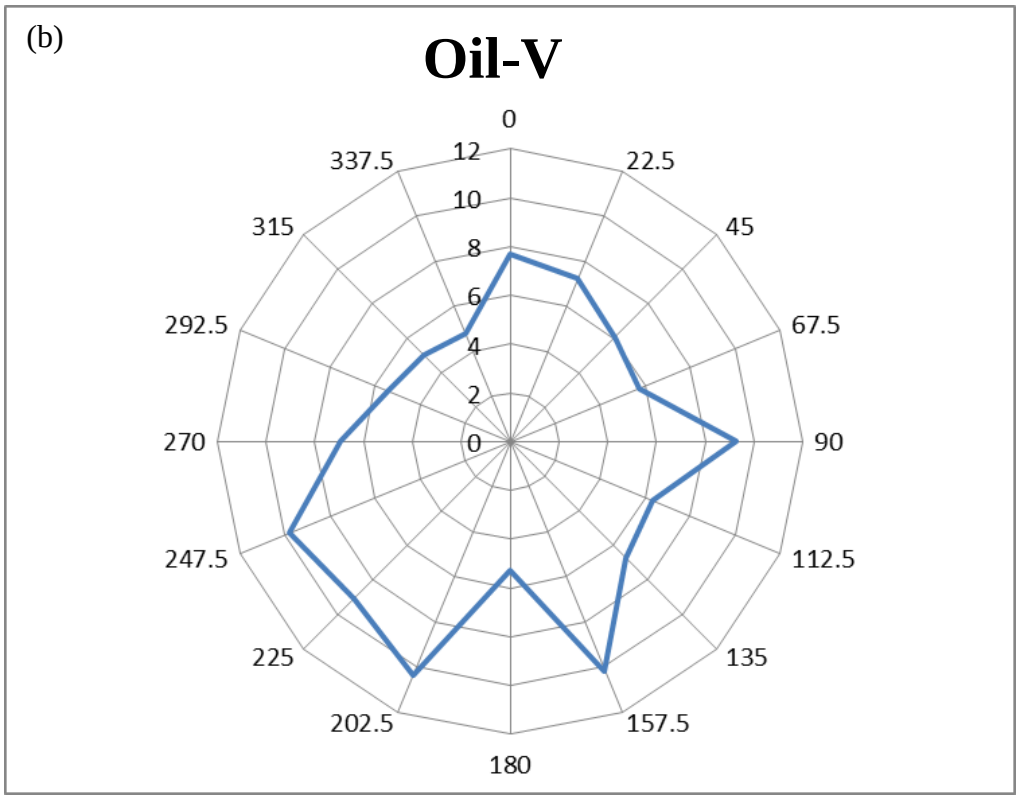

Figure A2.7 Wind dependence of (a) Sea-Salt and (b) Oil-V particle types observed during SAPUSS in Barcelona.

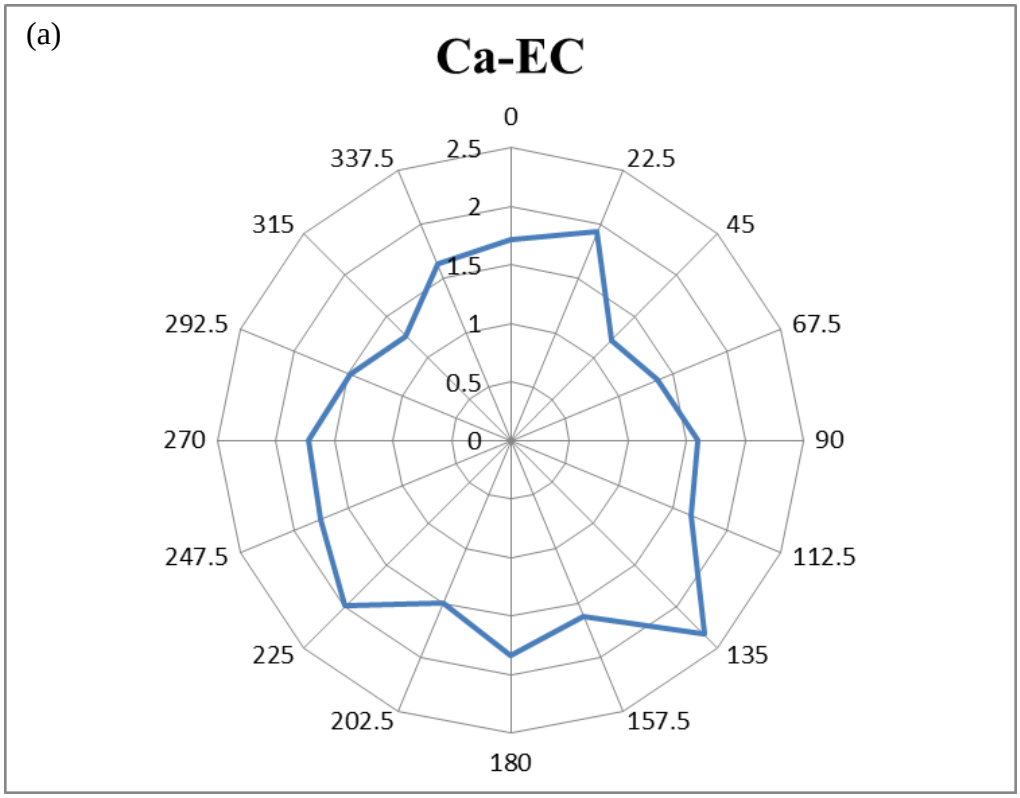

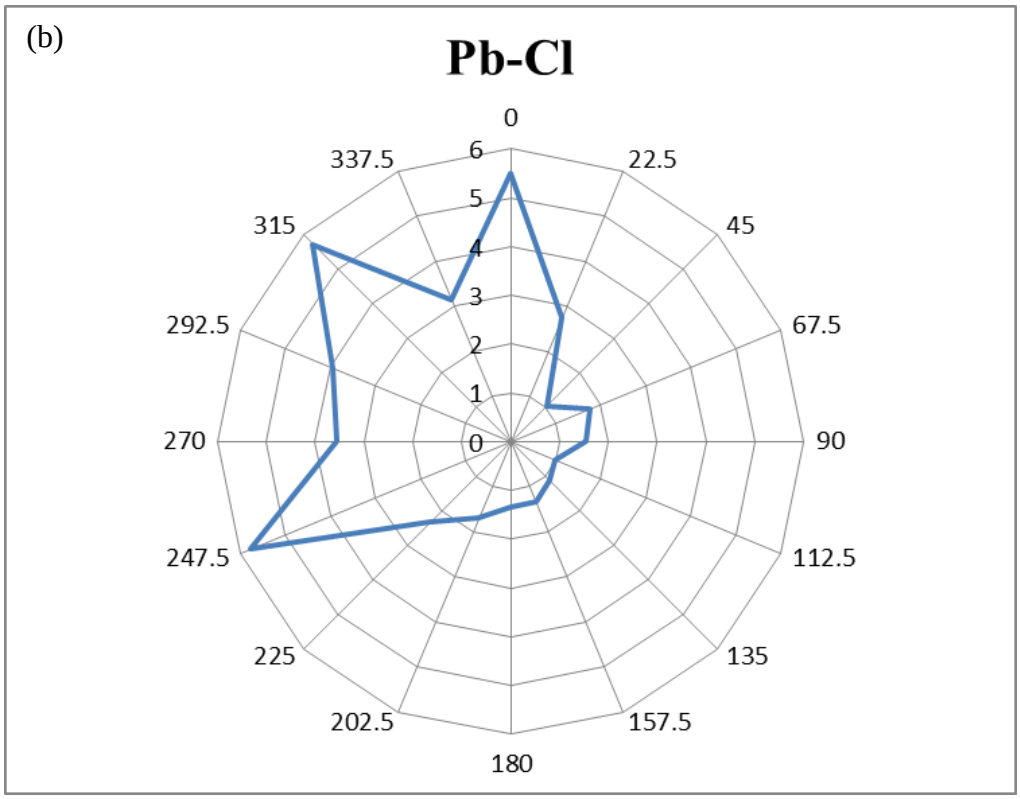

Figure A2.8 Wind dependence of (a) Ca-EC and (b) Pb-Cl particle types observed during SAPUSS in Barcelona.

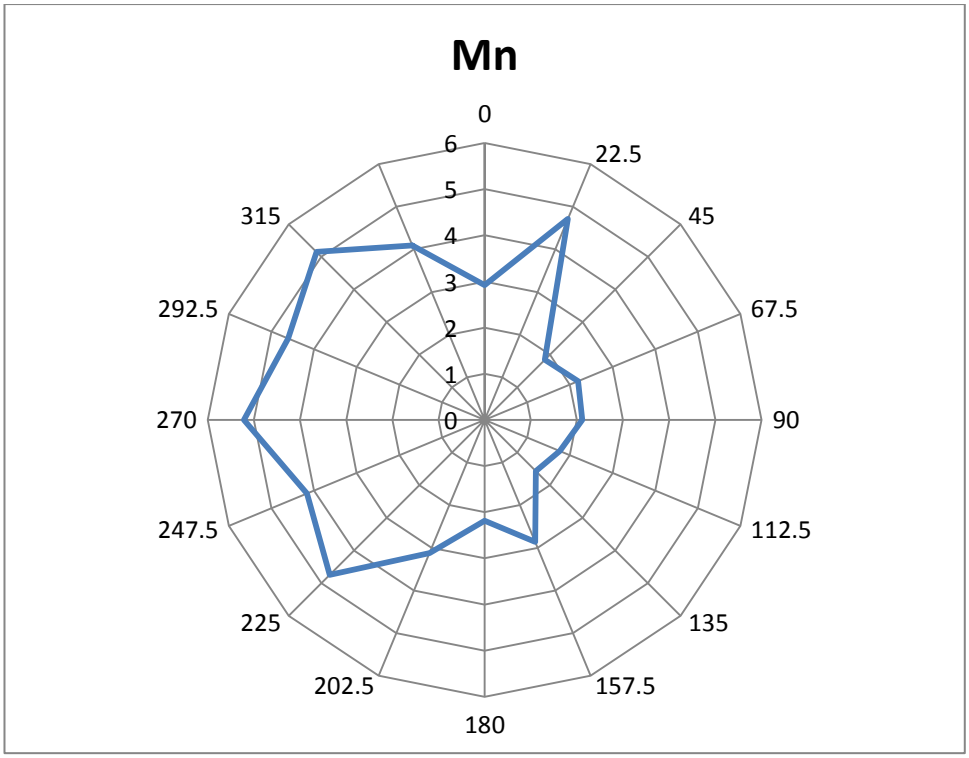

Figure A2.9 Wind dependence of the Mn particle type observed during SAPUSS in Barcelona.